Insights into turbulent free-shear-layer dynamics from vortex-gas computations and statistical mechanics

A Thesis

Submitted for the Degree of

DOCTOR OF PHILOSOPHY

by

SAIKISHAN SURYANARAYANAN

ENGINEERING MECHANICS UNIT
JAWAHARLAL NEHRU CENTRE FOR ADVANCED SCIENTIFIC RESEARCH
(A Deemed University)
Bangalore – 560 064

JULY 2014

To the Maharajas of Mysore and the Tatas

DECLARATION

I hereby declare that the matter embodied in the thesis entitled "**Insights into turbulent free-shear-layer dynamics from vortex-gas computations and statistical mechanics**" is the result of investigations carried out by me at the Engineering Mechanics Unit, Jawaharlal Nehru Centre for Advanced Scientific Research, Bangalore, India under the supervision of **Prof. Roddam Narasimha** and that it has not been submitted elsewhere for the award of any degree or diploma.

In keeping with the general practice in reporting scientific observations, due acknowledgement has been made whenever the work described is based on the findings of other investigations

_____

Saikishan Suryanarayanan

CERTIFICATE

I hereby certify that the matter embodied in the thesis entitled "**Insights into turbulent free-shear-layer dynamics from vortex-gas computations and statistical mechanics**" has been carried out by **Mr. Saikishan Suryanarayanan** at the Engineering Mechanics Unit, Jawaharlal Nehru Centre for Advanced Scientific Research, Bangalore, India under my supervision and that it has not been submitted elsewhere for the award of any degree or diploma.

_____

Prof. Roddam Narasimha

(Research Supervisor)

Acknowledgements

I am greatly indebted to my advisor Prof. Roddam Narasimha, who has been a source of inspiration and original ideas. I have not only gained insights on turbulent flows, but also on other facets of science, arts, philosophy, epistemology, history and culture through the numerous formal and informal discussions I have had with him.

I am very thankful to our collaborators, Prof. Garry Brown (Princeton) and Prof. N.D. Hari Dass (IMSc / Chennai Math. Inst.) for their active involvement in many parts of this work.

Our largest and most definitive simulations have been made possible by the access to supercomputing resources on the Tata EKA in the early stages of this study and at Intel more recently. In this regard, I am grateful to Drs. S. D. Sherlekar, R. K. Lagu (Intel Labs Bangalore, formerly CRL) and team. We also thank S. Sapre (TCS) and R. K. V. Malladi (Intel) for assistance in parallelizing and managing computer resources for running our code respectively. We acknowledge support from DRDO through the project RN/DRDO/4124 and from Intel through project RN/INTEL/ 4288.

I thank Prof. Rama Govindarajan (JNCASR / TIFR-H) for discussions particularly those related to instability and for providing access to her group's stability code. She has also been of great personal support. I thank Prasanth Prabhakaran (JNCASR) for discussions and for providing DNS results, which were used for comparison in Chapter 6.

The innumerable discussions I have had with Dr. Anubhab Roy and Dr. Sourabh Diwan have been very helpful. I am thankful to Prof. Uriel Frish (Grenoble) for taking his time to review a manuscript written during the early stages of this work, and to Prof. Anatol Roshko (Caltech) and Prof. N. Kumar (RRI) for detailed discussions.

Over the course of this work, I have had meaningful discussions with several other investigators, many of whom have provided me with useful suggestions. The list includes Profs. O.N. Ramesh, J. Mathew (IISc), Joel Sommeria (LEGI), Itamar Procaccia (Wiezmann), K.R.Sreenivasan (NYU), Harry Swinney (U.Texas), Fazle Hussain (Texas. Tech), J. Foss (Michigan.Tech.) Sharath Girimaji (TAMU), S.M. Deshpande, K.R Sreenivas, Santosh Ansumali, Ganesh Subramanian, Subhir Das, Kavitha Jain, N.S. Vidhyadhiraja and K.B. Sinha (JNCASR).

I thank my wife Aarthi, for her patience and passionate support, and also for discussions related to my work. My parents, K.S Suryaprabha and B. Suryanarayanan, and my uncle K.S.Muthukumar for their encouragement throughout my education. I also thank all of my friends, Vikram Devaraj and Varuna Gopalan in particular for their company. Senjuti, Anubhab, Sourabh, Rajesh, Prashanth, Jose, Sarath, Gayathri, Siddarth and Rakshith have made my time at JNCASR memorable.

I thank JNCASR faculty & staff for their support. Mr. Sharanappa and Ms. Vasantha from the dining hall deserve a special mention.

Abstract

Free turbulent shear flows (e.g. mixing layers, jets and wakes) are ubiquitous in a wide range of technologically relevant (e.g. combustion, chemical lasers) and geophysical flows. The convincing demonstration of the presence of 'coherent (vortical) structures' in a fully turbulent mixing layer by Brown and Roshko (1974), and the work that followed, revealed that turbulent shear flows are distinct in character from the widely studied statistically homogenous isotropic turbulence (H.I.T), due to the emergence (and sometimes dominance) of large scale order amidst chaos. If, as suggested by Liepmann (see Narasimha et al, 2013), H.I.T may not be the simplest problem from which to start for understanding a wider class of turbulent flows, a strong alternative candidate would be a temporally evolving plane free-shear layer. This thesis considers such a temporal free-shear layer in a vortex gas (point vortices in an inviscid fluid). This flow is investigated via extensive computer simulations. One of the objectives of this study is to investigate in great detail the central and controversial issue of universality or otherwise of the asymptotic self-preservation state (Narasimha 1990, George 2004), at least for this special case. This work makes comparison with experiments, instability and statistical-mechanical theories, describes applications to flow control and also presents results on the effects of viscosity, desingularization of the point-vortex and spatially evolving flows.

The temporal shear layer is a flow that is statistically homogeneous in the streamwise direction (x) evolving in the direction normal to it (y) from two counter-flowing streams initially separated by a thin vortical layer. It is the simplest free turbulent shear flow as it involves only one parameter, the velocity difference (ΔU) across the layer, in the high Reynolds number (Re) limit. It is favored for numerical simulations due to unambiguous boundary conditions and is usually studied in a periodic-in-x domain with period L. It is related to the spatial mixing layer which has been a subject of much experimental investigation (from Liepmann & Laufer 1947 to D'ovido & Coats 2013), via a Galilean transformation in the limit where ΔU is small compared to the convection velocity (U_m).

In the present work, the vortex gas analogue of the temporal shear layer is studied by numerically solving an appropriate initial value problem for a finite but large collection of (N) point vortices of same strength (γ) and sign in a singly periodic domain. The fluid-dynamical boundary conditions of velocity being $\pm\Delta U/2$ are satisfied at $y = \mp\infty$ by setting $\gamma = L\Delta U/N$. The evolution of this system can be described by $2N$ first-order non-linear ODEs that can be written in Hamiltonian form.

While the vortex-gas is strictly 2D and inviscid, it is not an inappropriate model to understand the large-scale momentum 'dispersal' in a turbulent free shear layer (at least before the mixing transition). The reasons are that turbulent free shear flows are largely independent of Re at sufficiently high Re; the coherent structures present in the flow have been shown to be quasi-2D (Wygnanski et al, 1979); and the vortex-gas model provides a weak solution of the Euler equations (Marchioro & Pulvirenti, 1993). Regardless of its possible connections with the 3D Navier Stokes (NS) mixing layer, it is highly worthwhile to study the vortex gas shear layer as a prototypical shear flow. Though more sophisticated vortex methods have been developed, the point-vortex model offers the possibility of connections between the dynamics of coherent structures in turbulent shear flows with the statistical mechanics of a 'vortex gas', first formulated by Onsager (1949), who proposed that the emergence of large scale order is consistent with the negative temperature states that the underlying Hamiltonian system implies. While there have been subsequent developments on both equilibrium statistical mechanics (see Eyink & Sreenivasan 2006 for a recent review) and vortex-gas kinetic theories (e.g. Chavanis 2001, 2012), they have been mostly applied to study atmospheric vortices such as the Jupiter's red spot. Attempts to relate such theory to evolving turbulent shear flows have been limited (e.g. Aref & Siggia, 1980).

There have been several earlier studies of the vortex-gas shear layer (Rosenhead 1931, Delcourt & Brown 1979, Aref & Siggia 1980) that broadly mimic such dominant features of shear layer evolution as clustering of vortices to form structures and linear growth of the layer thickness through amalgamation events between structures. The present simulations involve over 20 different classes of initial vortex y-displacements, vary N from 50 to 32000 (Delcourt & Brown use 750, Aref & Siggia use 4096), evaluate

statistics by ensemble averages over upto 10^3 realizations (no ensemble averaging has been attempted in earlier studies) and involve integration upto $3 \times 10^4 L/\Delta U$ (as against O(1) in earlier studies). All computations are carried out employing RK-4 and double precision. The time-step chosen ensures conservation of the Hamiltonian to within 0.001% per $L/\Delta U$ (Delcourt & Brown quote 6%; present long-time simulations use a smaller time-step ensuring a total change of less than 0.5%). Further, robustness of the present results has been established via detailed time step and (upto quadruple) precision studies and various internal consistency checks. The present simulations are thus far more extensive and accurate than any earlier study of this kind, and lead to the following conclusions that could not have been drawn from earlier work.

The simulations reveal the existence of three distinct regimes during the temporal evolution of the vortex-gas shear layer – an initial condition influenced Regime I (lasting over 1000 times the amplitude of the initial *y*-displacement of the vortices, for certain long wavelength initial conditions); a domain influenced Regime III; and an overlap self-similar Regime II of linear growth, relevant to the fluid-dynamic state of self-preservation (Townsend, 1956), and explained by intermediate asymptotics.

The present simulations, over a wide range of *N* and wide class of initial conditions that include both random and sinusoidal perturbations, show the Regime II spread rate in terms of the momentum thickness, $d\theta/d(t\Delta U)$, has the value 0.0166 ± 0.0002, strongly suggesting that it is universal. This represents a universality of the exponent (on *t*) as well as the coefficient in the relation between θ and *t*. However, Regime II is found to have large *N*-independent two-vortex correlations, hence neither equilibrium theories, nor existing vortex-gas kinetic theories that neglect correlations or consider them as O(1/*N*), would be relevant for describing this regime.

Regime III marks the departure from linear growth, and begins when the evolution is dominated by interaction among a small number of structures, as $t\Delta U/L$ becomes O(1). Eventually only one structure is left in the domain, and the rate of momentum dispersal is greatly reduced as the layer has no opportunity to grow by amalgamation. The present long-time simulations show that the single structure approaches its final state after two stages in relaxation, respectively characterized (Chavanis, 2012) as 'violent' and 'slow' and lasting over times of O(10) and O(10^4) of $L/\Delta U$ respectively (for $N = 400$). During the violent relaxation, excellent agreement with the 2D NS calculations (Sommeria et al, 1990, higher Re case) is observed both for layer thickness and the vorticity-stream function relation. This agreement suggests that the vortex-gas and the 2D NS approach the solution of the 2D Euler equation from different directions, and confirms the value of the vortex gas model in providing a weak solution of the Euler equations. At very long times (~10^4 $L/\Delta U$), the distribution of vortices relative to the single structure (which moves stochastically in *x*) approaches a steady state, and the vorticity-stream function relationship satisfies the 'Boltzmann distribution' proposed by Joyce & Montgomery (1973), with negative value for the temperature. Further, the distribution of the vortices within the structure is related to the Lundgren-Pointin (1977) equilibrium distribution. These results show that while Regime III can be described by equilibrium theories, Regime II (paradoxically labeled 'equilibrium' in the fluid-dynamical literature) is indeed very far from statistical-mechanical equilibrium. Thus an expansion around equilibrium seems to be an unlikely candidate to describe this strongly non-equilibrium Regime II, which we propose may legitimately called 'explosive relaxation' as it has a timescale shorter by at least one order of magnitude compared to what has been termed 'violent' relaxation.

The initial development of layer thickness observed in experiments with sinusoidal forcing (Oster & Wygnanski 1982) is quantitatively recovered as Regime I in the present simulations with appropriate space-to-time transformations. Further, the universal spread rate in Regime II is within the scatter of the quoted self-preservation spread rates reported in experiments with $\lambda \equiv \Delta U/2U_m < 0.3$, as well as LES/ DNS results for 3D NS temporal shear layers. This suggests that 2D inviscid interaction of the vortical structures via the Kelvin Biot-Savart mechanism is central to momentum dispersal in this flow. The present study also suggests that variations in growth rate reported across experiments and other simulations could be due to the inadequate appreciation of the time or distance required for relaxation to Regime II, very long memories of certain types of initial conditions, and insufficient averaging, rather than the existence of non-unique self-preservation states.

While some studies have suggested the relevance of linear (Morris et al, 1990) or weakly non-linear (Monkewitz, 1988) theories to understand fully turbulent free shear flow, the subject has been controversial (Husain & Hussain 1995). Present simulations with initial conditions representing a piece-wise linear mean velocity profile, show agreement with linear stability (Rayleigh) theory at early times. But the subsequent development (after the 'roll-up') shows that the Karman-Lamb instability theory based on monopoles is more relevant than that of Rayleigh. However, preliminary results suggest that neither approach provides a completely satisfactory explanation for Regime II, though there is a surprisingly good agreement with Rayleigh theory for the growing modes. The combination of the theoretical understanding derived from the above study and the computationally inexpensive vortex-gas simulations can be used to determine the optimal initial conditions for enhancing or suppressing the momentum dispersal (and hence mixing) for a given set of constraints. This is illustrated with examples.

While the above mentioned comparisons establish the relevance of the inviscid point-vortex simulations to high Re shear layers, the effects of viscosity are studied by incorporating them through the addition of a random walk component to the motion of each point vortex (Chorin 1973). Such 'viscous vortex gas' simulations, in which the Hamiltonian is no longer conserved, show an initially 'laminar' layer growing as $\sqrt{t}$, transitioning eventually (for $Re_\theta \gtrsim 50$) to linear growth at the same universal Regime II rate quoted earlier. An interesting finding is that over the range of Re that exhibits universal linear growth, the viscous shear 'stress' is not always negligible and can contribute upto 40% of the total shear stress, and that the Reynolds shear stress appears to 'adjust' itself to ensure self-similarity in the total stress. This suggests that the so-called 'fluid dynamical' equilibrium may have a sub-regime in which the self-similarity is in total stress rather than solely the Reynolds turbulent stress, via internal transfer or balance mechanisms that demand further investigation. There is some evidence (Redford et al, 2012) to support such a hypothesis in an axisymmetric wake. At later times, the viscous vortex gas shear layer also reaches a state with a single structure. Favorable agreement with the low Re number case of 2D NS simulations of Sommeria et al (1990) is observed in early Regime III. Far into Regime III, diffusion begins to dominate once again as the single structure 'melts' to form a uniform-in-*x* Gaussian-in-*y* distribution of vortices, and $\sqrt{t}$ growth is recovered. Simulations with desingularized vortices show a regime of scaling with the desingularization parameter, but eventually attain the same universal growth rate in Regime II.

The velocity ratio in spatially evolving shear layers plays an important role in the flow development as ΔU becomes comparable to U_m. The scatter among quoted equilibrium spread rates is most conspicuous at $\lambda = 1$ (single-stream), which raises questions on the applicability of universality at this limit. The spatial simulations with appropriate inflow and outflow boundaries, based on Basu et al (1995), show that the spread rate is very close to the temporal results near the shear-less limit and varies with λ along a curve that is concave upwards (in contrast to earlier suggestions) and is within the scatter of the experimental results through the entire range. While the equilibrium spread rate is found to be universal for a given velocity ratio, downstream boundaries can affect the flow upstream upto 80% of the domain length in the single stream limit. This may be a part of the reason for the relatively greater scatter in the experimental data for λ =1. The thesis presents a discussion of the recent experimental results of D'ovidio & Coats (2013), who report differences in structure growth mechanisms between a pre-mixing transition and a post-transition shear layer. They attribute the differences to the mixing transition and 3D mechanisms, even though the experiments were carried out at different velocity ratios (λ = 0.627 and 1.0 respectively). The present spatial vortex-gas simulations, which are purely 2D, performed at the same two velocity ratios, lead to observations similar to those in the experiment. This suggests that the change in the mechanism attributed to 3D, is more likely a consequence of the difference in λ.

List of Figures

List of Tables

Contents

Most of the work presented in Chapters 1 to 5 has been done in collaboration with Prof. N.D. Hari Dass (CMI) and has appeared in:
Suryanarayanan, Narasimha and Hari Dass "Free turbulent shear layer in a point vortex gas as a problem in nonequilibrium statistical mechanics.", *Physical Review E* 89.1 (2014): 013009.

Much of the work presented in Chapter 6 has been done in Collaboration with Prof. Garry Brown (Princeton).

The work presented in Chapter 7 has appeared (in part) in :
Suryanarayanan and Narasimha, "Vortex methods: A tool for optimal control of high Reynolds number free shear flows", *proceedings of Symposium on Applied Aerodynamics and Design of Aerospace Vehicle* (SAROD 2013) November 21-23, 2013, pg. 229-233, Hyderabad, India.

Chapter 1: Introduction

1.1. The turbulence problem

The word 'turbulence' is most commonly encountered during an in-flight announcement urging passengers to fasten seat-belts, in anticipation of unsteadiness due to the large scale turbulent motion in the atmosphere. However, turbulent flows are ubiquitous over a wide range of technologically relevant scenarios including energy, transportation and weather prediction. When the inertia associated with a fluid flow becomes much larger than the frictional forces due to viscosity (the ratio UL/ν is the Reynolds number), the smooth laminar flow transitions to turbulence (Reynolds, 1895) characterized by unsteady, multi-scaled, chaotic (Gollub & Swinney 1975, Maurer & Libchaber 1979) and rotational flow. This transition can often be observed in a faucet.

Turbulence is considered to be the last unsolved problem in classical physics (Feynman,1964) even though it is generally accepted to be governed by the same Navier-Stokes (NS) equations (Euler 1755, Navier 1823, Stokes 1845) that describe laminar flow. It is 'unsolved' in the sense that prediction based on first principles has not been possible even in simple scenarios. For example, when the flow is turbulent it is not possible to determine, purely from first principle analyses, even the order of magnitude of drag on a sphere in the limit of high Reynolds number (Re), or the amount of pressure drop require to pump a specified flow rate of a given fluid through a circular or rectangular duct or even the angle of spread of a jet.

One reason for this difficulty is that the solutions of NS become intractable (Millikan, 1928) at high Re. While the NS equations can be solved numerically on a computer, the range of scales greatly increases with Reynolds number and the computing effort increases as $Re^{13/4}$. As it takes an order of a month to simulate $Re \sim 10^3$ on a parallel computer (with over 10^2 processors), computing resources required for direct simulation of Navier-Stokes (DNS) for any real–world problem (e.g. aircraft $Re \sim 10^7 - 10^8$, cyclone $\sim 10^{12}$) are astronomical, and such simulations are unlikely to be possible in the foreseeable future (see Ch.7 of Davidson, 2004). The current engineering approach to study such flows is to use an averaged or filtered version of the NS and use ad-hoc expressions or equations to model the effect of the unresolved scales on the computed scales. Such models always involve non-universal adjustable constants that have to be tuned for specific flow configurations using appropriate experimental data. Limited understanding and unresolved fundamental issues even in canonical turbulent flows are bottlenecks in attempts to formulate more accurate models, especially for prediction of flows for which extensive experimental data is unavailable.

One approach to advancing the understanding of turbulence has been to extensively study 'simple problems'. An example which has been long favored for both theory and computations is homogenous isotropic turbulence. While there has been some historical success of this approach to provide results with broader range of applicability (e.g. the Kolmogorov -5/3 spectrum, 1941), further study, including some of the largest computer simulations of turbulence (Ishihara et al, 2007), has had limited success in terms of implications for real-world flows.

1.2. Turbulent shear flows and emergence of order

Most real-world turbulent flows are shear flows (the gradient of the mean velocity field has a non-zero symmetric component) which are inhomogenous (at least in one direction) and are not isotropic. Figure 1.1 shows some turbulent shear flows in aerospace and atmospheric contexts. Other relevant examples include flows within IC Engines, pollutant dispersal and in the human heart. One can

immediately observe that many of these flows show a certain large scale organization which is absent in homogenous isotropic turbulence.

Of particular interest to this work is a class of shear flows whose development is not strongly affected by interaction with solid boundaries. These are called free shear flows and include jets, wakes and mixing layers. One of the simplest among such flows is a spatially developing mixing layer or free shear layer (Fig. 1.2, 1.3a). This is a flow which develops between two streams moving with different velocities U_1 and U_2, separated from each other for $x < 0$ by a thin splitter plate, and mixing with each other for $x > 0$. While extensive measurements have been made on this flow for more than fifty years (Liepmann & Laufer 1947, Brown & Roshko 1974, Winant & Browand 1974, Oster & Wygnanski 1982 …, D'ovidio & Coats 2013), a particularly striking development was the convincing demonstration by Brown & Roshko (1974) of the till-then unsuspected presence of highly organized large-scale vortices as an integral part of what was a canonical fully developed turbulent shear flow in the region $x > 0$. This work established that turbulent shear flows could contain ordered motion, and led to the study of coherent structures in a wide variety of other shear flows (Liu 1989, Brown & Roshko 2012).

The general point that all this work drove home was that the character of turbulent shear flows is fundamentally different from that of statistically homogenous isotropic turbulence, to the extent that ordered motion plays a significant (sometimes dominant) role in determining certain characteristics of sheared turbulence, such as for example entrainment of irrotational ambient fluid into the rotational turbulent shear flow.

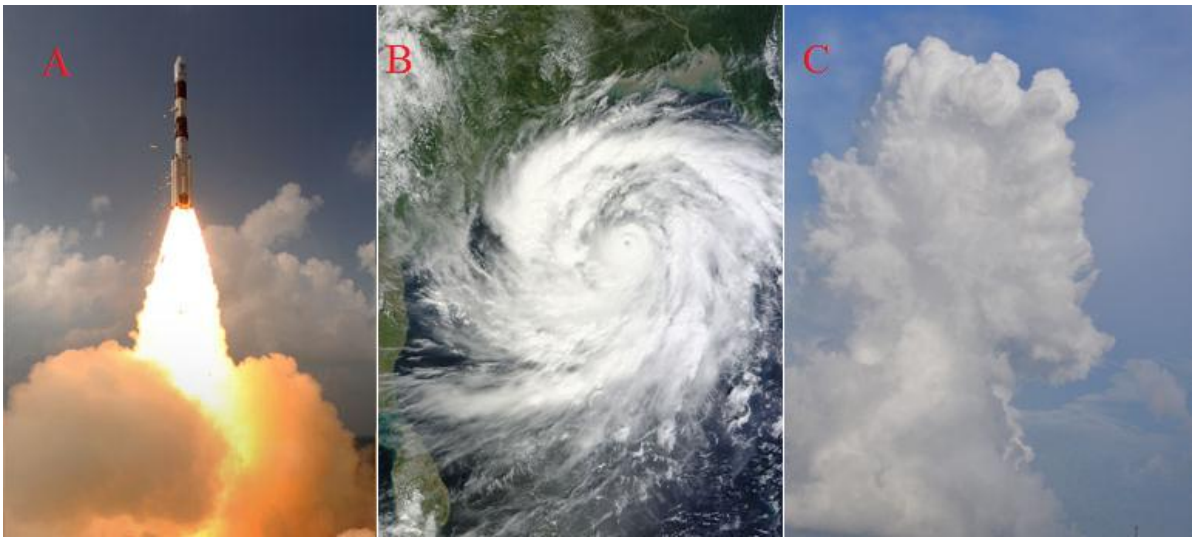

Figure 1.1. Some relevant turbulent free shear flows. Note the presence of large scale order.
A. Mars Orbiter Mission ('Mangalyaan') rocket launch, photo taken from : http://www.isro.org/pslv-c25/Imagegallery/launchvehicle.aspx
B. Cyclone Phailin, from NASAWorldview
C. Cumulus cloud, photo credit : Vybhav G.R.

Hence homogenous isotropic turbulence is perhaps not the appropriate simple problem to understand the underlying mechanics of most turbulent flows of interest. This view was summarized by H.W. Liepmann in his letter presumed to be addressed to G.K. Batchelor (Narasimha et al, 2013),

> "*The preoccupation of the turbulent physics community seems to me the statistics of vortex interactions that is, of course, a very important aspect of fluid physics but the usual limitation to homogeneous and sometimes isotropic conditions as well, limits the connection to realistic flow problems. It is by now quite clear that unlike the equilibrium Boltzmann distribution of perfect gases, the isotropic-homogenous state of turbulence cannot be used as the first step in a perturbation procedure a la Enskog-Chapman*".

Further discussion on general issues on turbulent flows can be found in Davidson (2004) and Narasimha (1990), and a recent review on turbulent free-shear flows in Brown & Roshko (2012).

Figure 1.2. Large scale coherent structures in a turbulent mixing layer (Konrad, 1977)

1.3. The temporal vortex-gas shear layer

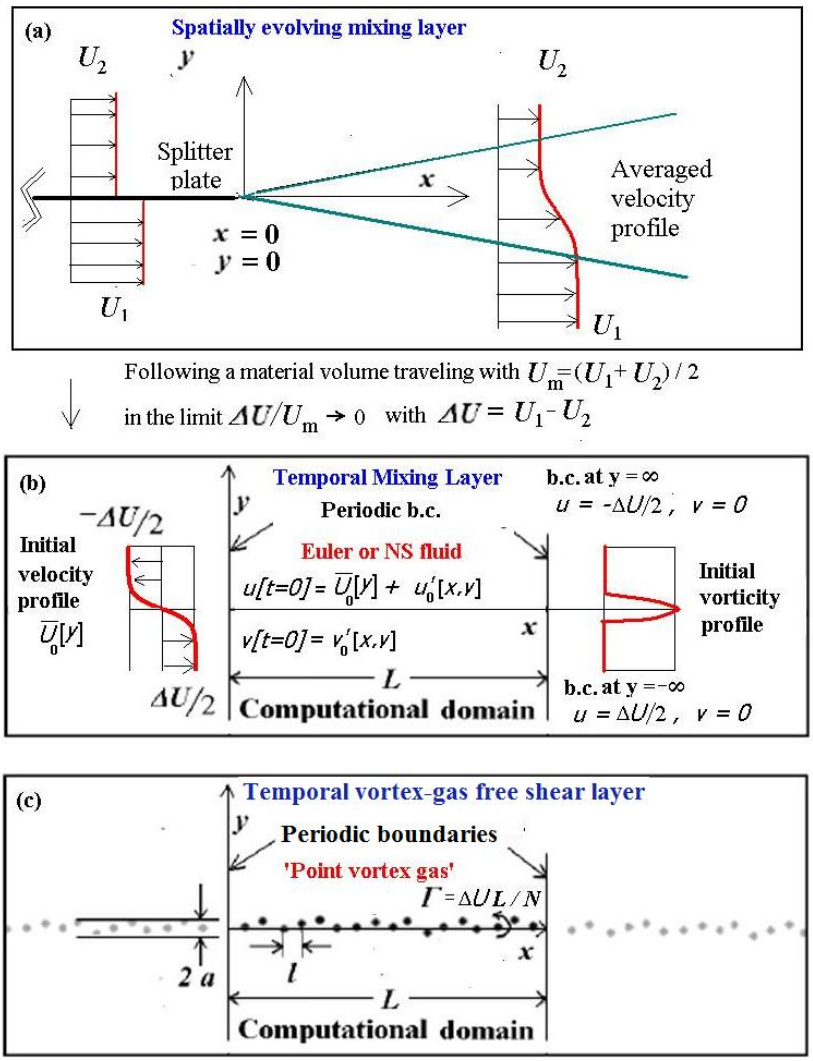

Figure 1.3 (a) Schematic of a spatially evolving mixing layer. **(b)** The temporal analogue (in an Euler or Navier-Stokes fluid), often studied in simulations. (Note that the present notations use Reynolds decomposition, $\overline{U}$ indicates averaged velocity that depends only on y, and u' and v' are the x and y components of the fluctuating velocity which has zero mean. Subscript 0 indicates initial value). **(c)** The vortex-gas formulation of the temporal mixing layer showing the configuration of vortices at the initial instant.

If homogenous isotropic turbulence is not the relevant simple problem, the incompressible plane temporal shear layer (Fig. 1.3 b), might be a suitable candidate for a starting point to understand the wider class of turbulent shear flows, as it is the simplest turbulent flow with shear and large scale organization.This is a time-dependent flow that is statistically homogeneous in the stream-wise direction x and evolves temporally in the normal direction y, from an initial condition at $t = 0$ when the two streams moving at $+\Delta U/2$ and $-\Delta U/2$ are separated by a vortex sheet or a thin vortical layer at $y = 0$. The temporal mixing layer is related to the spatial case described earlier (Fig. 1.2, 1.3a) via a Galilean transformation in the limit $\lambda \equiv 2(U_1 - U_2)/U_1 + U_2 \to 0$. The specification of the canonical (infinite domain) temporal shear layer involves only one parameter at high Reynolds numbers, namely the velocity differential ΔU across the layer. Further, it is favored for numerical simulations of the Navier-Stokes equations (e.g. Sommeria et al 1991, in 2D, Rogers & Moser 1994, in 3D), because of its simplicity and the unambiguous initial and boundary conditions that can be prescribed for the problem. It is usually studied in a domain $0 \leq x \leq L$ that is periodic in the flow direction x with period L. This is a valid approximation to the infinite-domain mixing layer, as long as the relevant length scales in the initial conditions and in the flow field are much smaller than the domain size.

Majority of this thesis is concerned with the vortex-gas analogs of shear layers. The vortex gas is a collection of large number (N) of point vortices (delta functions in vorticity) in an inviscid fluid. Set of point-vortices is a solution of the weak form of Euler (inviscid NS) equations which support singular solutions. Kelvin's theorem reduces all the dynamics contained in the Euler equations to be represented by the kinematic Biot-Savart relation. Hence the evolution of the vortex gas can be described by $2N$ ODEs. Even though the interactions between vortices are long range, the terminology 'vortex gas' is used (following Miller, 1990), since a collection of vortices placed in a box, tend to fill the box like molecules of a gas. In other words, even though the density of the fluid in which the vortices exist is a constant, the density of the vortices at any given location can change with time. Under certain limits a sufficiently large collection of point-vortices provides a weak solution of the Euler equations (Marchiro & Pulvirenti, 1993) in a coarse-grained sense (averaged over boxes sufficiently large to contain large number of vortices, but small compared to the characteristic length scales of the flow).

A temporal vortex-gas free shear layer is a singly periodic array of N-point vortices of identical sign, so that the x-averaged velocity field resembles that of a temporal shear layer. The chief object of the first part of the thesis is to revisit this problem (early attempts go back to Rosenhead 1931 and include Delcourt & Brown 1979, Aref & Siggia 1980) with modern computing resources. As shown in Fig. 1.3c, we consider the evolution for a class of initial conditions involving a single row of point vortices placed along the x-axis, equispaced in x and with small displacements in y. We make a detailed study of the statistical evolution of the system in the x-y plane for $t > 0$.

The temporal vortex-gas free shear layer should not be viewed as a discrete model of a continuous vortex sheet that rolls ups smoothly (for reasons that will be discussed in Appendix C), but rather as a statistical (chaotic) evolution of a gas of point vortices. Further, this 2D inviscid model should not be readily viewed as an approximation of the 3D NS temporal mixing layer due to the following objections.

The first is the obvious one about dimensionality. Both experiments and 3D NS simulations show a significant 3D motion to be present in both spatial and temporal shear layers. This is particularly evident after a 'mixing transition' (Konrad 1977, Brown & Roshko 1974, Dimotakis 2000) that takes place at Re ~ 10^4. However, the large coherent structures are quasi-2D (Wygnanski, 1979) and the role of 3D dynamics on the large scale evolution is not yet clear. Further, there are also other real-world flows which are quasi-two-dimensional in some sense: the most well-known of these is atmospheric motion at higher latitudes, where the large scales are governed by the dynamics of conserved potential vorticity oriented normal to the surface of the earth (Pedlosky, 1987). Indeed, the reverse energy cascade characteristic of 2D turbulence (Batchelor 1969, Kraichnan 1967) has given much insight into the

dynamics of terrestrial and other planetary atmospheres. Therefore a 2D model is not necessarily irrelevant, and in this case might provide useful insights on various aspects of shear layer dynamics.

The second limitation of the vortex gas is the complete absence of viscosity (and any molecular transport parameters that may be relevant for true mixing). No purely inviscid fluid can handle rigorously the phenomena of mixing and dissipation, both of which depend crucially on molecule-scale interaction, and consequently both the Richardson cascade and Kolmogorov-type similarity are beyond point vortex dynamics. The vortex-gas model does however describe what may be called the 'dispersal' of vorticity and hence also of momentum, both through the Biot-Savart relation. It has been argued (Eyink & Spohn 1993) that the long time evolution of vortex blobs in real fluids cannot be described by vortex-gas motions as the effect of viscosity (say ν), however small, does become manifest on time-scales of order ν^{-1}. Interestingly, this argument takes on a different complexion in shear flows, especially in mixing layers. One consequence of the stream-wise/temporal growth is that the local Reynolds number of the flow ($\delta\Delta U/\nu$, say, where δ is a measure of the layer thickness), actually increases with downstream distance x in spatially evolving flow, and with time t in the temporally evolving flow that is the chief subject of the present study. Thus the effect of viscosity progressively diminishes (equivalently a locally scaled $\nu \to 0$) as $x \to \infty$ or $t \to \infty$, and the viscous timescale of $O(\nu^{-1})$ consequently recedes to ∞ in the limit, *as long as the layer keeps growing*. In any case, some effects of viscosity can, if necessary, be taken into account by the addition of a random walk component in vortex motion (Chorin, 1973, more details in Chapter 7).

A third objection to the use of the vortex-gas model is the singularity in the velocity field of the vortex gas at the location of the vortices. In other words, the velocity close to any vortex can be arbitrarily large and hence is not representative of flow fields found in any real-world context. This can be overcome by desingularization of some kind (e.g. Krasny 1986), but it will be shown in Appendix C that desingularization does not affect our major conclusions and is unnecessary for studying the statistical evolution over long times.

In spite of such objections, early vortex-gas simulations (Delcourt & Brown 1979, Aref & Siggia 1980) were remarkably successful in mimicking several dominant features of evolving mixing layers as observed experimentally, including the emergence of 'coherent structures' and subsequent growth of the layer thickness through amalgamation events among the coherent structures. This success is all the more remarkable as the vortex-populations used were small and the accuracy of numerical schemes were modest, limited by the computing capabilities of that era, signifying the robustness of the vortex-gas picture.

1.4. Connections with statistical mechanics

Regardless of its relevance to 3D NS mixing layers, the vortex-gas free shear layer is worthy of study as a prototypical turbulent shear flow (in the sense it is a chaotic evolution of the vorticity field and the mean velocity field has shear). This is because this model offers the possibility of establishing a bridge with statistical mechanics –i.e. of predicting the evolution of the large-scale statistics of turbulent shear flow as a consequence of the collective interaction of a large number of vortices, in a fashion similar to how the relation between pressure, density and temperature of an ideal gas can be derived from molecular dynamics (Fig.1.4).

The first attempt to connect vortex dynamics with statistical mechanics was by Onsager (1949) who presented a penetrating discussion of statistical mechanics of a 'gas' of positive and negative point vortices in an ideal fluid on a celebrated paper titled *Statistical Hydrodynamics*. The motion of such a gas is governed by a Hamiltonian (first shown by Kirchhoff, 1876), and may be expected to lend itself to the formalism of statistical mechanics. (The demonstration that chaotic motion can occur in a collection of more than three vortices (Novikov & Sedov 1978, also see Aref 1983) establishes an underlying

stochastic dynamics that justifies a statistical treatment.) Onsager showed that the motion of the vortices could be analyzed in terms of energy and entropy as in classical statistical mechanics, but the temperature derived therefrom would have to be permitted to take negative values, as the entropy has a maximum with respect to the energy. He also showed that such a gas possessed equilibrium solutions which consisted of large-scale vortex clusters or structures, positive and negative segregated from each other. Since then considerable work has been done in analyzing the mechanics of point vortices (see Paul Newton 2001 for example). In particular the nature of the equilibrium state in such a gas has been extensively discussed (see for example Lundgren & Pointin 1977, Eyink & Spohn 1993), especially in connection with the emergence of large-scale, long-lived vortices in the vortex gas. Several attempts (beginning with Marmanis 1997, most recently Chavanis 2010) have also been made to derive a BBGKY hierarchy of equations governing vortex distribution functions, based on the Liouville equation, beginning with single-particle analogues of the Boltzmann equation and followed by higher members in the hierarchy involving two-point correlations or more (Chavanis 2012). A favored target for application of these ideas has been Jupiter's famous red spot (Miller et al. 1992, Chavanis 2005), seen as one dramatic example of the kind of large-scale long-lived vortex predicted by Onsager. However there have been few attempts to make connections between evolving turbulent flows with non-equilibrium statistical mechanics of a vortex gas. (There have been some other attempts to bridge turbulent flows with statistical mechanics (Kraichnan & Chen, 1989) that have focused on homogenous isotropic turbulence, which is not relevant to the present study, and hence not discussed here.)

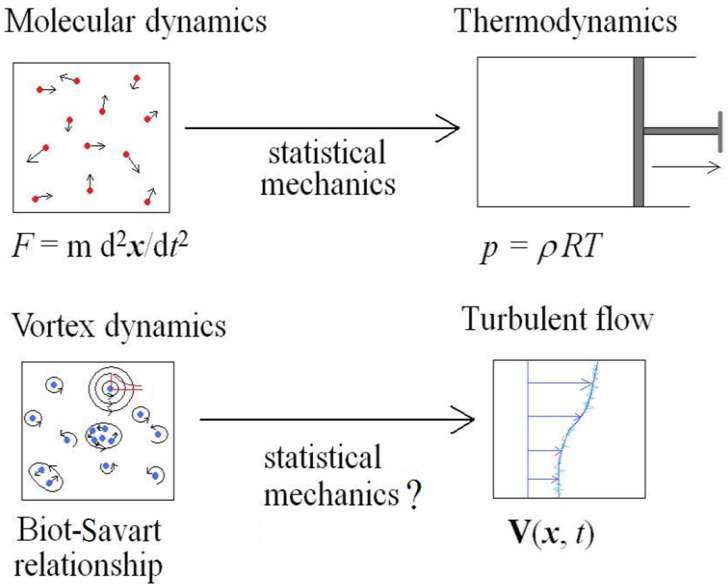

Figure 1.4. Illustration of the present philosophy

Our approach to the problem is akin to that of studying the statistical mechanics of a system of molecules via molecular dynamics. Therefore the complete evolutionary trajectory of the vortex-gas system is followed all the way from its initial conditions (such as that shown in Fig. 1c) to the final asymptotic state (if one exists) as $t \to \infty$. With today's computational resources, much more accurate and comprehensive study is possible compared to earlier work. The present simulations are much longer in time (by a factor of 10^4), far more precise (Hamiltonian conserved to within 10^{-5}), and involve large (500+ member) ensembles; these (as it shall be demonstrated) turn out to be crucial for obtaining the results reported here.

The majority of this thesis (Part I, Chapters 2 - 5) is concerned with the analysis of the evolution of the temporal vortex-gas free shear layer, which is analyzed from two view-points. The first is in terms of statistical mechanics, and describes the evolution of the vortex gas all the way from the initial condition to a final asymptotic state, through distribution functions, possible equilibrium states and temperatures. Such analyses point to the existence of certain universalities that appear to be novel in

non-equilibrium statistical mechanics. The second viewpoint is in terms of concepts that have been found useful in the study of turbulent shear flows, such as self-similarity, growth rate of the shear layer and effect of initial conditions on subsequent flow development. The two viewpoints together yield fresh insights into questions that have been widely discussed but remain controversial in the fluid-dynamical literature.

The organization of this part of the thesis is as follows. In Chapter 2, formulation of the temporal problem, a critical review of earlier calculations, the major unanswered questions and the present computational strategy are presented. Then the results of the present temporal simulations will be discussed, identifying and describing three distinct regimes in the temporal evolution, and present detailed results on universality of the intermediate regime in Chapter 3. Chapter 4 makes connections with statistical mechanics, beginning with comparison of long time solutions with equilibrium theories and then presents results on the relaxation, including on the applicability of vortex-gas kinetic theories. Chapter 5 makes comparisons and connections with 2D/3D NS simulations and experiments.

Part II (Chapters 6 - 9) of the thesis is concerned with more detailed fluid dynamic questions and the extensions of the vortex-gas shear layer to address them. Chapter 6 makes connections between the early development (Regime I) and hydrodynamic instability theories and Chapter 7 illustrates how the present simulations can be used for optimal control of shear layers. Chapter 8 discusses the effects of viscosity via temporal vortex-gas simulations with an additional random walk component to the vortex-motion. The effects of spatial feedback are studied in Chapter 9 by formulating a vortex-gas analog of the spatially evolving shear layer with appropriate boundary elements. The features of the single stream shear layer are discussed in great detail, and how some of its features have been incorrectly attributed to 3D mechanisms is demonstrated.

The thesis concludes with remarks on possible future directions. Some preliminary results from a nearest-neighbor interaction model and a discussion of other possibilities to understand Regime II are presented.

Chapter 2: Revisiting the vortex-gas free shear layer - Unsettled issues and present strategy

2.1. Present setup and formulation

Many of the earlier vortex-gas studies involve vortices in an infinite plane (e.g. Lundgren & Pointin 1977), or in a doubly periodic box (e.g. Montgomery & Joyce 1974) or on a cylinder (e.g. Bühler 2002). The object of the present study, a temporal free shear layer in a point vortex gas, is formulated as follows.

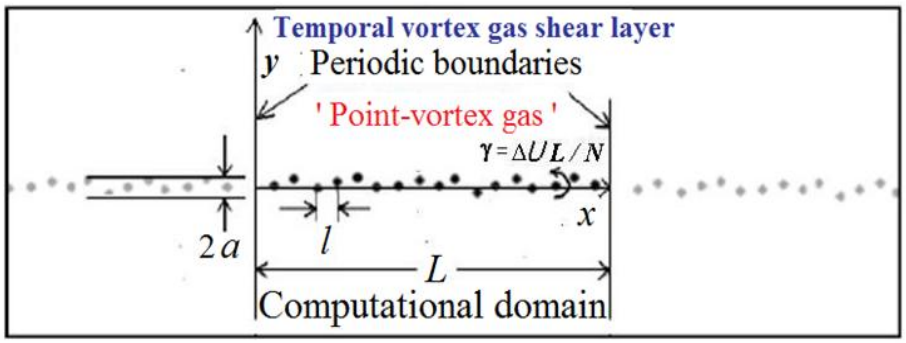

Figure 2.1. The vortex-gas formulation of the temporal free shear layer showing the configuration of vortices at the initial instant. Only the vortices in the L–domain, $0 < x < L$ (which are denoted by dark dots) are tracked. The governing equations account for the velocities induced by all the vortices in the L-domain as well as all those present in $x < 0$, $x > L$ (shown in light colored dots) at separations of $+ kL$ and $- kL$ respectively ($k = 1,2, .. \infty$) for each vortex. $l = L/N$ is the initial inter-vortex separation in x.

Consider an array of N point vortices each of fixed strength γ, initially distributed along or very close to the x-axis (equispaced in x) in a domain of length L containing an inviscid fluid as shown in Fig. 1c. Corresponding to any vortex i in the domain (say at (x_i, y_i)), there exist vortices at $\{(x_i \pm kL, y_i)\}$; $k = \{1, 2,\ldots\infty\}$, in the replicated domains extending to $\pm\infty$, so the boundary conditions are periodic. This formulation represents a canonical system of an infinite number of vortices in an infinite domain. Our objective is to study the evolution of this system in (x,y,t) space.

The state of the system at any time t is completely described by the location of all the vortices$\{x_i[t], y_i[t]\}$, $i = 1$ to N, as this is sufficient to determine the velocity field over the whole domain. The velocity induced at a distance r by a point-vortex is given by the Biot-Savart relation

$$u_r = 0, \qquad u_\theta = \frac{\gamma}{2\pi r}, \qquad r > 0$$

where u_r and u_θ are the radial and circumferential components of the velocity at the radial distance of $r = [(x - x_i)^2 + (y - y_i)^2]^{1/2}$.

The velocity with which any vortex moves is the vector sum of the velocities induced at its location by all the other vortices in the system; thus each vortex is a flow-marker and traces a particle path. In the present set up, the velocity of a vortex located at (x_i, y_i) in the L-domain is the sum of the velocities induced there by vortices at $\{(x_j + kL\,, y_j)\}; j = \{1 \text{ to } N\}, j \neq i;$ $k = \{-\infty..-2, -1, 0, 1, 2, .. \infty\}$. This leads to convergent series that sum up to the following expressions for the x and y components of the velocity (here, $\gamma_j = \gamma$ for all j):

$$u_i = \frac{dx_i}{dt} = -\frac{1}{2L}\sum_{j=1,j\neq i}^{N} \frac{\gamma_j \sinh\left(2\pi\left(y_i - y_j\right)/L\right)}{\cosh\left(2\pi\left(y_i - y_j\right)/L\right) - \cos\left(2\pi\left(x_i - x_j\right)/L\right)} \tag{2.1}$$

$$v_i = \frac{dy_i}{dt} = \frac{1}{2L}\sum_{j=1,j\neq i}^{N} \frac{\gamma_j \sin\left(2\pi\left(x_i - x_j\right)/L\right)}{\cosh\left(2\pi\left(y_i - y_j\right)/L\right) - \cos\left(2\pi\left(x_i - x_j\right)/L\right)} \tag{2.2}$$

These equations appear to have been first written down by Friedmann & Poloubarinova (1928). The first reported calculations using (2.1,2.2) were performed by hand by Rosenhead (1931). Subsequent work using (2.1, 2.2) will be reviewed in the Section 2.2.

Now the circulation γ is set to $L\Delta U/N$, so that $\pm\Delta U/2$ are respectively the induced *x*-velocities at $y = \mp\infty$ as shown in Fig. 1. It has to be noted that *x* is an angular variable as the system is *x*-periodic. In the numerical implementation, vortices that leave the domain during the evolution are relocated modulo *L* using the *x*-periodicity of the system. Thus if vortex *i* located at x_i^m ($0< x_i^m <L$) at time t_m would have to be moved to $\hat{x}_i^{m+1}>L$ at time t_{m+1}, it is relocated to $x_i^{m+1} = \hat{x}_i^{m+1} - L$. Similarly, if $\hat{x}_i^{m+1} < 0$. Such operations do not alter the induced velocities given by (2.1, 2.2), and ensure that *N* vortices all present within the domain $0 \leq x_i < L$ are tracked.

The point-vortex gas in an infinite plane possesses the Hamiltonian (Kirchhoff 1876)

$$\mathcal{H} = -\frac{\gamma^2}{4\pi}\sum_{i=1}^{N}\sum_{j=1;j\neq i}^{N} \ln\left(\left|\boldsymbol{r_i} - \boldsymbol{r_j}\right|/R_0\right) \tag{2.3}$$

where $\boldsymbol{r_i} \equiv \{x_i, y_i\}$ and R_0 is an arbitrary length scale, often taken as the radius of gyration of the vortex system, $\left[(1/N)\sum_{i=1}^{N}(x_i^2 + y_i^2)\right]^{1/2}$ .For the system shown in Fig. 1c, the Hamiltonian (often also called Kirchhoff's function) takes the form (Delcourt & Brown, 1979)

$$\mathcal{H} = -\frac{\gamma^2}{8\pi}\sum_{i=1}^{N}\sum_{j=1;j\neq i}^{N} \ln\left(\frac{1}{2}\left[\cosh\left(2\pi\left(y_i - y_j\right)/L\right) - \cos\left(2\pi\left(x_i - x_j\right)/L\right)\right]\right) \tag{2.4}$$

Equations (2.1) and (2.2) can be cast in the Hamiltonian form

$$\frac{d(x_i\sqrt{\gamma})}{dt} = \frac{\partial\mathcal{H}}{\partial(y_i\sqrt{\gamma})}\ ;\ \frac{d(y_i\sqrt{\gamma})}{dt} = -\frac{\partial\mathcal{H}}{\partial(x_i\sqrt{\gamma})} \tag{2.5}$$

a system of 2*N* ODEs that can be solved as an initial value problem. Note that in the present problem the notation *L* is used for the domain size and not the radius of gyration.

2.2. Preliminary simulations and major questions

Before posing the major questions some simple simulations over a relatively long duration are useful. These were performed with *N* = 800, initially equispaced in *x* and with initial values of the *y*-positions of the vortices from drawn randomly from a uniform probability distribution of amplitude *a*, $(P[y] = (1/2a)\text{for}|y| < a\ ;0\ \text{for}|y| > a)$.

Figure 2.2 shows the evolution of vortex positions with time for $a / L = 10^{-6}$.The initial evolution ($t\Delta U/L \lesssim 1$) is qualitatively consistent with earlier simulations of this kind (Delcourt & Brown 1979, Aref & Siggia 1980); in particular, as is clear from Fig. 2.2, the vortices cluster to form what has been called in fluid dynamical literature as 'coherent structures'. In general these structures grow in size by successive amalgamations (see amalgamation events A, B, C in Fig. 2.2). The average size of the structures and the spacing between them increase with time, while the total number of structures in the

domain decreases. We also find that beyond $t\Delta U/L$ ~ 4, there is only one structure left in each periodic domain, (as at $t\Delta U/L = 8.0$, Fig.2.2).

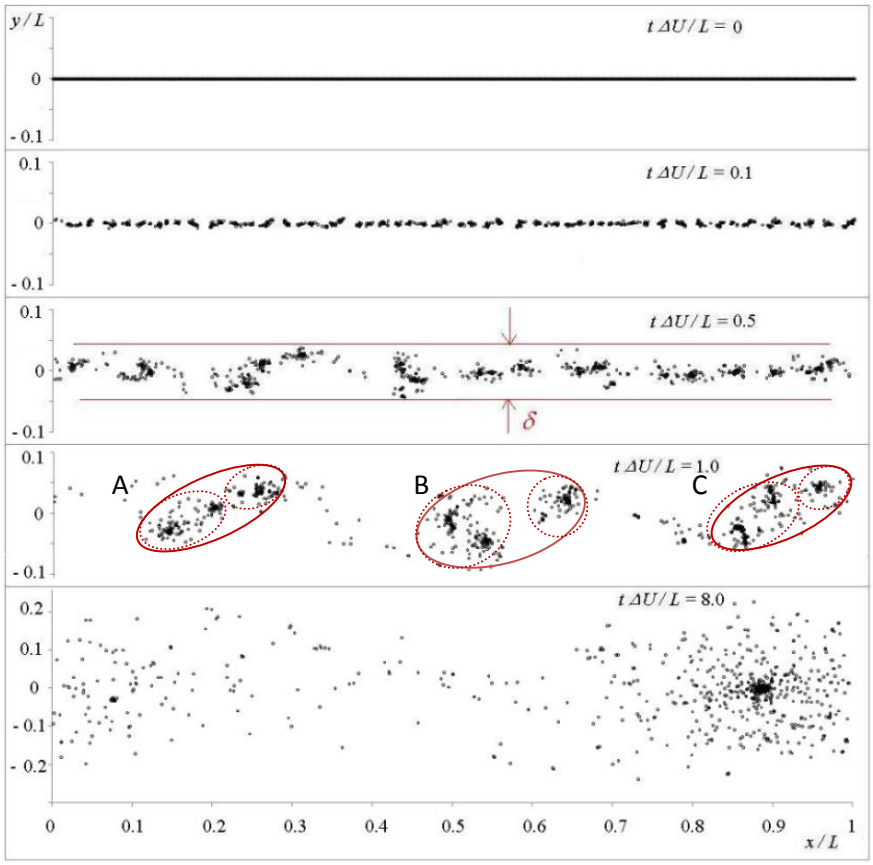

Figure 2.2. Typical evolution of vortex positions with time. (N = 800 , a/L = 10^{-6})

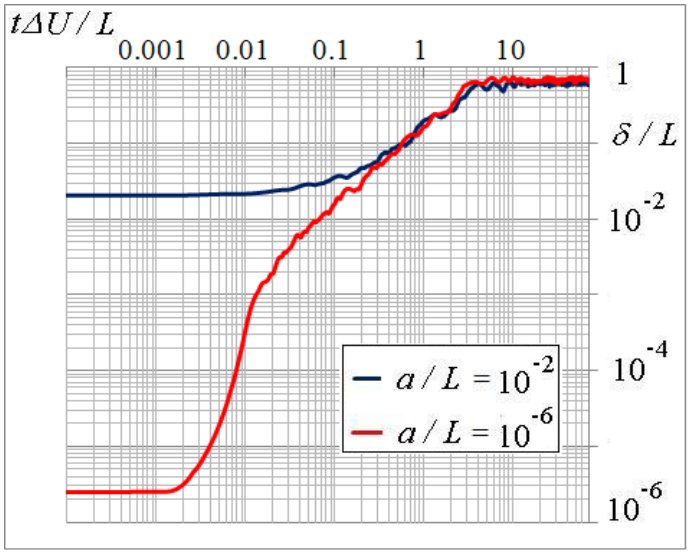

Figure 2.3. Evolution of thickness δ with time, in exploratory simulations of (2.1,2.2) (with N=800). Note the existence of different regimes in evolution.

To quantify these observations, we introduce a rough measure of layer thickness $\delta[t]$, defined as the maximum y-distance at time t between any two vortices in the system (see Fig. 2.2). (This measure is analogous to the visual thickness of a laboratory mixing layer.) The evolution of δ with time is shown in

Fig. 2.3 for $a/L = 10^{-6}$ and 10^{-2}. (Similar results are obtained if other measures of thickness are used instead of δ.)

It can be seen that (for $a/L = 10^{-6}$) δ grows approximately linearly between $0.04 \leq t\Delta U/L \leq 2$, saturating at about 0.8 for $4 \leq t\Delta U/L \leq 10^2$. At the much higher initial amplitude $a/L = 10^{-2}$, the onset of linear growth takes place much later at around $t\Delta U/L \sim 0.2$, but the trajectory beyond that point seems to roughly follow the simulation with $a/L = 10^{-6}$, indicating a possibility of universal growth.

These two simulations immediately highlight the presence of at least three regimes in the evolution. For some time after initiation, the solution strongly depends on the initial condition (which we shall call Regime I), but the effects seem weaker at later times as δ grows linearly in time (Regime II). At longer times the layer thickness seems to fluctuate roughly around a constant value of about 0.8 (Regime III), which has never been explored in earlier simulations.

These preliminary simulations raise the following basic questions:

a) What are the scaling laws in different regimes in the evolution of (1,2) ?

b) Are any of the regimes 'universal', if so which ones and in what variables?

c) Wherever there is universality, what is the statistical-mechanical explanation?

d) What is the nature of the solution as $t \to \infty$?

e) What is the relevance of the vortex-gas shear layer to 2D/3D NS mixing layers ?

We now briefly review earlier studies of vortex-gas free shear layers with the above questions in mind.

2.3. Review of earlier (temporal vortex-gas) simulations

Earlier vortex-gas simulations (mostly carried out with a fluid dynamical perspective) have not explicitly identified the above three regimes and hence no attempt has been made to tackle the questions raised above. This is due to one or more of the following factors:

a) Large statistical uncertainties due to small number of vortices, low accuracy and lack of ensemble averaging

The most extensive (non-desingularized) vortex-gas computations to date are due to Aref and Siggia (1980), who use 4096 vortices. They use a cloud-in-cell method which saves computer effort using integer algebra and look-up tables for the calculations, but the technique also introduces a numerical viscosity. With only a single realization they estimated the uncertainty level as 30% in the layer thickness. Delcourt & Brown (1979), also using a cloud-in-cell method, reported a 6% change in the Hamiltonian in the computations. No earlier work performs ensemble averaging, which is crucial for obtaining reliable statistics, as will be described in Sec. 2.5.

b) Short integration times

The maximum $t\Delta U/L$ reported in earlier work is 1.2 (Delcourt & Brown, 1979). This is grossly inadequate to reach an asymptotic state or even to uncover the different regimes observed in Fig. 3.For certain classes of the initial condition, e.g. those involving long-wave sinusoidal displacements of the point vortices (e.g. Rosenhead 1931, Acton 1976), the time of integration is too short even to move out of Regime I.

c) Inadequate scale separation between different regimes due to choice of initial conditions with respect to domain size

In some simulations (see Table.2.1), the length scale of the dominant initial condition (Λ_{ic}) is comparable to the domain size (L), leading to a lack of scale separation between the Regimes. Hence it is not possible to probe each regime in sufficient detail.

d) Desingularization and variable number of vortices

It has been noted that point vortices are 'too chaotic' to provide a satisfactory discrete model for a vortex sheet (Hama & Burke 1960, Moore 1971, see also Leonard 1980). This difficulty may be overcome by adopting a desingularized version of (1,2) following Krasny (1986). Recent studies include Sohn (2005, 2010) and Abid & Verga (2011). Such desingularization is relevant to investigations on the smooth roll-up of a vortex-sheet but not for an inherently chaotic object like turbulent shear flow, desingularization suppresses chaos, delays transition to Regime II and does not affect the final conclusions though the Hamiltonian (2.4) is no longer conserved (see Appendix C).

Some simulations (e.g. Sohn 2010) vary the number and strength of vortices in an adaptive fashion in order to better resolve the curvature of a continuum vortex sheet. These simulations are more closely related to discrete vortex sheet models (e.g. Basu & Narasimha 1992, Paul & Narasimha 2013) than a vortex gas and are not attractive for statistical-mechanics approaches.

2.4. Present computational strategy

The N point vortices, placed along the x-axis with a given inter-vortex spacing l, are displaced along y by a specified amount at $t = 0$. This displacement is typically randomly generated using a specified probability distribution for each case, but in a few special cases the displacement is taken as a sinusoidal function of x. To obtain the time evolution (2.1,2.2) are solved numerically using a standard (explicit) fourth order Runge-Kutta algorithm to advance in time the locations of all the vortices.

The time-step used for integration and the precision of the calculations play an important role in the level of fidelity of the computation to pure Hamiltonian dynamics (Krasny,1986b).To investigate this issue we perform a set of simulations (detailed results shown in Appendix A) with different time-steps, precisions and schemes (including symplectic). We find that the evolution of the relevant (ensemble-averaged) statistics, such as the layer thickness and single and two-particle distribution functions, show no significant variation for $\Delta t < 1.0\, l/\Delta U$ (although individual vortex trajectories are found to be different due to the inherently chaotic nature of the system). Most importantly, the spread rate in Regime II was found to vary by less than a percent as Δt is varied by a factor of 40 (from 0.025 to 1.0 $l/\Delta U$ for a case with $a/l = 10^{-3}$, $N = 1600$), or between double and quadruple precision simulations (for a case with $N = 400$). Hence all calculations in this work use double precision and adopt $\Delta t = 0.1\, l/\Delta U$ as the time-step except when stated otherwise. Note that in terms of outer units often quoted in other work, $\Delta t\, \Delta U/L = 6.25 \times 10^{-5}$ for $N = 1600$ and 7.81×10^{-6} for the simulation with $N = 32000$ (we use $\Delta t = 0.25\, l/\Delta U$ for the latter). This may be compared with the lowest value for $\Delta t\, \Delta U\, /\, L$ of 2×10^{-4} used by Krasny(1986b).

The accuracy of the algorithm used here has been further assessed monitoring the quantities conserved by the equations of motion. We find that for computations on vortices in an infinite plane (in which the x- and y-centroids, second moment and Hamiltonian are conserved, see Newton 2001) with similar initial conditions and parameters as in the x-periodic mixing layer, the Hamiltonian is conserved to within of 9×10^{-6} of its initial value at ($t\Delta U/L = 0.78$ for $N = 3200$). The first moments of the vorticity distribution about the x and y-axes are conserved to within $10^{-16} l$ and $3 \times 10^{-13} l$, and the second moment to within 1.3×10^{-9}, of their respective initial values. For the periodic-in-x vortex-gas

free shear layer the Hamiltonian (4) was conserved to within 2.5×10^{-5} of its initial value during integration over $t\Delta U/L = 0.75$, with $N = 3200$. (For other invariants of the present x-periodic system see Appendix A.)

Study of Regime III involves long-time integration so a shorter time-step of 0.025 $l/\Delta U$ is adopted. As a result the Hamiltonian is conserved to within 0.5% for an integration time of 3.6 x $10^4 L/\Delta U$ (0.58x10^9 time-steps). These numbers demonstrate that the current computations are substantially more accurate than any previous work.

To understand the role of numerical noise on the initial development, we simulate cases (with $N = 3200$) with $a/l = 0$ and $a/l = 10^{-10}$, each with two different time-steps, $\Delta t\ \Delta U\ /\ l\ =\ 0.1$ and 0.5 and with double precision. We found that the initial evolution (early Regime I) with $a/l = 0$ was different for the two different values of time-step, or (equivalently) of the magnitude of the numerical noise. It has to be noted that this initial condition is a stationary but unstable solution of the point vortex system. Therefore, the numerical noise was essential for triggering the instability and hence its value was important in determining the initial evolution. However, the subsequent evolution, especially Regime II, was independent but for a shift in the virtual origin in time. We find that for $a/l = 10^{-10}$ the evolution did not depend on time-step for $t > 0$. This suggests that as long as the 'disturbance' in the initial condition is sufficiently large ($a/l \geq 10^{-10}$), it dominates the effect of numerical noise throughout the evolution. The above results suggest that there is non-zero numerical noise in the present study due to the truncation and round-off errors that are inevitable in any computer simulation, the present results seem to be robustly independent of the magnitude of the numerical noise, provided it is small and non-zero.

We do not adopt desingularization for the reasons highlighted in the previous section except for the simulations presented in Appendix C. The conservation of the Hamiltonian prevents any two vortices from getting arbitrarily close to each other. We find that using the present algorithm and adopted time-step, the distance a vortex moves during any time-step rarely exceeds that to its nearest neighbor, and is almost always at least an order of magnitude less. Hence the unbounded velocity in the neighborhood of a point vortex does not present a serious issue in the numerical integration of (2.1,2.2).

Apart from δ (defined in Section 2.2) there are different metrics one can adopt to specify the 'thickness' of the layer such as moments of vortex y-positions. But in order to enable comparison with Euler & Navier-Stokes mixing layers, we adopt the so-called momentum thickness, as it is commonly used in the fluid dynamic literature and in several earlier vortex-gas free shear layer studies (e.g. Aref & Siggia 1980). The momentum thickness (θ) is defined in the usual way as,

$$\theta[t] = (1/4)\int_{-\infty}^{\infty} dy\ \left(1 - \left(2\overline{U}[y,t]/\Delta U\right)^2\right)$$

where, the x-averaged x-velocity

$$\overline{U}[y,t] = (1/L)\int_0^L dx\ u[x,y,t]$$

is computed by x-averaging the induced x-velocity u on a grid of 0.4 N points in x and 200 points in y once every 100 time-steps. (Note: There are rare occasions when a vortex can come arbitrarily close to a grid point and induce very high velocity. This can reflect in the x-averaged velocities and hence the momentum thickness. In principle this effect can be addressed by use of a very fine grid and by averaging over a thin strip which would lead to cancelling of the large induced velocities of opposite signs. But we find that neglecting the contributions made by those rare instances when x-averaged velocities with absolute value greater than $\Delta U/2$ while computing θ is an equivalent alternative easier for numerical implementation. We note that this strategy does not change the computed value of θ by more than 1% for 99.9% of cases when $t\Delta U/l > 10$. Further, it was observed that doubling the grid resolution changes the computed value of θ by less than 0.5% for $t\Delta U/l > 10$. Thus θ computed in this work is a robust

measure). We shall show in Chapter 4 that the major conclusions are not affected by the choice of measure of thickness.

2.5. Ensemble averaging

In statistical mechanics ensemble averaging is commonly adopted to reduce fluctuations. For measurements of turbulent flow in fluid dynamics long-time averaging is often adopted as an alternative to ensemble averaging in statistically stationary flows. As the present system is non-stationary in time but statistically homogenous in *x*, *x*-averaging is in principle equivalent to ensemble averaging. However we find that an average over an ensemble of realizations (with initial conditions varied within a clearly specified class) is adopted due to the following reasons.

We first note that the statistical error (at a given $t\Delta U/l$) may be expected to vary with N as $N^{-1/2}$ (observed also in our present simulations, as shown in Fig. 2.4),while the computational effort grows as N^2. But if we simulate n realizations with m vortices each, the computational effort grows as nm^2 while the statistical error goes as $(nm)^{-1/2}$ (Fig. 2.4). The errors will be the same if $N = nm$, which reduces the computational effort by $nm^2/N^2 = 1/n$. It is this result that makes the ensemble approach so attractive. But a sufficiently large $N = L/l$ may be required to have a sufficiently long extent and preserve the inherent distinction between the different regimes observed in Fig. 2.3. But once N is sufficiently large the ensemble averaging approach is computationally far more economical. It also has the practical advantage of using parallel computers more effectively, as different 'realizations' can be independently simulated on different processors without any need for data communication. We also find that the ensemble average of θ computed from the *x*-averaged velocity profile for each realization is not very different (for large N and n) from the value computed from the ensemble average of the (*x*-averaged) velocity. Throughout this study, we shall use the former for the sake of numerical convenience. We also note that, for a given initial condition class, the standard deviation of the Hamiltonian across realizations is never more than1% of its mean value for present simulations with more than 400 vortices, and is often much less: e.g. less than 0.01% for the set of simulations presented in Chapter 3. Hence the present ensemble can be considered a microcanonical ensemble.

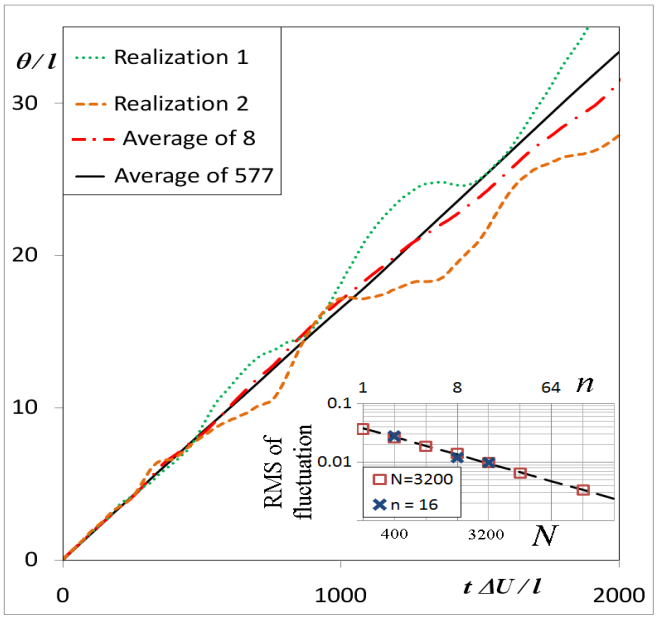

Figure 2.4. .Effect of ensemble averaging. Note that individual realizations have large fluctuations (even for N = 3200) and average over a large number of realizations is essential. The RMS departure from the respective means (at $t\Delta U/l$ = 160) ~ $n^{-1/2}$(shown in dashed line) for a given N and ~ $N^{-1/2}$ for a given n.

Ensemble averaging has not been adopted in earlier investigations of vortex-gas free shear layers. Statistical uncertainties associated with single realizations as seen in Fig. 2.4 make it impossible to address questions such as whether a Regime is universal or not, or how closely the vortex-gas simulations agree (if at all) with Navier-Stokes mixing layers.

A summary of the present simulation parameters and accuracy compared with earlier simulations in presented in Table 2.1. Also listed is the ratio of the domain size (L) to wavelength (Λ_{ic}) of the dominant perturbation in the initial condition (Λ_{ic} is taken to be equal to the wavelength of the imposed sinusoidal perturbation when specified. For several rows of vortices with random initial conditions, Λ_{ic} is taken the wavelength of the fastest growing mode given by Rayleigh theory for the analogous continuous vorticity field, see Ch.6 for details and justification) . This ratio roughly determines the maximum number of coherent structures formed at the beginning of Regime II and thereby extent of Regime II (as it determines the separation of scales between Regimes I and III, details in Ch.3). It can be seen that in terms of the number of vortices (both in terms of the maximum as well as in terms of the range), number of different initial condition classes, scale separation between the different regimes or maximum time of integration, the present simulations are vastly extensive compared to any earlier work. Therefore Table 2.1 clearly demonstrates why earlier simulations are unable to address any of the major questions raised at the beginning of this chapter and why the present simulations may provide insight.

Table 2.1. Comparison of present simulation parameters with earlier vortex-gas simulations (gray font indicates simulations with desingularization, which are not directly relevant and '?' indicates that data is not available)

	Number of vortices	**Number of initial conditions**	**Hamiltonian conservation (per $L/\Delta U$)**	**Max. number of realizations**	**Max. L/Λ_{ic}**	**Max $t\Delta U/L$**
Rosenhead (1931)	24	1	?	1	2	0.8
Acton (1976)	96	15	?	1	2	3
Delcourt & Brown (1979)	750	3	6×10^{-2}	1	~ 50	1.2
Aref & Siggia (1980)	4096	2	?	1	~ 40	1
Krasny (1986b)	1000	1	10^{-4} (Desingularized Hamiltonian)	1	1	4
Abid & Verga (2011)	32000 (initial)	2	?	1	4	1.4
Present	**50 to 32000**	**> 20**	**10^{-5}**	**1024**	**~ 10^{3}**	**3 x 10^{4}**

Chapter 3: Regimes, Scaling and Universality

In this chapter, we address the first two of the major questions raised in Chapter 2 regarding the temporal evolution of the vortex-gas free shear layers. We shall begin with an analysis of the three different Regimes noted in Chapter 2 and establish their scaling. The second part of this chapter will be devoted to determining whether the intermediate Regime II is universal or otherwise.

3.1. Scaling of the three regimes in evolution

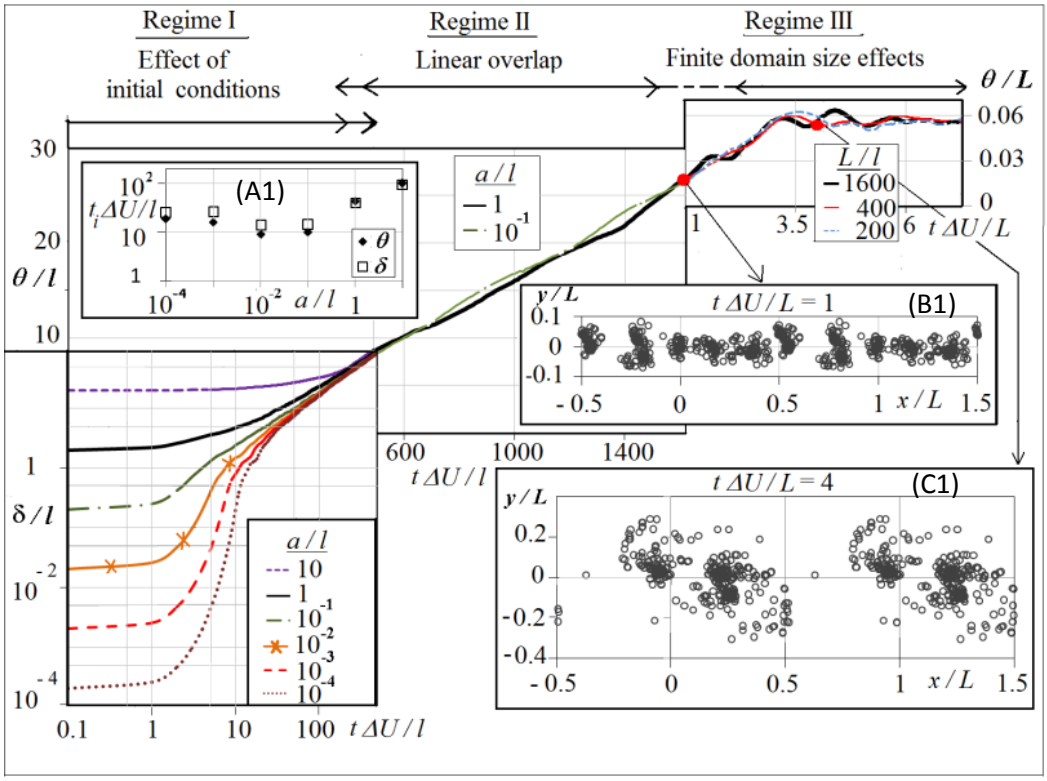

Figure 3.1 Composite diagram showing effect of initial conditions and domain size on the evolution of the mixing layer. Note use of δ and θ in different parts of the diagram, and change in the abscissa from$t\ \Delta U/l$ with a logarithmic scale up to 500, linear scale between 500 and 1500, and a switch to $t\ \Delta U/L$ thereafter. Appropriate changes have been made on both abscissa and ordinate to ensure that the evolution curve should go smoothly from one regime to the next. Inset A1 variation of initial transient with the amplitude of the initial vortex displacement. Insets B1 and B2 give pictures of the configuration of the vortices at $t\Delta U/L = 1$ and at $t\Delta U/L = 4$ respectively.

To determine the precise scaling laws in each of the three regimes, we carry out several additional simulations with different initial displacements drawn from uniform random distributions with amplitudes ranging from $10^{-4}l$ to 10 l, with different domain sizes ranging from 200 l to 1600 l, and with averages over up to 12 realizations. A summary of the results is presented in Fig. 3.1 as a composite diagram. In order to shed light on the different scaling laws in the different regimes, it is useful to adopt two different measures of the layer thickness, δ or θ (see Ch.2 for definitions) and of time, $l\ /\Delta U$ or $L\ /\Delta U$. It is therefore important to pay attention to the precise variables used as abscissa and ordinate in different parts of Fig. 3.1. The figure leads to the following observations about the different Regimes.

3.1.1. Initial condition dominated Regime I

As Fig. 3.1 displays, the evolution is widely different for different initial conditions during the initial Regime I with time scaled with $l/\Delta U$. The evolution is independent of L for the same initial

conditions (specified as a function of l), when scaled with l. A suitable measure of thickness in this regime is δ, as θ is not accurate for $t\Delta U/l < 10$ for reasons discussed Chapter 2. It is seen that the duration of this regime (t_{RI}), 10^{-2} to 10 times $l/\Delta U$ for the cases considered here, strongly depends on the initial conditions as shown in an inset in Fig. 3.1. However, for certain initial condition classes, including those where the y-displacement of vortices is a long-wave sinusoidal function of x, Regime I may be much longer (O(10^3) l/ΔU for case P1 shown in Chapter 4). In such cases the transition to Regime II may even be non-monotonic.

3.1.2. Domain-limited Regime III

Jumping now to Regime III, we find from Fig. 3.1 that, at times comparable to or larger than the domain size time-scale (i.e. $t\Delta U/L \geq 1$), the effects of finite domain size become noticeable and the growth of the layer departs from the linear variation with time seen in Regime II. As shown in the inset B1 in Fig. 3.1, the dynamics in the initial stages of Regime III are governed by the interaction among a small number of coherent structures. Figure 3.1 shows that the scaling length clearly changes from l to L in this regime, as confirmed by the approximate collapse of θ/L vs. $t\Delta U/L$ obtained from simulations with L/l ranging from 200 to 1600. Beyond $t\Delta U/L \sim 4$ the magnitude of changes in the thickness of the layer (in a statistical sense) is greatly reduced. This is because there is only one structure left in the domain (see inset B2 in Fig. 3.1), and hence there is no further opportunity for the layer to grow by amalgamation among structures. The evolution of the single structure to its final stage and its connections to vortex-gas equilibrium are discussed in detail in Chapter 4.

3.1.3. The intermediate asymptotics of Regime II

It can be observed from Fig. 3.1 that between Regimes I and III is an intermediate Regime II in which the layer exhibits linear growth.

From a mechanics view point, the transition between the short-time initial and long-time asymptotic states is governed by an intermediate asymptotics that can be derived by methods similar to those used by Millikan (1938) in channel flow and Kolmogorov (1941) in turbulence spectra (see Narasimha 1996). The argument can be applied to the present system as follows.

Let $\hat{\delta}[t]$ be a measure of the mixing layer thickness uniquely determined from $\{x_i(t), y_i(t)\}$ at each instant of time t. The value of $\hat{\delta}$ could be a statistic directly involving the position of the vortices (such as the RMS value of y - displacements of all vortices), or a thickness based on the computed x-averaged velocity field, such as the momentum or vorticity thickness. Dimensional analysis shows that the growth rate of the mixing layer can be written as

$$\frac{d\hat{\delta}}{d(t\Delta U)} = F\left[\frac{t\Delta U}{l}, \frac{L}{l}, \frac{\{x_i(0), y_i(0)\}}{l}\right] \tag{3.1}$$

where F is some function to be determined. (We choose ΔU as a basic variable instead of γ, as it is a large scale quantity that is more relevant for fluid dynamics, and this choice will not make any difference to the following analysis.) Here l is the initial inter-vortex spacing, but it is important to note that the following analysis holds if l were to be replaced by another characteristic length scale of the initial condition (such as amplitude or wavelength of periodic forcing). The limit $L/l \to \infty$ would imply that the domain size is much longer than any length scale characterizing the initial conditions. Such a limit would always be appropriate for any 'canonical' (Basu et al, 1992) temporal shear layer in an infinite domain.

If we hypothesize that the solution (3.1) evolves to a state independent of the precise initial configuration for sufficiently large $t\Delta U/l$,the third argument of F in (3.1) will drop out in the limit, so

$$\lim_{t\Delta U/l\to\infty} \frac{d\hat{\delta}}{d(t\Delta U)} = \lim_{t\Delta U/l\to\infty} F_1\left(\frac{t\Delta U}{l}, \frac{L}{l}\right) = F_2\left(\frac{t\Delta U}{l}, \frac{L}{l}\right) \tag{3.2}$$

where F_2 is the functional form taken by F_1 as $t\Delta U/l \to \infty$.

Assuming that this converges in the limit $L/l = N \to \infty$,

$$\lim_{N\to\infty,t\Delta U/l\to\infty} \frac{d\hat{\delta}}{d(t\Delta U)} = \lim_{N\to\infty} F_1\left(\frac{t\Delta U}{l}\right) = F_2\left(\frac{t\Delta U}{l}, N\right) \tag{3.3}$$

In what may be called the long-time or 'outer' limit (see Van Dyke 1964), we have $t\Delta U/L = O(1)$,so the solution maybe expected to be dominated by the finite domain size and hence depend on $t\Delta U/L \equiv (t\Delta U/l)\ /\ (L/l)$, which we observe as we approach Regime III in Fig. 3.1. This is known to happen in other areas of physics. Hence, in this regime, we may write (3.3) as

$$\frac{d\hat{\delta}}{d(t\Delta U)} \to F_3\left(\frac{t\Delta U}{L}\right),\ \ t\Delta U/l \to \infty, L/l \to \infty, t\Delta U/L \text{ fixed} \tag{3.4}$$

where F_3 is the functional form assumed by (3.3) in the limits stated above. The above argument would strictly hold only in the early part ($t\Delta U/L < 4$) of Regime III, as we shall show in Chapter 6.

If we postulate an overlap between (3.3) and (3.4) in the simultaneous limits $t\Delta U/l \to \infty$ and $t\Delta U/L \to 0$ (in the spirit of matched asymptotic expansions, Van Dyke 1964), the only possibility is an overlap Regime II in which

$$\frac{d\hat{\delta}}{d(t\Delta U)} = C_{\mathrm{VG}} \tag{3.5}$$

where C_{VG} is independent of time; i.e. the layer thickness grows linearly with time. This is the analog of the log law in channel flow and the $k^{-5/3}$ law in the spectrum. The above analysis only suggests that C_{VG} is a constant, but it may or may not be universal across different initial condition classes.

A similar analysis can be performed for Navier-Stokes temporal free shear layers (Townsend 1956, details in Chapter 5), resulting in constant growth rate (say C_{NS}). Whether C_{NS} is universal or not has been a subject of significant controversy (Balaras 2001, George 2004) in turbulent free-shear-flow literature. Regardless of the connection between C_{VG} and C_{NS} (which will be explored in Chapter 5), it is highly worthwhile to address the question of the universality of C_{VG} in the vortex gas, for the reasons discussed in Chapter 1.

3.2. The universality and self-similarity of Regime II

To answer the question on universality, a total of 12 cases, with widely different initial condition classes for y_{i0} domain lengths, number of vortices and ensemble size have been performed. The results are presented in Fig. 3.2.

The initial conditions considered include uniform random distributions (cases R1, R2, R3, R4-1600, R4-400, R5-400) with amplitude ratio a/l varying from 10^{-8} to 2; Gaussian distributions(G1); bi-modal distributions in the form of sums of symmetric or asymmetric displaced Gaussians (respectively BM1, BM2); and distributions varying sinusoidally in x (P1 and P2). In the case of random initial conditions each realization is initialized with a different set of random numbers from the same class. The different 'realizations' required for ensemble averaging for sinusoidal initial conditions ($y_{i0} = a\ \sin(2\pi x_i/\Lambda + \phi_o)$, where a and Λ are the amplitude and wavelength of the perturbation) can be generated with different initial phases (ϕ_o) of the wave at $t = 0$ with respect to that at the beginning of the domain ($x = 0$); small differences in numerics lead to different solutions in terms of evolution of individual vortex positions over time due to the chaotic nature of the system, but the statistics will remain robust. This strategy is used in case P2. An alternative is to add a small random noise component to the wave at the

initial instant, and draw it from some specified distribution. This is done for case P1 whose discussion is deferred to Chapter 5.

Table. 3.1. Details of initial conditions, number of vortices, size of ensemble and the best fit Regime II spread rate for different cases

Code	N	n	Initial conditions	Best fit $d\theta/d(t\Delta U)$
R1	3200	577	Uniform random, $a / l = 5 \times 10^{-2}$	0.016618
R2	10000	11	Uniform random, $a / l = 1 \times 10^{-1}$	0.016685
R3	1600	256	Uniform random, $a / l =$ **1×10^{-8}**	0.016587
R4-32000	**32000**	14	Uniform random, $a / l = 1 \times 10^{-3}$	0.016506
R4-1600	1600	512	Uniform random, $a / l = 1 \times 10^{-3}$	0.016532
R4-400	**400**	512	Uniform random, $a / l = 1 \times 10^{-3}$	0.016510
R5	400	512	Uniform random, $a / l =$ **2.0**	0.016562
G1	1600	512	Gaussian, $\sigma / l = 1.0$	0.016689
BM1	1600	1024	Symmetric bimodal, $\sigma_1 / l = \sigma_2 / l = 10^{-1}$, $d / l = 6 \times 10^{-1}$	0.016737
BM2	1600	1024	Assymmetric bimodal, $\sigma_1 / l = 10^{-2}$, $\sigma_2 / l = 2 \times 10^{-2}$, $d / l = 4 \times 10^{-2}$	0.016534
P1	3200	288	Sinusoidal, $a_w / l = 4 \times 10^{-1}$, $a_n / l = 4 \times 10^{-4}$, $\Lambda / l = 100$	0.016635
P2	1600	512	Sinusoidal, $a_w / l = 1.188 \times 10^{-2}$, $a_n / l = 0.0$, $\Lambda / l = 50$	0.016624

The respective growth histories in Regime II are shown in Fig. 3.2. A best fit to the growth is obtained by minimizing

$$\sum_{t=t_{IIb}}^{t=t_{IIe}} (1 - ((At\Delta\mathrm{U} + B)/\theta[t]))^2$$

with respect to A and B, where t_{IIb} and t_{IIe} are the estimated beginning and end of Regime II. We choose t_{IIe} to be 0.8 $t\Delta U/L$ or the end of the respective simulation, whichever is earlier. The time beyond which the local slope is within 10% of the overall slope is taken as t_{IIb} (except for sinusoidal initial conditions for which the criteria is the point beyond which fluctuation in local slope is less than 25% of the overall slope) and for the different cases t_{IIb} is indicated in Fig.3.2 by short vertical bars. We take as reference the best fit value for R1 (N = 3200 ; n = 577), in which Regime II extends over more than two decades in $t\Delta U/l$ (20 – 2400), and $d\theta/dt = 0.0166\,\Delta U$ + const.

Figure 3.2B shows the ensemble-averaged best-fit growth rates and the 95% confidence limits for the ten cases considered. Based on these results the evolution of momentum thickness in Regime II is given by

$$\theta_{\text{Regime II}} = 0.0166\,[\pm 0.00015]\,t\Delta U + C_3 \qquad (3.6)$$

with a universal slope and a non-universal intercept ranging from $-3.1\ l$ (P2) to $0.7\ l$ (G1) in the present simulations (the corresponding 'virtual origin' (intercept on the time axis) of the linear growth in Regime II, t_i, would be $186\,l/\Delta U$ and $-42\ l/\Delta U$). The departures in Regime II growth rate across the wide range of initial conditions are within a band of $\pm$1% from the reference, as compared to the 30% uncertainty quoted by the authors in the vortex-gas simulation of Aref & Siggia (1980). Further, we find that the universality extends to classes of initial conditions not included in Table 3.1, such as ones involving several rows of point-vortices to mimic a piece-wise linear velocity profile, which will be discussed in Chapter 6. (We shall also show, in Chapter 8, that this universality is robust to addition of a random walk to simulate diffusion and that it is unaffected by desingularization of the point-vortices in Appendix C).

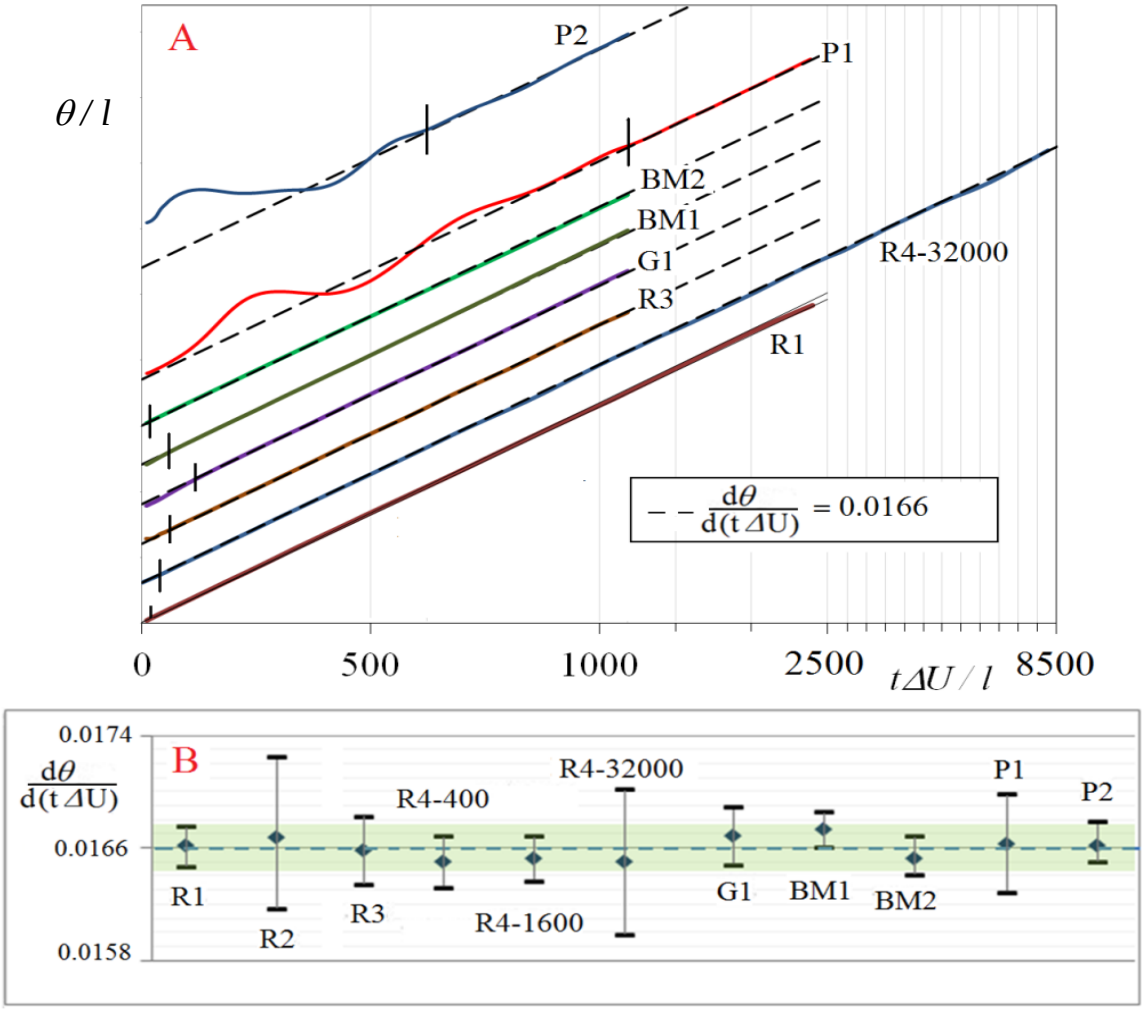

Figure 3.2. (**A**) Universality of Regime II. Note the wide range of initial conditions including those with very long transients, and the changes in scale at *tΔU/l* of 1000 and again at 2500. (**B**) Estimate of uncertainties in Regime II growth rates. The error bars show the 95% confidence limits (computed using Student's *t*-distribution). The dotted line is drawn through the reference (R1) growth rate.

For two illustrative cases (G1 and P2) Fig. 3.3 shows that the moments of the vortex positions, $m_k = < |y_i|^k >^{(1/k)}$, become universal multiples of the momentum thickness at sufficiently long times, in general longer for the sinusoidal initial condition (P2) compared to the Gaussian initial condition (G1), establishing similarity and universality irrespective of the measure used to describe layer thickness. These simulations thus provide overwhelming evidence for the existence of a universal growth rate for the vortex-gas turbulent free shear layer, over a large and diverse class of initial conditions (as well as for diffusion and desingularization).

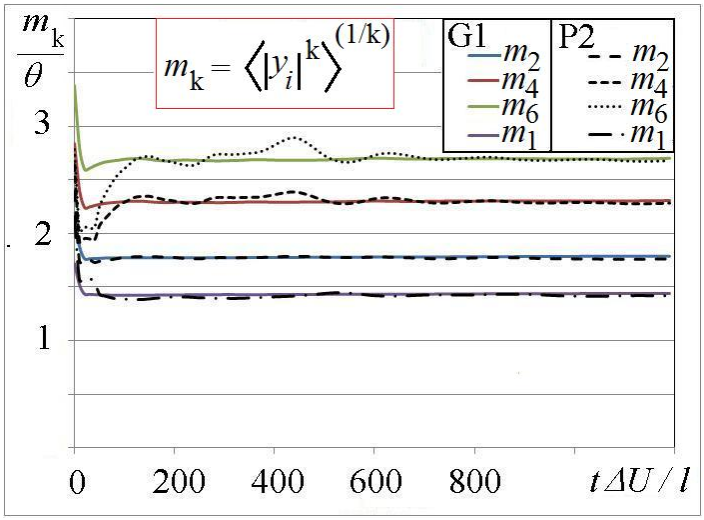

Figure 3.3. Evolution of various measures of thickness based on vortex positions for G1 and P2. All of them settle to a constant factor of θ in Regime II for the two very different initial conditions.

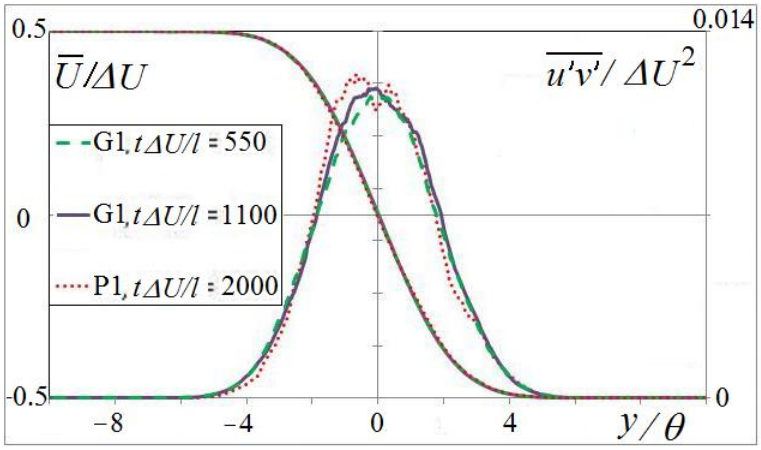

Figure 3.4. Self similarity and universality of *x*-averaged (fluid) velocity and 'Reynolds shear stress' profiles. The latter has been evaluated using integral of vorticity flux (computed from 64 member ensembles).

We now examine certain fluid dynamically relevant quantities. Figure 3.4 shows profiles of mean velocity and Reynolds shear stress for the case P1 and (at two different times) for the case G1. The Reynolds shear stresses are evaluated as follows. It is easily shown from the Reynolds-averaged Euler equations that, for the 2D temporal mixing layer considered, the stream-wise momentum balance reduces to $\frac{\partial \tau_{xy}}{\partial y} = -\overline{v'\omega'}$, where $\tau_{xy} = \overline{u'v'}$ *i*s the Reynolds shear stress and $\overline{v'\omega'}$ is the mean vorticity flux at *y*. In the present vortex-gas free shear layer, the Reynolds shear stress at *y* can be computed by evaluating $-\Sigma v_i \gamma_i / L$ over all the vortices with $y_i < y$, where v_i is the vertical velocity induced on the *i*th vortex. (Also note that in the present notation, the sign of the stress is opposite to what is normally adopted. We adopt this notation as $\partial\overline{U}/\partial y$ is negative in the present problem).

In the normalization used in similarity theory, with velocities scaled by ΔU and normal displacement with θ, it is seen that the three profiles agree for both mean velocity and Reynolds stress, indicating both self-similarity and universality, and hence of (fluid-dynamical) equilibrium in the sense of Narasimha & Prabhu (1972).This implies that universality extends to any measure of thickness based on the mean velocity profile. For example, in Regime II, vorticity thickness defined as, $\delta_\omega = \Delta U / \left|\partial\overline{U}/\partial y\right|_{\max}$ is 4.6θ, and the universal slope in terms of δ_ω, is 0.076.

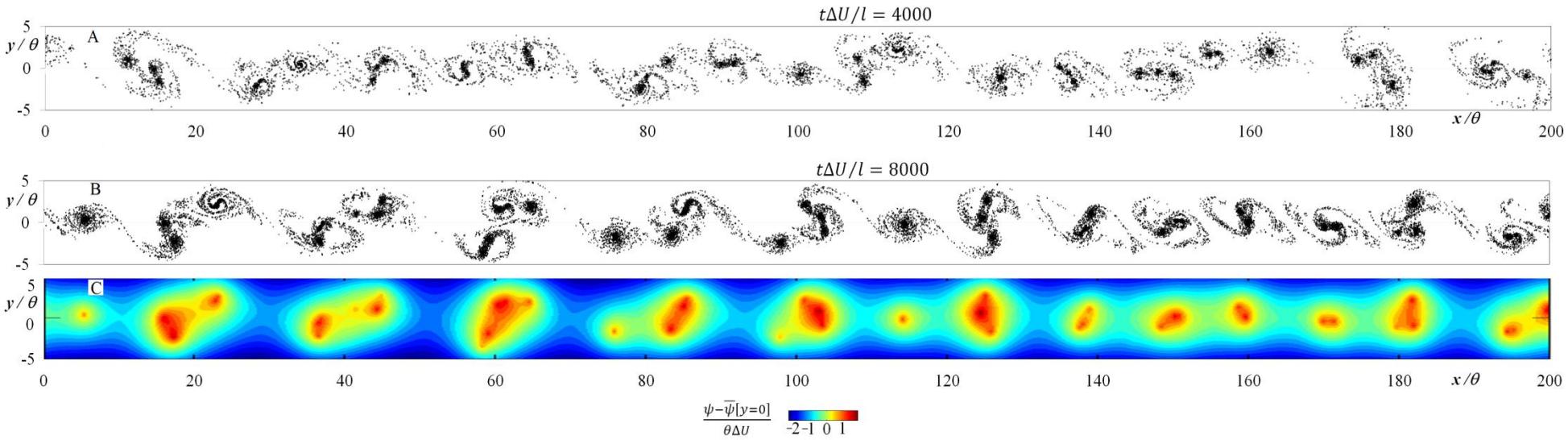

Figure 3.5. Snapshots of vortex-locations and stream-function in R4-32000.

Figure 3.5 shows the vortex locations at two different times from the largest of the present simulations, which employs 32000 vortices. It can be seen that both the internal details of the structures as well as the braids between structures are highly resolved at this value of *N*, with an average of 2000 vortices per structure at $t\Delta U/l = 8000$. Furthermore, when both *x* and *y* are scaled with the layer thickness, the entire solution appears statistically similar (at least at the large scales, say in terms of number and average size of structures) and this observation would be quantified in terms of distribution functions in Chapter 4.

The stream function ψ is related to the velocity field as $u = \partial\psi/\partial y\,, v = -\partial\psi/\partial x$. Using this relation and Eqs.(2.1, 2.2) the stream function for the present temporal-vortex-gas free shear layer is given by

$$\psi[x,y] = \sum_{i=1}^{N} -\frac{\gamma}{4\pi}\ln\left[\frac{1}{2}(\cosh[2\pi(y-y_i)/L\,] - \cos[(2\pi(x-x_i)/L)])\right] \tag{3.7}$$

Contours of constant stream function, called streamlines, are local tangents to the velocity field. The stream function also has an interpretation of 'local energy' in statistical mechanics. The contours of stream function shown in Fig. 3.5 (computed on 4096 x 401 grid for R4-32000) indicate the straining and rotational motion of the fluid in Regime II, and has features broadly similar to flow fields of Navier-Stokes shear layers (e.g. Brown & Roshko, 1974). All of this suggests that while one hand Regime II is characterized by universality and statistical self-similarity, on the other it has a complex flow field with multiple interacting structures.

Since the evolution in Regime II is independent of initial conditions and of *N* (at sufficiently large *N*, say $O(10^2)$ or more), it ought to be a characteristic of the internal dynamics which is entirely governed by a Hamiltonian. Therefore this result demands a statistical mechanical explanation. Furthermore, the evolution of thickness with time in Regime II is a universality of both the exponent on *t* (which is 1) as well as the coefficient in front (the spread rate). This is at the least unusual in statistical mechanics and hence worth exploring. Therefore, we shall study the statistical mechanics of the vortex-gas shear layer and seek an explanation in the following Chapter 4.

Chapter 4: Statistical Mechanics

Is there a statistical-mechanical explanation or analysis for the observed universality in Regime II? As discussed in the previous two chapters (see Fig. 3.5 in particular) Regime II is characterized by a linear increase in layer thickness with time (via interactions between several coherent structures). Hence, we have an essentially non-equilibrium evolutionary regime. It is therefore important to understand the whether the system has a final state and, if so, understand the statistical mechanics of the entire evolution over all the Regimes discussed in Chapter 3 as stages in the relaxation to that final state. In order to do so, we analyze the results (Fig. 4.1) of long-time integrations ($t\Delta U/L \gtrsim 10^4$) of Eqs.(2.1), (2.2) for different cases.

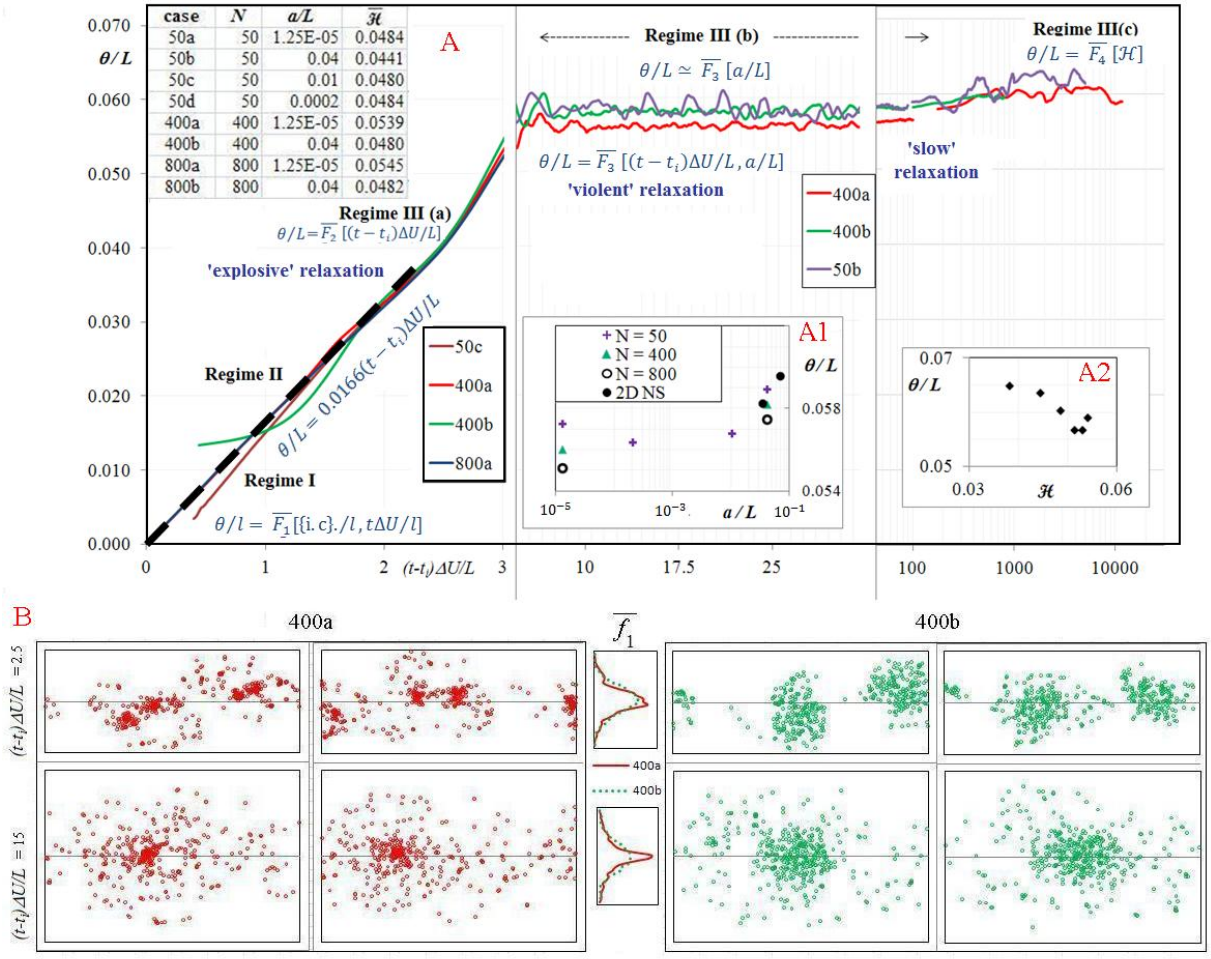

Figure 4.1. (A) Long time evolution of thickness for different cases. Note the switch to semi-log scale beyond $t\Delta U/L$ of 3. Beyond Regime II, there are several distinct relaxations, first involving a universal but not linear growth, then non-universal relaxation where θ/L is a function of a/L (shown in inset A1) and later a function of $\mathcal{H}$(shown in inset A2) before reaching what appears to be a stationary state. **(B)** Explanation for the 'loss of universality' in later Regimes.

While a more detailed explanation of Fig.4.1 will follow, here we point out certain striking features of the solution.

Firstly, it appears as if a final (steady) state does exist, but it is reached after very long times, of order $10^4\ L/\Delta U$ for N = 400, that is four orders of magnitude longer than the extent of the universal Regime II. This therefore suggests that Regime II is indeed very far from equilibrium.

Secondly, while the evolution beyond Regime II was classified as Regime III, it is important to note that it has distinct sub-regimes of relaxation to the final state, all of which will be analyzed in greater detail in this chapter.

The order of presentation in this chapter will follow the order of temporal evolution. Namely, we shall first discuss the non-equilibrium statistical mechanics of Regime II by computing single and two-vortex distribution functions and remarks on the applicability of vortex-gas kinetic theories. Then we shall analyze the relaxation to the steady state, using ideas of violent and slow relaxations (Lynden-Bell 1967, Chavanis et al, 1996, Chavanis 2012). Finally we shall analyze the statistically steady solution and make connections with equilibrium solutions (Joyce & Montgomery 1973, Lundgren & Pointin 1977). This order of narration is perhaps most appreciated by readers with a fluid-dynamical background. We refer the reader to standard texts (e.g. Landau & Lifshitz, 1980) for standard definitions and concepts in classical statistical mechanics and to chapter 6 of Newton (2000) for a brief review of statistical mechanical ideas applied to the vortex gas.

. An equally applicable approach (which especially readers from statistical mechanical background may find more compelling) would be to read the rest of the chapter in reverse order, namely beginning with connections to equilibrium.

4.1 Non-equilibrium statistical mechanics of Regime II

4.1.1. Single vortex distribution

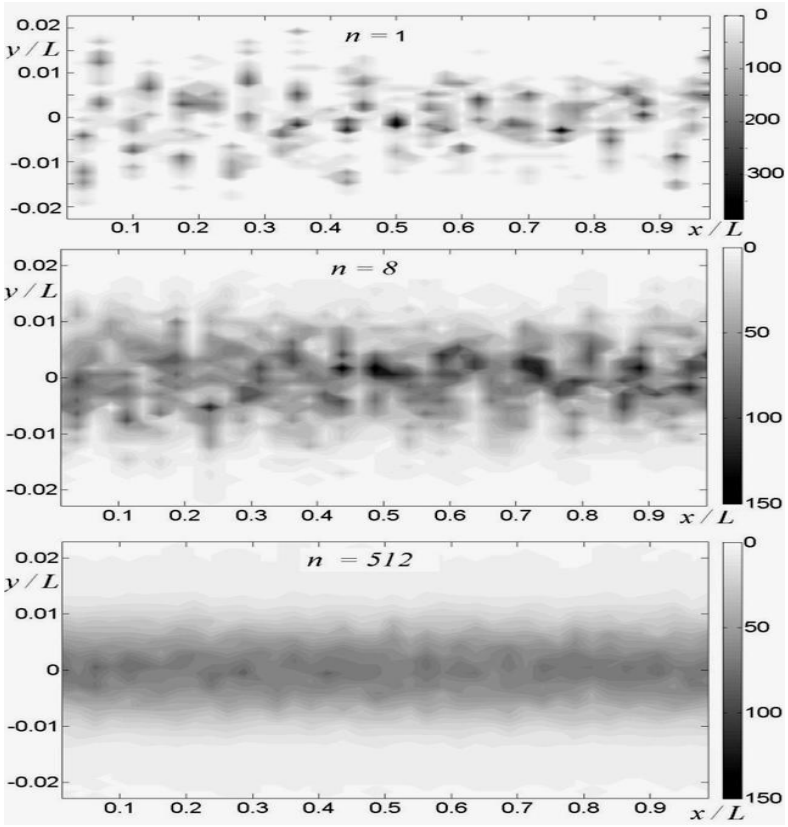

Figure 4.2 Sample contour plots of f_1 at three different ensemble sizes (for R4-1600) at $t\Delta U/L = 0.2$. Note that with increase in the size of the ensemble, the x-dependence is reduced as a consequence of x-homogeneity

We begin by exploring the possibility of existing kinetic-theory based approaches providing an explanation of the observed universality. In order to do so, we compute the single and two-vortex distribution functions. We consider cases R4-1600 and R4-400 as they involve a short Regime I and large ensemble sizes, and provide a better opportunity to assess the effect of the number of vortices in the simulations. We divide the domain into 40 by 40 boxes of equal size. While the width of each box (Δx) is fixed, the height (Δy) is increased linearly with time to cover the entire layer as it grows and to provide optimum resolution at all times. We record $N_v\,[x, y, t]$, the number of vortices present in each box of $\Delta x \times \Delta y$, centered at (x, y) at a given time instant t, and then compute ensemble-averages over 512 realizations to obtain the single particle distribution function f_1 defined as,

$$f_1[x, y, t] = L^2/(N\Delta x\Delta y)\ \langle N_v[x, y, t]\rangle$$

Note that this definition ensures that f_1 is normalized such that $\sum f_1 \Delta x\Delta y = L^2$ (We use this normalization for convenience as it renders f_1 dimensionless, in contrast with the conventional definition.) Note that this single-particle distribution function is related to the ensemble-averaged vorticity as $f_1 = \langle\omega\rangle/(\Delta U/L)$. Since the system is homogeneous in x, the ensemble-averages should be independent of x. This is verified by the observation from Fig. 4.2 that the variation of f_1 in x decreases with increasing ensemble sizes. However, even at an ensemble size of 512 members, there is up to 10% fluctuation in f_1 with x. Therefore, in order to improve the statistics, the single particle distribution is averaged over x to obtain $\overline{f_1}\,[y]$, with $\sum \overline{f_1}\Delta y = L$. (As a consequence of x-homogeneity, $f_1[x, y, t] \rightarrow \overline{f}_1[y, t]$ with sufficiently large ensembles.)

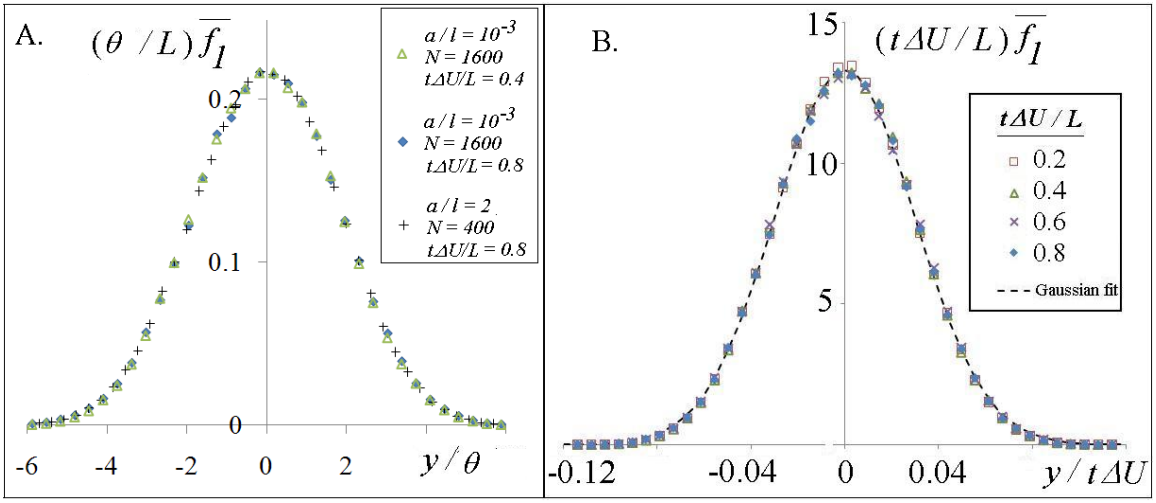

Figure 4.3 (A) Single particle distribution function for different cases when scaled by momentum thickness. **(B)** Self similar scaling of single particle distribution function (for R4-1600)

From Fig. 4.3.A, which shows Regime II data, at different times, for two cases in which initial conditions and number of vortices are both different, $\overline{f_1}[y, t]$ takes the universal form given by

$$\frac{\theta[t]}{L}\overline{f_1}[y, t] = \Phi_1\left[\frac{y}{\theta[t]}\right] \tag{4.1}$$

where Φ_1 is the self-similarity function; i.e. a function of two independent arguments y and t is reduced to a function of only a function of one argument $y/\theta[t]$.

Further, when $t\Delta U$ is such that $C_3 \ll t\Delta U \ll L$, Eq.3.1 shows that θ is linear in $t\Delta U$. Therefore, in the limit of $t/t_{RI} \to \infty$ (equivalently, $L/l \to \infty$ for a given a/l and $t\Delta U/L$), $\overline{f_1}$ follows self-similar scaling in Regime II :

$$\overline{f_1} = \frac{L}{t\Delta U}\Phi_2\left[\frac{y}{t\Delta U}\right] \tag{4.2}$$

This limit is closely reached for the case R4-1600 for $t\Delta U/L \geq 0.2$ as seen in Fig. 4.3B. This result is important, for the similarity form of the solution (18) is not admitted by the kinetic theory proposed by Chavanis (Eq. 129 of Chavanis, 2001).

4.1.2. Two-vortex correlation

To explore this issue further, we compute the joint two-vortex distribution function $f_2[x_1,y_1,x_2,y_2]$ by enemble-averaging the product of the number of vortices in two given boxes centered at (x_1,y_1), (x_2,y_2) respectively at a given time as,

$$f_2[x_1, y_1, x_2, y_2, t] = (L^2/(N\Delta x\Delta y))^2 \langle N_v[x_1, y_1, t]N_v[x_2, y_2, t]\rangle$$

We define the two-vortex correlation function f_2' as

$$f_2'[x_1,y_1,x_2,y_2] = f_2[x_1,y_1,x_2,y_2] - f_1[x_1, y_1]f_1[x_2, y_2]$$

If $f_1[x_1, y_1]$ is statistically indepenent of $f_1[x_2, y_2]$, i.e. if we make the analog of Boltzmann's 'molecular' chaos assumption, then the right hand side should vanish. Now due to x-homogeneity f_2' should depend only on y_1, y_2 and $|x_1\text{-}x_2|$ for a sufficiently large ensemble. Again averaging over x to improve the statistics we present $\overline{f_2'}[|x_1 - x_2|, y_1, y_2]$ versus $|x_1 - x_2|$ and fixed y_1 and y_2 (both set close to zero). It can be immediately seen from Fig. 4.4 that f_2' shows a systematic variation with $|x_1 - x_2|$. and that it can take values several times that of the local $f_1{*}f_1$ at small $|x_1 - x_2|$. Furthermore $\overline{f_2'}$ takes both positive and negative values, indicating the presence of strong two-vortex correlations of both signs alternating between each other.

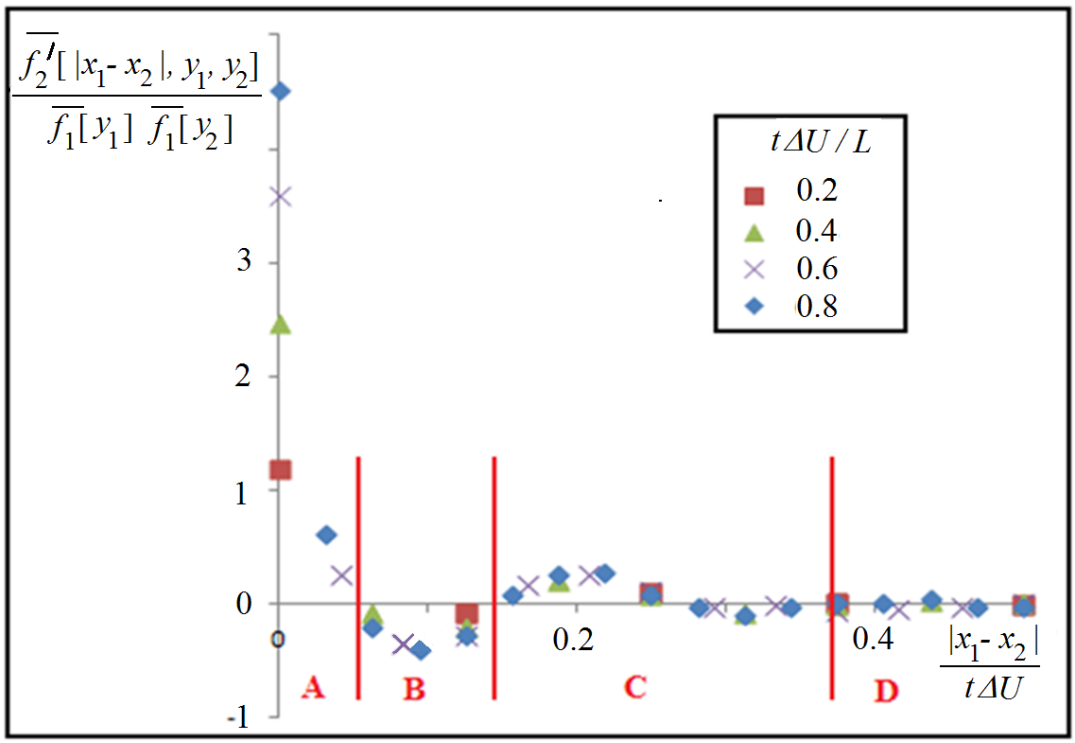

Figure 4.4. Temporal evolution of f_2'as a function of x-separation ($|x_1 - x_2|$) at $y_1 = y_2 = 0.0029\ t\Delta U$ during Regime II of case R4-1600. Note that there is self-similar scaling except at very small $|x_1 - x_2|$ (region A).

To understand the *r*-dependence of f_2' exhibited in Fig. 4.4, it is instructive to relate it to the coherent structures in the flow, in particular to the length-scales associated with their size and spacing. These are obtained as follows. From an analysis of the snapshots of the vortex configurations such as those in Figs. 2.2 and 3.5, we find that the average number of coherent structures in the *L*-domain during Regime II is approximately $4L/t\Delta U$ in the limit $C_3 \ll t\Delta U \ll L$ and hence the average *x*-distance between their centers is approximately (1/4) $t\Delta U$, equivalently about 15θ from Eq.12. Further, from Fig. 2.2, the size of the structures is approximately half the spacing between their centers, i.e. about (1/8) $t\Delta U$ or 7.5 θ. The nearest vortex-sparse ('braid') region and therefore stretches from approximately 0.06 to 0.19 $t\Delta U$ from the center of a given structure.

Returning to Fig. 4.4, it is seen that the functional dependence of f_2' on the *x*-separation exhibits four distinct regions.

A. At small separations ($|x_1 - x_2| < 0.05\ t\Delta U$ near the *x*-axis), which approximately correspond to distances within the same structure (i.e. less than half the average size of the structure), f_2' is several times $f_1 * f_1$ and positive.

B. At distances $0.05\ t\Delta U < |x_1 - x_2| < 0.15\ t\Delta U$, $\overline{f_2'}$ is of order f_1^2 and negative. This clearly characerizes the vortex-sparse region between two neighbouring structures.

C. At somewhat larger separations f_2' oscillates between positive and negative values, with amplitude diminishing with distance. The first positive peak is located at approximately $0.22\ t\Delta U$, which is roughly the distance to the center of the next structure,and reflects the degree of order in the arrangement of nearby structures. The peaks progressively decay with larger separation.

D. At large distances ($|x_1 - x_2| \geq 0.4\ t\Delta U$) $\overline{f_2'}$ is negligible, indicating that vortex positions are uncorrleated. It is only in this region that the analog of Boltzmann's 'molecular chaos' is valid.

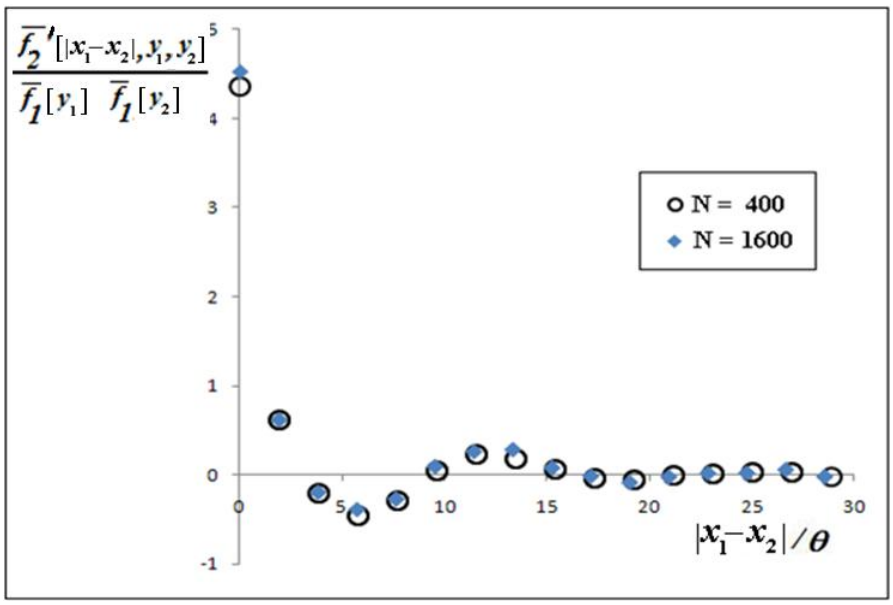

Figure 4.5. Variation of $\overline{f_2'}$ with number of vortices (case R4-400 and R4-1600 at $t\Delta U/L$ = 0.8 with y_1 = y_2 = 0.18θ). Note that the maximum value of $\overline{f_2'}$ changes by less than 5% from N = 400 to 1600 (which is within the statistical uncertainity).

We now examine the variations of f_2' with *N*. Fig. 4.5 compares $\overline{f_2'}$ (at $y_1 = y_2 = 0.18\theta$, $t\Delta U/L$ = 0.8) computed from simulations with *N* = 400 and *N* = 1600. The differences are so small that the

observed values of f_2' seem to be N independent and this is an evidence for the presence of strong correlations in Regime II. This is not surprising because of the nature of vortices to cluster and form coherent structures, as indeed the nature of variation of f_2' has been seen to be related to the observed size and spacing of the coherent structures. Hence, in the vortex-gas free shear layer, f_2' can neither be neglected as done in most Boltzmann inspired 'kintetic theories' (Chavanis 2001,2005,2010, Sano 2007) nor be considered as O(1/N) as proposed in a recent work (Chavanis,2012).

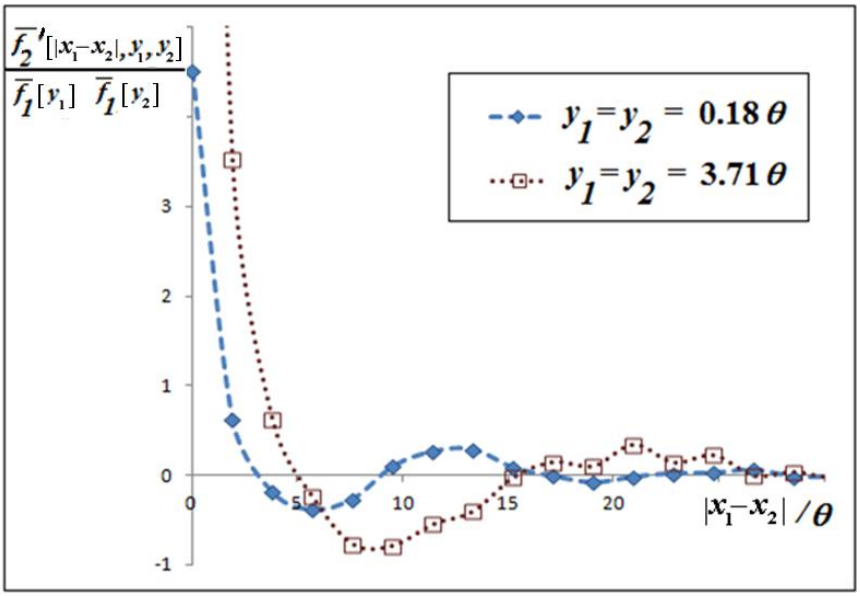

Figure 4.6 (A) Variation of $\overline{f_2'}$ with y at $t\Delta U/L$ = 0.8 for case R4-1600.

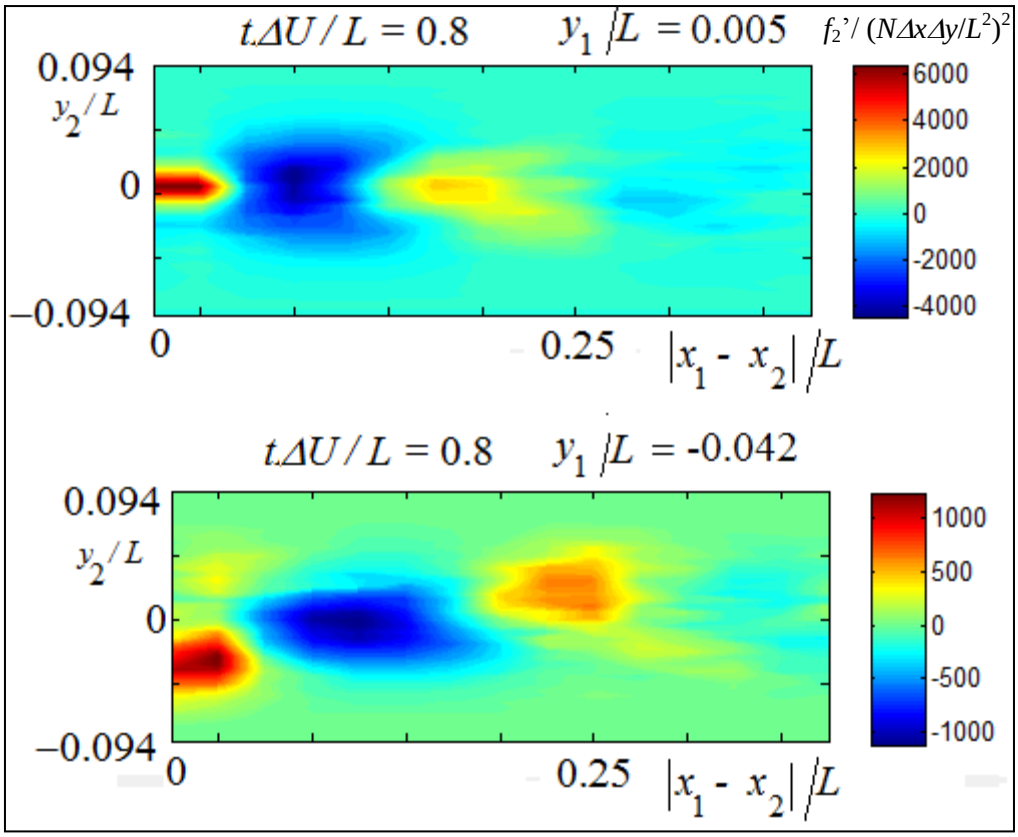

Figure 4.6 (Contd.) **(B)** Contour plots of f_2'in the $|x_1 - x_2|, y_2$ space for specified y_1.

Figure 4.6A compares $\overline{f_2'}$ at two different values of y co-ordinates. It can be seen that the variation of $\overline{f_2'}$ is qualitatively similar but quantitatively different at different values of the y co-ordinate when $y_1 = y_2$. Further insight can be obtained from the contour plots of $\overline{f_2'}$ in the $(|x_1 - x_2|, y)$ plane shown in Fig. 4.6B. It can be seen that for both cases shown, the maximum correlation occurs for $y_1 = y_2$, $|x_1 - x_2| \to 0$. However, the location of the second maxima corresponding to region C in Fig 4.4, is approximately at $y_2 = -y_1$. This can be clearly seen in the second diagram. Though a more detailed investigation is required before arriving at definitive conclusions on the shape of $\overline{f_2'}$ and its physical interpretation, Fig 4.6B suggests that for a given structure with y-centroid of above the x-axis, the y-centroid of the nearest neighbour is most likely to be below the x-axis (and vice-versa), by approximately the same normal distance from the x-axis.

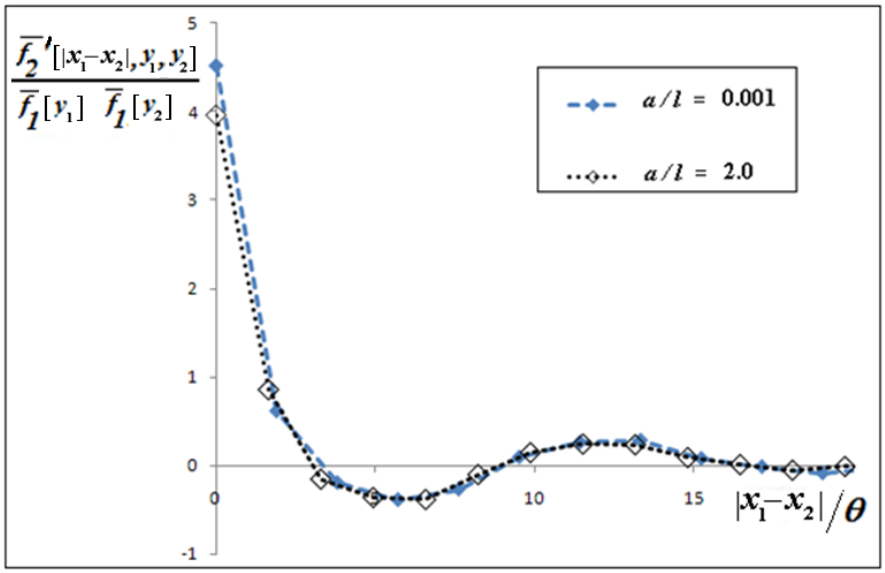

Figure 4.7. Dependence of f_2' on initial conditions ($t\Delta U/L$ = 0.8)

Figure 4.7 shows the variation of f_2' for two initial conditions whose amplitudes differ by three orders of magnitude. The differences are negligible in general, but become barely noticeable as $|x_1 - x_2| \to 0$. On returning to Fig. 4.4, we can also observe the lack of self similarity f_2' of as $|x_1 - x_2| \to 0$. However, there does not seem to be any evidence against self-similarity and universality of f_1 (Fig. 4.3).

A possible heuristic explanation for this apparent inconsistency is as follows. When the structures grow in size with time, the average inter-vortex spacing is expected to increase in most parts of the system. But this has to be balanced by the reduction of inter-vortex spacing somewhere in the system, possibly near the center of the structures, as demanded by the conservation of the Hamiltonian. This explanation would not be inconsistent with the observation of self-similarity of f_2' except near the center of the structures, i.e. when $|x_1 - x_2| \to 0$, where f_2' increases with time (because the vortex density and hence the correlations increase at the center of the structures as they grow in size with time). Similarly, a different class of initial conditions would have a different Hamiltonian that will be conserved throughout the evolution, and this dependence is likely to manifest near the center of the coherent structures. This dependence could be responsible for the slight difference in f_2' at $|x_1 - x_2| \to 0$, for the two different initial conditions shown in Fig. 4.7. However, it has to be noted that the coherent structures occur at different y-locations, as observed in Fig. 2.2. As a consequence, on averaging over different realizations, the effect of the vortex distribution within the clusters plays an insignificant role in determining the single particle distribution function f_1. This will be considered further during the analysis of Regime III in the following section. We shall show that as long as more than one structure is present (which is the case in Regime II), the vortex distribution within the structure does not alter the single particle distribution

function and therefore the mean vorticity and velocity profiles, and hence also the layer thickness, but becomes important when only one structure is left in the domain.

The central message these analyses convey is that the present system of the vortex-gas free shear layer is strongly correlated and existing 'kinetic theory'approaches based on the Boltzmann equation that neglect correlations or consider them as O(1/*N*) are inapplicable in Regime II. However, several of the features of the two particle correlation function can be qualitatively explained by relating them to the coherent structures.

4.2. Relaxation from the universal non-equilibrium Regime II to a steady state

In spite of the fact that Regime III is entirely a consequence of the finiteness of the domain (which would also be true of any real world system), and so not directly relevant to the canonical temporal mixing layer defined in fluid-dynamical studies ($L \to \infty$), it is relevant as the long-time solution of an initial value problem. It is of fundamental importance to understanding the connections between turbulent shear flows and the statistical mechanics of vortex-gas systems in equilibrium.

4.2.1. Regime III(a) – Interaction between a small number of structures

From Fig. 4.1A it is seen that the evolution of momentum thickness begins to depart from the linear growth of Regime II at around $(t\text{-}t_o)\Delta U/L \sim 1$. However, till about $t\Delta U/L \sim 3$, the variation of θ continues to remain universal with L as the length scale, independent of initial conditions or N, as illustrated in Fig. 4.1A for four widely different cases. We find that in this regime (III(a)) the number of structures can vary from 4 to 2.

Figure 4.1B shows a snapshot of vortex locations for the two cases 400a, 400b with two different realizations in each case. Both have the same number (400) of vortices, but initial y-displacements are drawn from uniform random distributions of widely different amplitudes, respectively $1.25 \times 10^{-5} L$ (low amplitude) and $0.04\ L$ (high amplitude). It can be observed from Fig. 4.1B that in the left panel, the low amplitude simulations show structures with dense cores, characterized by high concentration of vortices. With high initial disturbances (right panel, 400b) the cores are not so dense.

From the snapshots in the top panel in Fig. 4.1B, at $t\Delta U/L = 2.5$ corresponding to an early phase in Regime III(a), it can be seen that the size and relative locations of the two coherent structures present in the domain are similar. Also, there is almost no difference in the x- and ensemble averaged single-vortex distribution function $\overline{f}_1$. This suggests that the averaged vorticity and velocity profiles have a much stronger dependence on the distribution of the coherent structures in the domain than on the distribution of vortices within each coherent structure. In contrast the bottom panel, at $t\Delta U/L = 15$ in Regime III(b), shows significant differences in $\overline{f}_1$, which has a tall narrow peak at the centre, showing the small dense cores in the low amplitude case. These observations indicate why the evolution of θ obtained from the x- and ensemble averaged velocity distribution is universal for different initial condition classes, whereas the vorticity distribution within a single coherent structure is not: variations in the y - locations of the structures averages out the effect of vorticity distribution within each structure. This also explains the universality of $\overline{f}_1$ in spite of the non-universality of f_2' at small r in Regime II shown in Fig. 4.7.

4.2.2. Regime III(b) – Violent and slow relaxations

Figure 4.1 shows that, following III(a), the momentum thickness varies very slowly: $\Delta(\theta/L) < 0.01$during $4 < t\Delta U/L < 10^4$, a change less than 20% of that seen during $0 < t\Delta U/L < 4$. Further, beyond $t\Delta U/L \sim 4$, there is only one structure left in the domain (Fig. 4.1B); and the evolution of momentum thickness is no longer universal. We label this sub-regime III(b).

The lack of universality in Regime III(b) (and subsequently also in III(c)) is consistent with the argument presented above for Regime III(a), namely, higher vortex density in the core of the structure with the lower amplitude initial conditions. Since III(b) involves a single structure, and since the *y*-centroid is invariant in time, the ordinate of the core of the structure would be similar in different realizations. Hence, unlike in Regimes II and III(a), an altered distribution of vorticity within the structure does affect the ensemble averaged statistics (Fig. 4.1B). This explanation is consistent with the observation of lower thickness for the gentler initial conditions in Regime III(b), shown in Fig. 4.1A.

Regime III(b), for certain classes of initial conditions (*a/l* >>1), exhibits two distinct sub-regimes. During the early part of III(b), say $t\Delta U/L$ ~ O(10) the thickness is a function of only *a/L* as shown in the inset A1 of Fig.4.1A Further we compute the vorticity - stream-function relation in this sub-regime to make connections with existing statistical mechanical ideas on relaxation to equilibrium. We divide the space [0, *L*] x [-*L*, *L*] into 41 x 81 boxes and compute f_1 by ensemble averaging, using the same definitions and methods presented in section 4.1. But here, since we are interested in the vorticity distribution within the single structure, we compute the statistics in the frame of reference of the centre or core of the structure (zone of highest vortex density, taken as the *x*-location of the vertical strip with the highest number of vortices, out of the 101 vertical strips of equal thickness over the domain). This is required as the single structure at the end of Regime III(a) can be formed at any *x*-location, and is expected to occur at different *x*-locations for different realizations. This averaging can also be thought as a phase averaging. The averaged stream function ψ can be computed from the single particle distribution function from the definitions of ψ, f_1 and governing equations (2.1 and 2.2) as

$$\psi[x,y] = -\frac{\Delta U}{L}\left(\frac{1}{4\pi}\right)\int f_1[x',y']\ln\left[\frac{1}{2}\left(\cosh\left[\frac{2\pi(y-y')}{L}\right]-\cos\left[\frac{2\pi(x-x')}{L}\right]\right)\right]dx'dy'$$

The averaged stream function at the i^{th} box is determined numerically from the computed discrete values of f_1 using

$$\psi[i] = -\frac{\Delta U}{L}\left(\frac{1}{4\pi}\right)\sum_{j\neq i} f_1[j]\ln\left[\frac{1}{2}\left(\cosh\left[\frac{2\pi(y_i-y_j)}{L}\right]-\cos\left[\frac{2\pi(x_i-x_j)}{L}\right]\right)\right]\Delta x\,\Delta y)$$

In the *j* = *i* box, the contribution to the integral is computed by once again dividing the original box into 101 x 101 smaller boxes.

The statistical equilibrium for a point-vortex gas (Montgomery & Joyce (1974), see also Chavanis (2001)), neglecting correlations (i.e. setting f_2' = 0) and taking the limit $t \to \infty$ before the limit $N \to \infty$, is shown to be characterized by the Boltzmann distribution $f_1 \sim \exp[-B\psi]$, where the Lagrange multiplier *B* can be interpreted in terms of an inverse temperature. The Boltzmann distribution is obtained by maximization of $f_1 \ln[f_1]$, subject to the constraint that the Hamiltonian is conserved.

On the other hand, it has been proposed that an 'equilibrium state' for Euler flow (Robert & Sommeria, 1991) can be obtained by maximization of the Kullback entropy $(\int \{f_1 \ln[f_1] + (1-f_1)\ln[1-f_1]\}$ where f_1 is non-dimensionalized with its maximum value in the initial condition, subject to constraints of kinetic energy and linear and angular momentum of the Euler flow. This is a fluid-dynamical analog of the Lynden-Bell theory (1967) of stellar systems. This limit is expected to be reached if the limit $N \to \infty$ before the limit $t \to \infty$ (Chavanis, 2011).

The present results, shown in Fig. 4.8, suggest that the vortex gas has a tendency to relax towards the Robert-Sommeria Euler equilibrium at 'intermediate times' of O(10 *L/ΔU*), and to the Boltzmann type equilibrium at much longer times of O(10^2-10^4*L/ΔU*) for *N* = 400, *a/L* = 0.04. For the vortex-gas simulations *N*ln*N* ~ 2400 and (*Na/L*) ln (*Na/L*) ~ 45, putting them possibly beyond the parameter range where finite *N* effects become important. We may label these two sub-regimes of relaxation as III(b1) and III(b2).

This is not inconsistent with the recent theoretical results of Chavanis (2011), which suggest that relaxation to equilibrium in a vortex gas has two stages. The first is a 'violent relaxation' that closely

approximates Euler dynamics and the second is a 'slow relaxation' to the 'Boltzmann' distribution driven by finite N effects that appear at timescales of O(Nlog$N$). However, the values of N = 400 used in the present long-time simulations are not large enough for a rigorous verification of the proposed Nlog$N$ scaling or for a strict comparison with the proposed Euler equilibrium.

Hence the present simulations show that the evolution beyond Regime II undergoes distinct phases of interaction between small but more than one structure to a single structure, violent relaxation of the structure towards Euler equilibrium and finally a finite-N driven slow relaxation towards a state possibly described by the Boltzmann distribution. We shall make detailed study of the existence and the relation to vortex-gas equilibrium of the asymptotic state of the vortex-gas free shear layer in the following section.

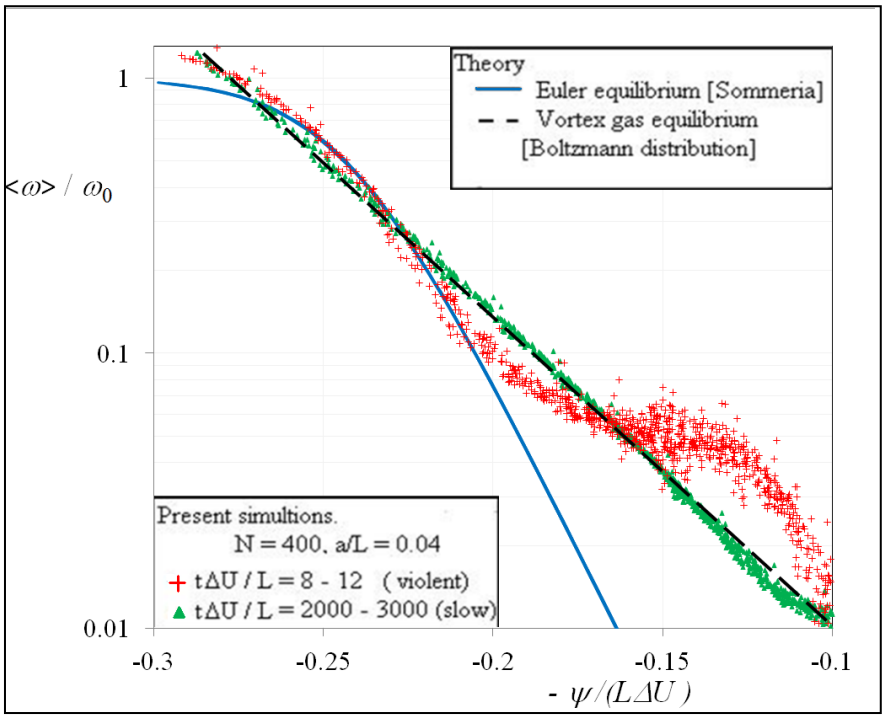

Figure 4.8. Comparison of present simulations at two times with Euler equilibrium of Robert & Sommeria (1991), and the 'Botlzmann' distribution of Onsager/Chavanis. Note that both the theoretical curves are two-parameter fits, and the averaging in the present simulation has been done relative to the centre of the structure.

4.3. Long time solution and relation to equilibrium statistical-mechanical theories

The single wandering structure

To study the possible existence asymptotic state as $t\Delta U/L \to \infty$, four very long-time simulations ($t\Delta U/L$ upto $3\text{x}10^4$) have been performed, with N ranging from 50 to 400. Figure 4.9 shows snapshots of the vortex locations at two different times 15000 and 21000 $L/\Delta U$, and it can be seen that at both times there is a single structure with a similar configuration of vortices within the structure, but the structure itself is present at different x-locations. The lone structure in the domain in fact keeps moving back and forth in x, sampling the entire domain over timescales of O($10^3\, L/\Delta U$) from Fig. 4.10A, which shows the time series of the position of the core (defined in 4.2.2) and, on the right, the PDF showing that the core samples the entire domain with roughly equal probability. From Fig. 4.10B, it is seen that the PDF of the velocity of the core does not change with time beyond 15000 $L/\Delta U$ and appears to agree well with a Gaussian distribution with zero mean. Therefore it is clear that $x_{\text{core}}(t)$ is a stationary stochastic process.

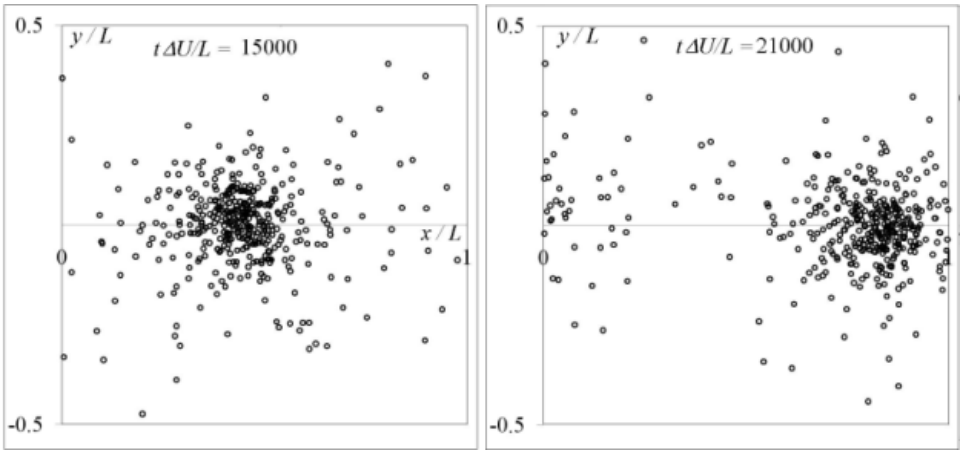

Figure 4.9. Snapshots of the lone vortex structure at two different times in III(c).

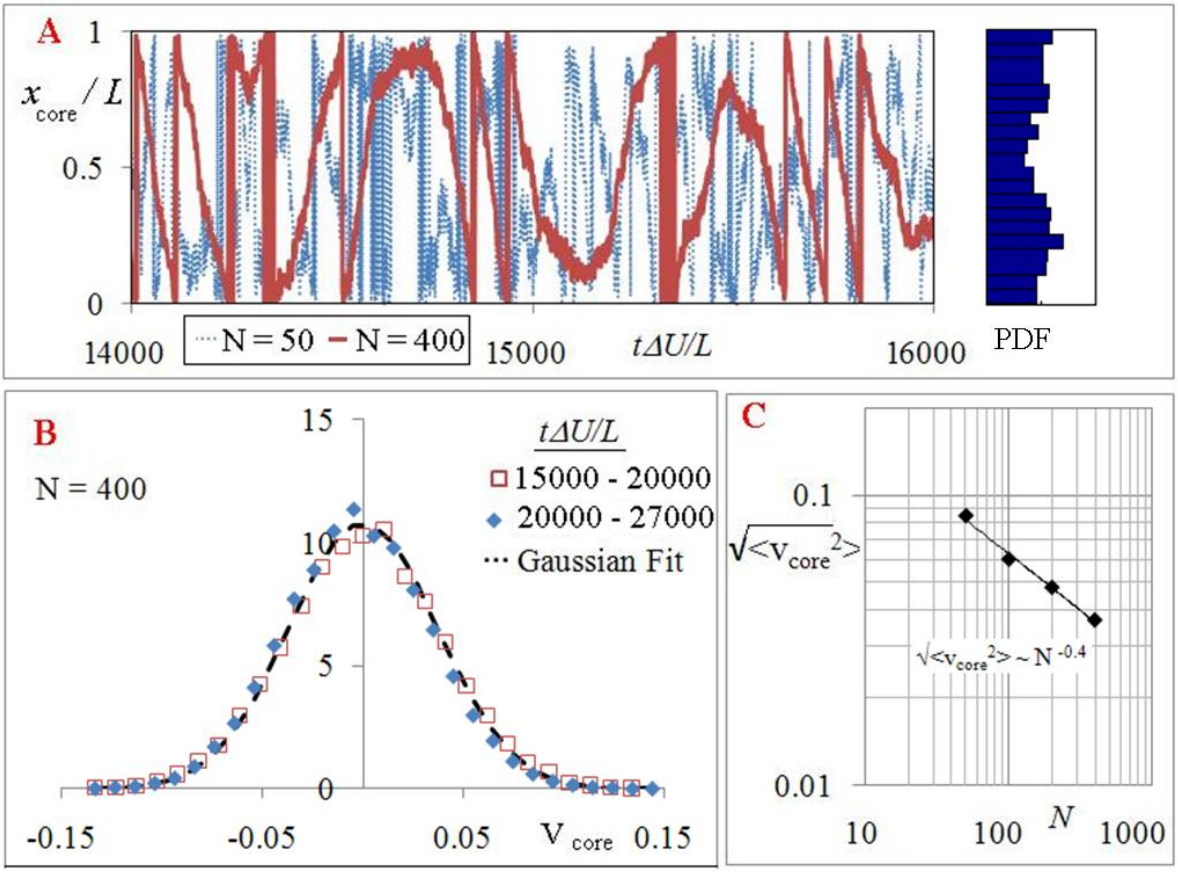

Figure 4.10. (A) Motion of the core of the structure in Regime III(b). The solution samples all x-translated states but with very long timescales that increase with increase in number of vortices. Also shown is a histogram of the locations sampled by the core over t = 15000 – 27000 $L/\Delta U$ for N = 400. (**B**) The motion of the core relaxes to a stationary stochastic process as can been seen from the PDF of a characteristic velocity (defined as the distance moved by the core as a fraction of the domain during one $L/\Delta U$). (**C**) The velocity of the core decreases with increasing number of vortices as $N^{-0.4}$.

Note that, unlike in the case of the infinite plane, the x-centroid (in the sense it has been used in this chapter) of the present x-periodic system is not conserved (see Appendix A). Therefore the observed stochastic motion of the vortex structure in x, sampling all the x-translated solutions with equal probability over sufficiently long intervals of time, is consistent with ergodicity. It is important to note that the size of the structure in the final state scales with L, hence the effect of boundaries cannot be neglected in III(c) however large the domain size. This shows that the common argument about

independence from the boundary, widely used in much of statistical mechanics, is not applicable to describe the final state of the present system involving long range interactions.

However, according to Fig. 4.10A the number of crossings of $x = 0.5\ L$ with $N = 400$ is roughly half that at $N = 50$, so the time taken by the structure for crossing the $L-$domain is about twice as long at $N = 400$. From Fig. 4.10C, the standard deviation of a characteristic velocity of the structure decreases like $N^{-0.4}$. This suggests that ergodicity may break down if the limit $N \to \infty$ is taken before the limit $t \to \infty$ (private communication, Sommeria). Thus, while the 'final state' consists of a single wandering structure that continually samples the entire x-domain in the limit $t \to \infty$ (N fixed), the possibility that the structure may be stationary if the limit $N \to \infty$ is taken first cannot be ruled out. The final asymptotic state therefore could depend on the order in which the limits $t \to \infty$ and $N \to \infty$ are taken (this has been pointed out by Chavanis (2011) in the more generalized context of vortex-gas statistical mechanics).

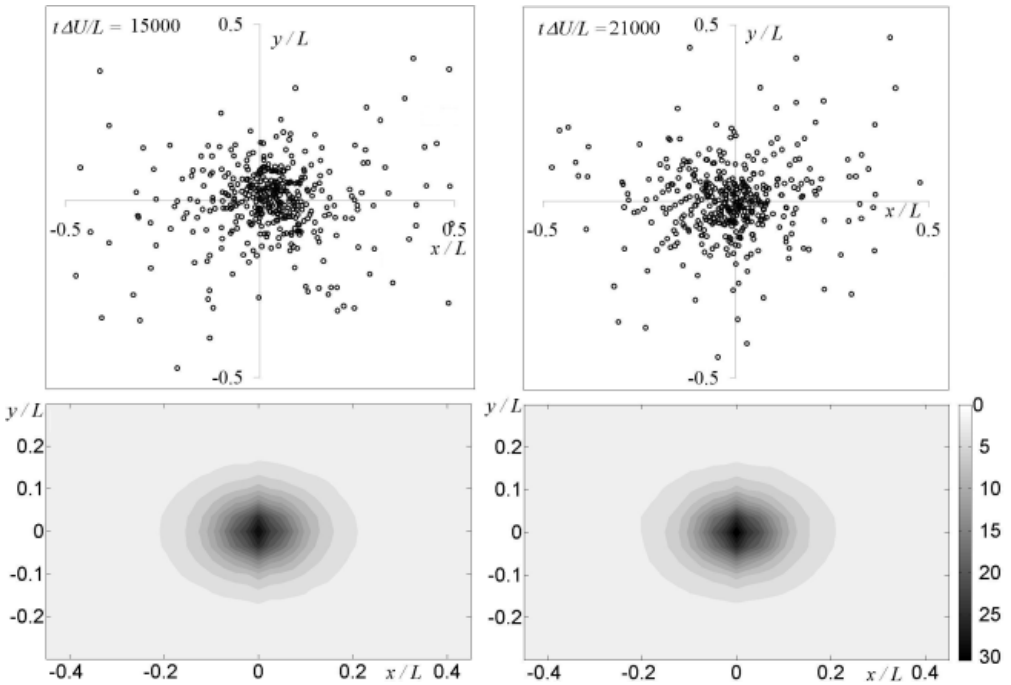

Figure 4.11. (A) Vortex positions relative to (moving) centre in Regime III(b),at times $t\Delta U/L$ = 15000 (left) and 21000 (right) (same data as in Fig.4.9). (**B**) The single-vortex distribution of (x-x_{core}, y) at $t\Delta U/L$ = 15000 and 21000, averaged over 250 $L/\Delta U$. Note invariance with time.

Therefore, one might argue that at large N, the motion of the structure might sufficiently slow down to probe via short-time averages, whether the vortex distribution around the structure reaches a stationary state and whether such a state can be considered a relative equilibrium in the sense of Newton (2000). Figure 4.11A shows snapshots of the positions of vortices re-centered around the core at two different times separated by 6000 $L/\Delta U$. We carry out a 'short-time average' (t_{avg} = 250 $L/\Delta U$) of the location of the vortices relative to the core, and these are shown in Fig. 4.11B. It is seen that there is very little variation between the single-vortex distributions across the two times. Further, as the orientation of the non-circular shape (the ratio of the major and minor axes is about 1.4) does not change in time, the structure as a whole is not in solid body rotation, but the individual vortices are in relative motion with respect to each other, as for example in the density wave motion in galaxies.

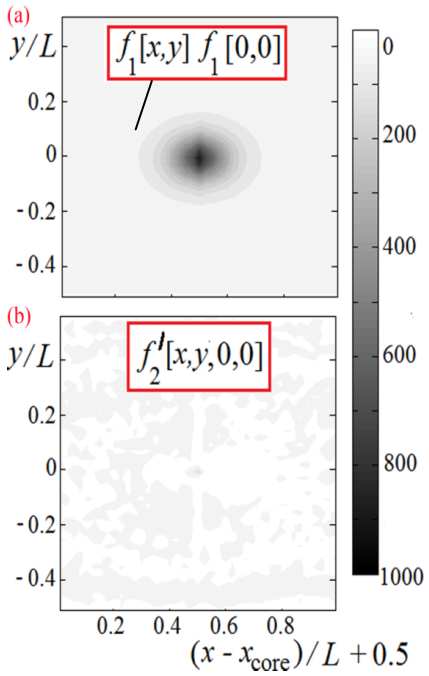

Figure 4.12 Comparison of distribution functions for vortices relative to the center in Regime III(c) (averaged over $t\Delta U/L$ = 15000 - 27000).

Connections to equilibrium

This leads us to perhaps the most important question in the statistical-mechanical analysis of any system, concerning whether a state of equilibrium (in our case, relative to the core of the moving structure) has been reached or not. We shall therefore try to assess whether the very long-term evolution of our system leading to regime III(c) represents a state of equilibrium, characterized by a well defined temperature. A necessary, but not sufficient, condition for the system to be in equilibrium is that (the equivalent of) *molecular chaos* should have set in. More precisely, the two-point correlation functions f_2' must vanish in such a state (in the thermodynamic limit $N \to \infty$). That would also be consistent with all higher order correlation functions being zero. This issue is specifically addressed in Fig. 4.12. It is seen here that f_2' computed from the time-averaged statistics in the frame of reference of the moving structure is small (less than 10%) compared to the f_1*f_1. This suggests that molecular chaos ($f_2 = f_1 * f_1$) might be a reasonable assumption to describe the statistics of the distribution of vortices within the moving structure. A comparison may be made with the two-vortex correlation in Regime II, where it was found to be of the same order and sometimes several times f_1*f_1 (Fig 4.4).

Now we turn to conditions that are both necessary and sufficient for equilibrium. The single particle distribution must first of all be independent of time, and secondly must be governed by a single parameter, namely the temperature. The time-independence of the distribution function across widely separated instants has already been demonstrated in Fig. 4.11.

Regarding the temperature, we approach the issue in two very different ways. The first is based on the results of Joyce and Montgomery (1973), and of Chavanis (2001). In this approach the equilibrium single-particle distribution function is expressed in terms of the stream function (ψ) and a temperature T via what is called the 'Boltzmann distribution' $f \sim \exp[-\mathrm{B}\psi]$ with $\mathrm{B} = \rho\gamma\beta$, where $\beta = 1/(k_B T)$, k_B is the Boltzmann's constant, and ρ is a suitable density (not necessarily of the fluid, see Appendix B for further discussion on appropriate density, thermodynamic limit and other related issues).

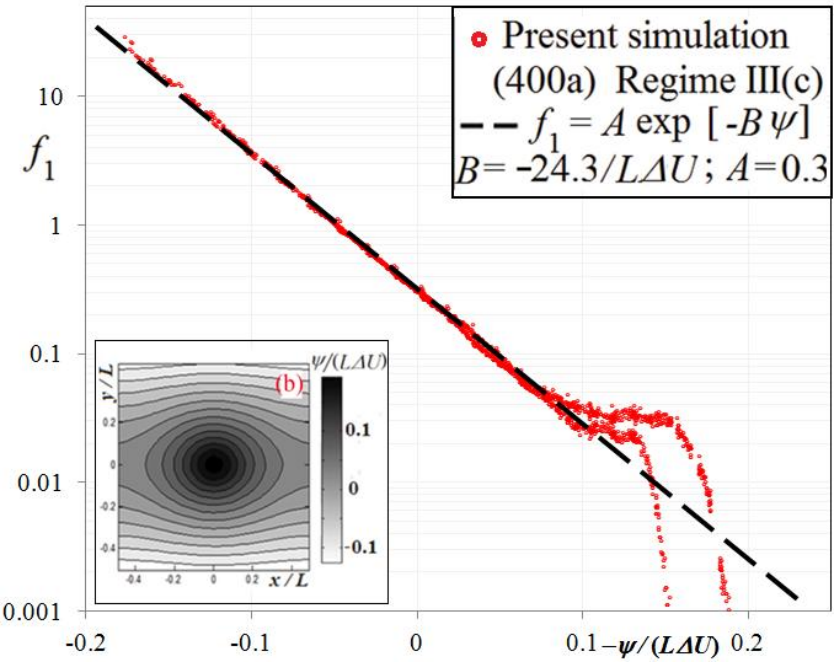

Figure 4.13. The stream function-vorticity relation in the frame of the moving structure in Regime III(c) (averaged over $t\Delta U/L$ = 15000 – 27000) for case 400a.

For the present simulation of case 400a, it is seen from Fig. 4.13 that the ψ-ω relationship in Regime III(c) follows the Boltzmann distribution for $f_1 > 0.03$, with the best fit $B = -24/(\Delta U\, L)$ for the time-averaged data. Note that this is negative, corroborating the seminal ideas of Onsager.

(Note that for $f_1 < 0.03$, there seem to be two distinct branches. It was found that the two branches correspond to data from the two sides of the shear layer and that there is only one branch if symmetry is forced by averaging f_1 from the top and bottom and then computing ψ from the mirrored distribution. This asymmetry in the calculated values of f_1 comes from inadequate sample size for the very low vortex-density region for the adopted time of averaging. Note that this region corresponds to $|y| \gtrsim 0.5\, L$, where there is hardly a single vortex at any given time instant in the present simulation as seen in Fig.4.11A. Further it is important to note that ψ is essentially computed via a double integral (i.e. by inverting the laplacian of f_1). Therefore any small asymmetry in f_1, say a delta perturbation ε due to a single vortex wandering bit further in the top half plane compared to the bottom half, which is purely a statistical fluctuation, will cause an apparently systematic shift of $\varepsilon\, y$ in ψ).

Since $\langle\omega\rangle = -\nabla^2\,\psi$, the Boltzmann distribution leads to a PDE for the stream function (Joyce & Montgomery 1973),

$$-\nabla^2\,\psi = A\exp[-B\psi]. \tag{4.3}$$

A comparison with the analytical solution of Stuart (1967) is presented in Appendix E. The final state of a variant of the temporal vortex-gas free shear layer has been studied by Shirkov & Berdichevsky (2009) who solve Eq.4.3 with a variant of the appropriate boundary conditions. The authors assume *x*-homogeneity in solving the problem, in which case Eq.(4.3) is not valid.

Lundgren & Pointin (1977) derived a solution for the final state of vortices in an infinite plane. The single particle distribution function in L-P solution depends only on the radial distance (r) from the centroid, and is given by

$$P[r/R_0] = \frac{\tilde{A}\exp[-(1+\lambda)(r/R_0)^2]}{\left(1-\pi\lambda\tilde{A}(r/R_0)^2\right)^2} \tag{4.4}$$

where R_0 is the radius of gyration $\sqrt{(1/N)\sum_{i=1}^{N}\left(x_i^2+y_i^2\right)}$, the inverse temperature $\lambda = \rho N\gamma^2/(8\pi k_B T)$ and $\tilde{A}$ is a normalization constant that ensures that the integral $\int_0^\infty 2\pi r P[r]dr = 1$.

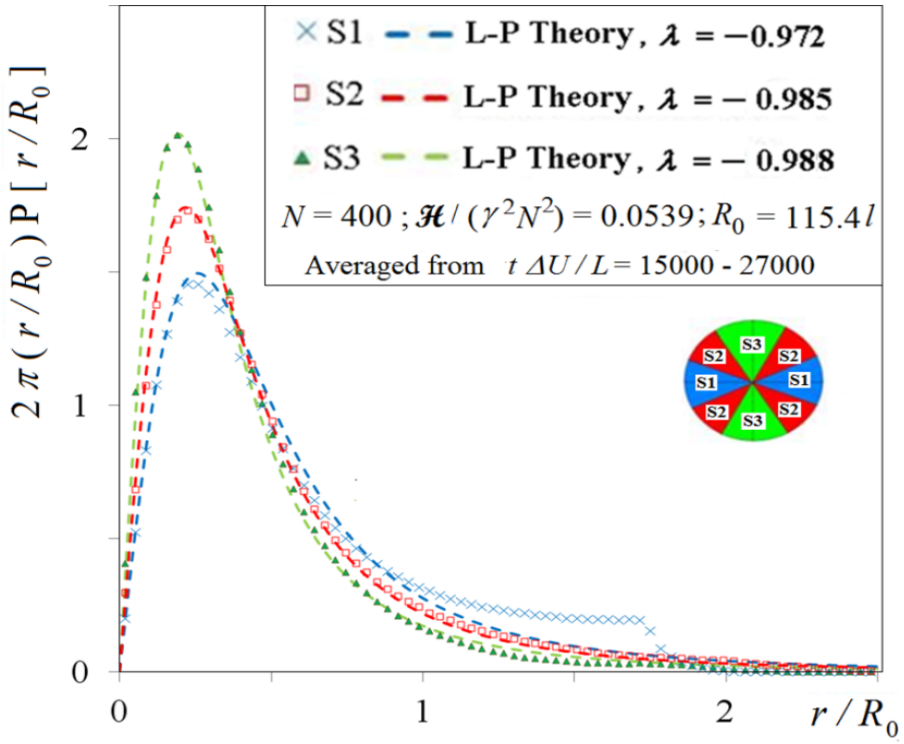

Figure 4.14. Sector averaged radial (core-centered) distribution function in Regime III. The each sector-wise distribution functions is similar to a Lundgren-Pointin equilibrium type but of different 'temperatures'. R_0 is the initial value of the second moment. Note that the sectors are chosen only for illustration and numerical convenience and that the 'temperature' is expected to continuously vary with $\tan^{-1}[x/y]$.

However, some words of caution are necessary in interpreting the results from the L-P theory for the free-shear-layer problem. The infinite plane problem studied by L-P has the Hamiltonian given by Eq. 2.3 is clearly different from the Hamiltonian given by Eq.2.4. Furthermore, the radius of gyration is not conserved in the present system.

The scaled temperature λ of L-P can be determined in two rather physically distinct ways. The two methods we have adopted for a determination of λ based on the LP relation between scaled energy $\tilde{E} = \mathcal{H}/(\rho N^2\gamma^2)$ and λ. We find $\lambda = -0.99999$ using this method. λ can also be determined by the best fit to the L-P distribution function (4.4). As seen in Fig. 4.11, the vortex distribution in the present problem is not isotropic. The source of this anisotropy is evidently due to periodicity only along the *x*-direction. To analyze the distribution we perform sector-wise averaging in the *xy* plane, and renormalize with the number of vortices in the respective sector. We then find (Fig. 4.14) that the radial distribution of vortices in each sector approximately follows a truncated Lundgren-Pointin distribution but with λ taking different values in different sectors. Thus the values of λ determined by the fit as we move the *x*-axis to the *y*-axis (from sector 1 to sector 3 in Fig 4.4) are -0.972 , -0.985 and -0.989 respectively. We note that the values of λ thus obtained are close to -1, the lowest value allowed by L-P.

This could be due to the present initial conditions, wherein the vortices are concentrated in a thin strip, which result in high energy configurations that lead to negatively high temperatures. We also note that λ computed from the ψ-ω relationship is $\lambda = \beta'/(8\pi) = -24/(8\pi) = -0.955$.

The above analyses show that the temperature of the present vortex-gas system, regardless of the method of estimation, is negative, corroborating the seminal idea of Onsager, namely the connection between emergence of order in the form of coherent structures and negative temperature states.

To summarize we have, through extensive simulations, uncovered here certain remarkable properties of the statistical evolution of a vortex-gas shear layer. Beyond Regime I affected by the initial conditions and the universal Regime II, the vortex-gas free shear layer undergoes multiple stages of relaxation towards what appears to be its asymptotic state. The domain-dependent evolution initially involving a few structures (IIIa) continues to grow via mergers that result in a single structure. The single structure relaxes initially via Euler dynamics (connection will be made stronger in Ch.5), followed by a finite-N driven stage, termed respectively as violent and slow relaxations (with outer time scales of $O(10)$ and $O(10^4)$). The distribution of vortices within the randomly moving structure reached at the end of the slow relaxation can be described by a truncated, anisotropic variant of the Lundgren-Pointin distribution, and the ψ-ω relationship approaches the Boltzmann distribution for the vortex gas, hence constituting a "relative" equilibrium in the sense defined by Newton (2000): namely, the distribution is time-invariant relative to the center of a non-stationary structure.

However, such connection with theory has not yet been possible in the most interesting and fluid-dynamically relevant Regime II, as it is far from equilibrium. Indeed, this regime lasts for just $t\Delta U/L = O(1)$, an order of magnitude shorter and more intense than the violent relaxation process, and can therefore be justifiably called an explosive phase. Furthermore, the existing non-equilibrium framework based on Boltzmann-inspired vortex-gas kinetic theories are shown to be not applicable in Regime II, as they do not account for the strong correlations due to multiple, interacting coherent structures of vortices that characterize Regime II.

While the results presented in this chapter do not provide a 'statistical-mechanical explanation' in the form of a closed form solution or a single theory, the detailed analyses presented in this chapter provide useful ideas on how such a theory might be constructed, e.g. accounting for the interaction at the level of the coherent structures appears to be the key in formulation of such a theory. Some further discussion and outlook on this is presented in Chapter 10.

Chapter 5 : Connections to Navier-Stokes mixing layers

So far we have considered the vortex-gas free shear layer as a prototypical problem in non-equilibrium statistical mechanics in its own right. It is however known that under certain conditions discrete point-vortex simulations weakly converge to smooth solutions of the 2D Euler equations (Beale & Majda 1983, Marchioro & Pulvirenti 1993) and, as discussed in the introduction, the effect of viscosity becomes vanishingly small at high Reynolds numbers in turbulent free shear flows. Furthermore, experiments show that plane mixing layers are dominated by the largely inviscid interaction of quasi-2D coherent structures and that growth occurs through interaction between such coherent structures (Brown & Roshko 1974, Wygnanski et al 1979). Vortex-gas simulations show the same mechanisms in operation. Therefore, it is of interest to analyze briefly connections with 2D and ('real') 3D Navier-Stokes mixing layers.

In this chapter we shall make the following two broadly different sets of comparisons. Firstly, (in 5.1) we shall compare present Regime III(b) solutions (non-universal violent relaxation of the single structure as described in Chapter 4), in terms of both thickness as well as vorticity-stream function relations with the appropriately long-time simulation of the 2D Navier-Stokes temporal mixing layer (Sommeria et al, 1991). The purpose of such a comparison is to estimate the relevance of the vortex-gas method to describing the detailed long time evolution of 2D Navier-Stokes for the same system.

The second set of comparisons (5.2 to 5.5) will involve comparing the evolution of layer thickness in non-universal Regime I and universal Regime II with experiments, as well as with direct numerical simulations of 3D NS. This set of comparisons, though involving only the gross large scale development, is aimed at answering whether or not the present temporal vortex-gas simulations are indeed relevant to the evolution of 'real' mixing layers, in which several additional complexities such as three dimensionality and spatial 'feedback' (considered separately in Ch.9) may come into play.

5.1. Comparison with 2D Navier-Stokes simulations in Regime III(b)

Regime III has, for obvious practical reasons, not been a subject of any experimental studies. However the long time 2D Navier-Stokes simulations due to Sommeria et al. (1991) are illuminating in this context, and we attempt a comparison of their results with the present work. The continuum constant-vorticity layer of finite thickness (with a piecewise linear velocity profile) solved by Sommeria et al (1991) for the Navier-Stokes equations, can be accurately represented by a suitable array of point vortices in the Euler limit. One way of defining the relevant vortex-gas formulation is a uniform random initial distribution with the inter-vortex spacing that is small compared to the thickness of such a layer, i.e. that $a/l >> 1$ (when $a/l >> 1$, the initial conditions mimic a shear layer with a finite initial vorticity thickness, $\delta_{\omega 0} = 2a$)

Sommeria et al. (1991) have studied 2D temporal Navier-Stokes mixing layers evolving from a constant vorticity band with two different thicknesses ($\delta_{\omega 0}$) of 2 x 0.017 L and 2 x 0.034 L, at Reynolds numbers $L\Delta U/\nu$ ranging from 9425 to 18850 (750 – 1500 in their units, where $L = 2\pi$ and $\Delta U = 2$). Their results show an initially rapid growth of momentum thickness, with slow changes beyond $t\Delta U/L \sim 4$. Since they do not perform ensemble averaging, and consider long wavelength initial (including modes with $\Lambda = L$) conditions, a rigorous estimation of spread rates in Regime II is not possible. However, we can still compare the evolution in the slowly varying Regime III(b).

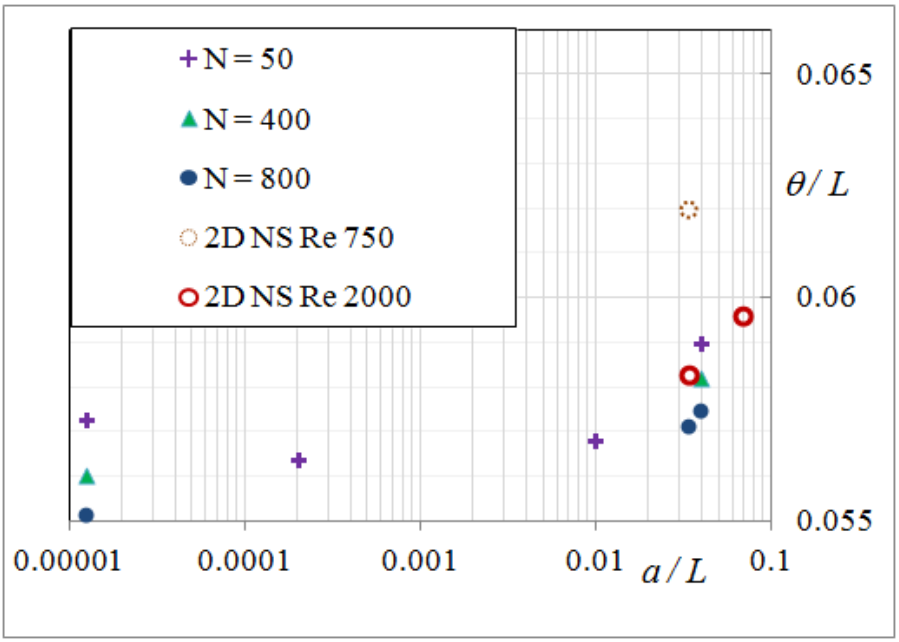

Figure 5.1. Comparison of momentum thickness in Regime III(b1) of the present vortex-gas simulations at different *a/l* and *N* with 2D Navier-Stokes (Sommeria et al, 1991)

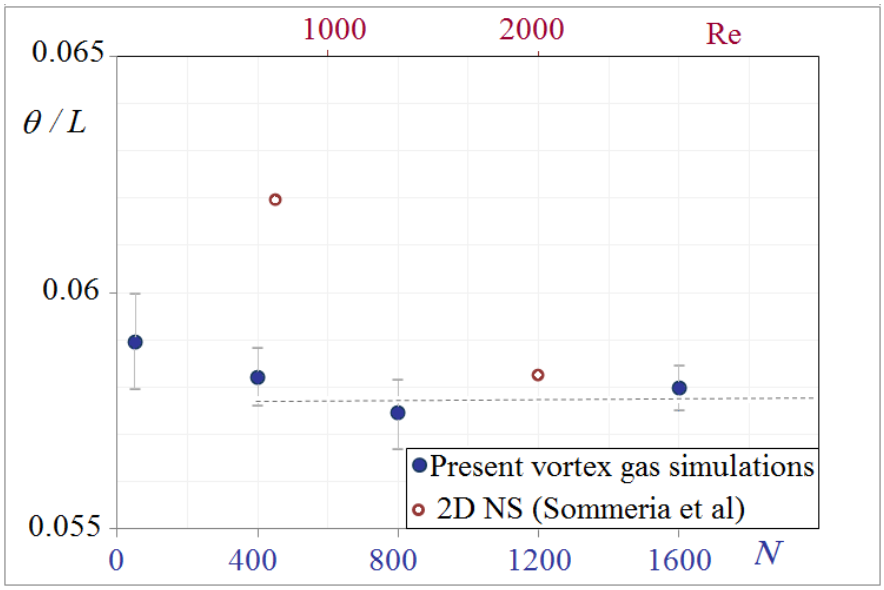

Figure 5.2. Comparison of momentum thickness in Regime III(b1) (averaged over $t\Delta U/L$ =14 to 16) of the present vortex-gas simulations with a/L = 0.04 with 2D Navier-Stokes with a/L = 0.034. Error bars show 95% confidence limits and the dashed line shows a possible asymptotic value of thickness.

Figure 5.1 plots the average value of θ / L between $t\Delta U / L$ of 14 and 16 as a function of a/L, for different N in the present vortex-gas simulations and for different Reynolds numbers for the 2D NS simulations. It can be seen that the differences between N = 400 and 800 is less than 1% for the range of a/L considered here (10^{-5} to 10^{-1}). This suggests that for sufficiently large N, the solution in this sub-regime (corresponding to the 'violent relaxation' described in Ch. 4) does not depend strongly on N in the vortex-gas simulations, and θ / L in Regime III(b) a function only of a/L. Furthermore, there is a reasonable agreement with the 2D NS results in terms of the trend with a/L, and the value the thickness observed in vortex-gas simulation with a/L = 0.034, N = 800 is only about 2% of the highest Reynolds number case of Sommeria et al for a/L = 0.034. Further, Fig.5.2 suggests that the 2D NS and vortex-gas appear to approach the same asymptotic solution with increasing values of Reynolds number and N

respectively. This is consistent with the 2D NS and vortex-gas converging to the Euler solution for free shear layers in the respective limits.

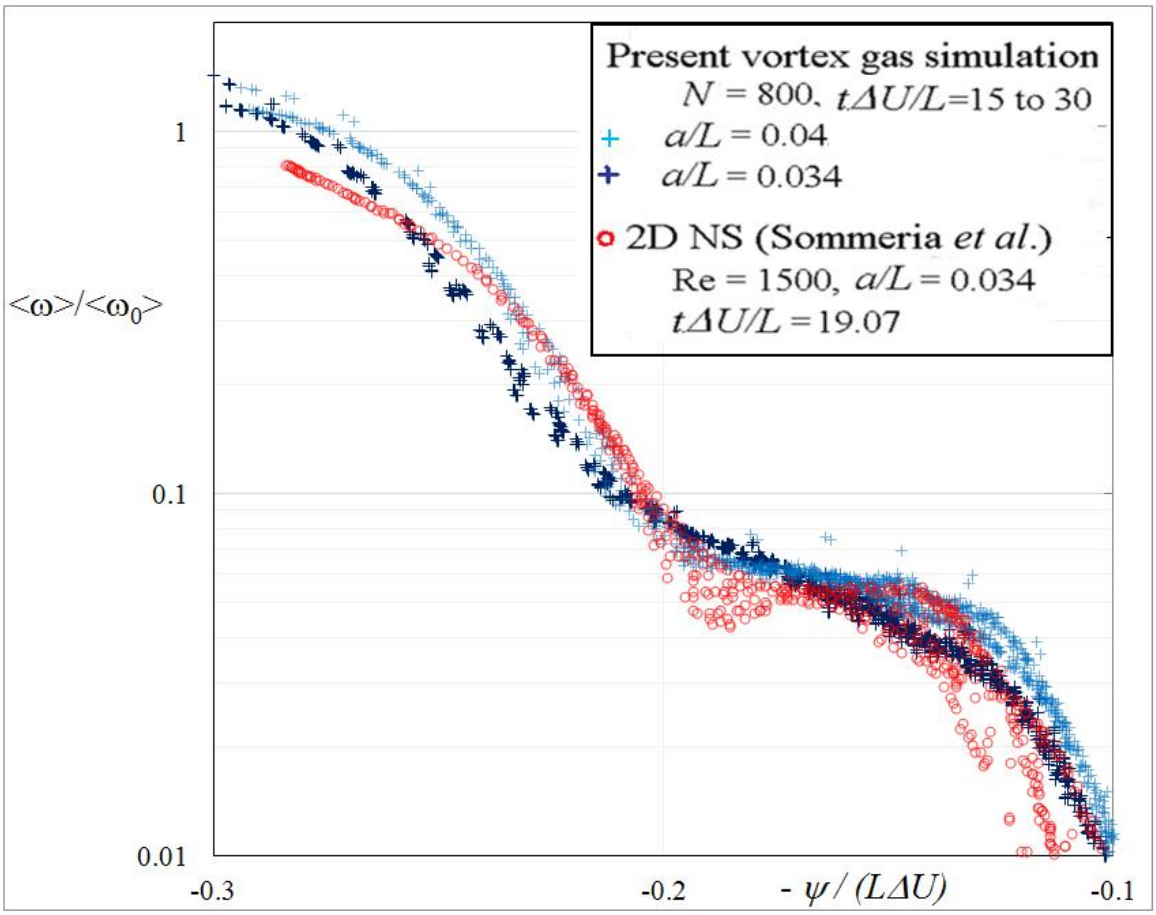

Figure 5.3. Comparison of the vorticity stream function relation between a present vortex-gas computation (a/L = 0.034 and 0.04) and 2D Navier-Stokes of Sommeria et al (a/L = 0.034). $\langle\omega\rangle$ is the time averaged vorticity ($f_1\ \Delta U/L$) and ω_0 is the maximum vorticity in the initial condition (ΔU / (2a)).

We next compare the vorticity-stream function relation between the vortex-gas and 2D NS solutions. As described in Chapter 4, the present simulations show a slowly wandering final structure in III(b). We may therefore compute ensemble and short-time averages in a frame of reference fixed with respect to the centre of the structure. Further, since ψ is defined upto an additive constant, it is adjusted to 0 at $y = \pm L$ (by subtracting the mean of the values at $y = L$ and $y = -L$) as done in Sommeria et al to enable a one-to-one quantitative comparison.

Figure 5.3 compares that the ψ- ω relation in 2D NS calculations of Sommeria et al (for a/L = 0.034; Re = 1500) with the present simulations (a/L = 0.034 and 0.04; N = 800). For the same a/L of 0.04, for a given value of ω/ω_0 the differences in $\psi/(L\Delta U)$ between the vortex gas and 2D NS are less than 10% for the range of data shown in Fig.5.2. (An even more significant agreement is observed between the 2D NS with a/L = 0.034 with the vortex gas with a/L = 0.04. This was also observed for thickness in Fig.5.1. This agreement is perhaps due to the higher initial thickness mimicking the effects of layer thickening due to viscosity, considering the modest Reynolds number of the 2D NS used in the comparison).

The overall agreement between the 2D NS and the vortex gas must be considered of great significance, for the close agreement between two such physically and mathematically distinct approaches to the same problem establishes the quantitative relevance of the vortex-gas results to high-Reynolds number 2D Navier-Stokes solutions.

5.2. Comparison of initial transient (Regime I) with sinusoidally 'forced' experiments of spatial shear layers

Many experiments (e.g. Brown & Roshko 1974, see Chapter 1) have suggested that the evolution of plane mixing layers is dominated by the largely inviscid interaction of quasi-2D coherent structures and that growth occurs through interaction of such coherent structures (though it is in part contradicted by D'Ovidio & Coats 2013, whose results will be discussed in detail in Chapter 9). Vortex-gas simulations show the same mechanisms in operation. It is therefore worthwhile to make some brief comparisons with 'real' (i.e. 3D Navier-Stokes) mixing layers. Regimes I and II are most relevant to what is observed in experimental studies of (spatial) mixing layers, and as an understanding of the two regimes is central to turbulent shear flows in general, it is particularly worthwhile to explore this issue in detail.

In this section, we shall confine ourselves to what is referred to in the fluid-dynamical literature as 'periodically forced' mixing layers. They provide excellent test cases for the purpose of comparison with vortex-gas simulations in Regimes I and II. One reason is that the most dominant initial perturbation is accurately known experimentally in these flows. A second is that experiments show that periodic forcing greatly alters the development of the mixing layer and this has led to strong doubts about universality (e.g. Oster & Wygnanski 1982, Ho & Huerre 1984). Periodic forcing can be imposed in many ways: oscillating the free streams (e.g. Ho & Huang, 1982), acoustic excitation by loud speakers (Husain & Hussain, 1995) or periodic deflection of a flapper at the end of the splitter plate (e.g. Oster & Wygnanski 1982, Gaster et al 1985, Naka et al 2010). The last method basically imposes a periodic deflection on a vorticity layer at its origin $x = 0$. The analogue for the temporal vortex-gas free shar layer is to have an initial ($t = 0$) y-displacement of vortices that varies sinusoidally with x, as with cases P1 and P2 discussed in Chapter 3.

On this basis, we compare experimental results of the spatial mixing layer reported by Oster & Wygnanski (1982) with the present temporal vortex-gas simulations using the Galilean transformation $x = U_m\, t$ (see Fig.1.3 in Introduction; more details in next section 5.3). Two such cases are shown in Fig. 5.4. We compare the evolution of thickness with time, both non-dimensionalized using the wavelength (Λ) of the perturbation as the length scale. The simulations are chosen to have approximately the same value of the amplitude (a_w) to wavelength ratio of the initial perturbation as in the experiment. The space-time transformation of the initial conditions implies initializing vortex locations in the simulations as $x_i = N\,(i\,/\,L)$; $y_i = a_w \sin[2\,\pi\, x_i\,/\,\Lambda] + a_n\, Y_i$, where Y_i is a random number uniformly distributed between -1 and 1, and $a_w/\,\Lambda = a_f\, f\,/U_m$, where a_f and f are amplitude and frequency of flapper motion in the experiment. We have added a random disturbance a_n to the periodic vortex deflection imposed at $t = 0$ to allow for the presence of tunnel free-stream turbulence, which is a source of facility-specific random disturbance on the flow. This may also be a proxy for effects due to spatial feedback or three-dimensionality.

Figure 5.4A shows the evolution of momentum thickness for $a_w/\,\Lambda = 0.0074$ for two different values of a_n/a_w. We find from both the simulations that the spread rate is first enhanced (higher than the Regime II value) and then suppressed, but finally appears to approach the universal spread rate in Regime II . The vortex-gas simulation with $a_n/a_w = 1.5$ agrees quantitatively with the Oster-Wygnanksi experiment (1982) with $a_f\, f\,/\,U_m = 0.0074$ all the way. If a_n/a_w is drastically reduced to 10^{-3}, the simulation still agrees qualitatively with the observed behavior of the mixing layer, but the temporal extent of suppression is longer. Interestingly, addition of the disturbance a_n hardly affects either the early evolution of the layer ($t\Delta\, U/\,\Lambda < 2$) or the Regime II spread rate (reached beyond $t\Delta\, U/\Lambda \sim 8$). (The reasons for this behavior are discussed in Ch. 6.) The agreement seen in Fig. 5.4A is therefore encouraging. (Note that the free stream turbulence intensity in the experiment is 0.2 % of the mean velocity, $u_t = 0.002\, U_m$. The value of a_n/a_w may be crudely calculated as $u_t\,/\,fa_f = 0.002/0.0074 \sim 0.3$. While this value is much lower than the required noise in the vortex-gas initial condition to provide the same evolution, it is important to note that the free stream turbulence acts as a continuous random

forcing, whereas in the temporal vortex-gas shear layer a_n is added only at the initial instant, and hence the crude conversion used here is perhaps not valid. Furthermore, the random noise in the vortex-gas initial condition could in part also be a proxy for the finite thickness and turbulence within the boundary layers at the trailing edge, for effects disturbances arising from 3D and from downstream)

In Fig. 5.4B we compare the results of case P1 (Table 3.1, a_w/Λ = 0.004) with the experiment with approximately the same amplitude to wavelength ratio ($a_f f / U_m$ = 0.004167). Here the experiments do not go beyond the initial growth-enhancement phase ($t\Delta U/\Lambda < 2$). However the simulation shows excellent agreement with experiment, but continues into the two later phases respectively of suppressed growth and recovery towards universality, shown in Fig. 5.4B.

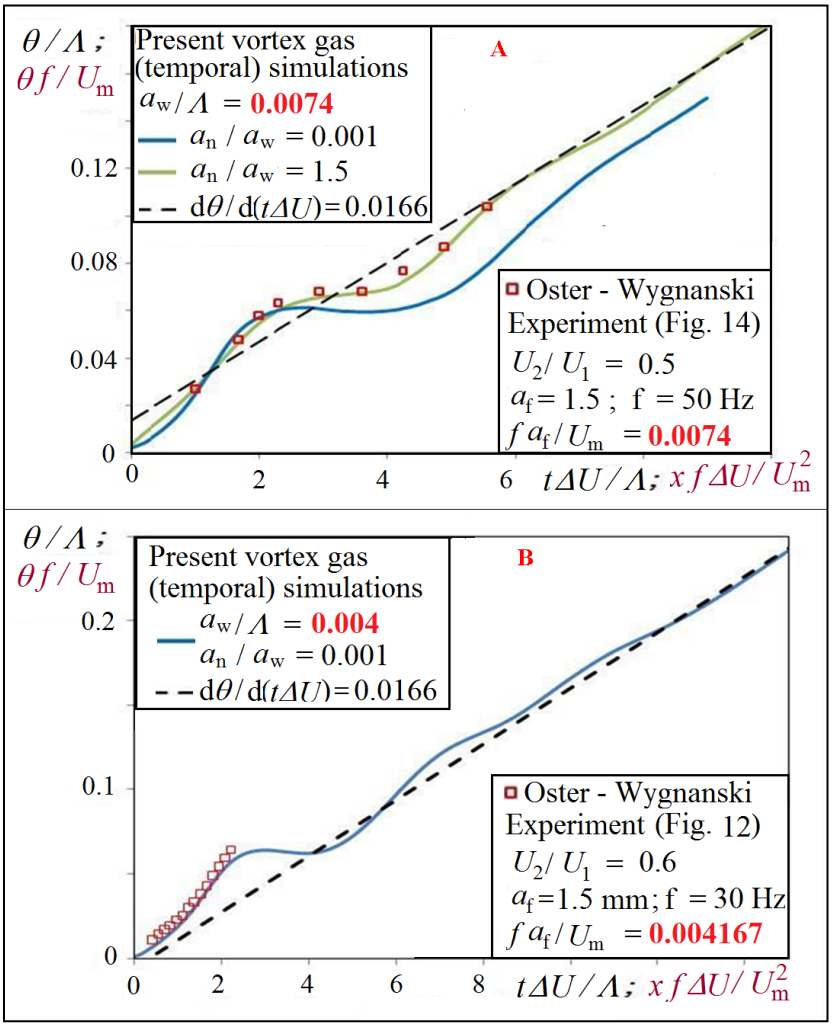

Figure 5.4. Comparison of temporal evolution of momentum thickness in the present vortex-gas computations with sinusoidal (in x) initial conditions (t = 0) with the spatial evolution of momentum thickness in experiments (Oster & Wygnanski, 1982) with sinusoidal (in t) forcing at x = 0.

One might argue that the above observed agreement does not necessarily suggest the relevance of the vortex gas to the self-preserving 3D Navier-Stokes shear layer, as the regions of comparison mostly involved the transient region still affected by 2D forcing. We shall address that question in the following (5.3 to 5.5) sections. However, the good agreement of the vortex-gas simulations with the experiment over the range of data available suggests that experimental data like those in Fig. 5.4A or B cannot be taken as evidence of lack of universality. An alternative explanation for the experimental data is that introducing strong long-wave periodic perturbations just makes the initial transient (Regime I) much

longer. Extrapolating from the simulation results of Fig. 5.4B on the time taken to reach Regime II, the distance necessary to reach the equivalent state would be six times as long as the spatial range available in the experimental facility used: the wind-tunnel test section length would have to be increased from 1.5m to about 9.0m. This conclusion is consistent with other evidences for the long memory of free-shear –flows (Kleis & Hussian (1979) for single-stream shear layer, Narasimha & Prabhu (1972), for plane wakes, Bradshaw (1966) for mixing layers, Carazzo et al (2006) for jets, and Redford et al (2012) for axi-symmetric wakes).

5.3. Comparison of universal Regime II spread rate with self-preservation spread rates reported in (unforced*) experiments of spatial shear layers

The explosively relaxing Regime II is analogous to the 'self-preserving' state in a turbulent shear flow, where the lower order turbulence statistics (in particular the Reynolds shear stress) are specified to be self-similar (Townsend, 1956). (It is ironical that the evolution or flow development that is labeled as 'equilibrium' flow in fluid dynamics is a highly non-equilibrium phenomenon in statistical mechanics.) Briefly, the first step in a fluid dynamical analysis of a canonical Navier-Stokes temporal mixing layer (with $L \to \infty$) would proceed as follows. From dimensional analysis,

$$\frac{d\hat{\delta}}{d(t\Delta U)} = F\,[Re, \{i.c.\}] \tag{5.1}$$

Two major hypotheses are introduced at this stage: (i) any turbulent flow (subjected to constant boundary conditions) evolves asymptotically to a state independent of the detailed initial conditions excepting for any integral invariants demanded by mass, momentum and/or energy conservation, and (ii) 'if the equations and boundary conditions admit a self-preserving solution the flow asymptotically tends to that solution'. Both hypotheses, while still controversial, are extensively used in turbulent shear flow analyses (see 'working rules' (2) and (3) in Narasimha (1990)).

Following the above hypotheses, if the initial conditions are assumed to be 'forgotten' as $t \to \infty$ and the effect of Reynolds number becomes vanishingly small as $Re \to \infty$, eqn 5.1 reduces to

$$\frac{d\hat{\delta}}{d(t\Delta U)} = C_{NS} \tag{5.2}$$

The question of whether the constant C_{VG} (in eq. 3.5) is universal in the vortex-gas shear layer is analogous to the controversy on the possible dependence of the self-preservation state of turbulent shear flows on initial conditions (extensively debated elsewhere, e.g. George 2004, Oster & Wygnanski 1982, Balaras 2001) i.e. whether C_{NS} is a universal constant. We discuss the relation between C_{VG} and C_{NS} in this section by comparing the reported self-preservation spread rates across 'unforced' experiments with that predicted by the present temporal vortex-gas simulations on appropriate Galilean transformation. The results are shown in Figure 5.5.

Galilean transformation is a space-time transformation that connects the temporally evolving (homogenous in x) shear layer (Fig 1.3b,c) with the spatially evolving (in x) temporally stationary shear layer (Fig 1.2, 1.3 a) by considering the former as a parcel of fluid moving with a mean speed in the latter. This is exact only in the limit $\Delta U/U_m \to 0$, as while the evolution of the spatial layer at any given x_0 can be affected by events at $x > x_0$, the evolution of the temporal layer at any given t_0 cannot be affected by events at $t > t_0$. In other words, while there can be upstream feedback in space (which will be discussed in detail in Chapter 9), the future cannot affect the present. For the spread rate, the Galilean transformation leads to

* The word 'unforced' as used in this thesis (as well in most fluid-dynamical literature) implies that no specified external forcing has been intentionally introduced. Facility specific forcing, free-stream turbulence and random disturbances may exist in such 'unforced' layers.

$$\left|\frac{d\hat{\delta}}{dx}\right|_{\text{spatial}} = \frac{\Delta U}{U_m}\left|\frac{d\hat{\delta}}{d(t\Delta U)}\right|_{\text{temporal}} = 2\lambda\left|\frac{d\hat{\delta}}{d(t\Delta U)}\right|_{\text{temporal}}$$

where $\lambda = (U_1 - U_2)/(U_1 + U_2)$. The above relation is exact in the limit $\lambda \to 0$.

In Regime II, the evolution of vorticity thickness is given by $d\delta_\omega/d(t\Delta U) = 0.0763$ and the corresponding Galilean transformation gives 0.0153 λ. We use vorticity thickness in this section, as a majority of experiments use this measure. The ratio between δ_ω and θ is found to be 4.6 in the present vortex-gas simulations. Values between 4.44 (which is the case for an error function velocity profile) to 4.8 have been used in literature for this factor, and its dependence on λ is not clear.

We use a factor of 4.6 to convert the spread rates quoted in terms of momentum thickness in Fig.5.5, except at λ = 1, where we use factor of 4.8, as it has been explicitly reported by Hussain & Zaman (1985). The uncertainties of velocity measurement in the tails of the velocity profile make it difficult to accurately estimate the momentum thickness in experiments and hence the factor. Regardless, $< \pm 5\%$ uncertainty in δ_ω/θ is small compared to the scatter and uncertainties in the spread rate across experiments ($> \pm 10\%$; $\pm 30\%$ at $\lambda = 1$).

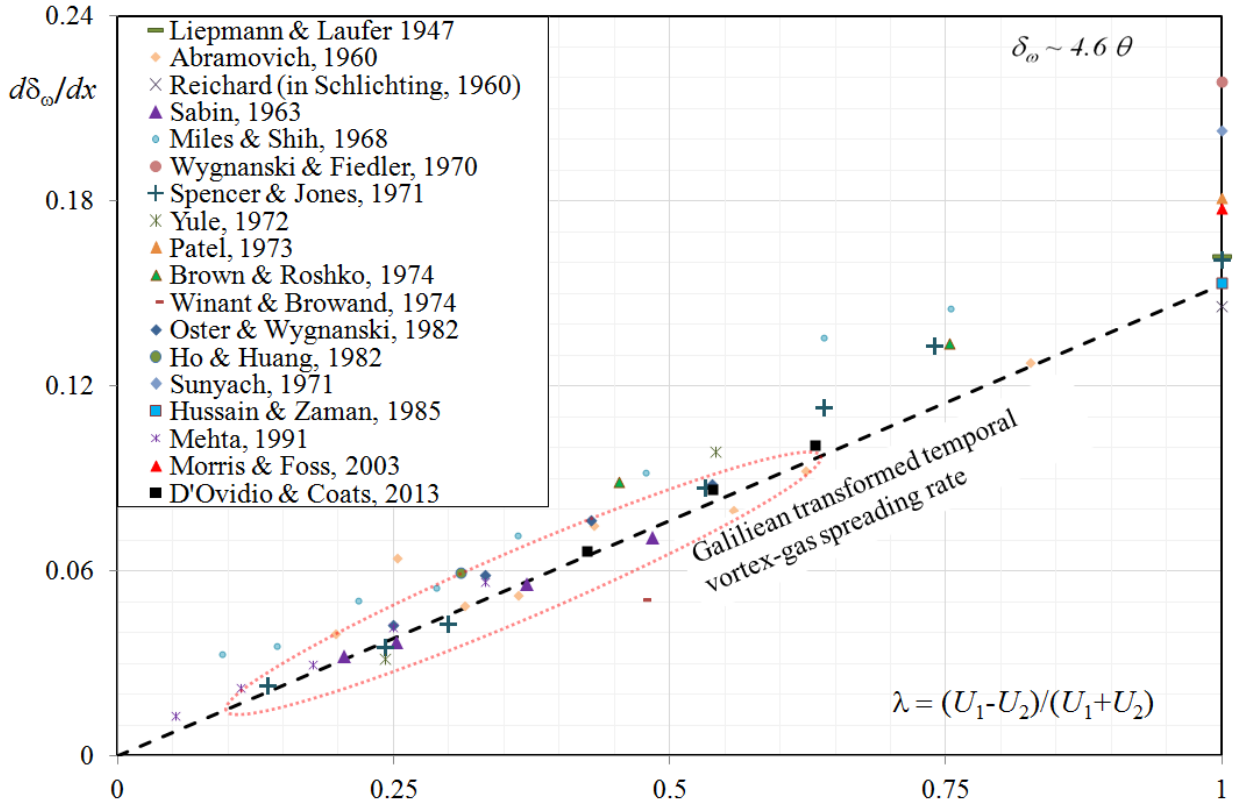

Figure 5.5. The self-preservation spread rate (in terms of vorticity thickness) quoted across different (unforced) experiments on spatially evolving mixing layers (performed over 1947 to 2013, list not exhaustive) plotted against λ = (U_1-U_2) / (U_1+U_2), and compared with the Galilean-transformed spread rate given by the present temporal vortex-gas shear layer in Regime II ($d\delta_\omega/dx$ = 0.0153 λ) shown in black dashed lines.

It can be seen from Fig. 5.5, the present temporal vortex-gas results are indeed in the same ball park and within the scatter of the experiments. While the large scatter has often been attributed to non-universal self-preservation states, the overall agreement with the vortex gas is encouraging. Many experiments with $0.1 \lesssim \lambda \lesssim 0.6$ (region shown in faint red dotted lines), particularly those of Spencer & Jones (1971, blue +) and D'Ovidio and Coats (2013, black squares) are in close agreement with the transformed temporal vortex-gas results (though there are quite a few experimental points with slightly

higher spread rates). At very small values of λ, the experiments may not be expected to provide a reliable self-preservation spread rate as the spatial extent required to reach the analog of Regime II would be very large ($x_{RII} \sim t_{RII}\Delta U/\lambda$). At large values of λ the effects of spatial feedback may become dominant and Galilean transformation is no longer valid (particularly interesting is the very large scatter in the single stream limit of $\lambda = 1$; this and other issues related to spatial feedback are discussed in Chapter 9). Therefore, it is consistent that the best agreement is observed at a moderate value of λ (the value of λ for the Regime I comparisons done in the previous section was 0.25). It is surprising however, the agreement is fair till λ as high as 0.6. This agreement suggests that the vortex-gas dynamics are indeed relevant to spatially evolving 3D NS and that the self-preservation spread rate in mixing layers is likely a universal function of velocity ratio (at least for $\lambda < 0.5$). While we do not explore the reasons for the differences in the reported spread rates for each of the experiments, lack of appreciation of the sometimes-very-long memories of initial conditions (as discussed in 5.1), inadequate flow development lengths, relatively low Reynolds number, inadequate averaging are all possible factors.

5.4. Critical assessment of DNS/LES results

We next examine results from Direct Numerical Simulations (DNS, no modeling) and Large-Eddy Simulations (LES, subgrid scales modelled, see Sagaut (2002) for reference) of 3D Navier-Stokes temporal mixing layers, listed in Table 5.1. The reported self-presevation (Regime II) spread rates, in terms of momentum thickness ($d\theta/d(t\Delta U)$) are found to in the range 0.012 to 0.02. As in the scatter across experiments, the differences in the spread rate in the temporal simulations have been used as an argument in support of existence of non-universal self-presevation states (see in particular Balaras et al, 2001). However, the vortex-gas simulations suggest there are several reasons why a reported self-preservation spread rate may apparently deviate from the universal Regime II value.

Firstly, as shown in Fig. 2.4 that inadequate averaging can result in upto 30% inaccuracy in estimation of the spread rate. We note that none of the DNS/LES simulations analyzed here (or reported elsewhere to the best of our knowledge) have performed ensemble averaging. Though all of them perform spanwise averaging, it is not an equivalent of ensemble averaging due to the quasi-2D nature of the solution.

The second reason is the presence of long memories of certain initial conditions as discussed in the Sec.5.2. We find that, one way of quatifying the relaxation towards Regime II (i.e. forgetting the memory of initial conditions) is via an estimate of the number of generations of mergers during the perceived linear growth regime using the expression, $\log_2[\theta_{LE}/\theta_{LS}]$. This parameter, hereby referred to as 'age parameter', takes the value unity when $\theta_{LE}/\theta_{LS} = 2$; this choice reflects the experience from the current simulations, which show that the momentum thickness doubles by the time that every structure at t_{LS} has gone through one merger on an average. This parameter also decribes the extent of the fit, which determines the confidence of estimation of the spread rate. So, larger the value of $\log_2[\theta_{LE}/\theta_{LS}]$, higher the likelyhood that the reported spread rate is a representation of the Regime II spread rate. It can be seen from Table. 5.1 most DNS/LES simulations have an age parameter less than 0.59 (shown in red in Table. 5.1), which means that the thickness of the layer has not even increased by one and half times in during the observed linear growth, suggesting that there have hardly been any amalgamations. Such simulations cannot be considered to provide a reliable estimate of Regime II spread rate of 3D NS mixing layers.

The third possible reason for the inaccurate estimate of spread rate in Regime II is that the spread rate deviates from its self-presevation (Regime II) value when $t\Delta U/L$ is of $O(1)$ as seen in Figs 3.1, 4.1, due to the effects of imposed periodicity of the finite domain. In the present study, we make a clear distinction between Regime II and Regime III(a), which involves more than one but less than 4 structures. However, this distinction has not been carefully made in other simulations. We note that the number of structures left in the domain at the end-point in the duration over which the fit is made, say t_{LE},

is approximately 4 $(t_{LE}\Delta U/L)^{-1}$, as on an average there are approximately 4 structures in the domain at $t\Delta U/L$ = 1, and the number of structures decreases linearly with increase in time during Regime II. Higher values of the parameter 4 $(t_{LE}\Delta U/L)^{-1}$, hereby referred to as 'population parameter', ensure that the temporal extent over which the fit (to determine spread rate) has been made is far away from the onset of Regime III. It also indicates that the statistics (including thickness) have been obtained as an average over larger number of structures. As seen in Table 5.1 many DNS/LES simulations have a population parameter less than 3 (shown in red in Table. 5.1) and hence the quoted spread rate in such simulations also includes part of Regime III.

Hence, for a robust indication Regime II spread rate, both age and population parameter have to be large. When we consider only simulations with both age parameter greater than 0.59 and population parameter greater than 3, the scatter in the spread rates comes down to 0.015 to 0.017, which is a reduction in scatter by about 75% and the extreme values are now within 10% of the universal Regime II value observed in the present vortex-gas simulations.

The age and population parameters for the cases presented in Table 3.1 is listed in Table 5.2 (in bold). It can be observed that for all the (bold) cases, (including for G1 and P1, but not for variants of G1 and P1 (shown in red), which will be described below), the age parameter is atleast close to one and population parameter is greater than or equal to 5. This has ben achieved by considering sufficiently large L and considering only the data over $t\Delta U/L$ < 0.8 respectively. The deviation of the observed self-preserving spread rates from 0.0166 is within a percent for all these cases. But if we perfomed poorly designed/ poorly analyzed simulations such that the age or the population parameter is inadequate, would the best fits over the perceived Regime II result in apparent deviations from the universal spread rate ? In order to answer this question, we consider the following additional cases, listed in Table 5.3.

Table. 5.1. Age, population and reported spread rates in DNS / LES of 3D NS mixing layers

		Population parameter	Age Parameter	Age x Population	Reported $d\theta / d(t\Delta U)$	% Deviation from C_{VG}
Rogers & Moser, 1994	DNS	3.33	0.42	1.41	0.014	-15.7
Rogers & Moser, 1994	DNS	3.33	0.47	1.58	0.014	-15.7
Rogers & Moser, 1994	**DNS**	**4**	**0.89**	**3.55**	**0.017**	**2.4**
Silvestrini,2000	LES	0.93	0.86	0.80	0.0207	24.4
Tanahashi, 2001	DNS	1.16	1.84	2.14	0.0189	13.6
Balaras 2001	LES	2.44	1.16	2.83	0.014	-15.7
Balaras 2001	**LES**	**4.4**	**1.07**	**4.71**	**0.015**	**-9.6**
Balaras 2001	LES	1.57	0.45	0.71	0.012	-27.7
Balaras 2001	LES	3.14	0.51	1.61	0.0135	-18.7
Patano & Sarkar, 2002	DNS	2.76	1.05	2.89	0.016	-3.6
Foysi & Sarkar, 2010	**LES**	**6.88**	**0.96**	**6.61**	**0.0161**	**-3.0**
Martiner 2011	LES	1.97	2.70	5.32	0.0145	-12.7
Martiner 2011	LES	2.56	1.00	2.56	0.0123	-25.9

Table. 5.2. Age and population parameters for the present vortex-gas simulations

	Population parameter	Age parameter	Age x Population	Observed $d\theta / d(t\Delta U)$	% Deviation from C_{VG}
R1	**5.33**	**6.66**	**35.49**	**0.016618**	**0.11**
R2	**22.99**	**5.55**	**127.52**	**0.016685**	**0.51**
R3	**5.38**	**4.88**	**26.26**	**0.016587**	**-0.08**
R4 – 32000	**15.46**	**7.84**	**121.25**	**0.016506**	**-0.56**
R4 – 1600	**5.00**	**5.46**	**27.30**	**0.016532**	**-0.41**
R4 – 400	**5.13**	**3.91**	**20.04**	**0.016510**	**-0.54**
R5	**5.00**	**1.14**	**5.72**	**0.016562**	**-0.23**
G1	**5.38**	**2.93**	**15.77**	**0.016689**	**0.54**
BM1	**5.38**	**3.93**	**21.14**	**0.016737**	**0.82**
BM2	**5.38**	**5.66**	**30.42**	**0.016534**	**-0.40**
P1	**5.36**	**0.99**	**5.30**	**0.016635**	**0.21**
P2	**5.38**	**1.17**	**6.31**	**0.016624**	**0.15**
G1b	4.44	0.51	2.31	0.0194	16.8
G1c1	1.33	3.08	4.11	0.0172	3.6
G1c2	1.6	2.89	4.64	0.0162	-2.4
P1b	9.48	0.13	1.26	0.0148	-10.8

Table. 5.3. Details of vortex-gas cases to illustrate the effects of inadequate age and population.

Case	Initial condition	L/l	$t_{bRII}\,\Delta U/\,l$	$t_{eRII}\,\Delta U/\,l$	N
G1	Gaussian, $\sigma/l = 1$	1600	120	1190	32
G1b	Gaussian, $\sigma/l = 1$	200	120	180	32
G1c1	Gaussian, $\sigma/l = 1$	400	120	1000	32
G1c2 (same data as G1c1)	Gaussian, $\sigma/l = 1$	400	120	1200	32
P1	Sinusoidal, a_w/l=0.4, a_n/l = 0.0004, Λ/l = 100	3200	1220	2390	288
P1b (same data as P1)	Sinusoidal, a_w/l=0.4, a_n/l = 0.0004, Λ/l = 100	3200	1220	1350	288

Note that that Regime II spread rates of G1 and P1 deviated by only 0.54% and 0.21% from 0.0166 respectively and that the G1b, G1c1 and G1c2 have the same initial conditions and $t_{bRII}\Delta U/L$ as G1 and the P1b same as that of P1. (Therefore any observed departure in spread rate cannot be attributed to initial conditions not being forgotten). However, the L/l and $t_{eRII}\Delta U/L$ are chosen such that either the age (G1b

and P1b) or population parameter (G1c1 and G1c2) is inadequate. It can be seen from Table 5.2 that all the four cases deviate by well over 2% from the universal spread rate, with of P1b deviating by -10% and G1b deviating by 16.8%. This is therefore consistent with the argument that attributes to the deviations observed in the DNS/LES at comparably inadequate age or population parameters.

Futhermore, when we analyze the deviations of the reported spread rates from the present Regime II value as a function of product of age and population parameters (Fig 5.6), there appears to be a trend of larger deviations (on both sides) with lower values of the product, with the spread rates from the vortex-gas simulations showing a similar trend to the DNS/LES mixing layers. The value of the product is usually low when either or both the parameters are inadequate (although this statement would not necessarily hold if one of the parameters is very large) and hence provides a compact description of the reliability of a given simulation. Additionally, the product also has a physical interpretation, namely it is a rough measure of the total number of participating structures over (a single realization of) the perceived Regime II of the given simulation.

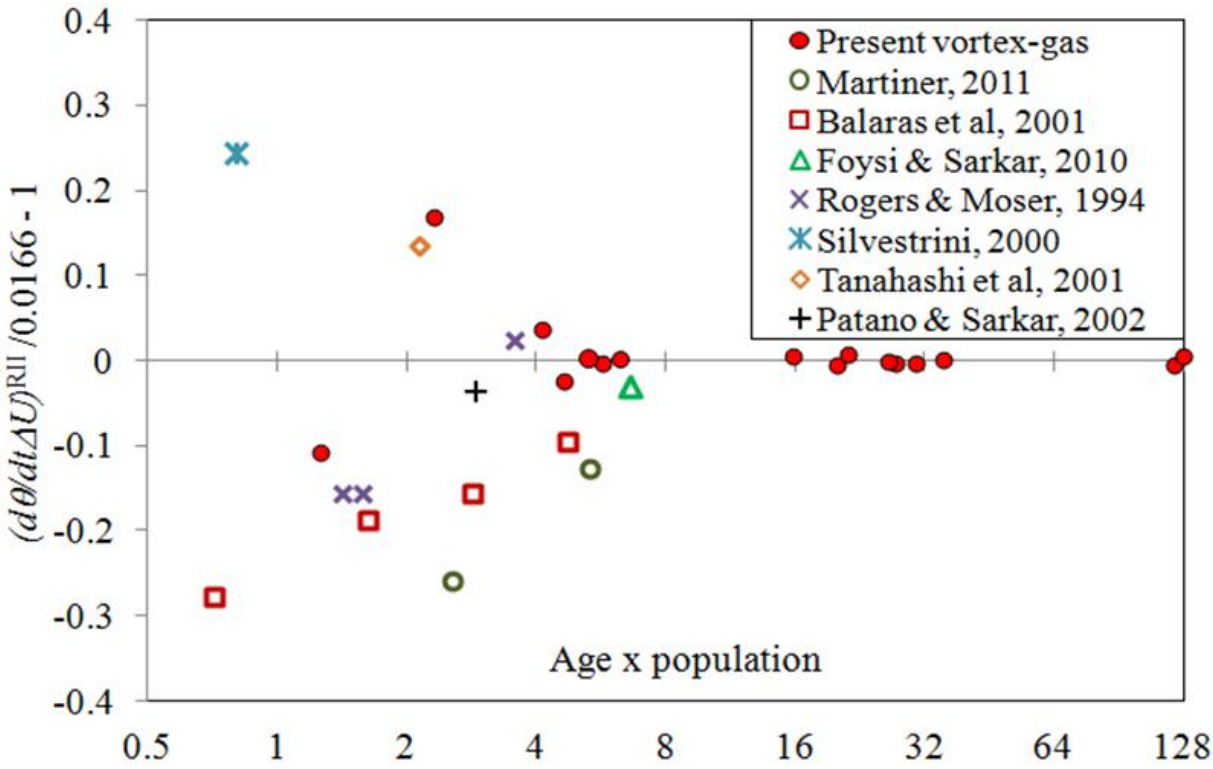

Figure.5.6. Departures of the reported growth rates in DNS/LES of 3D Navier-Stokes Temporal mixing layers and present vortex-gas simulations from the universal Regime II growth rate with the product of 'age' and 'population' parameters

Particular attention may be drawn to the work of Balaras et al (2001) who, reported results from four simulations, each of which gave a different growth rate; it was therefore concluded that the self-preservation spread rate of the temporal mixing layer is not universal. However Fig. 5.6 shows that the spread rates quoted by Balaras et al. are not inconsistent with a systematic approach towards the proposed universal value as the age-population parameter increases. Therefore, in addition to not accounting for the long memory of initial conditions and inadequate averaging, the low generational age and / or low end-point population of coherent structures seem to be responsible for deviations of the quoted spread rate from the preset Regime II value. The systematic trend in Fig.5.6 suggests that the observed scatter can neither be considered as an evidence for non-universal self-preservation nor for the non-applicability of vortex-gas simulations to describe 3D NS. The convergence to the vortex-gas spread rate at large

values of the age-population product supports the conclusions drawn in 5.3, namely the validity of the vortex-gas simulations to describe the large scale evolution of 3D Navier-Stokes mixing layers.

5.5. The question of multiple self preservation states

Another phenomenon that has been the subject of much controversy concerns the proposal that there are multiple self-preservation solutions in the growth of a mixing layer (i.e. C_{NS} is not only dependent on initial conditions, but can also vary with time over long times), leading to segmented growth curves consisting of short straight stretches.

Such segmented growth curves are encountered in single realizations of vortex-gas simulations as well. Figure 5.7A shows a single realization in Regime II of a temporal vortex-gas shear layer (case R1, N = 3200) over a duration of 0.3 $t\Delta U/L$. The evolution consists of four linear segments, each with a different slope varying from 0.0117 to 0.0275 (a factor of 2.35). However an ensemble average (over 577 realizations) yields an excellent linear growth throughout, very close to the universal value (0.0166) in each of the indicated segments as seen in Fig.5.7B. The explanation for the segmented growth in Figure 5.7a is contained in the vortex location snapshots of Fig. 5.7V. These reveal the presence of several co-oriented vortex 'trains' in each snapshot, the common orientation being indicated by the short lines on the left. As the structures co-rotate their orientation changes from $0\text{-}180^0$ to $90^0\text{-}270^0$, i.e. from low to high local thickness for the shear layer, each quarter of the rotation cycle providing a stretch of high or low growth rate. However there is jitter in the system (of the same kind as noted in spatial experiments by Bernal, 1981), and the segments are indeed 'transients'. Long spatial averages in a temporal simulation, or long temporal averages in a spatial simulation, and / or a large-ensemble average in either, removes the segmentation to produce the universal growth rate. This behavior in the vortex-gas shear layer is consistent with the concept of transient metastable states proposed by Narasimha (1990). It is thus possible that reports of multiple or serial self-preservation states (George 2004, Carton de Wiart et al, 2010) are the result of averages over short samples.

5.6. Summary

In summary, the series of comparisons and analyses presented from 5.1 to 5.5, taken together, strongly suggest the following two major conclusions. First is that the vortex gas is indeed relevant to 2D NS as well for growth rates in 3D NS mixing layers in spite of the apparently severe modeling assumptions in the concept of the vortex gas. This implies that 2D inviscid interactions given by Kelvin/ Biot-Savart mechanism dominate large-scale momentum dispersal in free shear layers, supporting the argument that strictly 2D approximation of the vortex-gas approach is not unduly restrictive for determining layer growth, as the coherent structures in plane mixing layers tend to be quasi-2D. Further, this is also consistent with the conclusions of the nonlinear calculations of Corcos and Sherman (1984) and Corcos and Lin (1984), who show that 3D instabilities are inhibited by the growth of the 2D instabilities and are slow growing relative to the 2D coherent-structure amalgamations.

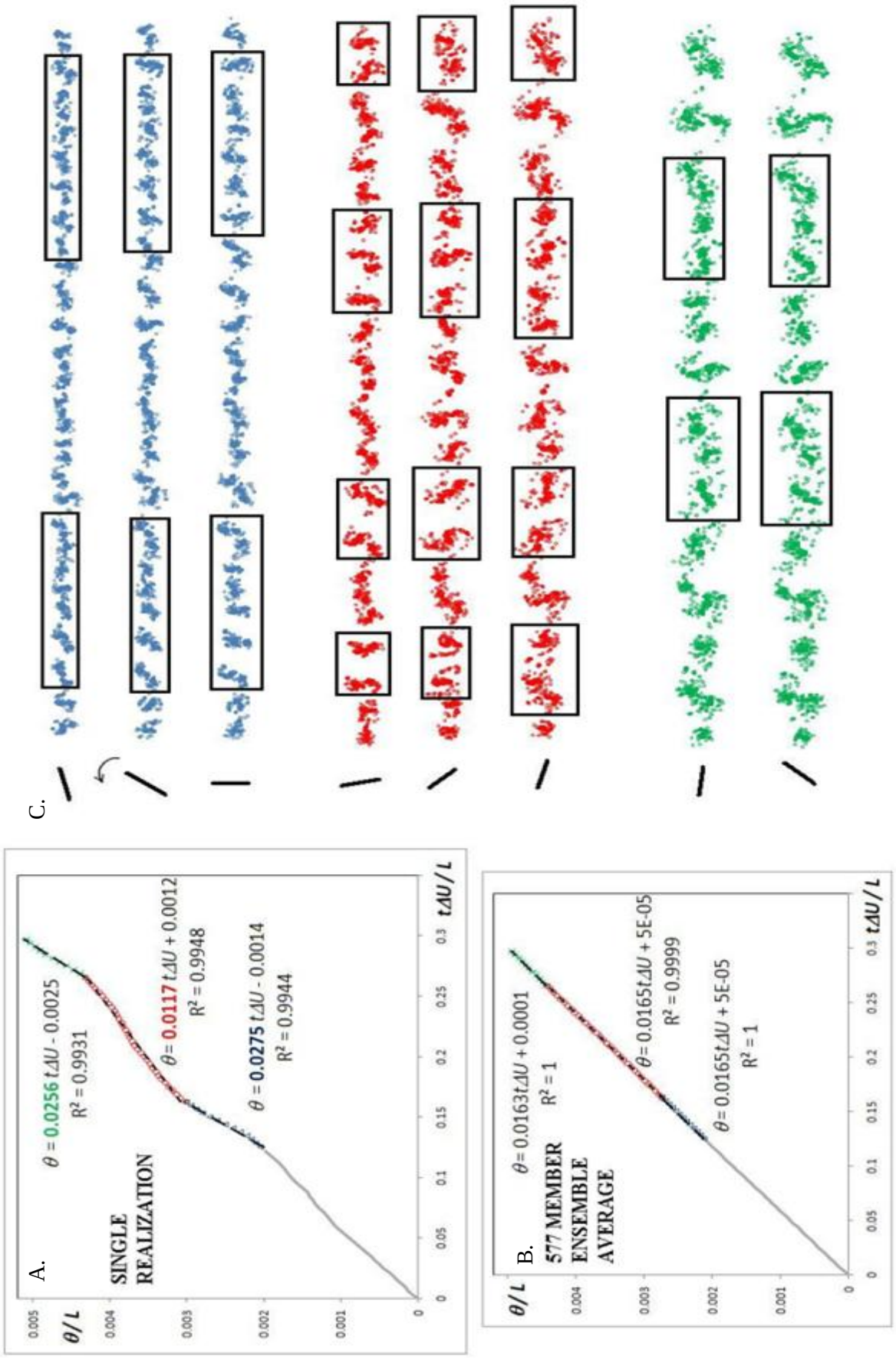

Figure 5.7. Insufficient averaging may lead to apparent non-universal or multiple 'local self preservation states' with different spread rates. The orientation of train of structures (marked in boxes) may be locally coherent (orientation indicated by the black lines) and may lead to a linear growth for a substantial duration but with a very different slope compared to the average.

The temporal vortex-gas shear layer also satisfactorily describes the spatial mixing layer for $\lambda \lesssim 0.5$ ($\lambda > 0.5$ particularly $\lambda = 1$ is discussed in Chapter 9). Therefore the universality of spread rate in Regime II suggests that the self-preservation spread rate in real mixing layers also likely to be universal and $C_{VG} = C_{NS}$. Second is that controversies about asymptotic states appear to be due to grossly inadequate appreciation of the long memory of initial conditions, the need for averaging over sufficiently long or large sample sizes and unreliablity of fits made over short temporal and / or spatial domains. In many temporal simulaton, there is also lack of appreciation of the beginning of Regime III during which the size of the flow domain becomes an additional parameter in the problem.

The implied universality self-preservation in mixing layers may also extend (in appropriate variables) to other shear flows. There has been a recent demonstration of the same in a temporally evolving DNS of an axi-symmetric wake (Redford et al, 2012). Such evidence in other flows, taken together with earlier work on plane wakes (Prabhu et al 1973, also see Narasimha 1990), and analyses such as that presented in this chapter support the view that turbulent shear flows are likely to possess asymptotically universal self-preservation states, though such states may be observable only under certain conditions like very long flow development in space and/or time, that may not be realizable in most experiments or technological scenarios. However, the existence of a unique asymptotic self-preserving state is a fundamental issue of great importance and changes the way of thinking about turbulent shear flows. Even if the universal self-preserving state is not reached in the domain of interest of a given application, it is still relevant for the simple reason that the flow of interest can now be seen as a part of a relaxation towards such a state. The models that one would then make for computing a flow, say, a RANS approach would be of a different class. Such models have been proposed (eg. Nee & Kovasznay 1969, Narasimha & Prabhu 1972), and need more attention.

The validity of the vortex gas to describe the large scale evolution of 3D NS mixing layers motivates us to explore several fluid dynamically relevant issues using vortex-gas simulations, and sets the tone for part II of this thesis.

PART II

Chapter 6 : Connections to instability theory

In this chapter we assess the role of hydrodynamic instability in attempts to understand the evolution of the temporal vortex-gas free shear layer, and by extension Navier-Stokes mixing layers (as substantiated in Chapter 5).

Most instability analyses involve the study of the evolution of a small (usually sinusoidal) perturbation in time or space, enabling the linearization of the governing equations around the prescribed base state. Such a linear analysis allows for a normal-mode decomposition, as each perturbation mode evolves independently. A normal mode decomposition of a linearized version of the Euler or Navier-Stokes equations (known respectively as Rayleigh and Orr-Sommerfeld equations) leads to an eigen-value problem that can be solved analytically or numerically (depending on the complexity of the base profile) to determine the initial response of the system to different perturbations. A detailed review of hydrodynamic instability analysis can be found in Drazin & Reid (2004) and Schmid and Henningson (2001).

Free shear layers are susceptible to inviscid instability as they have an inflectional velocity profile satisfying the Fjortoft criteria (1950). Linear analyses of the inviscid equations are hence applicable to describing the initial development of free shear layers, and such analyses have been done since Helmholtz (1868), Kelvin (1871) and Rayleigh (1879). Though turbulence is generally considered to be a strongly non-linear phenomenon, the possible relevance of linear stability theory has been discussed (Roshko, 2000) and there have been attempts to use linear (e.g. Gaster & Wynanski, 1985) or weakly non-linear (e.g. Monkewitz, 1988) stability theories to describe the growth of perturbations in a turbulent free shear layer. Though such studies have achieved reasonable success in predicting growth rates of externally imposed perturbations (see Ho & Huerre, 1985 for a review), they have been controversial (Husain & Hussain, 1995). Furthermore, there have been attempts to relate the self-preservation growth of a shear layer (Regime II) with ideas from linear instability theory (Morris et al, 1990). We therefore assess the usefulness of linear stability theory to describe free-shear-layer dynamics in Regimes I and II.

Many of the simulations presented in this section have several rows of vortices to better approximate a continuum constant-vorticity field with a well defined initial thickness. The resulting shear layer has an initially piece-wise linear velocity profile. As we shall see, the Regime II spread rate for this class of initial conditions (as long as L is much larger than the length scale of the initial perturbations) is the same as for the initial condition classes analyzed in Chapter 3. However, the several-row initial condition provides further insight into the initial development of the layer (Regime I), particularly in establishing connection to stability theories, as linear (Rayleigh) instability of the piece-wise linear velocity profile can be exactly calculated (see Drazin & Reid, 2004). In this chapter, we first examine the evolution with a single mode initial perturbation, followed by two modes and finally with filtered and white-noise. We shall track the evolution of the different modes and make comparison with stability theories to establish their usefulness and limitations.

Much of the work presented in this Chapter has been done in collaboration with Prof. Garry Brown (Princeton).

6.1. Linear and non-linear instability of a single mode in a piece-wise linear shear layer

In this section we shall consider the evolution of a single-mode perturbation on a vortex-gas analog of a free shear layer with an initially piece-wise linear velocity profile. The case simulated here has 19 rows of vortices with 140 vortices per row (N = 2660), equispaced in both x and y (contributing to an unperturbed 'thickness' of 18 inter-vortex spacings, which we shall consider as $\delta_{\omega 0}$). At t = 0, all the vortices are given a sinusoidal perturbations in y, with a wavelength Λ_f exactly equal to the length of the periodic domain L and with an amplitude that is 0.005 Λ_f.

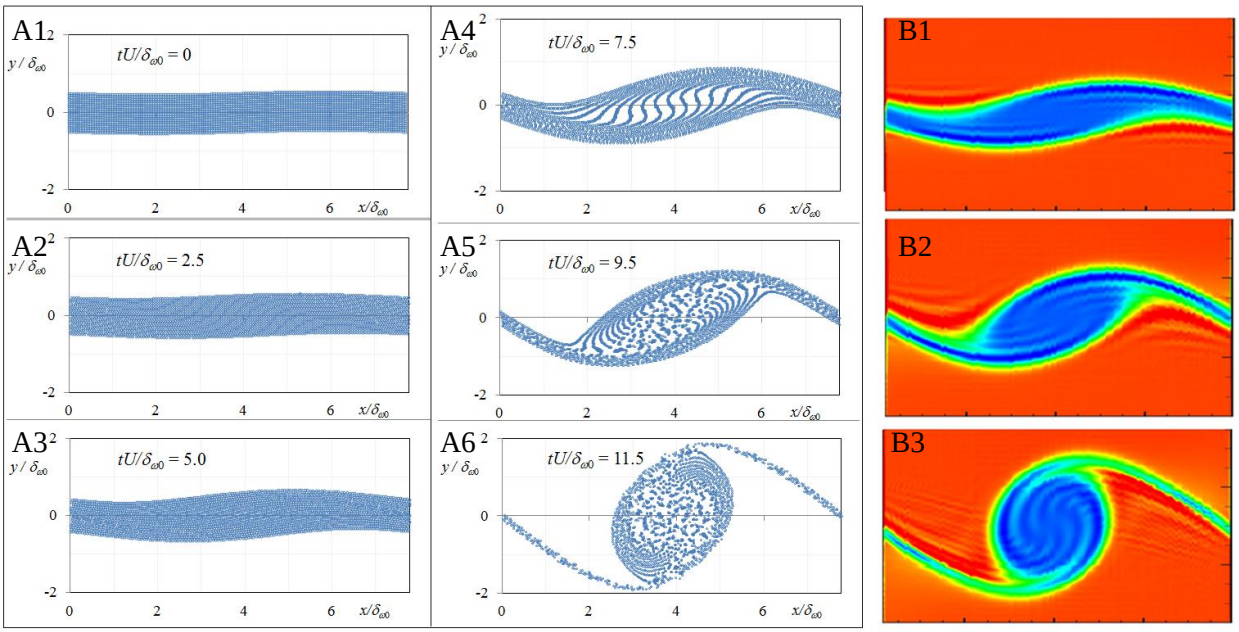

Figure 6.1. (A) Temporal evolution of the vortex-gas analog of the constant-vorticity free shear layer with a single mode perturbation. **(B)** Contours of constant vorticity of 2D NS (finite difference simulations, provided kindly by Prasanth P) simulations corresponding to the vortex-gas solutions at $tU/\delta_{\omega 0}$ of 7.5, 9.5 and 11.5 (after adjustment of virtual origin in time).

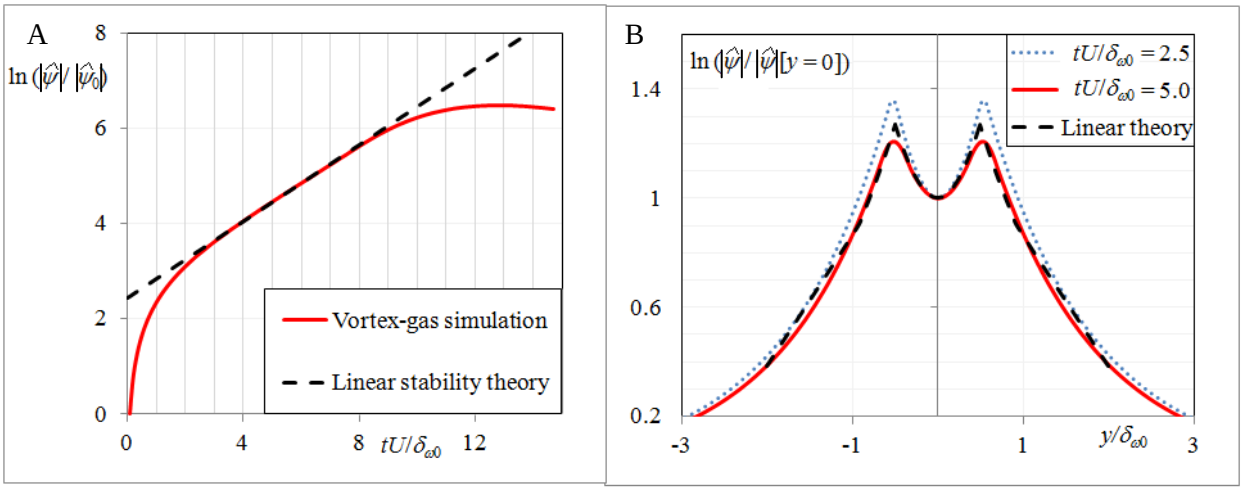

Figure 6.2. (A) Evolution of the modal amplitude of the perturbation stream function at y = 0, shown in log-linear scale. Note that the growth is exponential (linear in log scale) between $tU/\delta_{\omega 0}$ ~2.5 to 8.5 and the exponent is in agreement with that predicted by Rayleigh theory. **(B)** Variation of the perturbation amplitude with y during the exponential evolution. Notice that the shape of the 'mode' does not significantly change and is close to the Rayleigh eigen-function.

The temporal evolution of such a layer is shown in Figure 6.1. It can be seen that the sinusoidal perturbation grows in time before culminating in the 'roll-up' to a structure at later times ($tU/\delta_{\omega 0}$ = 9.5 to 11.5, note that we use $U = \Delta U/2$ as the velocity scale in this chapter). The evolution of the perturbation can be quantified via the amplitude of the perturbation stream function (introduced in Ch.3) at $y = 0$, computed at 256 equispaced locations in x. The evolution of the absolute value of the Discrete Fourier Transform of the perturbation streamfunction,

$$\left|\hat{\psi}\right| = \sqrt{\hat{\psi}[\kappa = 1, y = 0]\,\hat{\psi}^{*}[\kappa = 1, y = 0]},$$

is shown in Fig. 6.2. It can be seen that after a short initial transient (which occurs due to the initial condition not being the exact eigen-mode), the perturbation grows exponentially over $tU/\delta_{\omega 0}$ between 2.5 and 8.5 and the amplitude increases by nearly 20 times. The growth exponent, G, determined by a best-fit to data between these two times, is 0.401, which is within 0.25% of that predicted by Rayleigh theory (0.402, Drazin & Reid 2004).

Furthermore, it can be seen from Fig.6.2B that the distribution of the perturbation amplitude in y also agrees with the Rayleigh eigenfunction for the perturbation stream function. Figure 6.3 shows that the growth exponent during this linear regime agrees with Rayleigh analysis not only for the most amplified mode studied so far, but also for a range of different wave numbers. It has to be noted that the present simulations without desingularization still lead to a smooth roll-up of the shear layer as a whole (with the exception of local regions of disorder around the centre of the structure), when several rows of vortices are used.

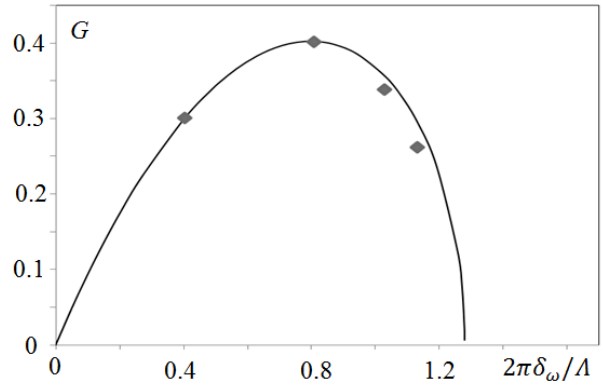

Figure 6.3. Comparison of growth exponents observed in vortex-gas simulations with the predictions of Rayleigh theory for different wave numbers

On one hand, the agreement between the vortex-gas solution and linearized Euler is expected as the vortex gas weakly converges to the smooth solution of the Euler equation (Marchioro & Pulvirenti, 1993) and the linear assumption is valid when the perturbations are small. However, it has to be noted that in the case of the Rayleigh equation, the vorticity is strictly confined between $\pm\delta_{\omega 0}/2$ and the solution is obtained by matching pressures at the interfaces, whereas the vortex-gas formulation permits non-linear behavior from $t = 0$ and condenses all the dynamics into the kinematics of the Biot-Savart relationship. Therefore, it is remarkable as to how the two apparently distinct mathematical approaches lead to nearly the same solution at least during these early times.

Beyond $tU/\delta_{\omega 0} \sim 9$, the evolution of the perturbation departs from exponential growth and eventually saturates around $tU/\delta_{\omega 0} \sim 12$ (as seen in Fig. 6.2A). It can be seen from Fig.6.1A that this corresponds to the non-linear roll-up into a structure. (Due to the choice of the initial condition with $\Lambda_f = L$, there is only one structure per L, which is an analog of Regime III. Therefore there is no Regime II in this simulation). From Fig.6.1B it can be seen that the vortex-gas solution is in agreement with 2D NS simulation during this distinctly non-linear phase of evolution, once again confirming the conclusions drawn in Chapter 5.

Thus, the two major conclusions from this section are : (i) the usefulness of Rayleigh theory is limited to times before the formation of coherent structures and (ii) the vortex gas has no such limitations and hence is a powerful method for studying the non-linear evolution.

6.2. Evolution with two modes and regime of monopole dynamics

Before proceeding to study a 'turbulent' (Regime II) free shear layer, whose evolution is presumably governed by the interaction of a large number of modes, we study the evolution of two modes and their interaction. We solve a system of 5320 vortices, arranged in 19 rows as before. At t = 0, we perturb the y-positions of the vortices with two modes. The mode with the shorter wavelength $\Lambda_f = L/2$, which we shall call the fundamental (in accordance with the fluid-dynamical literature), has an amplitude a_f = 0.005 Λ_f. The mode with the longer wavelength, called the sub-harmonic, has wavelength $\Lambda_s = L = 2\Lambda_f$ and amplitude $a_s = 0.001\,\Lambda_f$. The initial configuration and subsequent evolution of the vortex locations are shown in Fig. 6.4.

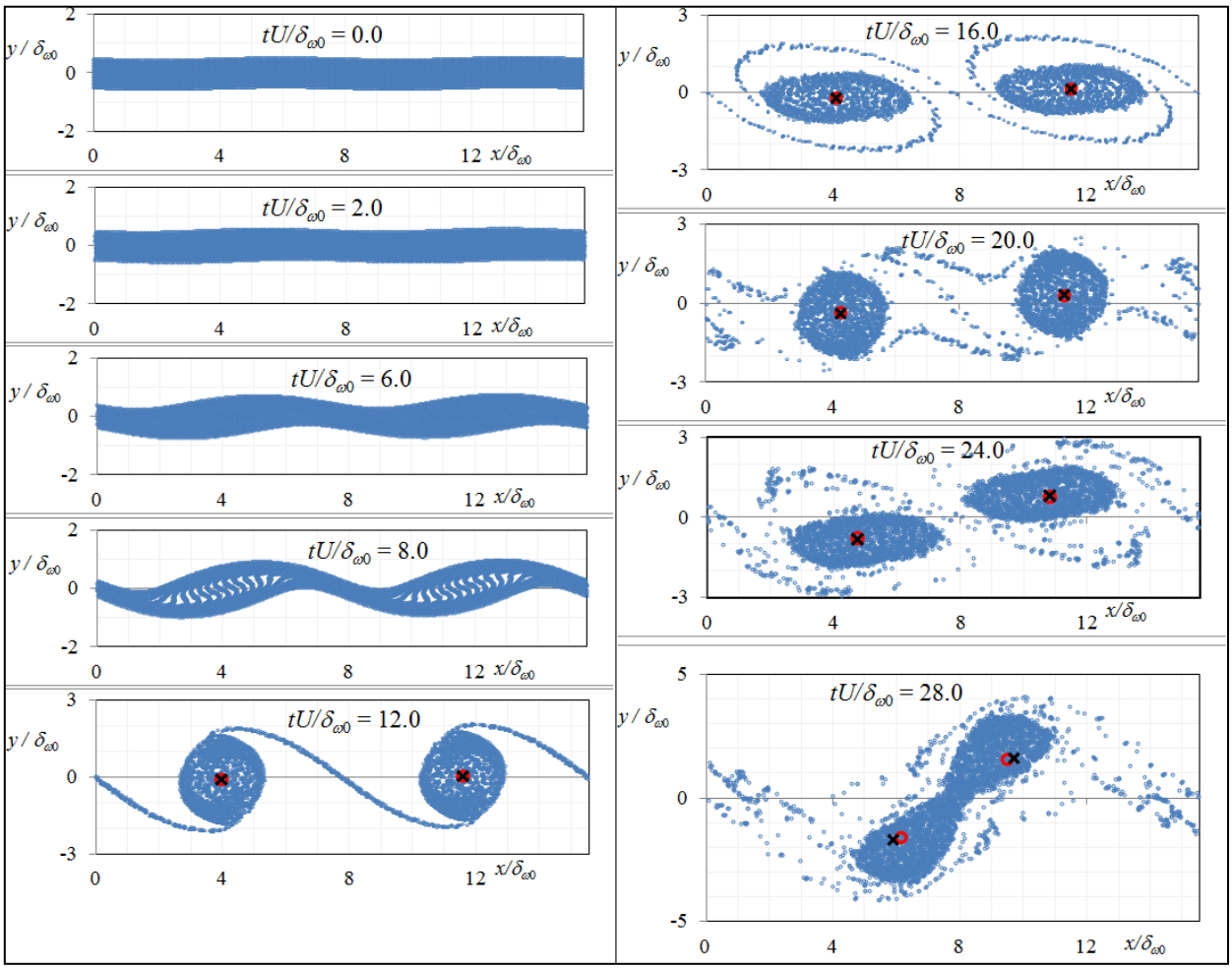

Figure 6.4. Snapshots of evolution of vortex-gas analog of constant vorticity shear layer with two-mode perturbation. The black crosses show the centroids of the vortices in the first and second half of the domain. Red circles are the locations of monopoles (being a single point vortex replacing a structure), that are initialized at the location of the centroids at $tU/\delta_{\omega 0} = 12$.

As in the case of the single mode perturbation, it can be seen that the waves roll up into structures at $tU/\delta_{\omega 0} \sim 8$. Beyond this time, the evolution seems to be dominated by what appears to be an interaction of the two structures, as the right structure moves upwards and towards the left and the left structure moves downwards and towards the right (clearly seen by $tU/\delta_{\omega 0}$ = 20). They eventually get close to each other and begin to 'merge' at $tU/\delta_{\omega 0} = 28$.

Further insight on the applicability of stability theory to the evolution of the free shear layer with two modes can be obtained by studying the evolution of the perturbation stream function amplitudes corresponding to each of the two modes. This is shown in Fig. 6.5, from which it can be seen that between $tU/\delta_{\omega 0} = 2.5$ to 8.5, both the fundamental and the subharmonic grow exponentially. The exponent corresponding to the fundamental is nearly identical to the case where the subharmonic was absent (Fig. 6.2 A), and is in agreement with Rayleigh theory. However, the exponent corresponding to the evolution of the subharmonic is about 25% higher than the value when the fundamental was absent (Fig. 6.3). This suggests that even during these relatively early times, while the evolution of the fundamental is governed by linear dynamics, the evolution of the subharmonic appears to be affected by the fundamental; the problem is therefore weakly non-linear even at early times.

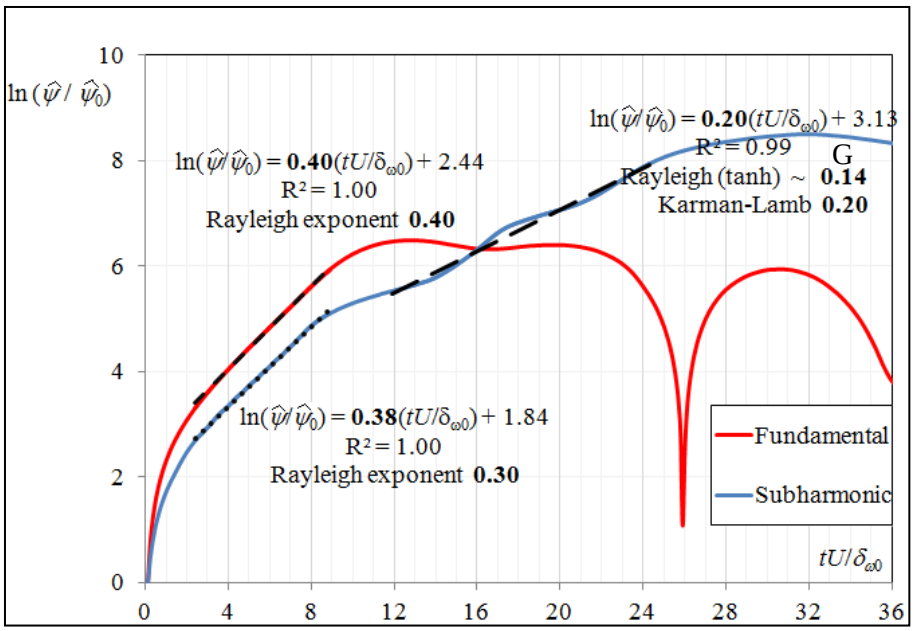

Figure 6.5. Evolution of the perturbation stream function amplitudes corresponding to the fundamental and subharmomic

Interestingly, as seen from Fig. 6.5, the subharmonic enters a new regime of exponential growth between $tU/\delta_{\omega 0} \sim 12$ to 24. Note that $tU/\delta_{\omega 0} \sim 12$ approximately corresponds to the time at which the fundamental saturates as a result of the roll-up and formation of structures (see Fig. 6.4). The exponent of 0.20 is significantly different from 0.14 obtained by the Rayleigh analysis (for a tanh profile, Michalke, 1965), applied to the 'new base flow' (averaged velocity profile between $tU/\delta_{\omega 0} =$ 12 to 24 is well approximated by a tanh profile with $\delta_\omega = 2.3\ \delta_{\omega 0}$). This disagreement is not surprising considering that the (coarse-grained) perturbation vorticity is of the same order as the maximum mean vorticity. Thus, the saturation of the fundamental is a non-linear process and therefore there is no reason to expect linear stability theory with a uniform base flow to describe processes that follow the roll-up. In other words, describing the flow field at say $tU/\delta_{\omega 0} = 12$ (Fig. 6.4) as a small perturbation over a uniform-in-*x* base flow does not seem appropriate.

The other extreme approximation to describing the flow field at $tU/\delta_{\omega 0} = 12$ is to consider each structure as a single point vortex (referred to as monopoles), located at the respective centroid and with a strength equal to the circulation of the structure (which, for the vortex-gas case is equal to the sum of the strengths of all the point vortices contained within the structure). Since the number of vortices located in the thin braids is small (less than 10%) compared to the number in the structure, we can crudely approximate the locations of the monopoles based on the centroid of vortices with $x < L/2$ and $x > L/2$ respectively. Further, we shall also consider monopoles of equal strength ($\Gamma = \gamma N/2$), though there are 2661 and 2559 vortices in the left and right half of the domains at $tU/\delta_{\omega 0} = 12$. Such an approximation is shown in Fig.6.4, with the locations of the monopoles (red circles) initialized at the locations of the

centroids (black crosses). We now simulate the system of two monopoles and compare their trajectories with those of the centroids of the structures in the full simulations in Fig. 6.4 over $tU/\delta_{\omega 0} = 12$ to 28.

It can be seen (Fig. 6.4) that the evolution of the monopole locations is nearly identical with the evolution of the centroids till $tU/\delta_{\omega 0} = 24$ and hence this approximation seems sufficient to provide a simple description of the evolution, before the onset of merger of the two structures (furthermore, note that at times $tU/\delta_{\omega 0} > 24$, the centroid of the vortices in the left or the right half-plane is no longer a reasonable approximation to the centroid of the respective structure). When the monopole displacements from their 'base' locations ($x = L/2 \pm L/4, y = 0$) are small compared to the distance between them ($\Delta x_m = L/2$), the evolution of their perturbations can be analytically calculated to be exponential, with an exponent of $\Gamma\pi/4(\Delta x_m)^2$. This was first proposed by Karman and Rubach (1912) and reproduced in detail by Lamb (1932). For the present flow for $12 < tU/\delta_{\omega 0} < 24$, the displacement of the monopole locations is less than 15% of the initial distance between them, and hence this approximation may hold. Indeed, we find that the exponent computed using $\Gamma\pi/4(\Delta x_m)^2$, with $\Gamma = \gamma N/2$ and $\Delta x_m = L/2$, is $\pi U/L = 0.20U/\delta_{\omega 0}$, very close to the observed value of the exponent in the interval $12 < tU/\delta_{\omega 0} < 24$ (Fig. 6.5).

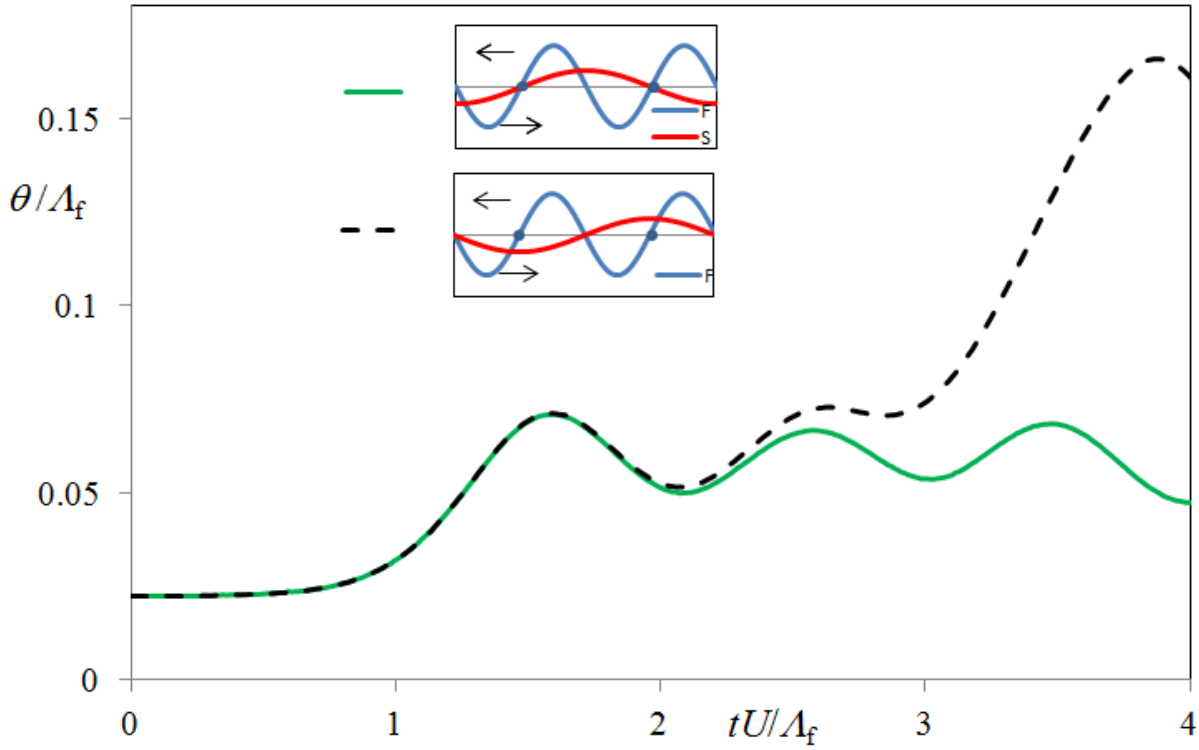

Figure 6.6. The effect of phase difference between fundamental and subharmonic in the evolution of the layer

Another piece of evidence, which suggests that the mechanics beyond $tU/\delta_{\omega 0} \sim 12$ is significantly better approximated by Karman-Lamb theory than Rayleigh, is the dependence of the evolution of the layer on the phase difference between the fundamental and subharmonic. This is shown in Fig. 6.6. The effect of the subharmonic is the highest when the phase difference is such that the peaks and troughs of the subharmonic coincide with the roll-up locations of the fundamental, and when the phase difference is such that the zero crossings of the subharmonic coincide with the roll-up locations of the fundamental, the evolution is nearly identical to the case where the subharmonic is absent. This effect of the phase difference, which has been observed in experiments (Husain & Hussain, 1995), is consistent with Karman-Lamb theory (the subharmonic perturbation translates to the perturbation of the monopole locations in the first case, but not in the second case), and is inconsistent with Rayleigh theory (though the weakly non-linear theory due to Monkewitz incorporates the effect of phase). The reader is referred to

a related discussion by Husain & Hussain (1995), who attempt to explain the observed phase difference using vortex-dynamics concepts, and to Winant & Browand (1974) who have suggested a model akin to the present monopole model to describe the growth of the turbulent mixing layer.

To summarize, the study of the vortex-gas shear layer with two modes suggests that the evolution is satisfactorily described by a Rayleigh theory only at early times before the roll-up of the fundamental, though there is a departure in the evolution of the subharmonic even at these early times. At times beyond the saturation of the fundamental, Rayleigh theory is no longer applicable, as the uniform-in-*x* base flow is no longer a reasonable approximation. On the other hand replacing the rolled-up structures with monopoles and using the associated linear theory due to Karman & Lamb provides a more accurate description of this phase of the evolution.

6.3. Evolution with multiple modes and relaxation to Regime II

While the simulations presented in 6.1 and 6.2 showed the limits of validity of Rayleigh and Karman-Lamb theories, the turbulent free-shear-layer evolution could involve strong non-linear interaction between several modes. As noted in Ch. 3 and 4, Regime II (which cannot be observed in 6.1 and 6.2 as Λ_{ic}/L, being 1.0 and 0.5 respectively, is not small) is governed by the long range interaction of several structures, and by amalgamations which are not described by the monopole approximation.

In order to shed light on the issue of applicability of stability theory to Regime II, or at least to the later phases of the relaxation to Regime II, we therefore perform additional simulations with two different initial-condition classes, each with several modes. The first is with white-noise, and second is white-noise filtered to have only the modes with 33 – 64 waves in the domain ($\kappa L, \kappa\delta_{\omega 0} = 0.118 - 0.229$). Note that this filtered noise does not contain the subharmonic corresponding to the most amplified mode predicted by Rayleigh theory. Both simulations have 4 rows of vortices, with 1120 vortices in each row (N = 4480). We use a Krasny-type desingularization for these simulations, with $\epsilon/l = 1$ (which does not affect the evolution, as shown in Appendix C). The combination of the present initial condition and desingularization results in an initial vorticity thickness $\delta_{\omega 0} = 4$. The results presented below are averages over 16 realizations.

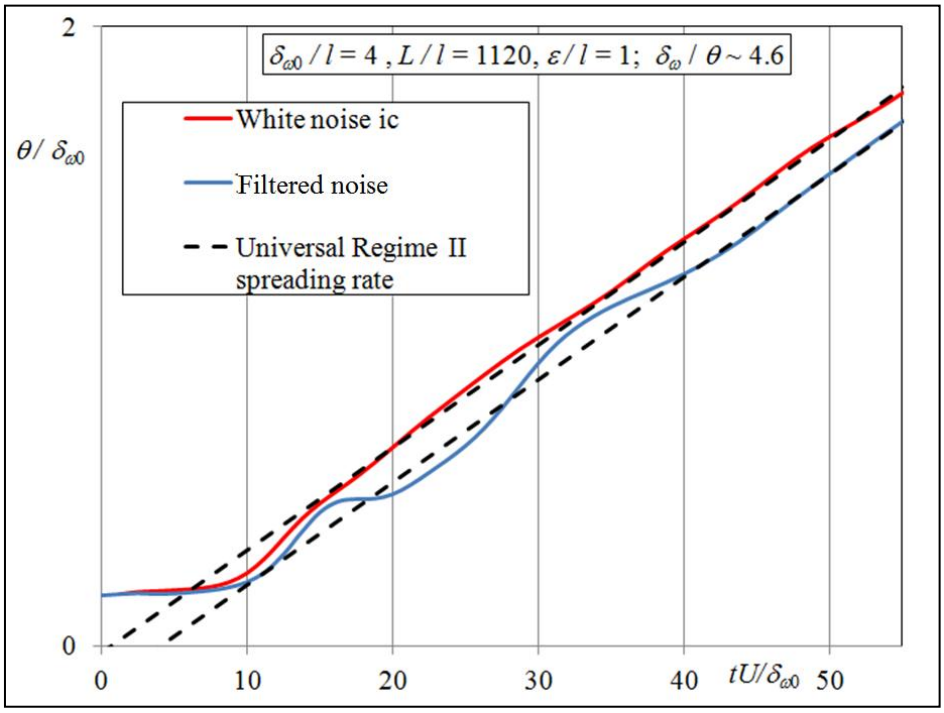

Figure 6.7. Evolution of momentum thickness of vortex-gas (thick) shear layers with white and filtered noise.

The evolution of momentum thickness in both cases is shown in Fig.6.7. At early times, $tU/\delta_{\omega 0} \lesssim 5$, there is hardly any change in the bulk thickness of the layer. Subsequently, around $tU/\delta_{\omega 0}$ ~ 10, there is a rapid growth of layer thickness. In case of the filtered noise, there is a plateau between $tU/\delta_{\omega 0}$~ 15 and 20 beyond which the layer resumes rapid growth before eventually relaxing to a constant spread rate. In the case of white-noise, the relaxation to constant spread rate is smoother and is achieved slightly earlier. Eventually, at later times of $tU/\delta_{\omega 0} \sim 50$, it can be observed that both initial conditions relax to a state of constant spread rate which is the same as the universal Regime II spread rate noted in Ch.3 for the single-row initial conditions. We shall examine the spectral content and the growth rates of different modes over different segments of the relaxation process and make comparisons with the predictions of Rayleigh and Karman-Lamb theories.

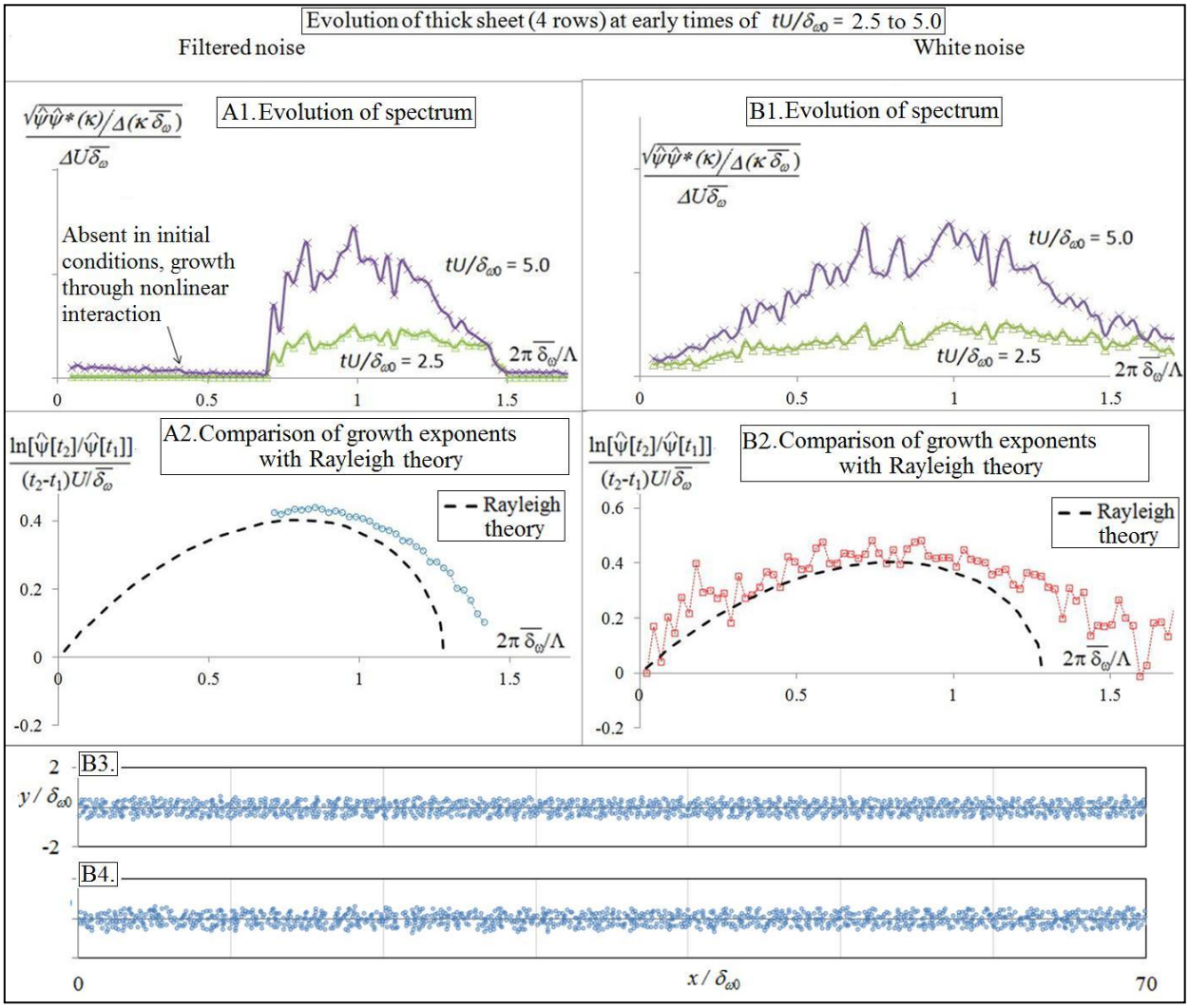

Figure 6.8. Spectral evolution during early times ($tU/\delta_{\omega 0}$= 2.5 to 5.0). A1 and B1 show the power spectral density of the perturbation stream function for filtered noise and white noise initial conditions, A2 and B2 show the respective growth exponents, B3 and B4 show the vortex-positions at $tU/\delta_{\omega 0}$= 2.5 and 5.0 for a realization of the white noise initial condition.

We first study the evolution at early times of $tU/\delta_{\omega 0}$ = 2.5 to 5.0. It can be observed from Fig. 6.8A1 and B1 that there is an increase in the amplitude of the perturbation modes with $2\pi\delta_\omega/\Lambda \lesssim 1.5$, with some modes (around $2\pi\delta_\omega/\Lambda$ ~ 0.8) growing by over a factor of two. Figure 6.8 A2 and B2 show the computed values of estimates of a local growth exponent, $(d/dt)\,(\ln\hat{\psi})$, for the different modes. It can be observed that for filtered as well as white noise initial condition, there is broad agreement between

the observed growth exponents and those predicted by Rayleigh theory, particularly near the maximum growth rates. This is consistent with the observations made in Sec.6.1 and 6.2 to the effect that the initial evolution, particularly of the most amplified mode is well described by Rayleigh theory. This is also an expected consequence of the observation (Fig. 6.7) that the momentum thickness of the shear layer hardly varies till $tU/\delta_{\omega 0}$ ~ 5, which implies that the perturbations do not yet significantly alter the base flow. This can also be seen from Fig. 6.8B3 and B4, which show the growth of wavy perturbations does not greatly change the constant vorticity base state, i.e there are no coherent structures at these times.

However, the modes away from the maximum growth exponent ($2\pi\overline{\delta}_\omega/\Lambda \lesssim 0.3$ and $2\pi\overline{\delta}_\omega/\Lambda \gtrsim 1$) show higher values compared to the theory. This suggests that they are enhanced by non-linear interactions. The generation of modes that were absent in the filtered noise initial conditions as shown in Fig. 6.8A1 further supports the argument that even at early times nonlinearity may play a role.

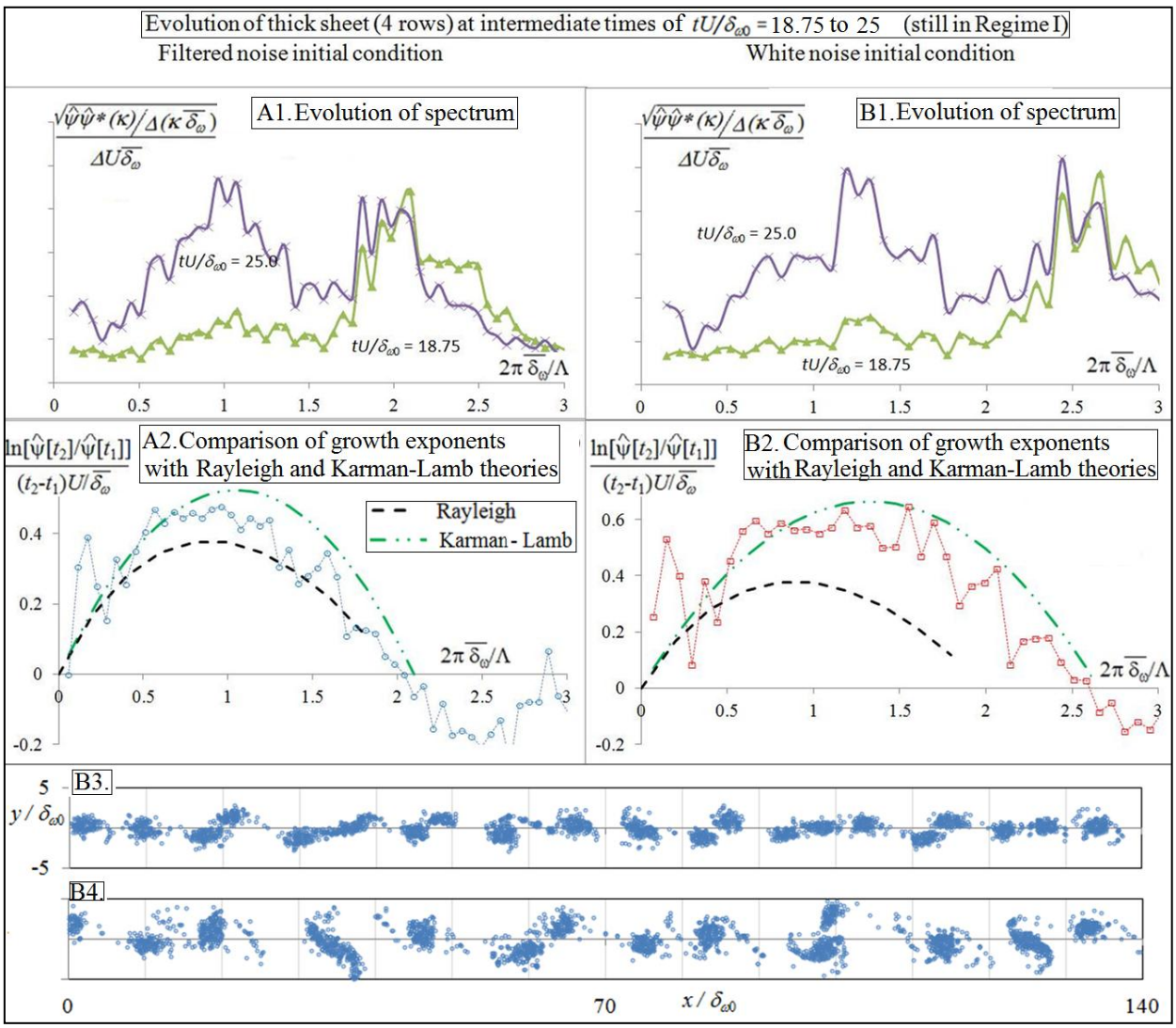

Figure 6.9 Evolution during intermediate times (after formation of coherent structures, $tU/\delta_{\omega 0}$= 18.75 to 25.0). $\overline{\delta_\omega}$ is the average thickness during the evolution considered. A1 and B1 show the power spectral density of the perturbation stream function for filtered noise and white noise initial conditions, A2 and B2 show the respective growth exponents, B3 and B4 show the vortex-positions at $tU/\delta_{\omega 0}$= 18.75 and 25.0 for a realization of the white noise initial condition.

We next examine the spectral evolution at $tU/\delta_{\omega 0}$ between 18.75 and 25.0 in Fig.6.9. This corresponds to the duration of rapid growth just beyond the plateau in the case of the filtered noise initial condition (see Fig.6.7). At these times, the instability waves have rolled-up and formed coherent

structures, as shown in Fig.6.9B3. Figures 6.9A1 and B1 show, for both initial conditions, that while the modes which have the maximum amplitude appear to have saturated, there is a significant growth of modes which have approximately twice the wavelength. This observation is similar to the saturation of the fundamental and subsequent growth of the subharmonic analyzed and discussed in Sec.6.2, though the 'fundamental' and the 'subharmonic' in this case each corresponds not to a single mode, but to a range of modes. Thus the structures are not equally spaced, but have a preferred range of spacings corresponding to the preferred initial amplification of the perturbations.

The growth exponents computed during intermediate times are shown in Fig. 6.9A2 and B2 and compared with both Rayleigh (which depends on the thickness) and Karman-Lamb (which depends on the monopole spacing) distributions. The spacing between the monopoles for the Karman-Lamb is taken to be equal to the wavelength of the most amplified mode at $tU/\delta_{\omega 0}$ = 18.75. Though the structures are neither equally spaced nor of equal strength, it can be seen that the agreement with the Karman-Lamb is reasonable and significantly closer than the exponents given by Rayleigh corresponding to the mean base flow. Therefore, this supports the discussion in Sec. 6.2 that the evolution after the roll-up is dominated by monopole interactions, eventually leading to mergers, and this is also observed in the vortex snapshots, shown in Fig.6.9B4.

Figure 6.10 shows the spectral evolution during $tU/\delta_{\omega 0}$ = 46.25 to 52.5. The evolution of momentum thickness (Fig. 6.7) suggests that at these times, the white noise initial condition is well into Regime II, while the filtered noise initial condition has just begun to grow at universal spread rate (the higher order statistics may not yet have relaxed to their respective universal states). The differences in the spectrum between the two initial conditions (Fig. 6.10 A1 and B1) suggest that either or both of the flows have not yet completely relaxed to Regime II.

The growth exponents of the different modes during this evolution are shown in Fig. 6.10 A2 and B2 and compared with the Rayleigh and Karman-Lamb theories as before. Interestingly, the ratio thickness to wavelength of the dominant mode is such that the predictions of both theories are in close agreement with each other except at short wavelengths. Surprisingly, the computed exponents in the amplified part of the spectrum are closer to the values given by Rayleigh theory than Karman-Lamb. The snapshots in Fig.6.10 B3 and B4 show that the structures have greater variability and jitter than those observed in Fig. 6.9 B3. Therefore the deviation from Karman-Lamb theory is not unexpected, but the agreement with Rayleigh theory is. However, it must be noted that there is a part of the spectrum beyond $2\pi\delta_\omega/\Lambda \sim 2$ which shows decaying modes. Decaying modes are absent in any linear inviscid theory, and this clearly shows the role of non-linear transfer from short wavelengths to longer wavelengths, consistent with the appearance of larger structures and (the 2D) reverse cascade.

Since the simulations above discussed have relatively small ensemble sizes, we revisit case R1 presented in Ch.3 to provide more precise spectral statistics in Regime II. The results are shown in Fig.6.11. It is seen from Fig. 6.11A that the spectrum is universal over $tU/l = 200$ to 420 when scaled with thickness at the respective instant of time. The evolution of the different modes can be observed, when scaled with averaged thickness over short times as shown in Fig 6.11B. It can be observed that there is growth of longer wavelength modes and a decay of short-wavelength modes consistent with the observations in the thick shear layer. The growth exponents are shown in Fig.11C, and Fig. 11D shows the data after locally averaging in wavenumber space provides greater clarity. It can be observed that the growth exponents in Regime II are also universal and self-similar. Most significantly, once again a remarkable agreement can be observed with Rayleigh theory for the positive exponents. However, consistent with the observations in the thick sheet, the negative exponents do exist (in this case, definitely beyond the uncertainty of statistical scatter) and their description is beyond linear theory.

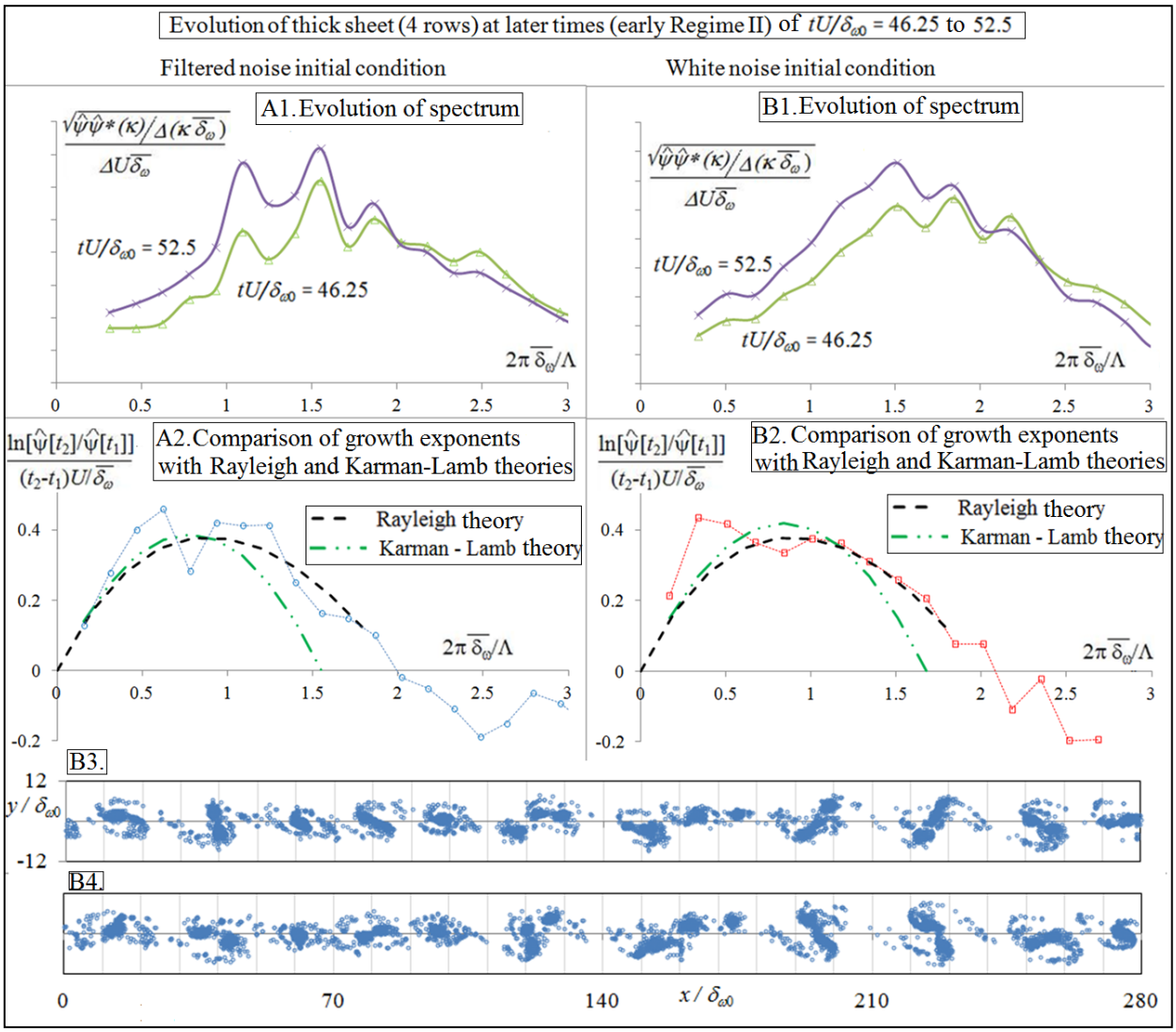

Figure 6.10. Evolution during later times (transition to Regime II, $tU/\delta_{\omega 0}$= 46.25 to 52.5). A1 and B1 show the power spectral density of the perturbation stream function for filtered noise and white noise initial conditions scaled with the time-averaged thickness, A2 and B2 show the respective growth exponents, B3 and B4 show the vortex-positions at $tU/\delta_{\omega 0}$ = 46.5 and 52.5 for a realization of the white noise initial condition.

Even though the Karman-Lamb theory (as applied here) does not provide a satisfactory description at shorter wavelengths, it does not rule out the dominance of monopole dynamics in describing the large scale evolution of the layer. This is because the lack of agreement with Karman-Lamb could be a consequence of the violation of assumptions of small monopole displacements and equal monopole strengths made by the Karman-Lamb theory, rather than the approximation of representing each coherent structure with a monopole, as the analysis of structures in Regime II show the standard deviation of monopole strengths is 30% of the mean value and that of spacing is 15%.

Figure 6.12 shows the evolution of structures and the independent evolution of monopoles initialized at the centroids and with the strengths of visually identified structures at $t\Delta U/l$ = 600. (In this model, the strengths of the monopoles are initially different from each other but remain constant with time). It can be seen from Fig.6.12 that the monopole picture does provide a satisfactory approximation except during mergers.

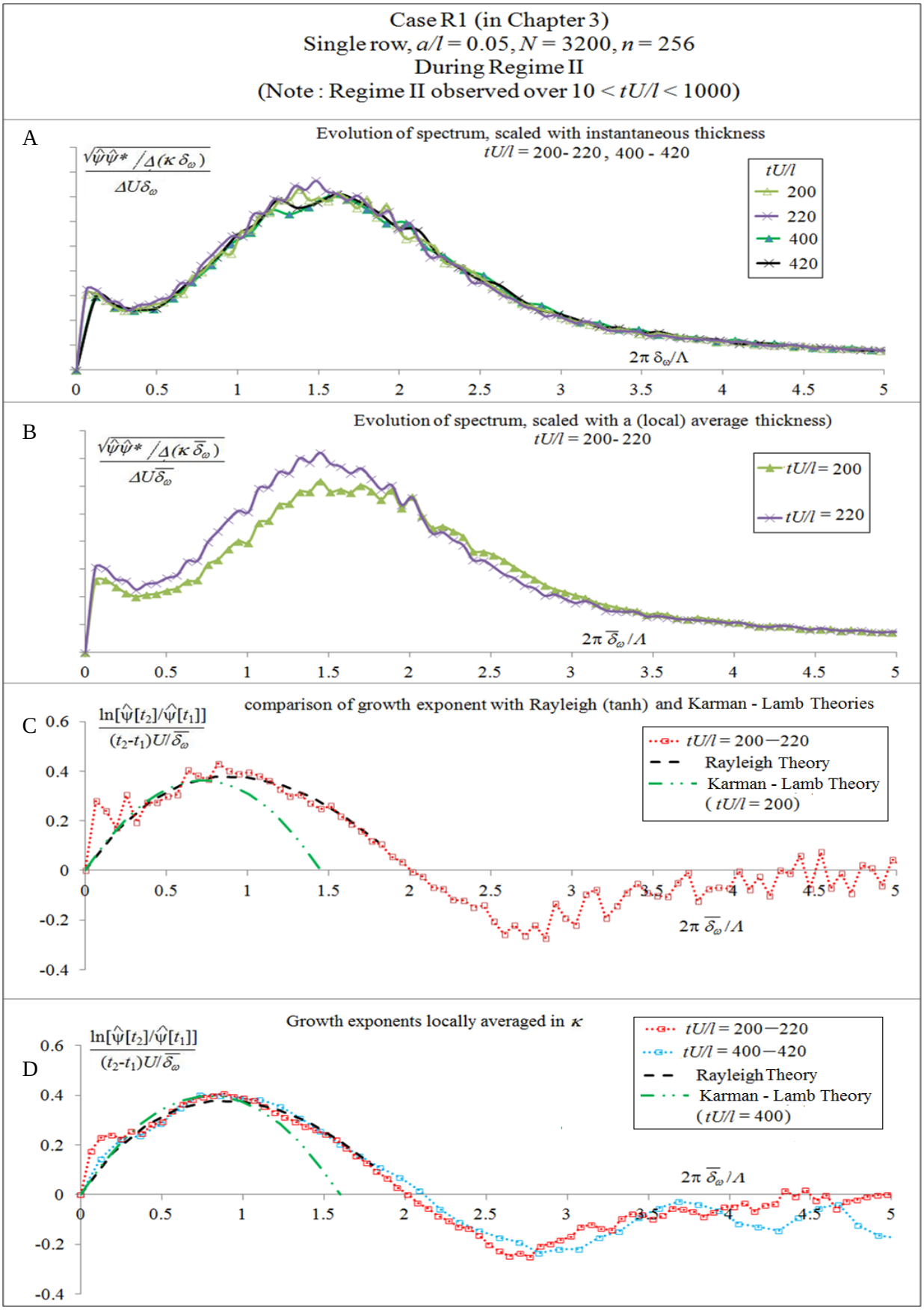

Figure 6.11. Spectral evolution in Regime II for case R1. Note that δ_ω indicates vorticity thickness (computed from the x-averaged velocity field) at the specified time and $\overline{\delta}_\omega$ is the short-time averaged vorticity thickness (between t_1 and t_2 which are respectively 200 and 220 in B, C and for the red line in D and 400 and 420 for blue line in D).

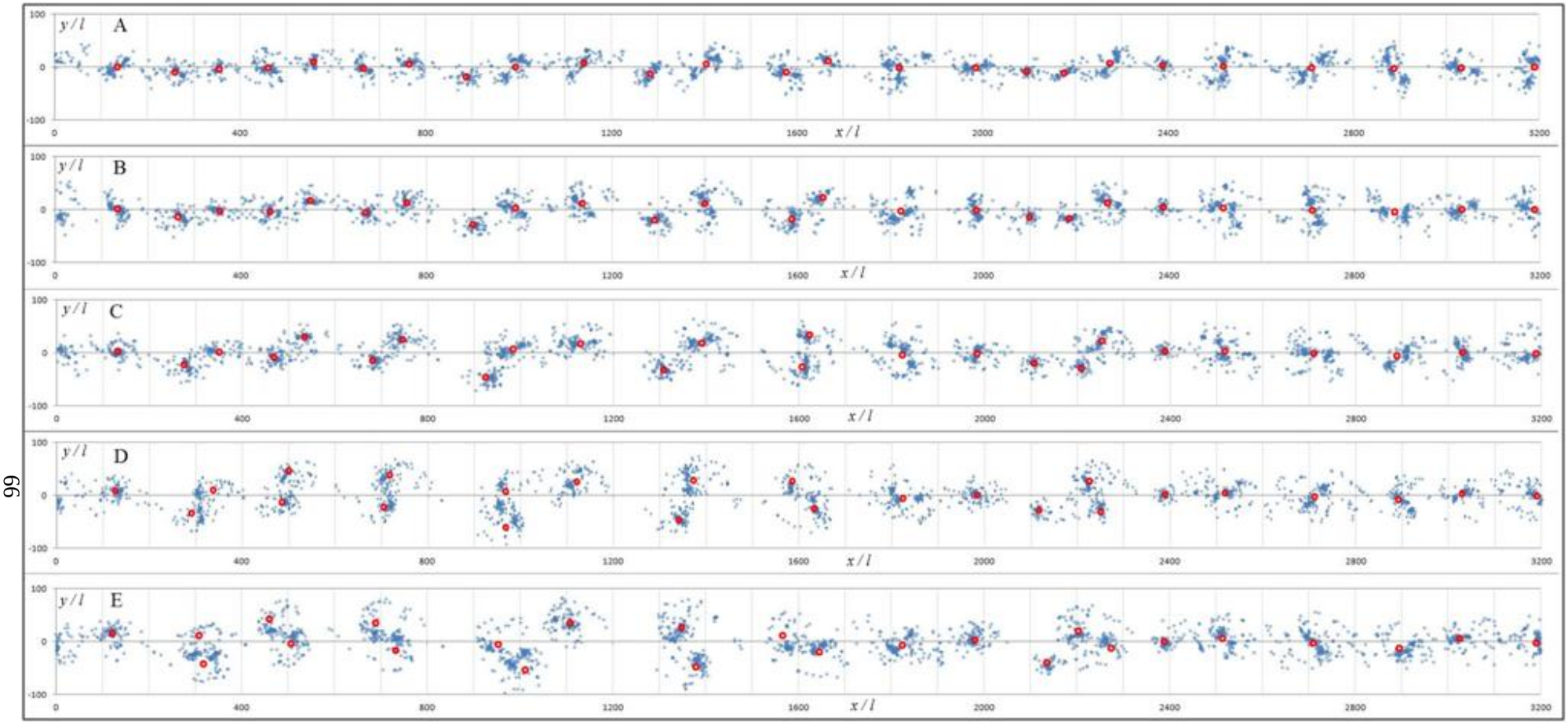

Figure 6.12. Evolution of the structures and monopoles (red circles) in (a single realization of) R1 between $t\Delta U/l$ = 600 to 1000.

This suggests that, strangely, the two opposite extreme approximations, one involving small perturbations to a uniform-in-*x* base flow and the other that replaces each coherent structure with a single monopole, both appear to provide a reasonable understanding of positively growing modes in Regime II. This is possibly due to ratio of the thickness of the layer to the dominant spacing between coherent structures attained in Regime II (the peak of the spectrum in Fig.6.11A corresponds to $\Lambda/\delta_\omega \sim 4$). The underlying mechanics which led to such a thickness to spacing ratio is not yet clear.

The present results suggest that there are two possible explanations for the agreement with Rayleigh theory for the exponents of the growing modes in Regime II. One possibility is that, the agreement is not because the underlying mechanics are linear, but due to the two extreme idealizations of small perturbations and monopole dynamics leading to very similar results for the observed thickness to spacing ratio in Regime II. Supporting this conclusion are : (i) the observations of non-linear transfer even at very early times (Fig. 6.8), (ii) the failure of Rayleigh theory immediately after the roll-up of the fundamental, and (iii) the negative exponents at shorter-wavelengths in Regime II, all of which indicate that non-linear processes are at play.

However, the other possible explanation is that the dynamics at the relevant scales are indeed (at least, in part) linear. The examination of velocity profiles averaged over *x*-extents of $6\delta_\omega$ (which is roughly the wavelength at which maximum growth exponents are observed; see Fig. 6.11D) show that the velocity fluctuations from the mean are of the order of 10% of the velocity difference across the layer. It might be possible that this perturbation of the velocity field averaged over the relevant length scale, is sufficiently small so that linear theory is indeed valid in describing the evolution of modes at the scales corresponding to the growing modes.

Further analysis is needed before determining which of the above two arguments (for why Rayleigh theory is useful in Regime II) is correct. Though the present results fall short of a complete description of the turbulent shear layer in terms of instability, they do shed some light and also raise some questions, particularly on the controversial issue of the usefulness of ideas from linear (and by extension weakly nonlinear) stability theory for fully turbulent flow.

Chapter 7 : Applications to flow control

Experiments such as those of Oster & Wygnanski (1982, see Section 5.2) have shown that the spreading of a mixing layer can be greatly enhanced or suppressed by introducing appropriate sinusoidal perturbations in the flow. It was also shown in Section 5.2, that the spread rate eventually relaxed to the universal value in Regime II; however the extent of the affected region (Regime I) can be very large with respect to the amplitude of the perturbations (e.g. The flow can be strongly influenced upto a downstream distance of over 3 m for perturbation amplitude 1.5 mm, see Fig 5.2) , and in the experiments it can correspond to a significant part of the flow development. Such perturbations can be introduced in several ways - a flapper at the end of the splitter plate (Fiedler & Wygnanski 1981,Oster & Wygnanski 1982, Gaster & Wygnanski 1985), by using loudspeakers (Husain & Hussain, 1995), or by perturbing the free stream velocity (Ho & Huang, 1982) or using piezoelectric devices (Naka et al,2010) .

This effect of 'periodic forcing' can be exploited for enhancing / suppressing mixing in applications such as combustion chambers and chemical lasers, and for reduction of drag and aerodynamic noise (Bridges & Hussain, 1987). (Though 'mixing' at the molecular level is greatly influenced by smaller scales, the region of momentum or vorticity dispersal determines the mixing zone and therefore is an important factor.)

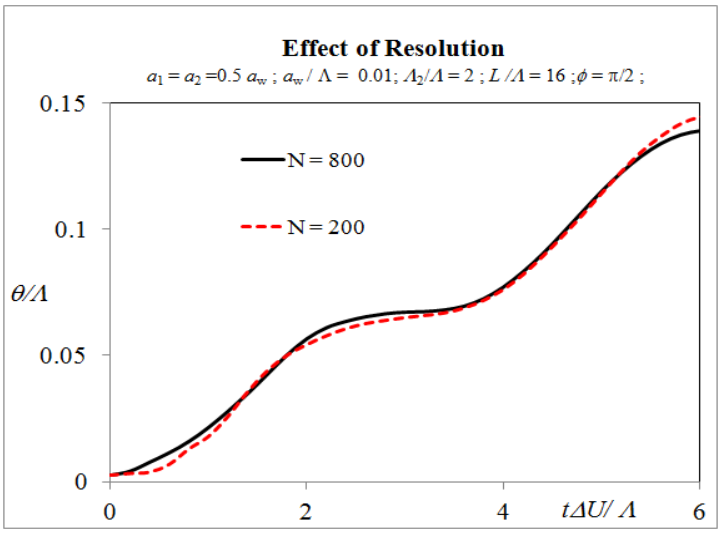

Figure 7.1. *N*-independence study of a vortex-gas free shear layer with a sample two-mode initial condition (see text for definitions of parameters).

As discussed in Chapter 6, while there have been several experimental studies and stability-based arguments to explain the role of periodic perturbations, a theoretical understanding remains incomplete. The initial growth of the fundamental mode is adequately represented by linear stability theory, the subsequent development is observed to be nonlinear, and this limits the applicability of theoretical analysis to determine optimal multimode forcing. (Even though some encouraging agreement was observed later at Regime II, the saturation of the fundamental and evolution of the subharmonic were shown to be beyond Rayleigh theory.) However, as seen in Section.5.2, the vortex gas quantitatively recovers the effect of periodic perturbations and shows excellent agreement with experiments. Thus it

---

Work presented in this chapter has in part appeared in:
Suryanarayanan and Narasimha, "Vortex methods: A tool for optimal control of high Reynolds number free shear flows", *Proceedings of Symposium on Applied Aerodynamics and Design of Aerospace Vehicle* (SAROD 2013) November 21-23, 2013, pg. 229-233, Hyderabad, India.

provides an inexpensive and effective nonlinear tool for optimization in flow control applications, and could be more practically feasible than those based on LES/DNS (Delport et al, 2010).

In this study, we shall focus on two-mode forcing, with single-mode forcing recoverable as a special limit. The two-mode strategy is suggested by the experimental observation (e.g. Ho & Huang 1982, Husain & Hussain, 1995) that forcing around the subharmonic leads to enhanced spreading. The present strategy serves to demonstrate optimization via vortex-gas simulations, as the complete evolution of the shear layer with such a forcing is beyond any (single) known stability theory, as noted in Ch. 6. An example of the behavior of a flow subjected to two-mode forcing is shown in Fig. 7.1 for different *N*.

Interestingly, it can be observed from Fig.7.1, the evolution of the momentum thickness does not significantly vary between N = 200 and N = 800 for the two-mode initial condition considered, suggesting that simulations with as few as 200 vortices can provide reasonable estimates of spread rate, provided $\Lambda \ll$ L. This is significant as a single realization of with N = 200 takes less than 20 seconds on a single-processor core. This permits simulating a large number of cases and carrying out an extensive optimization study. In comparison, a 2D DNS even with very modest Reynolds numbers would take at least a few hours for a single realization on the same single-processor.

The initial position of the vortices $\{x_i, y_i\}$ for a generic two-mode initial condition (with noise) is specified as

$$x_i(t=0) = L\,(i-1)/N,$$

$$y_i(t=0) = \; a_1 \sin\left(\frac{2\pi x_i}{\Lambda}\right) + a_2 \sin\left(\frac{2\pi x_i}{\Lambda_2} + \phi\right) + a_n * Y_i \;,$$

where Y_i is a random number uniformly distributed between -1 and $+1$.

The different parameters involved in the initial conditions of the above form are

L – Length (in x) of the periodic-in-x domain
N – Number of vortices ($l = L/N$ is the initial inter-vortex spacing in x)
a_1, a_2 – Amplitudes of periodic perturbations with shorter and longer wavelength.
a_n – Amplitude of noise
Λ, Λ_2 – Wavelengths of periodic perturbations with shorter and longer wavelength.
φ – Phase difference between the two periodic perturbations.

Present simulations are averaged over 16-member ensembles except when noted.

We first investigate the effects of various parameters including the amplitudes and the phase difference between the perturbations, and the noise level. The results are shown in Figure 7.2. The observations can be summarized as follows. Single mode initial conditions are characterized by an initially accelerated growth, followed by suppression and an eventual relaxation to the universal self-preservation state. In case of two-mode initial conditions, the features of the single-mode initial conditions are observed at early times ($t\Delta U/\Lambda < 2$) corresponding to the growth and roll-up of the shorter wavelength, however following the suppression there is an another cycle of enhancement and suppression (before an eventual relaxation to the universal Regime II). Figure 7.2A suggests that the balance between the suppression after the initial growth (due to the saturation of the shorter wave) and the accelerated growth immediately after (due to the growth of the longer wave) can be controlled by varying the relative amplitudes of the two waves.

It can be seen from Fig. 7.2 B that the enhancement beyond the initial suppression is most significant when the second mode has twice the wavelength of the first, and when the phase difference is such that the peaks and troughs of the sub-harmonic coincide with the roll-up location of the fundamental (Fig. 7.2C). This is consistent with the theoretical ideas of sub-harmonic resonance (Ho & Huang, 1982) and with the experimental observations (Husain & Hussain, 1995), and follows the analyses and explanations presented in Ch.6.

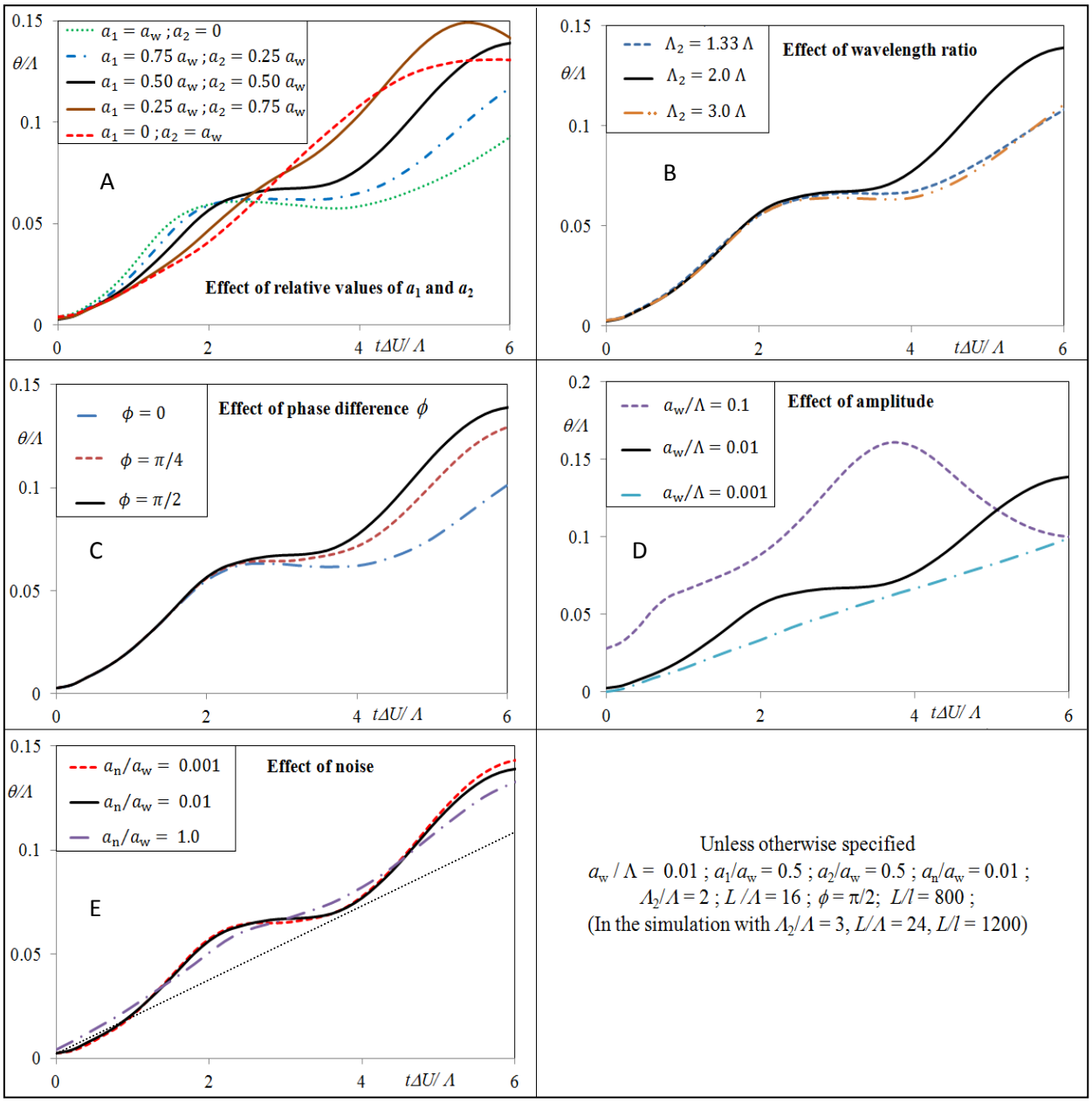

Figure 7.2. Influence of various parameters on the evolution of the layer

The effect of the periodic perturbations is higher at higher amplitudes (Fig. 7.2D, though the enhancement is not higher at all times, the maximum enhancement obtainable appears to be higher with higher amplitudes) and at lower values of noise (Fig. 7.2E), along expected lines. However, it is found that the effect is appreciable even when the amplitude is less than a percent of the wavelength and when noise is comparable to the signal. This suggests that relatively low intensity signals of the correct nature can be used to achieve substantial control of the spreading.

Having obtained a rough understanding of the influence of the various parameters on the evolution of the layer, we next conduct a sample study to determine the optimal initial condition to maximize enhancement of thickness for a given set of constraints. The thickness of a vortex-gas free shear layer with a two-mode initial condition can be written as

$$\theta = F[a_1, a_2, a_n, \Lambda, \Lambda_2, \phi, t\Delta U, L, l] \tag{7.1}$$

We shall fix $\Lambda_2/\Lambda = 2$ and $\phi = \pi/2$ as they provide the maximum enhancement. Since the signal to noise ratio is likely to be a constraint of the application, we conduct this study at a fixed value of a_n / a_w fixed at 0.5. Furthermore, as long as $\Lambda/l \gg 1 \gg \Lambda/L$, L and l are not relevant (in Regimes I and II we are interested in). Therefore Eq.7.1 can be written in dimensionless form as

$$\frac{\theta}{\theta_{\mathrm{uf}}} - 1 = F\left[\frac{a_1 - a_2}{a_1 + a_2}, \frac{\Lambda}{a_1 + a_2}, \frac{t\Delta U}{a_1 + a_2}; \frac{\Lambda_2}{\Lambda} = 2; \phi = \frac{\pi}{2}; \frac{a_n}{a_1 + a_2} = 0.5\right] \tag{7.2}$$

The left hand side is non-dimensionalized by the spreading of the unforced layer, θ_f ($= 0.0166\, t\Delta U$), as we are most interested in the relative enhancement or suppression. All other length scales are non-dimensionalized by $a_w = a_1+a_2$. It may be noted that Λ was used to non-dimensionalize length scales in Fig. 7.2. This was because, Λ is a mechanistically appropriate choice and roughly determines the time to reach and momentum thickness of the first plateau, observed to be of the order of $\Lambda/\Delta U$ and $0.06\ \Lambda$ respectively (for the range of other parameters considered here, see Fig. 7.2). The reason for using a_1+a_2 instead of Λ, in Eq.7.2 (and in Fig.7.3) is that it is more likely to represent physical constraint in a real-world flow control application, say by the use of a flapper. While changing wavelength of the perturbation requires changing the frequency of the flapper, which can presumably be done with hardly any limitation, there are going to be sterner limitations on increasing a_1+a_2 in any given setup, as it may require increase in flapper dimensions. Still, mechanistic parameterization is also useful because of possible universalities and hence we shall also analyze the same data scaled with Λ in Fig 7.4.

Figure 7.3 shows the contours of $(\theta/\theta_{\mathrm{uf}} - 1)$ in the $(a_1 - a_2)/(a_1 + a_2)$ - $\Lambda/(a_1 + a_2)$ plane for different values of $t\Delta U/(a_1 + a_2)$. For a given velocity ratio, the value of $t\Delta U/(a_1 + a_2)$ is related to the ratio of the length of the setup (more precisely, the x-location where the maximum enhancement is desired) to the sum of the amplitudes of the introduced perturbations. Therefore $t\Delta U/(a_1 + a_2)$ is constrained by the setup and actual requirements. Each snapshot in Fig.7.3 shows, for the given set of constraints, the effect obtained by changing $(a_1 - a_2)/(a_1 + a_2)$ and $\Lambda/(a_1 + a_2)$. The latter two are both the adjustable parameters for a given setup, as they determine the frequency content of the signal for a given sum of amplitudes. The first adjustable parameter, $(a_1 - a_2)/(a_1 + a_2)$ represents the relative amplitudes of the two modes, recovering the single-mode limits of subharmonic only at -1 and fundamental only at $+1$. The second adjustable parameter $\Lambda/(a_1 + a_2)$ determines the wavelength (and hence flapper frequency) of the fundamental and hence the subharmonic (as Λ_2/Λ = 2 by definition). The results shown in Fig.7.3 have been computed from a total of 399 cases: 21 values of $(a_1-a_2)/(a_1+a_2)$ and 19 values of $\Lambda_1/(a_1+a_2)$), each averaged over an ensemble of 32 realizations, resulting in a total of 12768 individual simulations.

It can be observed from Fig 7.3 that the maximum enhancement that can be obtained by varying the frequency content of the imposed forcing (for given sum of amplitudes) is inversely proportional to the ratio of the sum of amplitudes to the size of the setup. E.g., a maximum enhancement of 150% in θ over the unforced case can be obtained for $t\Delta U/a_{\mathrm{w}} = 75$, only 74% can be obtained for $t\Delta U/a_{\mathrm{w}} = 375$. This is consistent with the results shown in 7.2D, namely larger amplitudes provide higher enhancement capability. (Though the enhancement obtained at given Λ and $t\Delta U$ is not always higher for higher values of a_w, the maxima in the Λ/a_w - $(a_1-a_2)/a_w$ plane is always higher for higher values of $a_w/t\Delta U$).

The set of contour plots shown in Fig.7.3 can be readily translated and applied to obtain optimal perturbation for maximum enhancement in spatially developing shear layers. For example, consider the case where we wish to enhance the spread rate at 1 m downstream of the flapper in a 2 stream mixing layer with velocities 10 m/s and 4.55 m/s (note that $(U_1 - U_2)/(U_1 + U_2) = 0.37$, hence temporal results are useful to describing the spatial evolution, see Ch.5.3) under the constraint that the sum of the perturbation amplitudes (introduced by the flapper) is 2 mm. Appropriate space to time transformation (as described in Sec.5.2) leads to $t\Delta U/a_{\mathrm{w}} = (x/U_m)\Delta U/a_w = 375$. It can be seen from Fig. 7.3, for $t\Delta U/a_{\mathrm{w}} = 375$, the maximum enhancement of 74% over the unforced case can be obtained for $(a_1 - a_2)/(a_1 + a_2) = -0.6$ and $\Lambda/(a_1 + a_2) = 83.3$. This result on utilizing an appropriate Galilean transformation, provides the optimal flapper forcing as a combination of 0.4 mm amplitude at 43.6 Hz + 1.6 mm at 21.8 Hz (shown in Fig. 7.5A), which would result in an enhancement by 74 % (Fig. 7.5B). It is noteworthy that the maximal enhancement via single-mode forcing for the same case is only 47%.

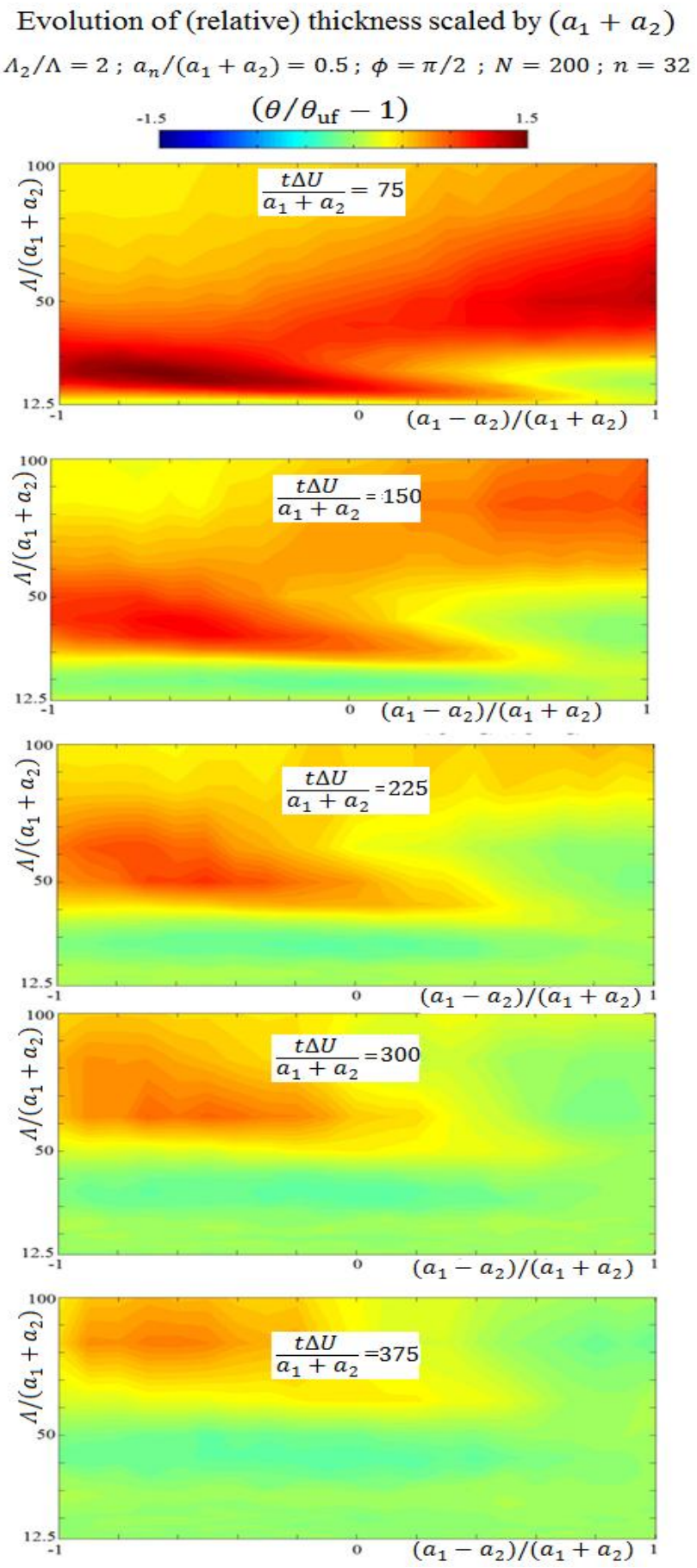

Figure 7.3. The evolution with time of thickness relative to unforced layer in the amplitude-wavelength plane.

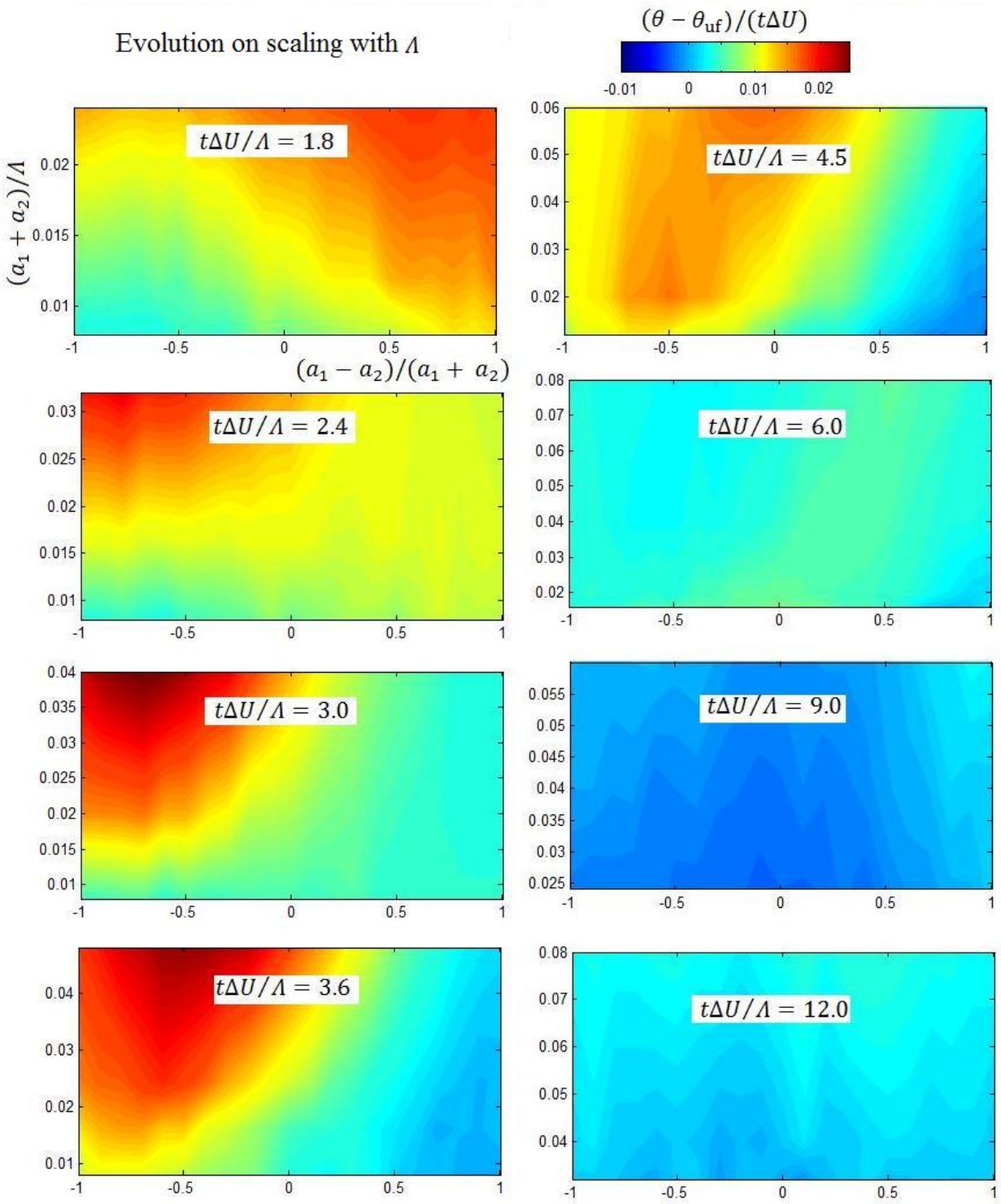

Figure 7.4. Data presented in Fig.7.3 on scaling Λ.

Figure 7.4 replots the same data using mechanistically more appropriate scales. Each snapshot plots the enhancement in momentum thickness scaled by $t\Delta U$, in the $[(a_1-a_2)/\Lambda, (a_1-a_2)/(a_1+a_2)]$ plane for a given value of $t\Delta U/\Lambda$. It can be seen that consistent with Fig. 7.2, the evolution is most economically characterized as a function of $t\Delta U/\Lambda$. The insight obtained from Fig.7.4 can be summarized as follows. For $t\Delta U/\Lambda < 2$ the best enhancement is obtained by forcing primarily around the fundamental, as this time duration corresponds to the growth and roll-up of the fundamental. But beyond this time, the optimal forcing for enhancement shifts towards the subharmonic. This is because the fundamental saturates and further evolution (via the Karman-Lamb mechanism described in Ch.6) depends on the

perturbation to the monopole location provided by the subharmonic. In fact, forcing with only the fundamental at these times would actually lead to a lower thickness than in the unforced case, as these times correspond to the region of suppression seen in the single mode initial conditions.

The maximum enhancement is obtained around $t\Delta U/\Lambda = 3.6$, and corresponds to the saturation of the subharmonic resulting from the merger of the structures at that scale. The second region of suppression follows. This is best seen at $t\Delta U/\Lambda = 9.0$, where the entire plane of forcing is dominated by suppression. At times of $t\Delta U/\Lambda \gtrsim 12$, the effects of forcing gradually disappear as the layer relaxes towards Regime II.

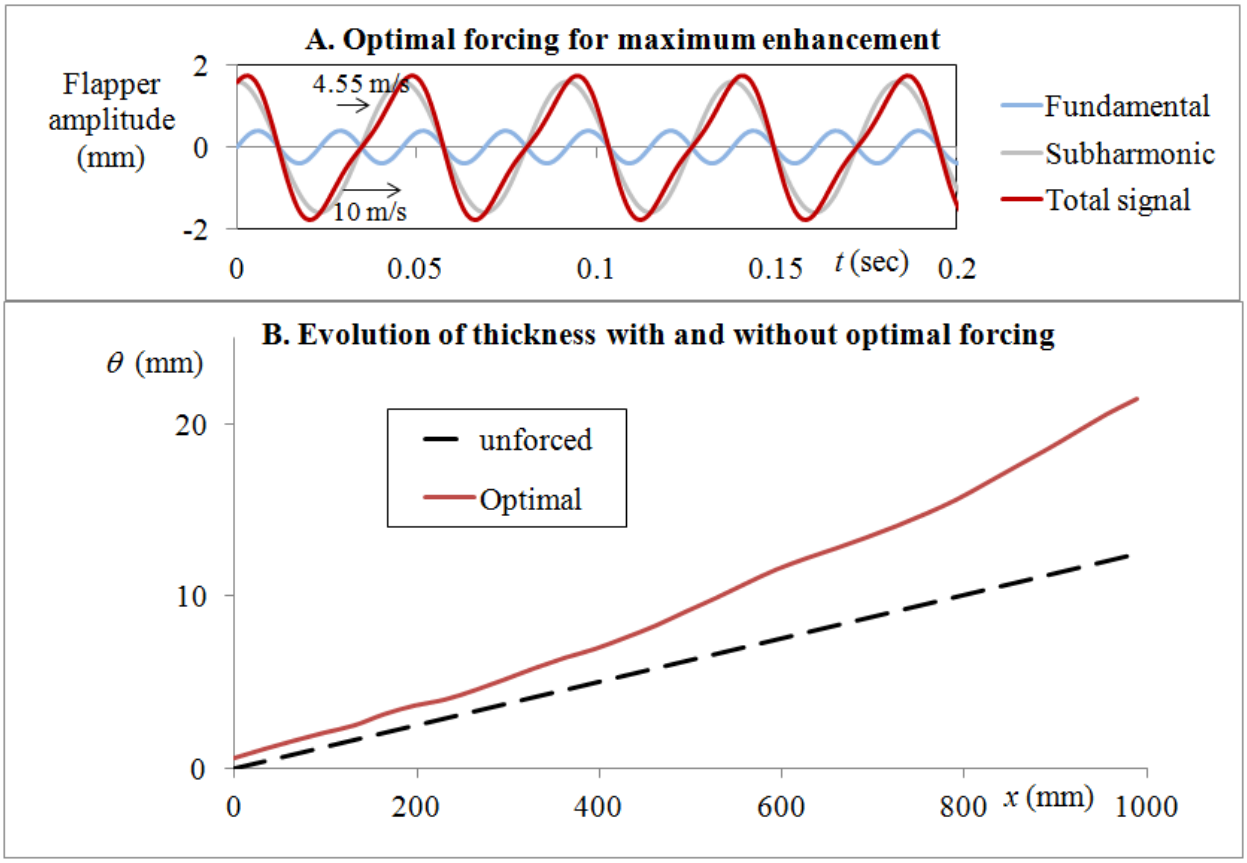

Figure 7.5. (A) Optimal forcing and **(B)** evolution in spatial variables (with appropriate Galilean transformation).

Turbulent flow control remains a semi-empirical science due to the limitations of existing stability theory, and the expensive nature of high fidelity options like DNS and incapability of RANS models in predicting the effects of periodic forcing. In this chapter, we have shown that the vortex gas provides an inexpensive and accurate alternative to study optimal control of free shear layers. While the present demonstration has involved only two-mode forcing, and did not implement any gradient or adjoint based optimization techniques, it should be a straightforward extension to implement such algorithms for multi-mode optimization. Furthermore, it is highly worthwhile to explore the usefulness of vortex-gas (or similar) calculations to aid in control of other turbulent shear flows.

Chapter 8 : Effect of viscosity

The vortex-gas free shear layer has been observed to have three distinct Regimes, among which Regime II is characterized by a universal spread rate (Ch.3). One of the limitations of the vortex-gas model is the total absence of viscous diffusion. As argued in Chapter 1, the effect of viscosity on the large scale evolution of the flow is expected to diminish as Reynolds number keeps increasing. Consistent with this argument is the agreement (Ch.5) observed between the vortex-gas free shear layer with experiments and DNS strongly suggesting that the vortex-gas is not irrelevant to describing the large scale evolution of high Reynolds number Navier-Stokes mixing layers. However, the role of viscosity at moderate Reynolds number is not entirely clear, and in this chapter we examine the same.

The effects of viscosity are simulated by adding a random walk component to the motion of individual vortices as proposed by Chorin (1973). This is based on splitting the advection and diffusion parts of the Navier-Stokes equation. Variants of this method have been used in to simulate viscous flows in engineering contexts (e.g. Ghoneim 1987, also see Cottet & Koumoutsakos, 2000).

Furthermore, since random walk causes dissipation of the Hamiltonian, it is not clear what effect this might have on the underlying statistical mechanics such as on the evolution of distribution functions and long time statistics. Further, the simulations reveal an unexpected interplay between the viscous and turbulent 'stresses' at intermediate Reynolds numbers, which is worth investigating. We shall explain the formulation and problem setup in Section 8.1 and discuss results on initial development & universality of Regime II, interplay between viscous and turbulent stresses, long time evolution and comparison to long time 2D NS solutions in Sections 8.2, 8.3, 8.4 and 8.5 respectively.

8.1. Problem setup for the viscous vortex-gas free shear layer

It is well known that for a set of particles undergoing a random-walk, the evolution of the probability distribution is a solution to the diffusion equation with diffusion coefficient α that is related to the standard deviation σ of the random displacement as $\alpha = \sigma^2/(2\Delta t)$, where Δt is the time-step. This is the basis of modeling the viscous diffusion of vorticity using random walk of point-vortices, first proposed by Chorin (1973). The 2D vorticity equation (derived from the 2D Navier-Stokes) is

$$\frac{\partial \omega}{\partial t} = \underbrace{-u\frac{\partial \omega}{\partial x} - v\frac{\partial \omega}{\partial y}}_{\text{Advection}} + \underbrace{\nu\left(\frac{\partial^2 \omega}{\partial x^2} + \frac{\partial^2 \omega}{\partial y^2}\right)}_{\text{Diffusion}} \tag{8.1}$$

A numerical time integration can be split into advection and diffusion steps. In a system with a large number of point vortices (that represent a continuous vorticity field), the diffusion part can be modeled by a random walk of point vortices. Note that the point-vortices themselves do not diffuse in this formulation, in which the distance moved by a vortex during a time-step is given by (Friedmann & Poloubarinova 1928, Chorin 1973)

$$\Delta x_i = \left(-\frac{\gamma}{2L}\sum_{j=1, j\neq i}^{N} \frac{\sinh\left(2\pi\left(y_i - y_j\right)/L\right)}{\cosh\left(2\pi\left(y_i - y_j\right)/L\right) - \cos\left(2\pi\left(x_i - x_j\right)/L\right)}\right)\Delta t + g_1\sqrt{2\nu\Delta t} \tag{8.2}$$

$$\Delta y_i = \left(\frac{\gamma}{2L}\sum_{j=1, j\neq i}^{N} \frac{sin\left(2\pi\left(x_i - x_j\right)/L\right)}{cosh\left(2\pi\left(y_i - y_j\right)/L\right) - cos\left(2\pi\left(x_i - x_j\right)/L\right)}\right)\Delta t + g_2\sqrt{2\nu\Delta t} \tag{8.3}$$

where g_1 and g_2 are Gaussian random variables with zero mean and unit variance. Detailed results on convergence of this method can be found in Cottet & Komousatakos (2000).

Alternatively, the effects of viscosity can also be introduced by changing the strength of the vortices (Cottet & Mac-Gallic, 1983, Raviart 1983). While such a method might have higher point-wise accuracy (see Cottet & Komousatakos, 2000), we adopt the simpler random walk method in this script to enable more direct connections to the results on vortex-gas free shear layer and statistical mechanics.

The setup is similar to that described in Ch.2. The simulations are initialized with N vortices distributed along the x-axis in a domain with period L and uniform inter-vortex spacing $l \equiv L/N$ and with y-displacements drawn from a uniform random distribution with amplitude a. The circulation of each vortex is $\gamma = L\Delta U/N$, so that the velocities at $y = \mp\infty$ are set to $\pm\Delta U/2$. The time integration of the advection part implemented by fourth order Runge-Kutta with time-step $\Delta t = 0.1l/\Delta U$, and at the end of each time-step, a random number drawn from a Gaussian distribution with the standard deviation that would provide the specified viscosity is added to the *x* and *y* location of each vortex. The mean-velocity and momentum thickness using the same expressions (Ch.2) used in the inviscid point-vortex case, i.e. the random-walk component is added only to the motion of each of the vortices.

8.2. Initial evolution and universality of Regime II

We simulate a number of cases, with initial vortex *y*-displacements chosen from uniform random distributions with different amplitudes, different number of vortices and different values of ν. As the thickness provides a bulk description of free shear layers and since one of the central results in the inviscid case is the universality in the evolution of thickness, we first analyze the evolution of momentum thickness with time for the different simulations.

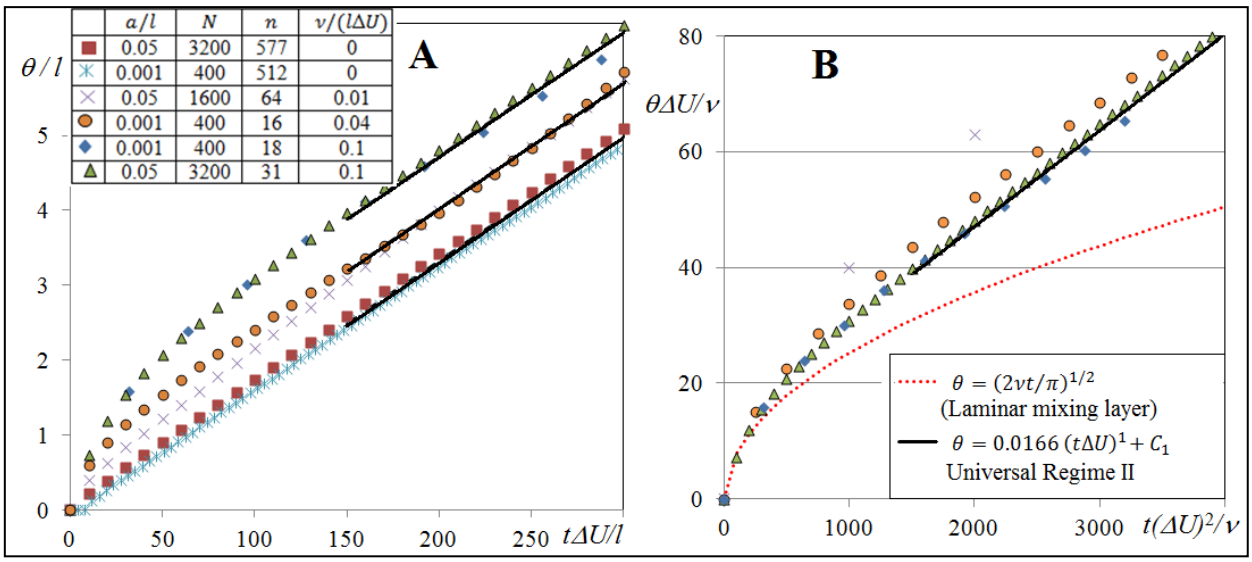

Figure 8.1. **(**A) The evolution of momentum thickness with time for different cases. (B) The same data plotted in scales non-dimensionalized with ν.

It can be seen from the results shown in Fig. 8.1 that the momentum thickness is initially given by $\sqrt{2\nu t/\pi}$, which is the laminar mixing layer solution. This suggests that the early evolution is dominated by diffusion. This laminar evolution is followed by a 'transition', beyond which the evolution of thickness departs from the $t^{1/2}$ scaling. The exact beginning and duration of the transition depends on initial conditions (both $a\Delta U/\nu$ and $l\Delta U/\nu$), for the cases considered here, the departure from the laminar evolution seems to take place around $\theta\Delta U/\nu \equiv Re_\theta \sim 20$ and the beginning of linear growth at about 40. Beyond this point, the layer appears to grow linearly with the same spread rate ($d\theta/d(t\Delta U) = 0.0166$) as in Regime II of the inviscid case (Ch.3) across the different initial conditions (*a*/*l* = 0.05 and 0.001),

values of $\nu/l\Delta U$ (0, 0.01, 0.04, 0.1) and N (400, 1600, 3200) considered here. For the case with $\nu/l\Delta U = 0.1$, $N = 3200$ the spread rate determined from the best fit of data from $t\Delta U/l = 150$ to 600 is 0.016658. This is within 0.25% of the value for inviscid case. This strongly suggests that universality in Regime II is independent of viscosity and (at least for the cases considered here) can be observed from a Reynolds number as low as 40, at which viscous effects are not expected to be negligible. We also note that for the same case, the change in the Hamiltonian is around 2% during the observed evolution (over 10^3 times larger than for the inviscid case over the same duration). From a statistical-mechanics point of view, this leads to an important implication that the universality in the non-equilibrium evolution is robust to small changes in the Hamiltonian.

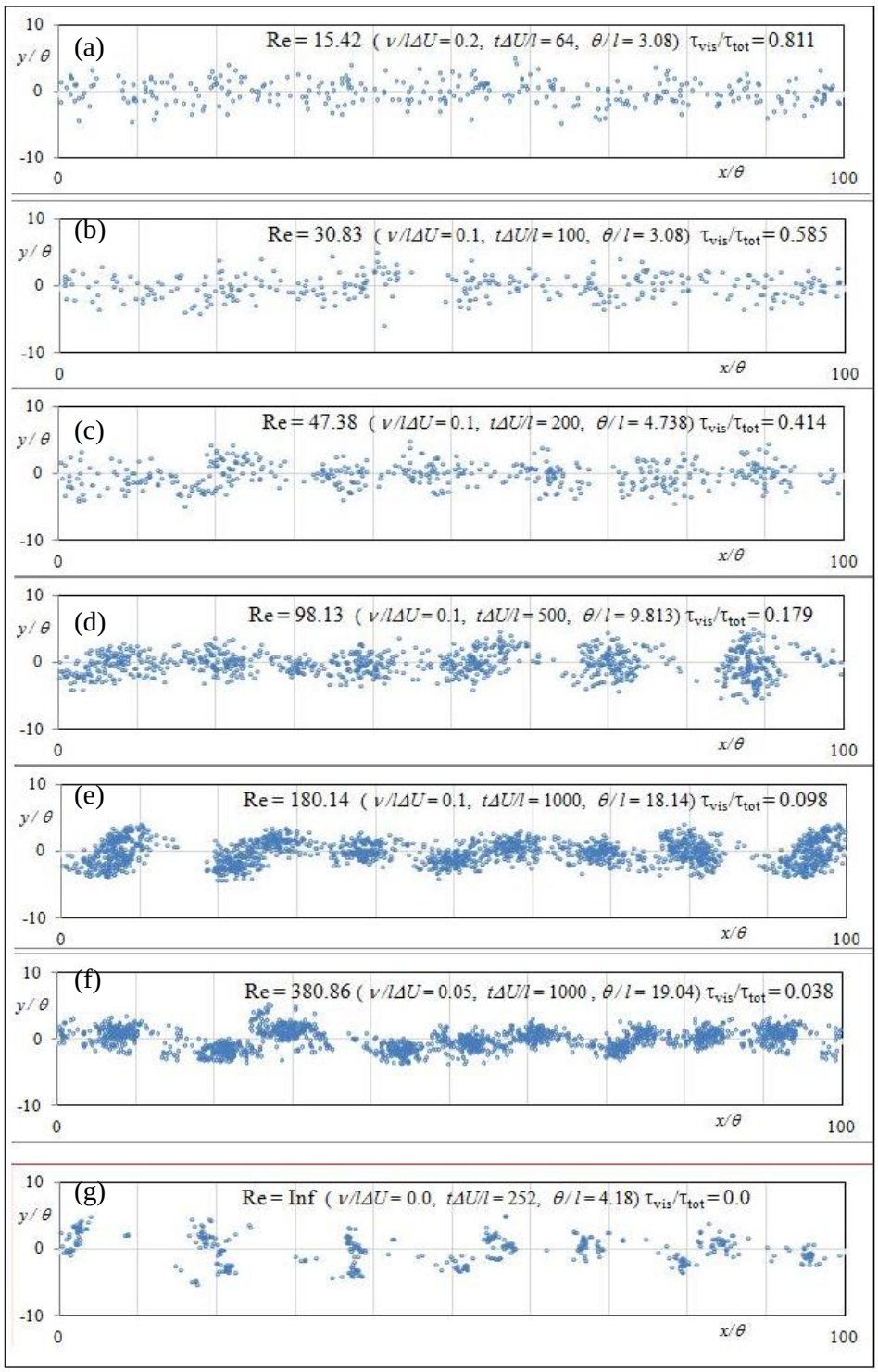

Figure 8.2. Snapshots of vortex locations (scaled by local thickness) at different Reynolds numbers.

The snapshots of evolution of the vortex locations are shown in Fig.8.2. It can be seen (from Fig. 8.2a) that there is almost no organization during the 'laminar' evolution (but there appears to be a wave-like disturbance). Coherent structures begin to appear in the form of weak clusters at around $Re_\theta \sim 30$ (Fig.8.2b), which approximately marks the onset of linear growth. The level of organization is observed to increase with Re_θ. However, even at the Reynolds number of 380.86 (Fig. 8.2f) shown in the snapshot, the coherent structures in the viscous case are relatively less well defined as compared to the inviscid case (Fig. 8.2g).

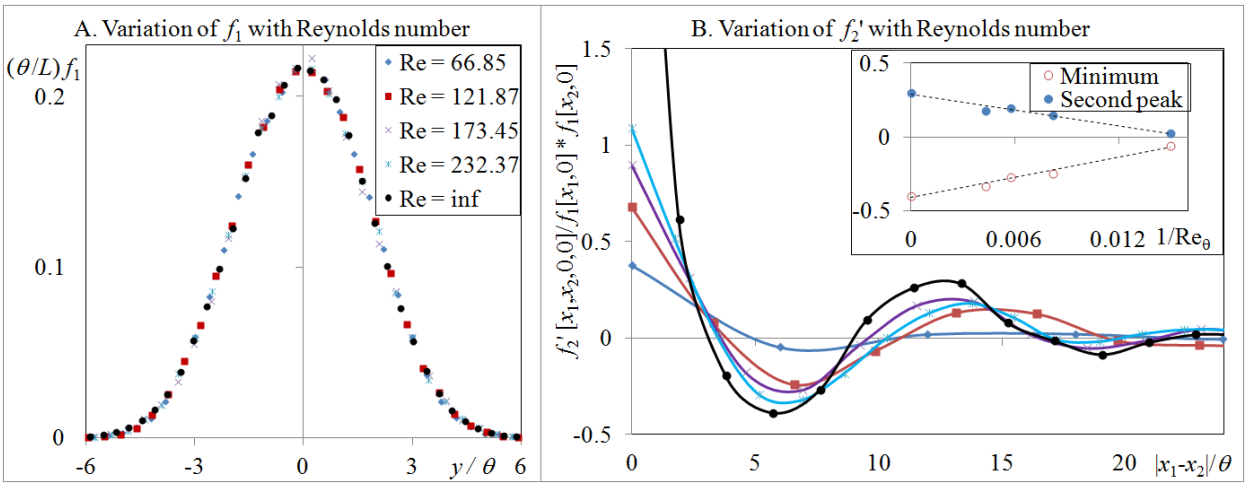

Figure 8.3. Effect of Re_θ on single and two particle distribution functions (N = 1600, a/l = 0.001, $\nu/l\Delta U$ = 0.1, n = 32)

We can quantify these observations by computing the distribution functions following the methodology described in Ch.4. It is found that the single particle distribution functions (Fig.8.3A), which contain information on the x-averaged vorticity distribution, show no noticeable difference with change in Re_θ between 66.85 and ∞. But it can be seen from Fig. 8.3B that the two-particle correlation function, which contains information on the coherent structures, is indeed different for different Reynolds numbers. While the overall shape of f_2' computed in the viscous case is similar to that in the inviscid case, the magnitude of the minimum or the second peak (shown in inset in Fig 8.3B) is lower by an order at Re_θ of 66.85. This implies that the average spacing of the coherent structures (scaled with the local thickness, roughly given by the location of the second peak in the correlation function) is not greatly affected by diffusion, although the structures themselves are more diffuse. If the coherent structures and their interaction are responsible for growth of the layer, it becomes important to understand how the viscous layer grows at the same universal rate even when the correlations are an order of magnitude lower (in early Regime II).

8.3. Internal balance between viscous and Reynolds stresses

To answer this question we next analyze the viscous and non-viscous contributions to the growth by computing the stresses in the present vortex-gas simulations, even though 'stress' is generally a continuum mechanics concept. But as it has been rigorously demonstrated that the inviscid vortex gas converges to a weak solution of the Euler equation (Marchioro & Pulvirenti, 1993, also see Ch.5) taken together with Chorin's theorem (1973), this justifies the computation of the terms in the Reynolds averaged Navier-Stokes (RANS) equation using the induced velocity field of the vortex gas.

For a homogenous-in-*x* system, the RANS evolution of the averaged *x*-velocity field is given by

$$\frac{\partial \overline{U}[y,t]}{\partial t} = -\frac{\partial \tau_{xy}}{\partial y}\,, \tau_{xy} = \tau_{\text{vis}} + \tau_{\text{turb}}$$

Where the viscous and turbulent Reynolds stresses are respectively given by

$$\tau_{\text{vis}} = -\nu\frac{\partial \overline{U}}{\partial y}\,, \qquad \tau_{\text{turb}} = \overline{u'v'} = \int_{-\infty}^{y} \overline{v'\omega'}\; dy = -(1/L)\sum_{y_i<y} v_i\gamma_i$$

(Note : If the maximum mean velocity gradient occurs at the centerline, as in the cases considered here, the centerline viscous stress is related to the vorticity thickness $\delta_\omega \equiv \Delta U/\max\left(\partial\overline{U}/\partial y\right)$ as $\tau_{\text{vis}}[y = 0] = \nu\Delta U/\delta_\omega$. For the inviscid case, it was found that $\delta_\omega/\theta \sim 4.6$ in Regime II (Ch.3). For the laminar mixing layer solution (error function profile), $\delta_\omega/\theta = 4.44$ (which is only 3% less than the Regime II value). Further, it can from Fig. 8.3A that the δ_ω/θ $(= 1/\max(f_1\theta/L))$ is within 2% of 4.6 for $66.85 < Re_\theta < \infty$. Hence, we evaluate centerline viscous stress as $\nu\Delta U/(4.6\theta)$ as this method leads to significantly less scatter, being based on an integral quantity. However the viscous stresses are directly evaluated in Fig. 8.4B and 8.4C)

Figure 8.4A shows the evolution of the centerline viscous and turbulent stresses for three different values of $\nu/l\Delta U$. All the three cases show the following broad features. Initially (i.e. upto $Re_\theta \sim 10$) viscous stresses dominate and can be several times the Reynolds stress. The Reynolds stresses are seen to initially increase with Re_θ but the viscous stresses decrease as expected. However, at the Reynolds number (~ 50) that corresponds to the transition (from the laminar $t^{1/2}$) to the turbulent t^1 growth (Regime II) with the same slope as in the inviscid case, the viscous stresses contribute to over a third of the total stress. It is important to note that the t^1 law is derived in turbulent shear flow literature based on dimensional grounds ('equilibrium self-preservation analysis') after assuming viscous stresses are negligible (Townsend 1956, also see Ch.5 for results specific to the temporal vortex-gas free shear layer).

Further, it can be observed that beyond $Re_\theta \sim 60$ (for $a/l = 0.001, N = 1600, 0.05 < \nu/l\Delta U < 0.2$) the value of the total centerline-stress is a constant and is equal (to within statistical fluctuations of $\pm 10\%$) to the Reynolds stress in inviscid simulations (0.0118 ± 0.0004) and Figure 8.4B shows that the Regime II is characterized by the similarity of total stress and not Reynolds stress. The above finding is in contrast to traditional view, which would is shown (in Figure 8.4A) to be valid only in the limit of high Reynolds numbers ($Re_\theta \gtrsim 10^3$), where the distinction between total and Reynolds stresses becomes increasingly irrelevant.

This finding is further validated by performing an initially viscous simulation in which viscosity is 'switched off' at $t\Delta U/l = 200$, shown in Fig. 8.5A. It can be observed that the new total stress which now contains only the Reynolds stress, relaxes to the earlier value of total stress much faster than in the case where viscosity is not switched off (Fig. 5A). Further, Fig 8.5B shows the evolution of an initially inviscid simulation (in which Regime II is reached at $t\Delta U/l \sim 30$) in which viscosity is suddenly turned on at $t\Delta U/l = 200$. It can be observed that the sudden addition of viscosity leads to a step-increase in the total stress (which is now equal to Reynolds + viscous stresses), but further evolution shows that the Reynolds stress decreases to allow for relaxation of the total stress to the universal Regime II value.

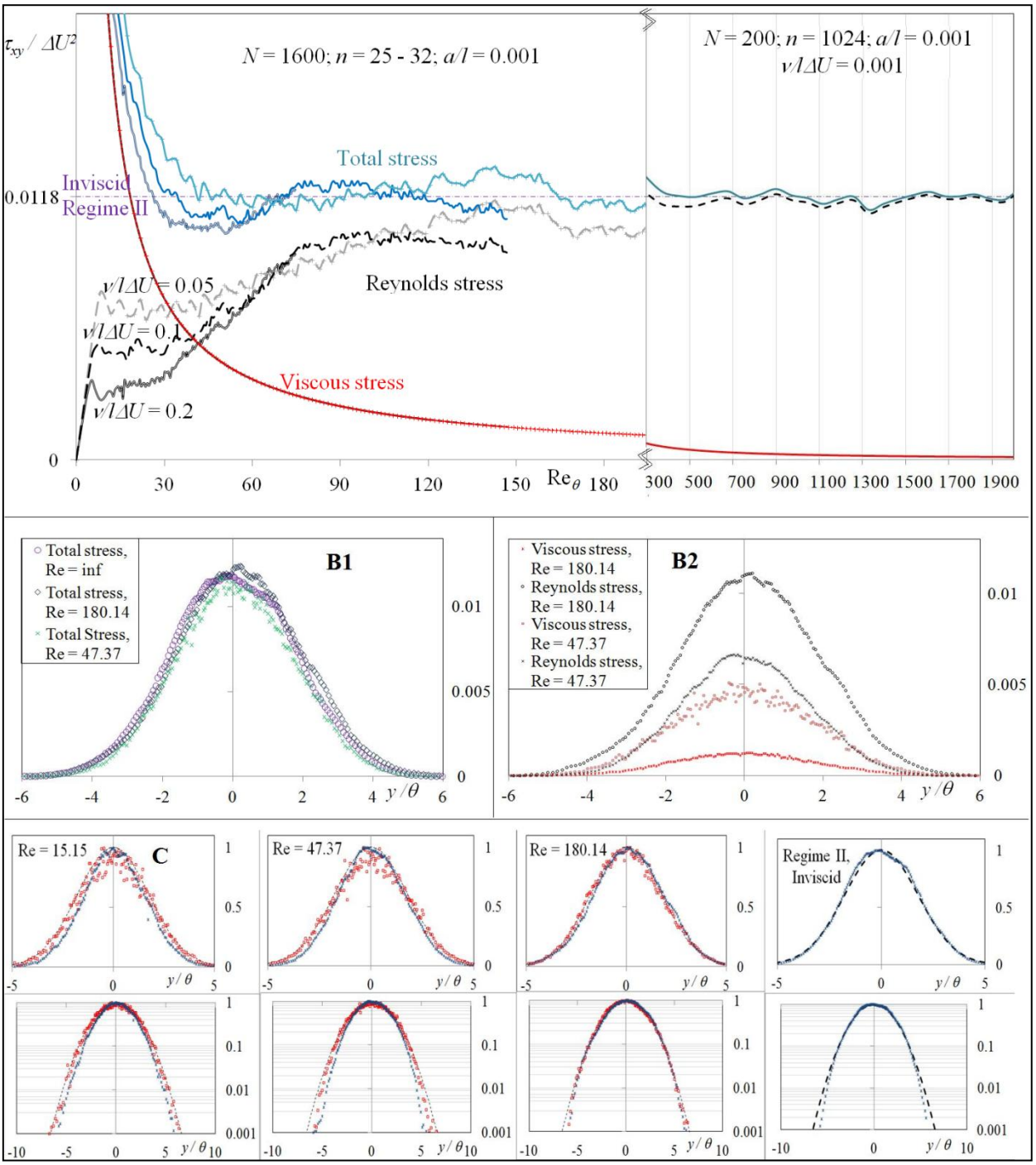

Figure 8.4A. Evolution of viscous and turbulent shear stresses. Note that the total stress reaches the inviscid Regime II value (and the layer grows with the universal constant spread rate) even when the viscous stress is over a third of the total stress. **B** Self-similarity of total stress (B1) though the contributions of the viscous and Reynolds stress are different (B2). **C.** Viscous (red squares) and Reynolds (blue crosses) stresses normalized by the respective maxima at different Reynolds numbers; bottom panel shows the same data in log-linear scale.

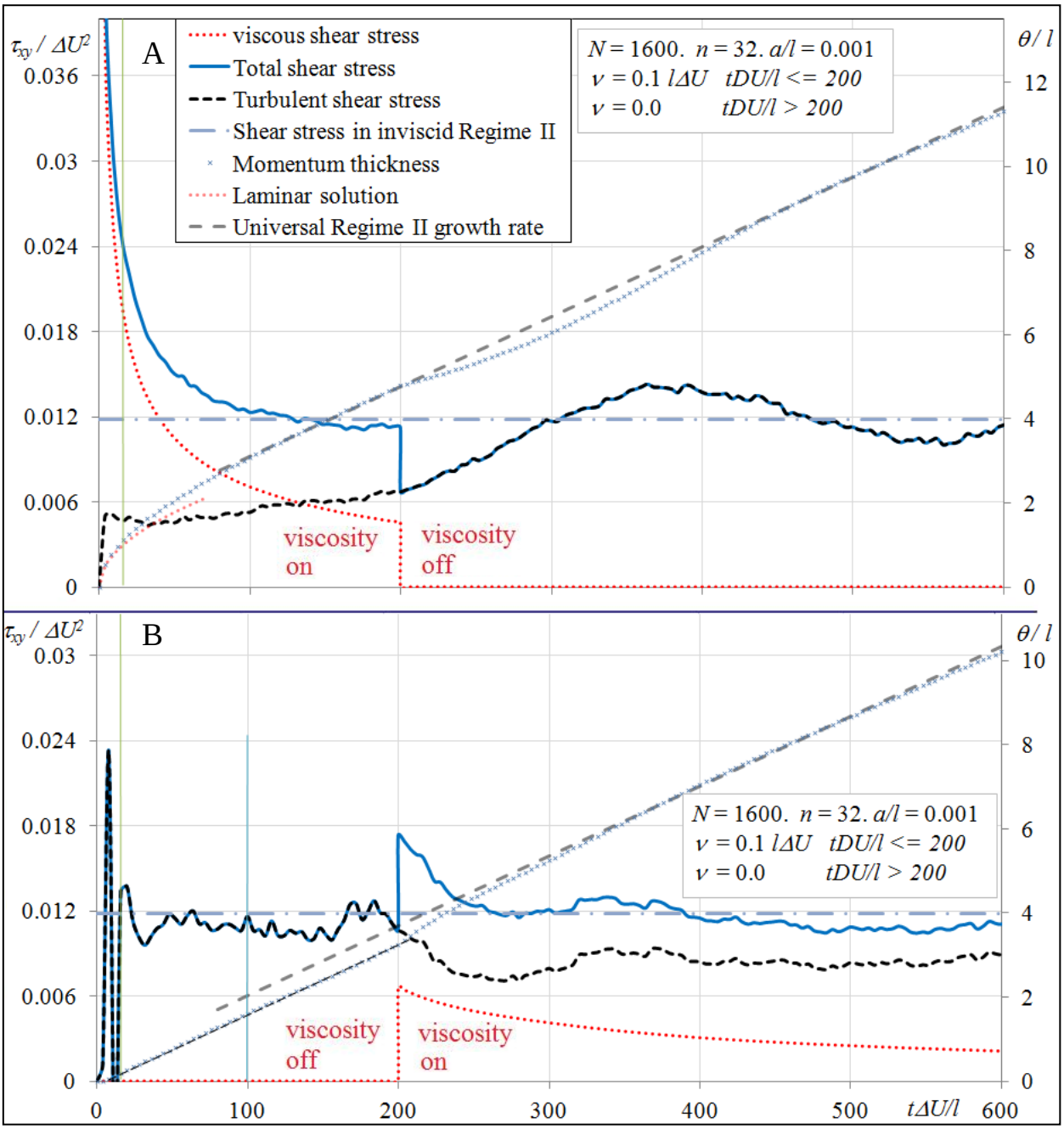

Figure 8.5. Evolution of viscous and turbulent shear stresses for cases for which viscosity is suddenly 'switched-off' (A) or switched on (B).

It might be argued that the present finding is a peculiarity of the vortex-gas model or the method by which diffusion is simulated, but as we shall shown in the following section (8.4) the present vortex-gas simulations with viscosity simulated by random-walk are indeed representative of 2D Navier-Stokes. A further argument could be that this observation is might be a feature of mixing layers where the viscous and turbulent stresses are similar in shape (except at the tails, see Figure 8.4C) and may not be applicable to other free shear flows. But 3D Navier-stokes simulations (DNS) of axi-symmetic (temporally evolving) wakes by Coleman et al (2012) also show a similarity of the total stress as against the similarity of Reynolds stresses, suggesting that the present findings may have a wider implication to free shear flows in general.

8.4. Subsequent evolution of viscous vortex-gas shear layers (Regime III)

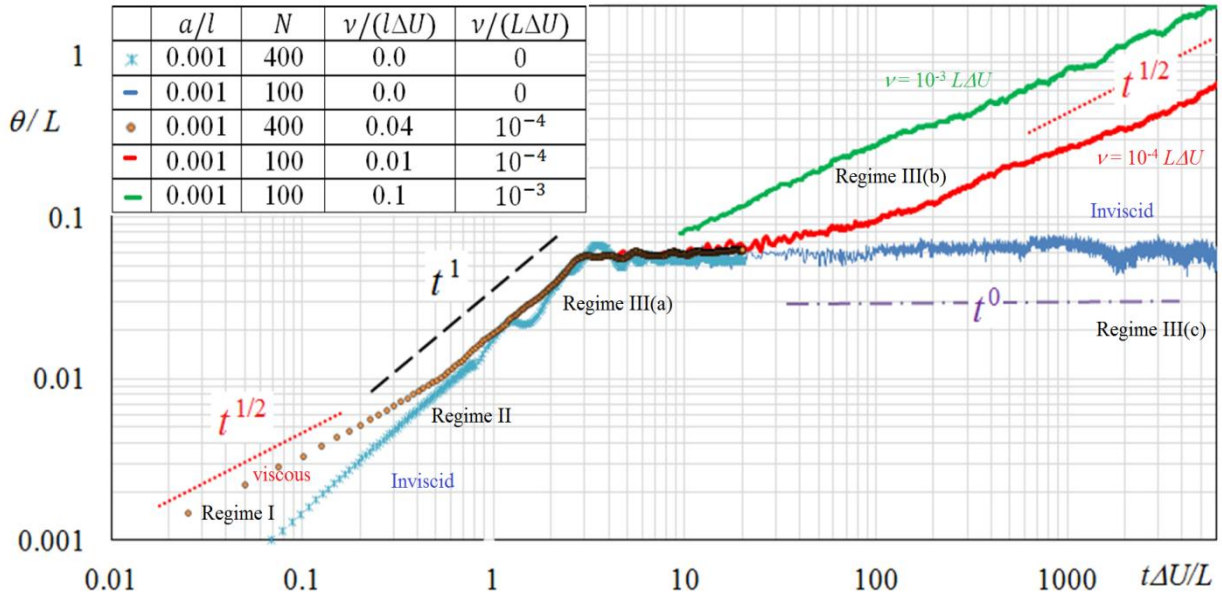

Figure 8.6. The different temporal regimes of evolution. (θ is taken as $\delta_{\mathrm{RMS}}/1.77$ for N = 100 simulations)

To understand the influence of viscosity over long time, we perform simulations with N = 400 and N = 100 over $t\Delta U/L$ of 10 and 10^4 respectively. The results on the evolution of thickness are shown in Fig. 8.6, from which the following observations can be made.

As described earlier, the viscous vortex-gas free shear layer initially grows as $t^{1/2}$ before 'transitioning' to Regime II, during which the layer thickness grows as t^1. Other than the reduction of fluctuations (for a given number of vortices and realizations), the early part of Regime III (III(a) as in Ch.4) immediately following Regime II is similar for the cases with and without viscosity. Namely, while the growth of the layer departs from the linear evolution of Regime II, it continues to grow rapidly till about $t\Delta U/L \sim 4$, flattening at $\theta/L \sim 0.06$. In the inviscid case, the spreading is greatly reduced beyond this point as there is a single structure left in each periodic domain and growth by amalgamation is no longer possible.

However, beyond this point, the thickness of the viscous vortex-gas continues to increase (at a significantly higher rate than in the inviscid case) due to viscous diffusion (scaling as $\theta/L \sim F[t\Delta U/L, \nu/(L\Delta U)]$) and the even the viscous layer with the lowest viscosity (highest initial Reynolds number) considered here ($\nu = 10^{-4}\, L\Delta U$) is about 15% thicker than the inviscid layer at $t\Delta U/L \sim 20$. At much longer times, the growth by diffusion dominates and the viscous shear layer grows as $t^{1/2}$ and the thickness is over 10 times that of the inviscid layer at $t\Delta U/L \sim 6 \times 10^3$. Hence the viscous layer does not have a final steady state. This is further seen in a series of vortex snapshots shown in Fig. 8.7

In the inviscid case (as shown in Ch.4), the single structure slowly relaxes towards a stationary distribution of vortices (relative to the core that moves stochastically in x and satisfies ergodicity) over timescales of $10^4\, L/\Delta U$. On the other hand, the continuously diffusing single viscous structure retains identity only to about $t\Delta U/L \sim 50$ (for the case shown in Fig.8.7), beyond which it 'melts' to have a nearly uniform-in-x and Gaussian (whose width increases as $\sqrt{t}$) in y distribution of vortices. Such a distribution is not a solution to the Boltzmann distribution (Joyce & Montgomery, 1976).

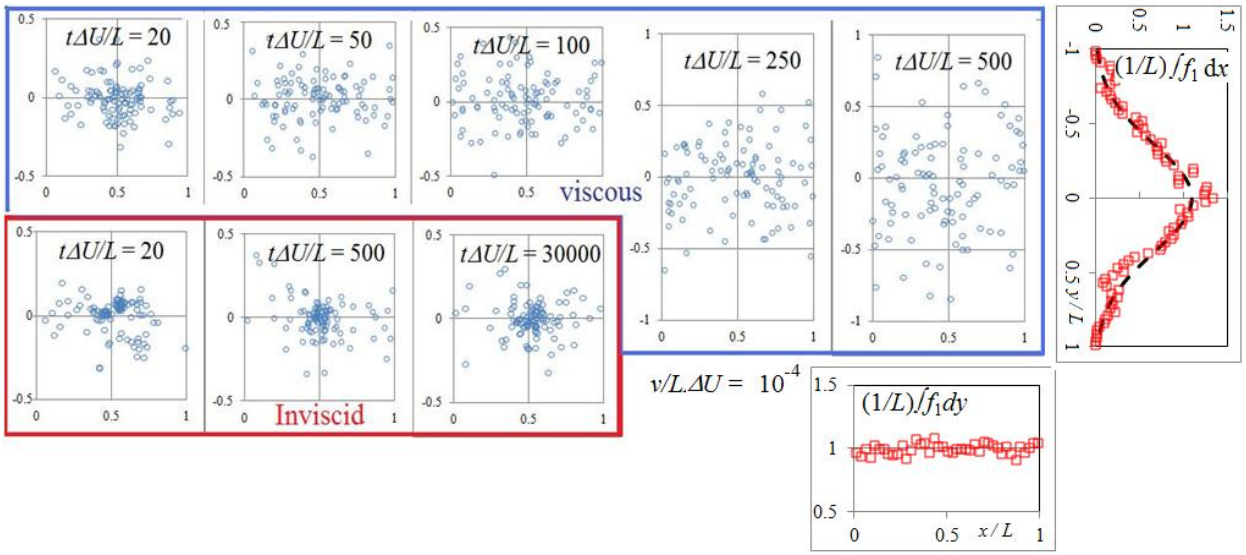

Figure 8.7. Comparison of long-time evolution of vortex locations for inviscid and viscous ($\nu = 10^{-4}\, L\Delta U$) vortex-gas shear layers ($a/l = 0.005 \;\; N = 100$).The vortex locations are translated in x such that the 'center' of the structure is approximately at 0.5 for clarity of presentation. Also shown are the single-vortex distribution function at $t\Delta U/L$ = 500 (averaged between 475 and 525, note that this is less than the timescale of the structure wandering across the domain in inviscid simulations, indicating the uniform-in-x distribution is a consequence of the melting of the structure rather than wandering).

A fit of the Lundgren – Pointin equilibrium distribution (1977) for the inviscid case (Sec.4.3) revealed high negative temperatures in all directions (though it was anisotropic). In the viscous case, a uniform distribution in x would lead to L-P temperature of $+\infty$ and Gaussian in y would imply zero temperature.

Connections to long time solutions of 2D NS

It was shown (in Sec.5.1) that the (inviscid) vortex-gas simulations (with appropriate initial conditions and sufficiently high N) tend to approach Euler equilibrium during the 'violent' relaxation of the single structure. The solutions from the early Regime III(b) also compared favorably with the corresponding results from the higher Reynolds number case of 2D Navier-Stokes simulations of Sommeria et al (1990), both in terms of layer thickness and vorticity-stream-function plot.

Here we compare the results from the lowest Reynolds number case with vortex-gas simulations with random walk to provide the same viscosity and with the same initial thickness. Figure 8.8A shows the evolution of thickness for the 2D NS and viscous vortex-gas calculations. The momentum thickness is observed to be slightly higher (by about 4%) for the vortex-gas case. However on adjusting for the virtual origin (due to the long wave sinusoidal perturbations used in 2D NS not in the present vortex-gas simulations) the long-time evolution is nearly identical. Figure 7B shows that the ψ-ω plots (after adjustment of the virtual origin) show good agreement with the 2D NS. This can be considered as a validation of the viscous vortex-gas method (with the present numerical scheme and N) to accurately describe viscous (2D) Navier-Stokes shear layers and hence the relevance of the present conclusions for the same.

8. 5. Concluding Remarks on viscous vortex-gas shear layers

Extension of the temporal vortex-gas shear layer via addition of a random walk to the motion of the vortices has yielded some interesting results, some of which are relevant to understanding the dynamics of turbulent free-shear flows at relatively low Reynolds numbers. The agreement with the laminar mixing layer solution at early times and with the stream function vorticity relationship of long time simulations of 2D NS, establish the validity of the random-walk method to studying viscous shear layers.

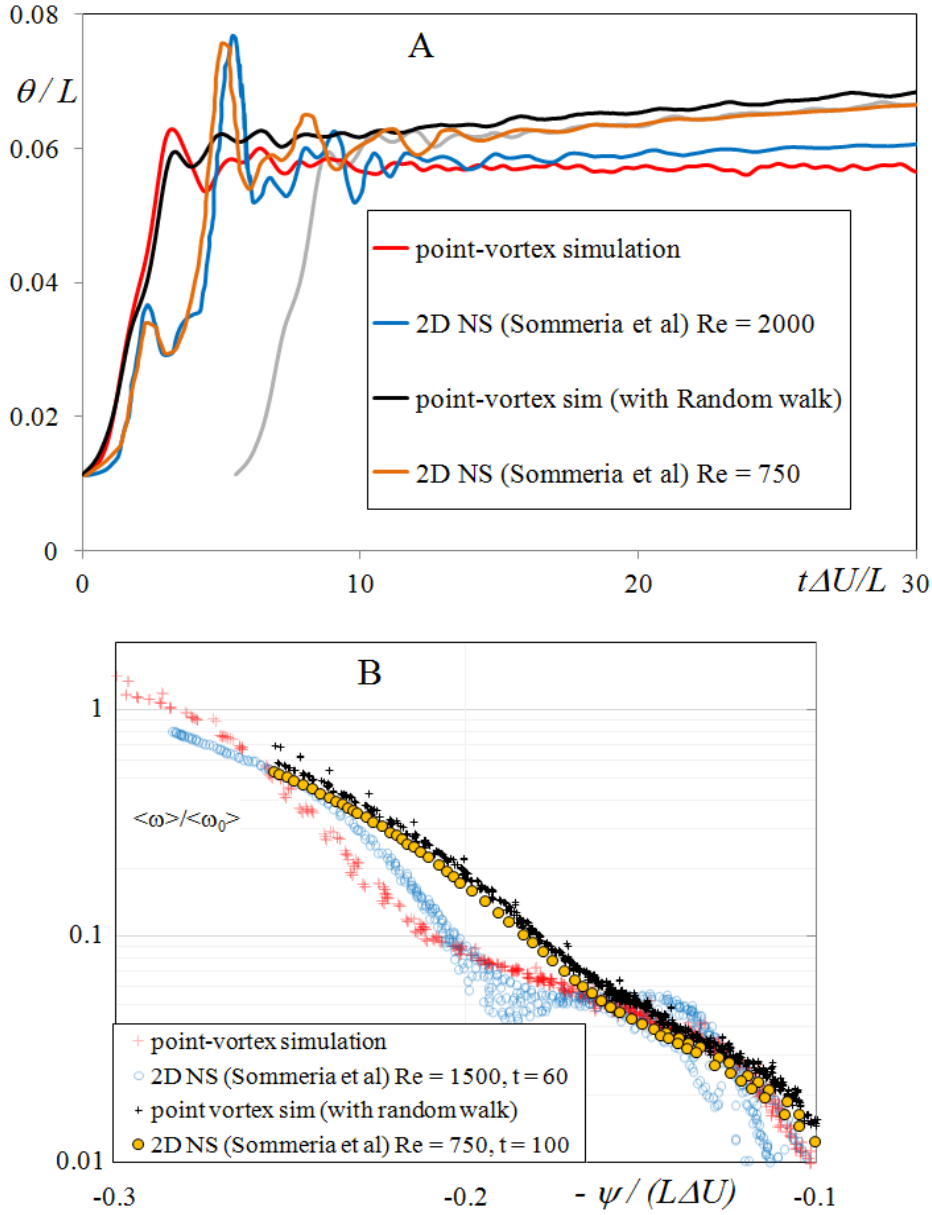

Figure.8.8 **(A)** Comparison of temporal evolution of layer thickness (shown in light grey is the viscous simulation displaced in time). **(B)** with the (short-time averaged) ψ-ω relation, of the inviscid and viscous vortex-gas simulations with low and high Reynolds number 2D Navier-Stokes calculations of Sommeria et al (1990)

Once again, the central results deal with the intermediate non-equilibrium Regime II. The viscous vortex-gas simulations show that, the slope of the linear growth in this Regime is not only universal, but also identical to that of the inviscid simulations. This is noteworthy considering that both the early-time as well as long-time regimes are different for the viscous and inviscid cases. Furthermore, in the viscous vortex-gas simulations there exists a sub-regime within Regime II, corresponding to $Re_\theta \sim 50 - 200$ where the viscous effects are not negligible and the viscous contribution to growth is 10 – 40 %. In this sub-regime, the spread rate is the same as the inviscid case, even though the coherent structures are less distinct and the two vortex correlation functions are significantly weaker. Further probing of the stresses reveals that this Regime is characterized by the similarity of the total stress rather than turbulent stress. This is consistent with observations made in recent 3D DNS studies of an axi-symmetric wake (Redford et al, 2012).

Chapter 9 : Effect of spatial feedback

As argued in Ch.1, when the velocity difference $\Delta U = U_1 - U_2$ is small compared to the average velocity $U_m = ½ (U_1 + U_2)$ (the ratio $(U_1 - U_2)/ (U_1 + U_2)$ is denoted by λ), it is possible to relate the spatially evolving to the temporally evolving shear layer via a Galilean transformation. This was also supported by the results presented in Sections 5.2 and 5.3. In particular, it was observed (Fig. 5.5) that the universal spread rate (on Galilean transformation) was within the scatter of reported self-preservation spread rates in experiments with $\lambda \lesssim 0.5$.

However, Fig. 5.5 also shows that spread rate quoted by experiments with $\lambda \gtrsim 0.5$ deviate from the Galilean-transformed temporal vortex-gas result, and this is particularly true for the single-stream shear layers ($\lambda = 1$). It is important to note that the scatter in the spread rates quoted across experiments is largest for single stream shear layers. This not only suggests that the temporal result is not valid in this limit but also raises the question whether the conclusion drawn on universality from the temporal simulations applies in this limit. Further, even if the spread rate is a universal function of the velocity ratio, its functional dependence on velocity ratio and the role of spatial feedback are not clear due to the scatter in the experimental data. The above questions cannot be tackled by temporal simulations.

Therefore, in order to derive some insight on the above issues, we revisit the vortex-gas analog of the spatially evolving shear layer. While there have been several early spatial vortex-gas simulations (e.g. Ashurst 1979, Inoue 1985, Inoue & Leonard 1987, Ghoniem & Ng 1987), the simulations of Basu, Narasimha & Prabhu (1995) were the first to rigorously handle the upstream and downstream boundaries. The present simulations are based on the method of Basu et al (1995), but with a crucial improvement that ensures global conservation of the circulation by adding a downstream buffer-vortex, whose strength is adjusted at each time-step in the simulation.

Another issue we shall discuss in this chapter is the interpretation of the recent experimental work of D'ovidio & Coats (2013). Two different mechanisms by which structures in the shear layer increase in size were observed in different experiments. In one set of experiments, mergers were largely responsible for the growth in size of structures. This was confirmed by studying the evolution of size of individual structures with time/downstream distance, which showed constant size between mergers and step changes in size coinciding with merger events. In the second set of experiments, the structures grew approximately linearly with downstream distance, even between mergers, and mergers did not make a significant difference. The first set of experiments were pre-mixing transition shear layers and second set corresponded to post-mixing transition shear layers, based on which the observed change in mechanism was attributed to mixing-transition and three dimensionality by the authors. However, the comparison involved different velocity ratios and since the effect of velocity ratio of shear layer growth and evolution is yet to be understood, it cannot be ruled out as a contributing factor. The present spatial vortex-gas simulations, though are strictly 2D, may provide some insight in this regard, and we shall present an analysis of the influence of velocity ratio on structure growth dynamics.

We first describe the setup used in the present simulations in Section 9.1 and then discuss the results on growth rate in Section 9.2 followed by detailed analysis of dynamics of structures at different velocity ratios presented in Section 9.3. Some supplementary information is presented in Appendix D.

9.1. Present computational setup

The present setup, shown in Figure 9.1, is broadly based on Basu et al (1992,1995). The numerical method used in the present work is similar to the temporal case (Ch.2), namely double precision

calculations with fourth order Runge Kutta for time integration, with the time-step $\Delta t = 0.1l/U_m$, similar to the Δt that ensured conservation of Hamiltonian to 10^{-5} in the temporal simulations.

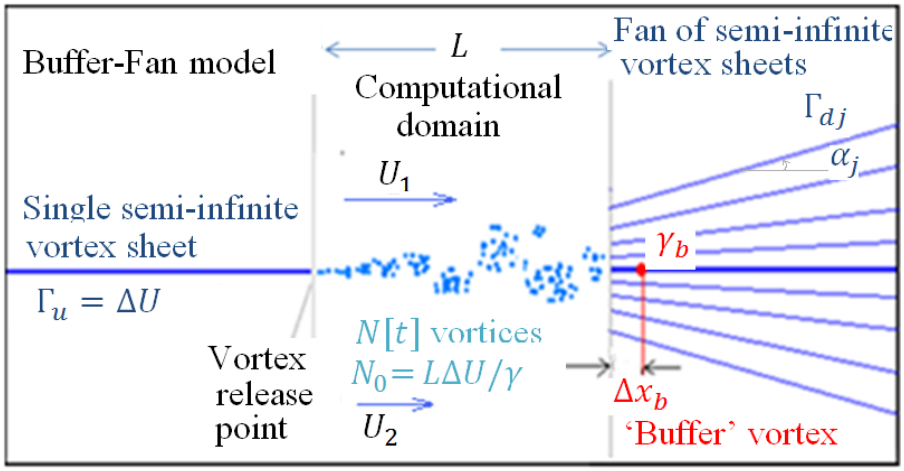

Figure 9.1. The present buffer-fan model for spatially evolving vortex-gas shear layer used throughout this work, unless specified otherwise.

There are two major differences between the earlier temporal simulations and the present spatial simulations. The first is that, in addition to the induced velocity due to other vortices, we also include a uniform x-velocity of U_m to ensure the x-velocity boundary conditions at $y = \pm\infty$ and the contributions due to other elements in the flow in the present spatial setup (Fig.9.1) namely a semi-infinite vortex-sheet upstream, a fan of semi-infinite vortex sheets downstream (the infinite contributions cancel, see Basu et al, 1992) and a buffer vortex (which will be described below). The second difference is that while the temporal simulations tracked a fixed number of vortices in a singly periodic domain, vortices enter and leave the computational domain in the spatial case. Constant strength (γ) vortices are released at $x = 0$, $y = y_i$ (y_i drawn from a uniform random distribution) once every t_r, such that ½ $(U_1 + U_2)$ $t_r \Delta U = \gamma$. Note that $l \equiv L/N_0$ is the inter-vortex spacing at $x = 0$, and the initial number of vortices is $N_0 = L\Delta U/\gamma$. After every time-step of integration, vortices with $x > L$ are 'removed' from the computations. Therefore the number of vortices in the domain can fluctuate with time, $N = N[t]$. Hence total circulation of vortices in the domain is not conserved at each instant, unlike in the temporal case.

The strength of the upstream vortex-sheet is given by $\Gamma_u = \Delta U$. The strengths $\{\Gamma_{dj}\}$ and angle made with the x-axis $\{\alpha_j\}$ of the downstream vortex sheets are chosen to approximate a symmetric, linearly spreading Gaussian vorticity profile, with the standard deviation at $x = L$ and rate of spread computed from the upstream solution between $x/L = 0.2$ and 0.5. We use 13 vortex sheets in the simulations reported in this work (though it will be shown that the solution till $x < 0.7\,L$ is not significantly affected even if a single downstream vortex sheet is used, see Fig.A1 in Appendix). It is also ensured that $\Sigma\Gamma_{dj} \cos\alpha_j = \Delta U$. In this formulation, the $\cos\alpha_j$ factor and the symmetry about the x-axis are required to cancel the infinite contributions to the vertical and horizontal velocity components respectively. The simulations reported here are started with a single downstream vortex sheet, and the fan is spread at $tU_m/L = 20$, based on the upstream solution averaged between $tU_m/L = 10$ to 20. Beyond this point, the angle of the downstream vortex sheets is dynamically varied using the instantaneously computed cumulative upstream solution.

Though the above characteristics are similar in spirit to those adopted in Basu et al (1995), the present setup differs in two ways, namely the lack of a doublet sheet on the splitter plate and the introduction of a 'buffer vortex'. The reasons and justifications for the same are as follows. A doublet

sheet at the splitter plate is necessary to ensure the physically realistic zero normal velocity on the plate. However, preliminary simulations with discrete doublet sheets revealed that it did not make any significant difference on the self-preservation spread rate (see Fig.D2). We also considered releasing vortices at a rate based on the instantaneous induced velocity at the tip of the plate, but the effect of such an implementation was also found to be negligible on the evolution of the layer beyond $x = 100\ l$ (Fig. D3). Hence the more complex realistic conditions at the splitter plate are not adopted in the present work as they do not justify the higher computational cost and complexity arising due to additional parameters.

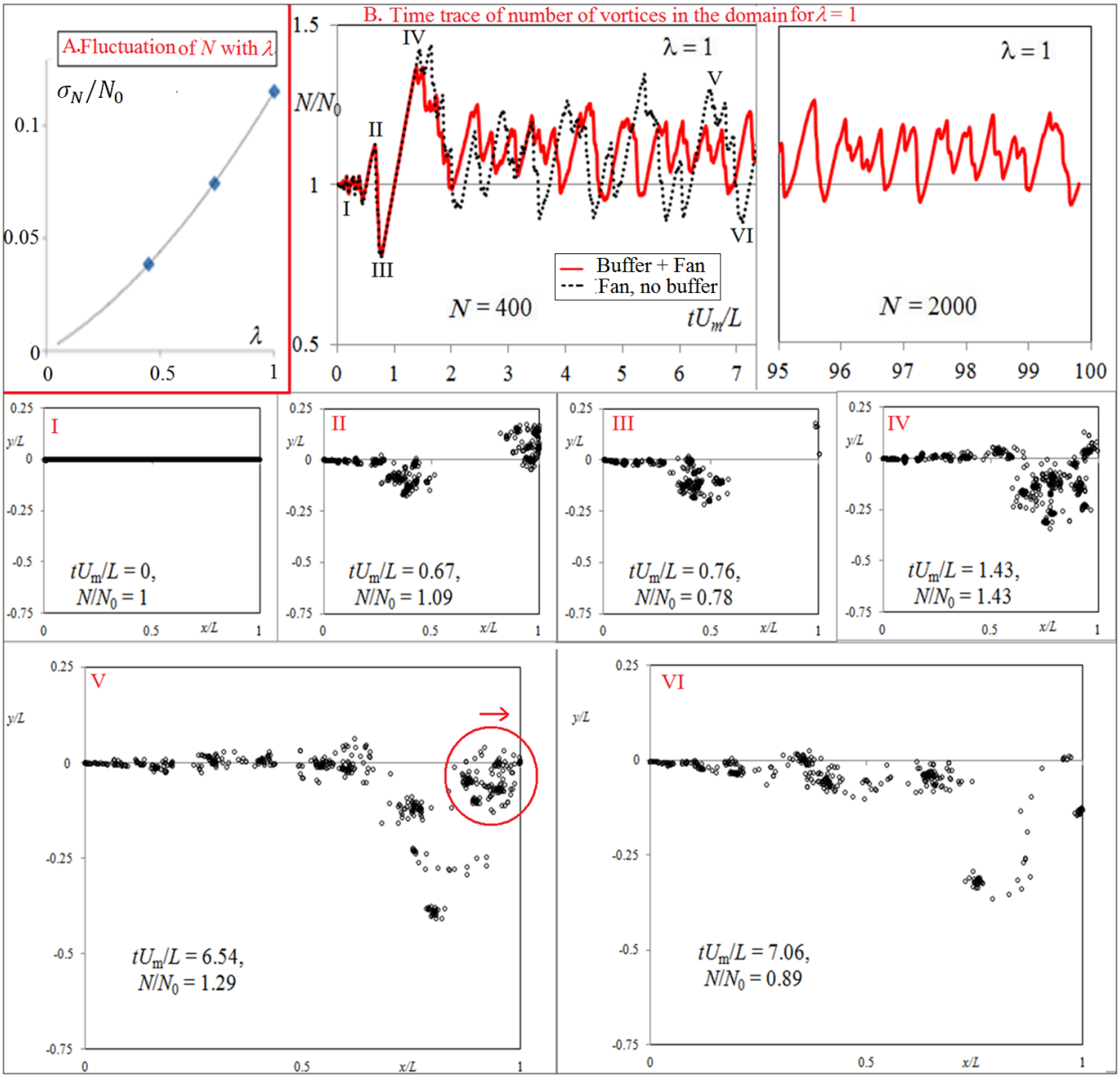

Figure 9.2 (A) RMS fluctuation of the number of vortices in the domain as a function of velocity ratio (for $N = 400$, no buffer). **(B)** Time trace of the fluctuation of number of vortices for $\lambda = 1$ with snapshots of the vortex-locations at times I to VI (shown below). For initial condition (I) in the present formulation, there is an initial transient (II – IV) that leads to a non-zero excess due to accumulation of vortices towards the end of the domain. The fluctuations continue to persist in the steady state (V, VI). The local maxima (V) appear to correspond to times just before a structure leaves the domain (as indicated in V); and the local minimum occurs (VI) immediately after such a structure has left the domain. The qualitative picture remains the same on the introduction of the buffer-vortex.

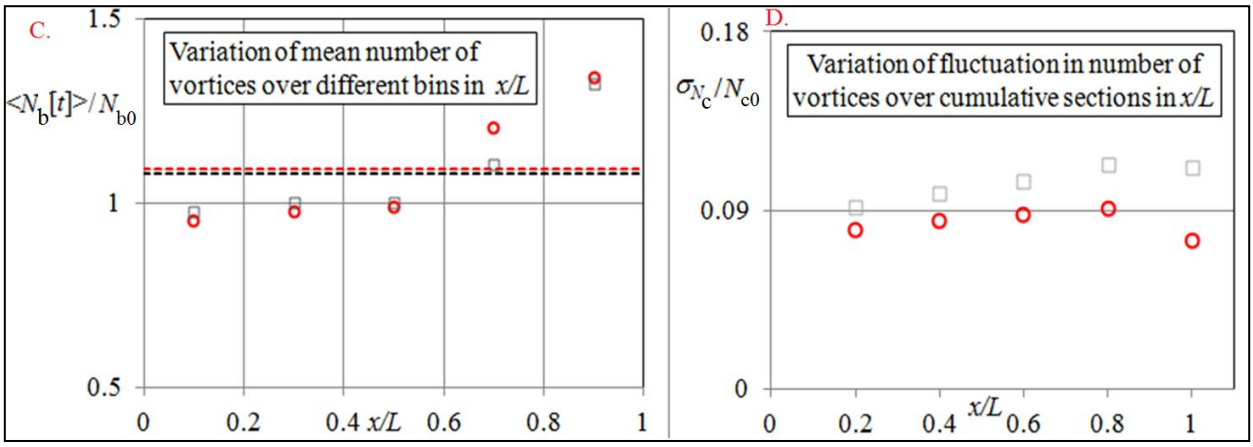

Figure 9.2 (contd.) **(C)** The distribution of average number of vortices across bins of width 0.2 L for N = 2000 (red circles indicate buffer-fan results, grey squares simulations without buffer and the dashed lines the respective means over the entire domain). Note that for $x/L \lesssim 0.6$ there is hardly any excess over the initial value (N_b refers to the number in each bin, with initial value N_{b0} = 0.2 N_0). **(D)** Standard deviation of fluctuation of number of vortices in the region between 0 and x (σ_{Nc}) as a function of x, normalized by the initial number of vortices in the corresponding region ($N_{c0} = x / L\ N_0$)

Figure 9.2A shows the RMS fluctuation in the number of vortices in the domain (in simulations without the buffer vortex) as a fraction of the initial number for different velocity ratios. It can be seen that the RMS fluctuation increases with λ (can be over 10% for λ = 1) but as a fraction of the total number of vortices, is independent of N. To understand the origin of these fluctuations, we examine the time evolution of the number of vortices in the domain for λ = 1, shown in Fig. 9.2B with insets showing the snapshot of vortex locations at the corresponding times. It can be seen that there is a net accumulation of vortices during the initial transient, beyond which the number of vortices fluctuates with time around a stationary mean (which is about 10% higher than the initial number of vortices). As seen in Fig. 9.2C, the excess in the mean is concentrated towards the edge of the domain, whereas the fluctuations are approximately self-similar across the domain (Fig. 9.2D). Most significantly, the fluctuations are present even after the layer reaches a statistically steady state, and having constant (at steady state) strength vortex-sheets as downstream boundary conditions leads to an instantaneous fluctuation of the total circulation of the system, in time.

It is important to note that while the flux of vorticity into the domain is a constant (as vortices are released at a constant rate at the edge of the splitter plate), the vortices in the domain form clusters (Fig 9.2B), with vortex-rich 'coherent structures' and vortex-depleted 'braid regions' between the structures. As observed from the vortex snapshots (Fig.9.2B), this clustering is responsible for the fluctuation in the instantaneous flux of vortices leaving in the domain. Further, the fluctuations occur in the timescale 0.5 L/U_m (~ 3 δ_ω [$x = L$]/U_m) for λ = 1, which roughly corresponds to the average period between passage of structures at $x = L$ (also supported by data at other λ not shown here).

Regardless of the physical nature of the fluctuations, it is reasonable to introduce a fluctuation in circulation opposite in sign to the fluctuation of circulation in the domain in order to instantaneously preserve the total (global) circulation (in the infinite domain at steady state) in accordance with Kelvin's theorem. Also, since the fluctuation of vorticity in the domain should arise from the fluctuation of the vorticity out flux downstream at $x = L$ (as the vorticity flux from upstream is a constant), it is reasonable to introduce the opposite-sign fluctuation immediately downstream of the domain. A first-order approximation to vorticity conservation would be to introduce this via a single stationary 'buffer vortex', say at $(L + \Delta x_b, 0)$, with a circulation fluctuating with time as $\gamma_b[t] = -(N[t] - N_0)\gamma$.

A physical argument for the introduction of the buffer vortex is as follows. The number of vortices in the domain dips from the mean when a structure leaves the domain (e.g. see snapshots V and VI in Fig.9.2B). In reality the structure, and hence an associated vorticity excess, would then appear just downstream of the domain. Similarly the maximum excess of the vortices in the domain occurs when a vortex-depleted braid region is convected out of the domain (just preceding the exit of a structure from the domain), and one would then expect a corresponding deficit immediately downstream. This excess/deficit of vorticity downstream during the deficit/excess of vortices in the domain is compensated for as a buffer vortex.

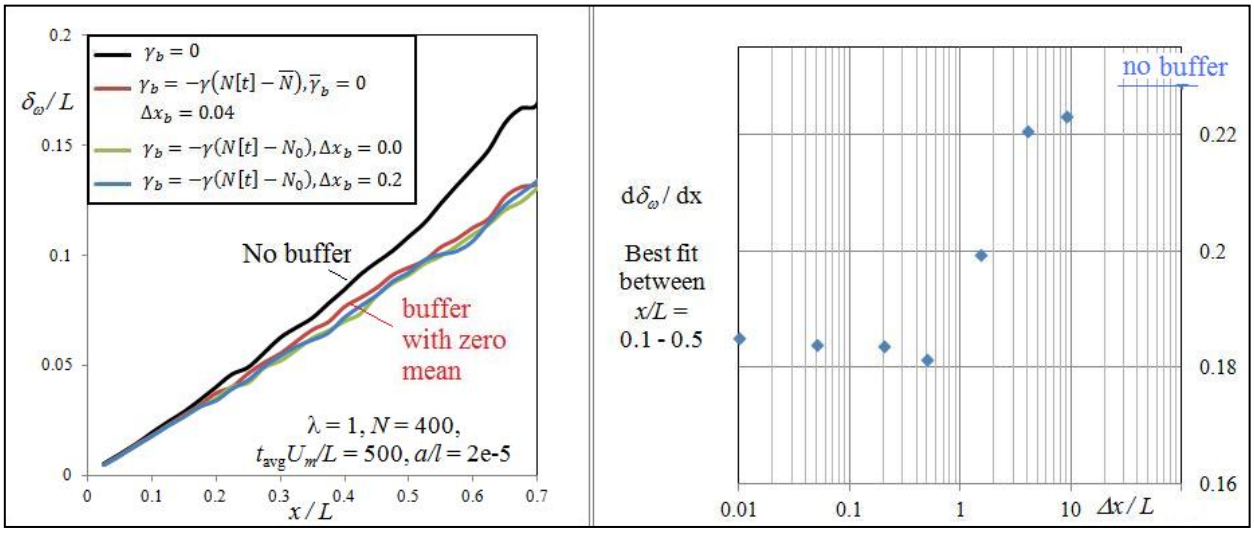

Figure 9.3. (A) Evolution of a single-stream vortex-gas shear layer with buffer vortex placed at different distances downstream, compared to evolution without buffer vortex. **(B)** Spread rate determined via best fit for data from *x/L* between 0.1 and 0.5.

Before we discuss the significant differences to the development of the layer due to the buffer vortex, it has to be noted that in the present formulation the buffer-vortex has a non-zero (negative) mean circulation. This is because the mean number of vortices in the domain is higher than the initial value as noted earlier. Since the excess in the mean is concentrated near the downstream edge (Fig 2C), being compensated by a buffer vortex placed near the downstream edge with a negative mean is reasonable. Regardless, the change in δ_ω, due to the direct contribution of $\overline{\gamma}_b$ to the induced velocity field, is only around 2 % at *x/L* = 0.7 (for $\Delta x_b = 0$), and the change is even less significant further upstream. Further, it can be seen, from Fig 9.3A, that 'switching off' the mean circulation (by defining $\gamma_b = -\gamma(N - \overline{N})$) results in nearly identical development of the layer as the case with the non-zero mean and both cases contrast with the one without the buffer. This suggests that only the fluctuating part of γ_b contributes significantly to altering the evolution of the layer.

The evolution of the layer is more strongly affected by the presence of the buffer-vortex, as $\lambda \to 1$. Thus, for the single-stream case, the spread rate without the buffer-vortex can be upto 30% higher over the last 70% of the domain. However, as shown in Fig. 9.3, the results are robust to the location of the buffer vortex provided $\Delta x_b \lesssim L$.

Furthermore, it can be seen in Fig 9.4, that the evolution of a single-stream vortex-gas shear layer from a buffer-fan simulation with *N* = 400 agrees with evolution in the same spatial region (in terms of *x/l*) in a simulation with a much longer flow development domain (*L/l* = 2000). It also has to be noted that for the longer flow development simulation the spatial extent shown is within the first 10% of the domain, and is largely invariant to the downstream boundary condition (the difference between buffer-fan and no buffer with single downstream sheet is < 5% for *x/L* < 0.1). This suggests that the buffer vortex is a valid proxy for the effect of the downstream fluctuations.

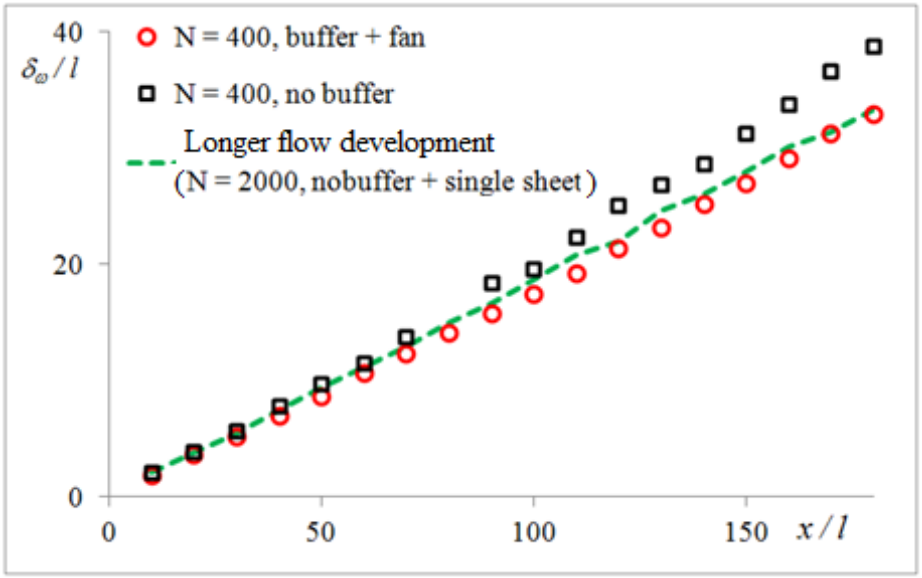

Figure 9.4. The evolution of layer thickness from a simulation with and without buffer-vortex compared to simulation with larger domain (in terms of l).

9.2. Results on spread rate

We first address the question of universality of spread rates in the single-stream limit. Figure 9.5 shows the evolution of thickness in two single-stream vortex-gas simulations with disturbance amplitudes at $x = 0$ varying by a factor of 10^5, and also with different number of vortices (400 and 2000). It can be seen that, the variation in self-preservation spread rate is within 2% across the two cases. Furthermore, different upstream (Fig. D1, D2 in Appendix D) and downstream boundary conditions (Figure 9.4, D3), while greatly altering the extent of the self-preservation zone, do not significantly affect the value of the spread rate. These two observations taken together, strongly indicate that there is a universal spread rate at a given velocity ratio, even at the single-stream limit.

Figure 9.6 shows the self-preservation spread rate as a function of velocity ratio. It can be seen that for $\lambda < 0.5$, the spatial vortex-gas results closely agree with the Galilean-transformed universal Regime II ($d\delta_\omega/dx = 2\lambda\, d\delta_\omega/d(t\Delta U) = 0.0153\lambda$) from the temporal vortex-gas simulations (Ch.3).

This is consistent with the Galilean transformation being exact at the shear-less limit. Beyond $\lambda \approx 0.5$, the spatial vortex-gas simulations show a concave upward trend for the spread rate vs. λ. The results are within the scatter across experimental data. At the single-stream limit, the spread rate from the present vortex-gas simulations (0.184 for N = 1000, $t_{avg}U_m/L$ = 980; 0.185 for N = 2000, $t_{avg}U_m/L$ = 80, where t_{avg} is the duration over which the steady state statistics are averaged) is within 10% of the Morris-Foss (2003) experiment. This experiment is probably the most reliable measure of spread rate, as Reynolds numbers of 10^5 were reached, the top-wall was as far away as the length of the measurement zone, and the downstream boundary was nearly 10 times as far. (In many other experiments, it is difficult to rule out the effect of the top and downstream boundaries, based on the insights provided by the vortex-gas simulations on the sensitivity of the single stream, see Fig. D7.) The rough agreement with experimental data throughout the range of velocity ratios suggests the dominance of the 2D Biot-Savart interactions in determining the large scale momentum dispersal for spatially evolving plane free shear layers.

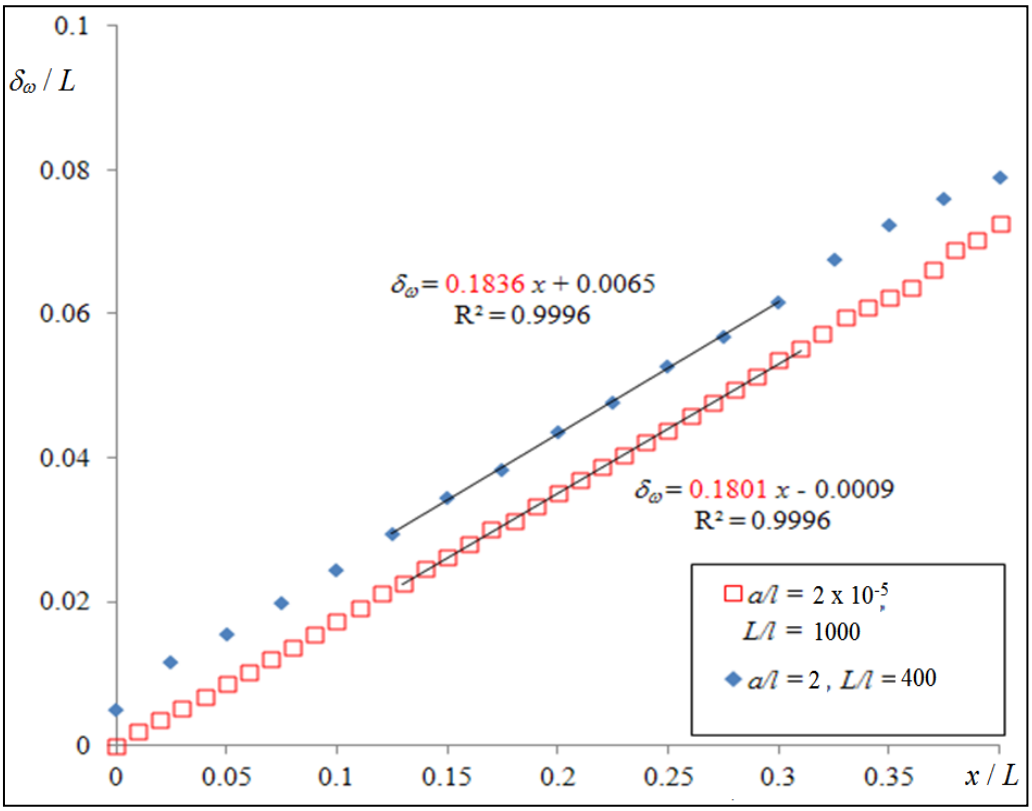

Figure 9.5. Universality of spread rate for λ = 1

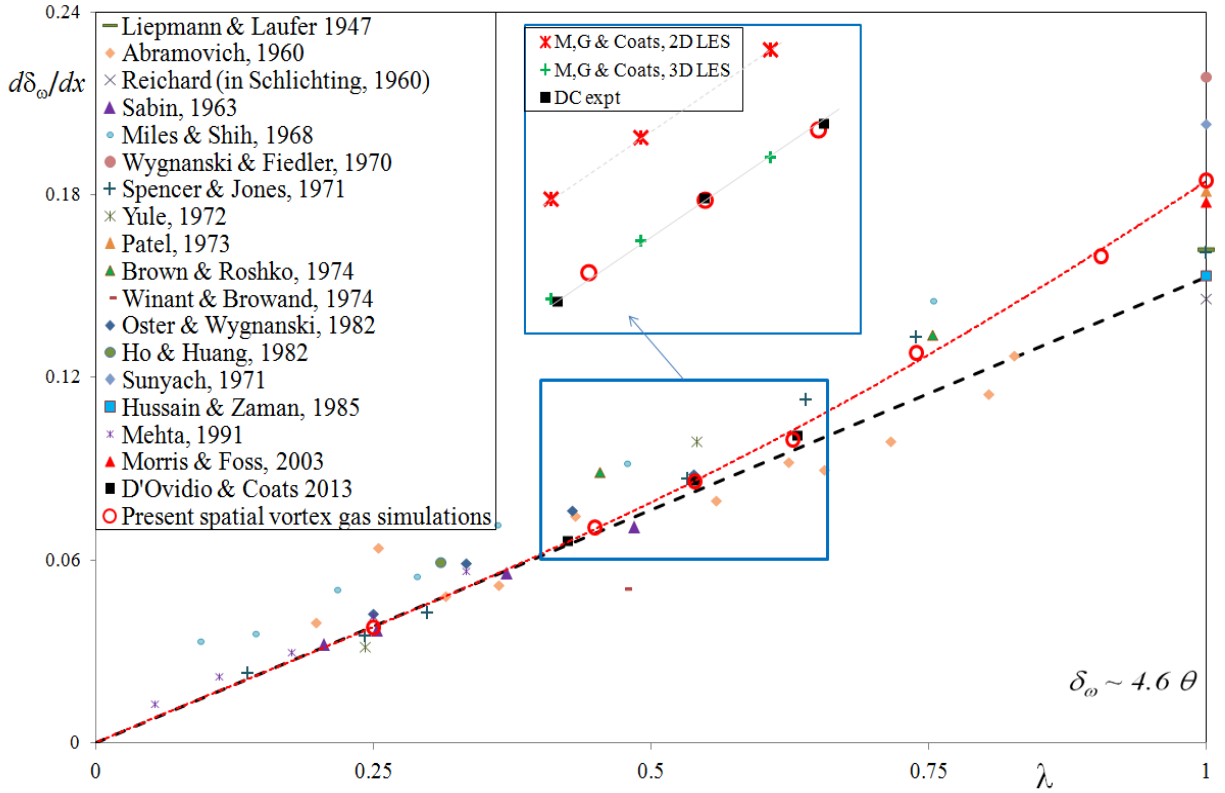

Figure 9.6. Spread rate in the present vortex-gas simulations as a function of velocity ratio and comparison with experiments. Inset shows the comparison with experiments (D'Ovidio & Coats, 2013), 2D and 3D LES (McMullan, Gao & Coats, 2010) over $\lambda = 0.4$ to 0.66.

The applicability of 2D models to study shear layers has been most recently contested by McMullan, Gao & Coats (2010) and D'Ovidio & Coats (2013, henceforth referred to as DC), based on the results of high Reynolds number experiments and large eddy simulations (LES). The inset on Fig. 9.6 shows the spread rate observed in their experiments, 2D LES, 3D LES and present vortex-gas simulations for λ between 0.42 and 0.63. (It has to be noted that for this range of velocity ratio, the vortex-gas shear layer was found to be largely insensitive to downstream conditions.) McMullan et al (2010) observed that, while the results of their 3D LES agreed with DC experiments, but their 2D LES predicted upto 25% higher spread rates. Based on this finding McMullan et al concluded that 2D simulations are 'wholly inadequate' for describing the large scale momentum dispersal in high Reynolds number free shear layers. However, as seen in Fig. 9.6, the spread rate from present vortex-gas simulations, which are strictly 2D, very closely agree with both the DC experiments and 3D LES of McMullan et al (2010). We speculate that the 2D LES led to significantly higher spread rate due to either or both of the following reasons. First is the use of 3D type sub-grid models for the 2D simulations, the rigor of which can be questioned considering the very different small scale behavior of 2D and 3D turbulence. Second is the presence of opposite signed vorticity due to the choice of initial condition with two boundary layers. Preliminary studies (Prasanth, Suryanarayanan & Narasimha, unpublished) have suggested that the spread rate of 2D wakes may be higher than 3D planar wakes, due to additional contribution to momentum dispersal via dipole motion, a mechanism that may be absent or significantly weaker when 3D fluctuations are present. Regardless of why 2D LES predictions are not in agreement, the suggestion 2D is irrelevant is not justified in the light of the remarkable agreement between the present 2D vortex-gas simulations with both high Re experiments and 3D LES.

9.3. Analysis of coherent structures

In this section, we analyze the evolution of 'coherent structures' in the vortex-gas shear layers at different velocity ratios. The main motivation for this investigation is the DC experimental finding that there are two distinct mechanisms through which the coherent structures in the flow (and by extension, the thickness of the layer) grow as they are convected downstream. First is the traditionally known mechanism of growth by amalgamation (or mergers), where the size of the structures change little in between but undergo a step change during well defined mergers between (usually) two structures. Second is the not so well known mechanism via which each individual structure grows linearly with downstream distance, with mergers playing an insignificant role in the overall evolution of the layer. DC observed merger-dominated evolution in pre-mixing transition layers and continuous linear growth of structures in post-transition mixing layers. Based on this observation, it was concluded that the mixing transition was responsible for the change in growth mechanism, and the continuous growth of structures was attributed to 3D effects. However, the conclusions were drawn based on comparisons between pre- and post-mixing transition layers that did not have the same velocity ratio. Thus, for the constant density case (to which the present discussion will be limited), the pre-mixing transition layer (in which merger-dominated evolution was observed) had $\lambda = 0.627$, whereas the post-transition layer (in which continuous growth was observed) was a single-stream shear layer ($\lambda = 1$). Hence it is not possible to determine whether the observed effects were a consequence of mixing transition or differences in velocity ratio.

To explore this question, we have conducted simulations of two vortex-gas shear layers ($N = 2000$, $a/l = 0.001$, buffer-fan setup) at the same two velocity ratios DC used in their experiments. The respective evolutions are shown in Fig. 9.7. It can be seen that for $\lambda = 0.627$, the evolution is merger dominated. This is best illustrated by tracking the green (G) and violet (V) structures. Their sizes change very little among the first snapshots and the well-defined merger (over snapshots 3 and 4) leads to a new structure that whose area is roughly the sum of the areas of the original two structures.

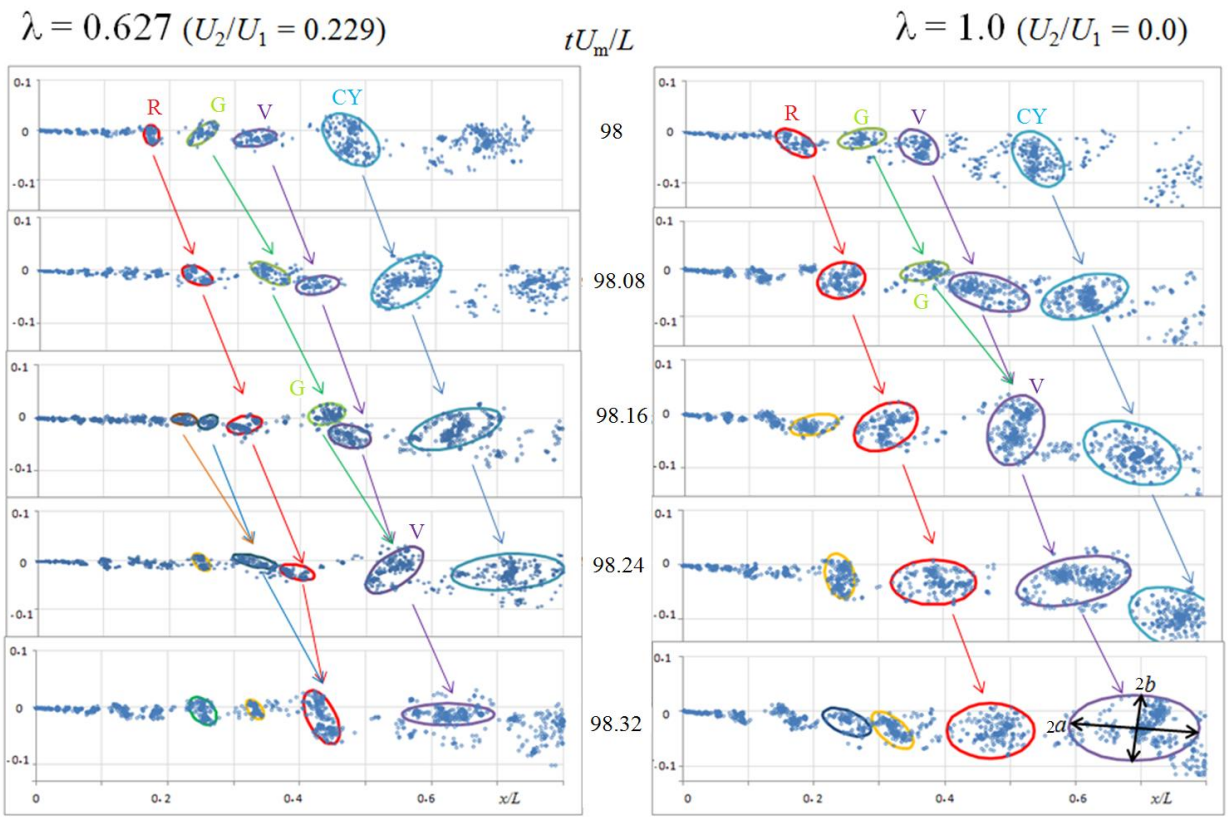

Figure 9.7. Sample comparison of evolution of structures at λ = 0.627 and 1.0 in the present vortex-gas simulations

This may be contrasted with the observations for λ = 1. E.g. the red structure (R) does not seem to undergo any distinct merger event, yet grows to over twice its original size as it travels downstream from x/L ~ 0.2 to ~ 0.5. The green (G) and violet (V) structures do amalgamate (between the second and third snapshots), but overall evolution of the violet structure does not seem to be greatly affected by the amalgamation. If one follows the violet structure alone, it appears to grow continuously with time/downstream distance. Similar observations can be made for several other structures. Therefore the observation that structures individually undergo continuous growth, made from the present (2D) vortex-gas simulations at λ = 1, are consistent with the experimental observation of DC at λ = 1. This suggests that the differences in mechanism noted by DC can be adequately explained by differences in the velocity ratio, without appealing to mixing transition or associated 3D mechanisms.

Figure 9.8 displays the data shown in Fig. 9.7 extended in time to 98.48 L/U_m, in terms of x-t, and size vs. x diagrams, presented in a fashion similar to DC. Unlike DC, we fit ellipses instead of circles (as the structures are clearly elliptical) and define an effective radius of the structure as a geometric mean of the major and minor axes of the ellipse. There is a certain degree of subjectivity involved in fitting the ellipses as it is done visually, a limitation shared with the analysis of DC. Nevertheless, the central conclusion is clear, that structures in the single stream case undergo continuous linear growth, unlike those in the λ = 0.627 case which shows increase in size only during well-defined merger events. (It must be noted that the DC results show lower scatter in the size vs. x diagrams than the present vortex-gas simulations. This could be due to the span-wise averaging the DC visualization implies).

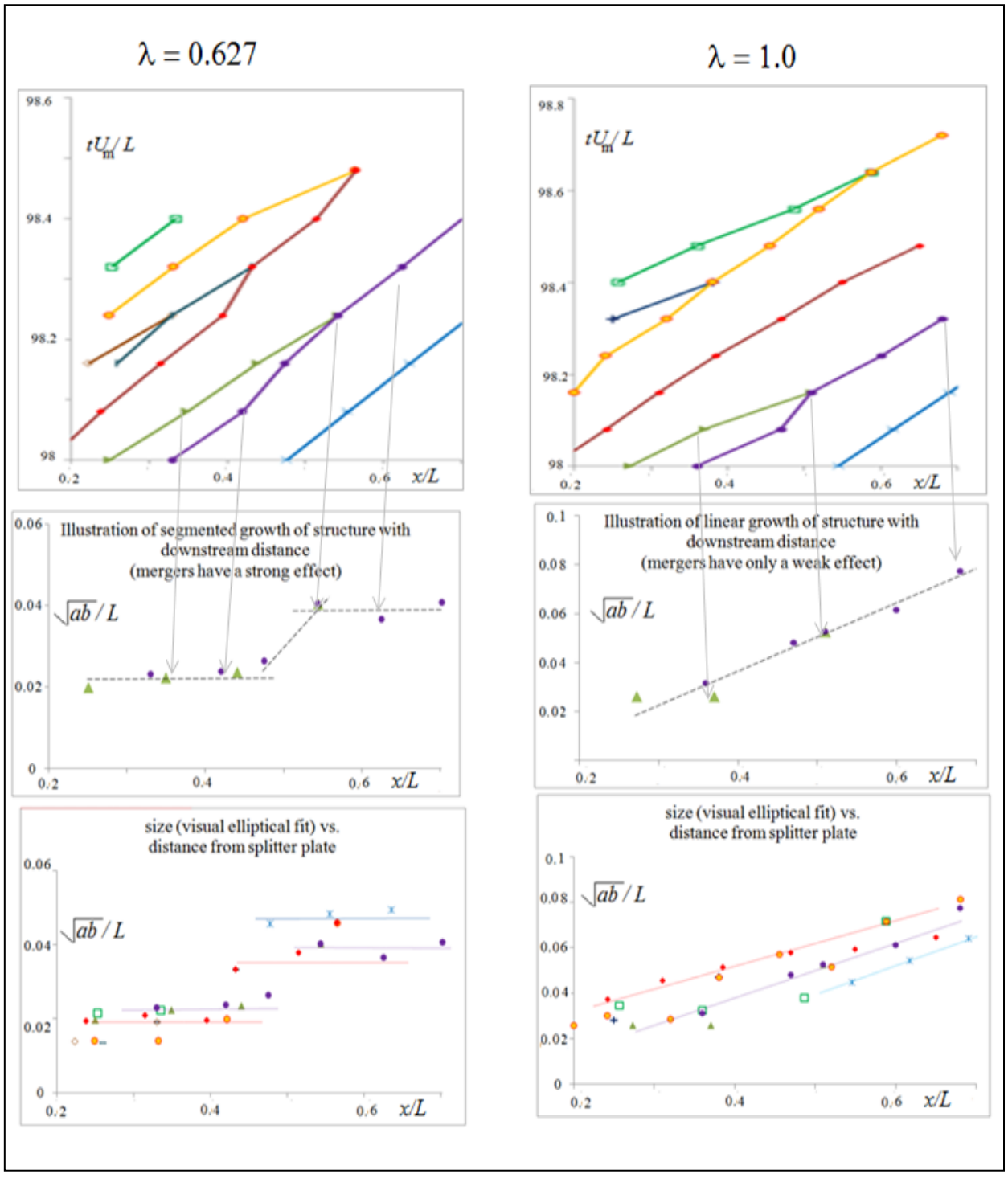

Figure 9.8. Comparative evolution of downstream location and size of structures at $\lambda = 0.627$ and 1.0.

This analysis repeated over another randomly picked time (tU/L = 82 – 82.5) led to similar results (see Fig.D4, also results are qualitatively similar for other downstream boundary conditions as shown in Fig. D5). Yet, we must enter a note of caution that these relatively short times (though comparable to DC analysis) may not necessarily provide representative statistics over long timescales. Therefore we perform the following (independent) objective analysis over much longer times (tU_m / L = 20 to 80). We compute at each time instant (beyond the initial transient) the number of vortices (proportional to the circulation) within $x = L/2 \pm \delta_\omega[x = L/2]$. As seen from Fig. 9.8, the average size of a structure is O(δ_ω) and the spacing between structures is over twice the size, so the sampled extent is expected to contain a single structure on an average. We compute the local maxima of the circulation over $\pm tU_m/\ \delta_\omega[L/2]$, which corresponds to a structure passing time. Hence this statistic is expected to reflect the circulation over each structure that passes through $x = L/2$. Note that there is no subjectivity

involved in this analysis other than the selection of the bin size, which is chosen to be the same fraction of the local thickness for both cases. The probability distribution function (PDF) of this quantity is computed from the time-series for λ = 0.627 and 1.0 simulations, and are shown in Fig. 9.9.

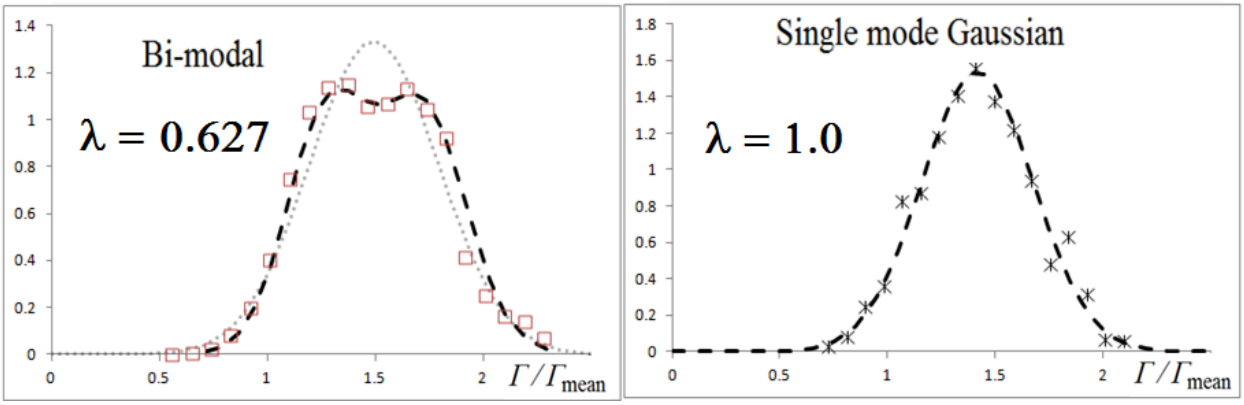

Figure 9.9. Comparison of PDF of circulation in of local maxima of circulation in the region $x = [L/2 - \delta_\omega[L/2]\ ,\ L/2 + \delta_\omega[L/2]]$ $y = [-\infty,\infty]$ between different velocity ratios. Note that the distribution at λ = 0.627 (left) agrees with a bi-modal fit (shown in dashed line) as opposed to the Gaussian (faint dotted line) corresponding to the mean and variance. This is in contrast with the distribution for λ = 1 (right), which is adequately described by a uni-modal Gaussian (dashed line).

It can be seen that for λ = 0.627 the distribution of circulation is bimodal, indicating that the structures that pass $x = L/2$ have two preferred values of size. This is consistent with the earlier observation of structure size strongly affected by mergers, with the two preferred size ranges possibly corresponding to structures that have undergone mergers before and after the zone. On the other hand, we observe a unimodal Gaussian for λ = 1.0, supporting the conclusion that mergers do not cause a step change in structure size for the single stream case.

Furthermore, we find (Fig.D6) that λ = 0.905 shows intermediate behavior. At this velocity ratio mergers still play an important role causing significant step increases in size, but the structures also undergo linear growth. This intermediate point establishes that the trend is neither accidental nor the unique peculiarity of the single stream case.

The results on studying evolution of individual structures (presented in Figs. 9.7 and 9.8), taken by themselves, should not be considered as strong evidence of purely 2D dynamics. But they do strongly suggest that the DC evidence is inadequate to support in the claim that 3D mechanisms play a significant role, as qualitatively similar observations are made using similar analyses in the present 2D study. Furthermore, when those results are taken together with the independent objective analysis presented in Fig. 9.9, it appears likely that the mechanism of structure interactions does change with velocity ratio.

2D mechanisms responsible for shift in structure interaction

While the present simulations and analysis do not conclusively indicate the (2D) mechanism responsible for the shift in the behavior, a plausible explanation is that it has its origins in the dissimilarity in size and/or strength between interacting structures. In order to provide more insight into details of the underlying mechanism, we examine the evolution shown in Fig. 9.7 for λ = 1 in greater detail. Figure 9.11 tracks individual vortices that belonged to individual structures at tU_m/L = 98.0, over a time span that covers tU_m / L = 97.84 to 98.32.

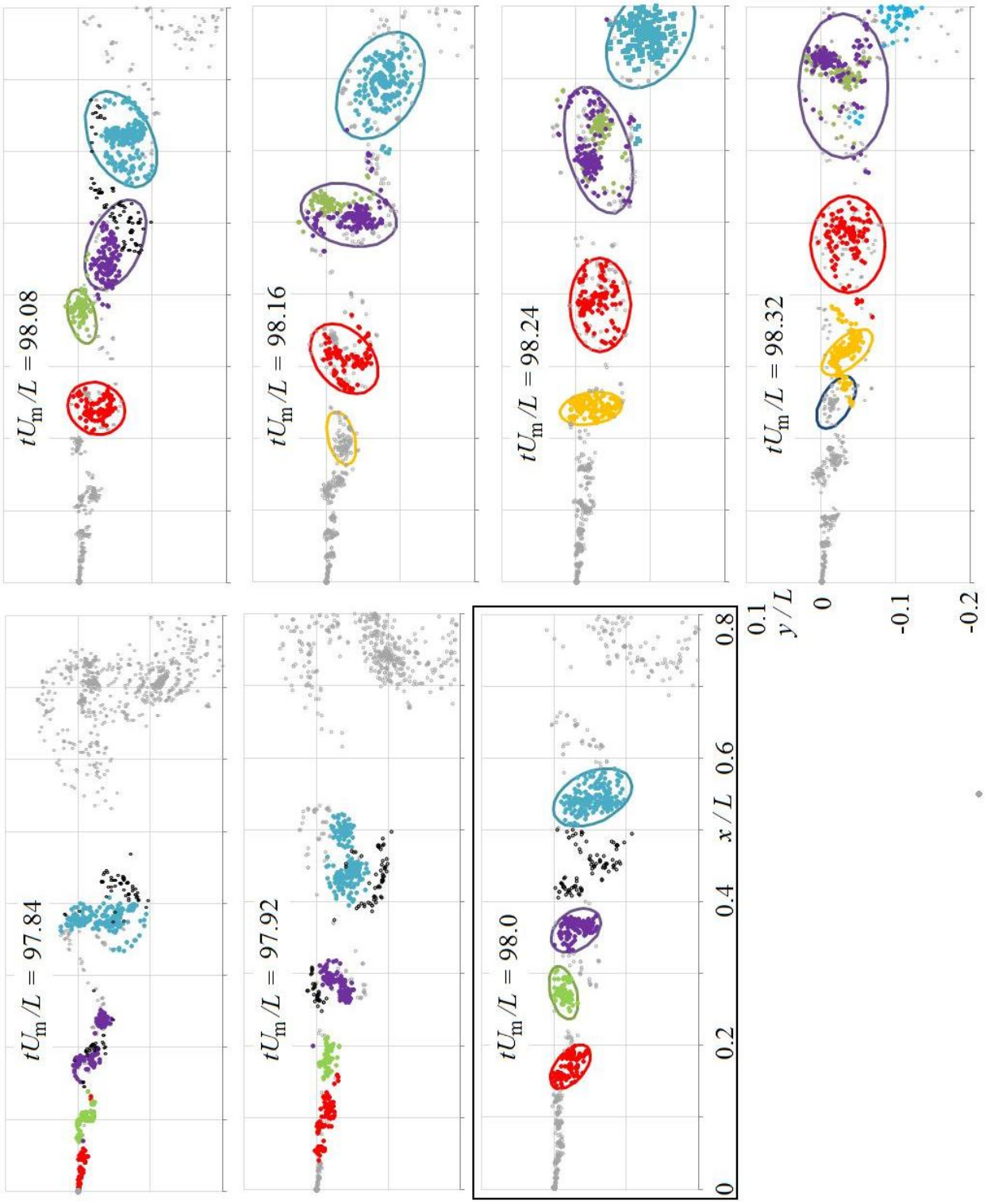

Figure 9.10. History and evolution of vortices belonging to individual structures for $\lambda = 1$(at tU_m/L = 98.0, except for yellow vortices, that are tracked from tU_m/L = 98.24). Disorganized vortices between the violet and cyan structures at tU_m/L = 98.0 are indicated in black and tracked from tU_m/L = 97.84 to 98.08. Vortices that are not tracked are shown in gray.

It can be seen that the increase in size of violet structure from tU_m/L = 98.0 to 98.16 has three contributions.

(i) The obvious merger with green completed just before tU_m/L = 98.16, which was noted in Fig. 9.7. But the following two other contributions become clearer from Fig. 9.10.

(ii) Capturing of (green) vortices from the green structure by the violet structure before the actual merger (tU_m/L = 98.08) between the two structures. A similar observation can be made on the interaction between the red- yellow and dark blue structures at tU_m/L = 98.32.

(iii) The capture of background vorticity present between the violet and cyan structures at tU_m/L = 98.0, shown as black vortices. This cluster of vortices is not a coherent structure (and therefore not marked with an ellipse in Fig. 9.7) because its vorticity (circulation per unit area) is less than a fourth of the neighboring structures. By tracking the history of these disorganized black vortices, it is observed that their lifetime as a cluster is indeed very short (seen as a single cluster only in one frame, whereas an average structure can be seen as a distinct entity for at least four frames in Fig 9.10). Some of the disorganized vortices are 'ejected' during a merger between two structures (to form what would become the violet structure) between tU_m/L = 98.84 and 98.92, and the rest are torn from the edges of the cyan structure.

These observations can be summarized as follows. In spatial mixing layers with higher λ, large downstream structures feed on the vorticity from either smaller upstream structures (higher the λ, higher the $d\delta_\omega/dx$ and larger the disparity in size between interacting structures, as seen in Figs. 9.6 and 9.7) or disorganized background vorticity. (The disorganized clusters are ejected during violent mergers or torn from outer parts of large structures during interactions with neighboring structures). A combination of these two processes leads to continuous, nearly linear growth in size of many of the structures over a substantial part of their lifetimes. This can be illustrated via the cartoon shown in Fig. 9.10. This finding is indeed consistent with what is well known from two-vortex merger studies (e.g. Yasuda & Flierl, 1995), that when one vortex is much larger or stronger than the other, the former tends to filament the smaller vortex and absorbs the vorticity, thus giving it an apparent continuous growth.

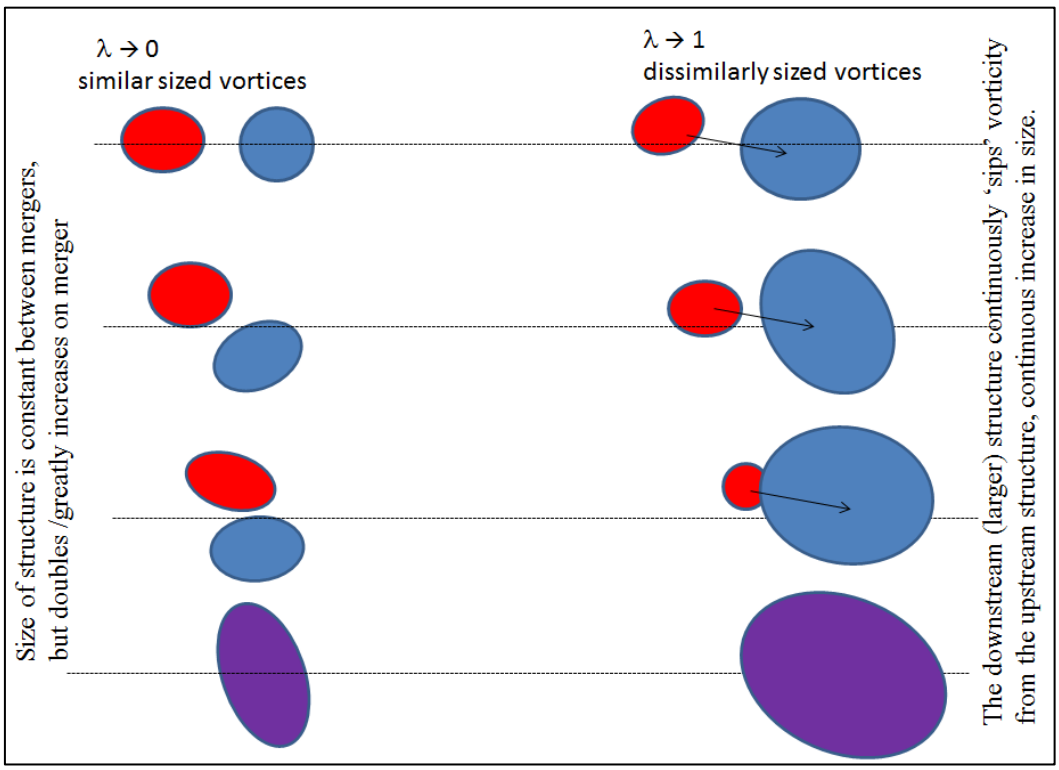

Figure 9.11. Cartoon illustrating the possible role of dissimilarity in structure size on evolution

This observation also suggests that whether the evolution is merger-dominated or occurs by continuous growth of structures depends on the size disparity between neighboring and hence the mechanism depends indirectly on the velocity (and also on density) ratio through the spread rate. This is consistent with the observation of continuous growth by DC for $\lambda = 0.63$ but for density ratio of 7.2. The spread rate in this case is much more than the uniform density case at the same velocity ratio, and is close to the constant density case with $\lambda \sim 0.9$.

9.4. Conclusions from spatial vortex-gas simulations

The present spatially evolving vortex-gas simulations show that the spread rate is a universal (concave upward) function of velocity ratio (under conditions of sufficiently long flow development for initial conditions to be forgotten, and the measurement zone to be sufficiently far from downstream boundaries and no interference from top wall). Agreement of present vortex-gas simulations with experiments and 3D LES (McMullan et al, 2010) over a range of velocity ratios suggests spreading by 2D mechanism provides adequate representation of the real flow. Analysis of the evolution of structure sizes and locations suggests that the change in mechanism from step increase in size during mergers to continuous linear increase in size observed in the recent experiments of D'ovidio & Coats (2013), are likely to be effects of velocity ratio. The attribution of the change to mixing transition and 3D mechanisms is not supported as similar results are observed in the present vortex-gas results in purely 2D flow.

Chapter 10 : Concluding remarks and outlook

In part I of the thesis, we showed that the temporal vortex-gas free shear layer, a Hamiltonian system relevant to a class of turbulent free shear flows, has interesting features such as the emergence of order (in the form of large vortex clusters or 'coherent structures') and distinct stages in its relaxation to an asymptotic state. Connections to statistical mechanics were made for the long-time solution including the final stages of the relaxation. The long-time solution attained after 10^4 outer times ($L/\Delta U$) was shown to be in relative equilibrium – in the sense that it involves a single structure randomly moving in x, but with the vortex-distribution within the structure relative to (say) the core of the moving structure being described by equilibrium theories. In the frame of reference of the moving structure, the vorticity-stream function relationship was found to agree with the vortex-gas analog of the Boltzmann equilibrium distribution proposed by Joyce & Montgomery (1973), and the vortex distribution with an anisotropic truncated version of the Lundrgen-Pointin (1977) equilibrium solution for vortices in an infinite plane. The relaxation of the single structure to the asymptotic solution has two stages that are known in vortex-gas statistical mechanics as well as in stellar systems as 'violent' (Euler) and 'slow' (finite-N) relaxations.

Preceding the formation of the single structure, the dynamics are complex and more interesting, in part due to their relevance to evolving shear flows. Following an initial regime (I), where the solution was dependent on the initial condition, and preceding a regime (IIIa) of interaction among a few structures, there exists an intermediate asymptotic regime (II), during which the thickness of the vortex-gas free shear layer grows linearly. The central result of this thesis is the finding that the spread rate in Regime II is universal and independent of initial conditions over a wide class of initial conditions, for N ranging from 400 to 32000. The momentum thickness in this regime is given as $\theta = 0.0166\,(t\Delta U)^1 + C_3$. This non-equilibrium universality is special because it is not only the universality of the exponent (= 1) in the above relation, but also of the pre-factor coefficient (which is 0.0166 for the momentum thickness). Furthermore, this universality is robust to both the initial value of the Hamiltonian as well as to small perturbations to the Hamiltonian. The statistics relevant to both statistical mechanics and fluid dynamics were shown to be self-similar in Regime II. It is important to note that, while being an analog of the asymptotic state in fluid dynamics, the entire duration of Regime II is O(1 $L/\Delta U$), which is 10^{-4} of the total duration of the relaxation process and one order shorter than that of the 'violent' relaxation of the single structure. Hence it can justifiably be considered as 'explosive relaxation'. While the universality of Regime II demands a statistical-mechanical explanation, neither equilibrium theories nor Boltzmann-inspired vortex-gas kinetic theories are applicable in this Regime, as it is far from equilibrium and characterized by strong correlations arising from presence of multiple coherent structures. In spite of what may at first appear as gross simplification, detailed comparisons with experiments show that the temporal vortex-gas free shear layer is remarkably relevant to high Reynolds number turbulent free shear layers. The inviscid temporal vortex-gas simulations have thus enabled tackling long-standing controversies on issues such as the universality or otherwise of asymptotic self-preservation.

The second part of the thesis exploits this general agreement between the vortex-gas and Navier-Stokes free shear layers, and the former was demonstrated to be useful as an inexpensive non-linear tool to study connections with hydrodynamic instability theories as well for flow control applications. Supplemented by the spatial and viscous simulations presented in the last two chapters, the vortex gas has also provided new insights into the dynamics of turbulent shear flows, including the effect of spatial feedback on structure interaction and internal balancing of viscous and Reynolds stresses. Hence, unlike most other statistical-mechanical models, the vortex-gas has proved itself to be well beyond a toy model to study plane free turbulent free shear flows.

To summarize, the extensive simulations and analyses presented in this thesis reveal that the vortex gas is indeed a promising bridge between plane turbulent shear flows and statistical mechanics, and possibly opens up a new way of understanding what is considered the last unsolved problem in classical physics.

Directions of current and future research

The vortex-gas simulations presented in this thesis have provided some conclusive understanding and new insights into the dynamics of turbulent free shear layers. However, they also raise several interesting questions that are yet to be resolved. The following is a list of such issues, many of which are currently being explored and some preliminary ideas and results are presented below.

i) Models with finite interaction range – statistical-mechanical and stability implications

Nearest neighbor models are often used to greatly simplify *N*-body problems. The Ising model in magnetism and the hard-sphere model in molecular dynamics are classic examples. The nearest neighbor model is justified in such systems which have short-range interactions.

The present vortex-gas problem on the other hand has long-range interactions. However, preliminary simulations show that limiting the interaction distance between two vortices by a length that scales with the local thickness yields interesting results (for case R4-400 in Table 3.1), as shown in Fig.10.1.

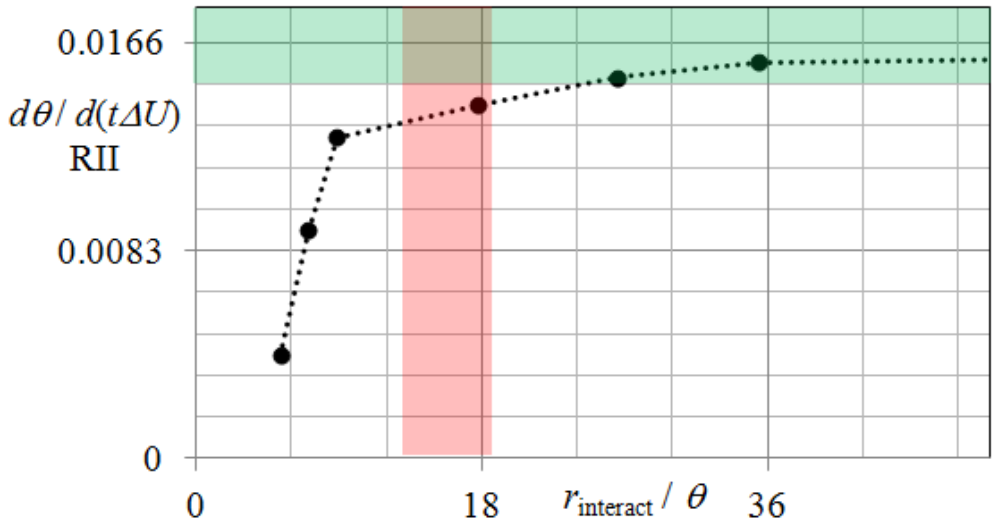

Figure 10.1. Effect of limiting maximum interaction range.

The governing equations (2.1 and 2.2) are same for these cases, except that $u_i = v_i = 0$ when

$$\cosh\big(2\pi(y_i - y_j)/L\big) - \cos\big(2\pi(x_i - x_j)/L\big) < \tfrac{1}{2}\Big(\tfrac{2\pi}{L} r_{\text{interact}}\Big)^2$$

We perform a set of simulations with the same initial condition class and the value of *N* (= 400) as R4-400 (see Table 3.1). After $t\Delta U/l$ = 20, we limit the maximum interaction to a fraction of the local thickness, say $r_{\text{interact}} = C_{\text{interact}}\,\delta_{\text{RMS}}$. The results on the spread rate are plotted against $r_{\text{interact}}/\theta$ (using $\theta = \delta_{\text{RMS}}/1.77$). The results show that the spread rate in Regime II is within 10% of the universal value as long as r_{interact} is greater than 24θ. It is interesting that the average inter-structure spacing is ~ 15 θ. This therefore implies that the nearest-neighbor interactions (not in terms of vortices, but in terms of coherent structures)

contribute to the bulk of the spreading in Regime II. This could greatly simplify the problem, both from statistical-mechanical and hydrodynamic stability points of view.

The picture of nearest-neighbor coherent structures would imply that f_2' could be modeled considering only the nearest-structure correlation as a first step towards a realistic vortex-gas kinetic theory that is capable of describing Regime II. Another approach under consideration utilizes this nearest-structure approximation in conjunction with the monopole approximation (discussed in Ch.6) and the vortex-collision models of P.K. Dutta (1988).

Similarly, to consider only the nearest structure in a hydrodynamic stability framework would imply considering only the interactions between modes around the fundamental and subharmonic, and possibly incorporating the non-linear interactions responsible for the negative growth exponents observed in Fig. 6.11.

ii) Connections between growth rate and mechanism in single-stream shear layers

The results presented in Sec. 9.2 show that with increase in λ, the spread rate is increasingly larger than the Galilean-transformed temporal rate. Analysis of coherent structure interaction (Sec 9.3) at larger values of λ showed that there is a shift of mechanism from merger-dominated step-increase in structure size to continuous structure growth via capturing vorticity from smaller structures or disorganized background vorticity. The details of the connection between the shift in the mechanism and the increased growth of the layer are currently being investigated.

iii) Understanding the interplay between viscous and turbulent stresses in intermediate Reynolds number shear layers

Results presented in Ch.8 showed that there exists a sub-regime during which the viscous and Reynolds stresses adjust themselves in such a way that their sum is the universal Regime II stress. The detailed underlying mechanisms responsible for this observation are under investigation.

References

M. Abid and A. Verga, “Turbulence driven by singularities in vortex sheet dynamics”, *Phys. Rev. E* **84**, 026318 (2011).

G.N. Abramovich, *Turbulent Jets Theory*, Gosudarstvemioye Izdatel' Stvo Fiziko-Matematicheskoy Leteratury, Moscow, 1960; English translation by Scripta Technica, The M.I.T. Press, Cambridge, Mass.

E. Acton, “The modelling of large eddies in a two-dimensional shear layer”, *J. Fluid Mech.* **76**, 561 (1976).

H. Aref, “Integrable, chaotic, and turbulent vortex motion in two-dimensional flows”, *Ann. Rev. Fluid Mech.* **15**, 345 (1983).

H. Aref and E.D. Siggia,” Vortex dynamics of the two-dimensional turbulent shear layer”, *J. Fluid Mech.*, **100**, 705 (1980).

W.T. Ashurst, “Numerical simulation of turbulent mixing layers via vortex dynamics.”, *Turbulent Shear Flows I. Springer Berlin Heidelberg*, 402-413, (1979).

E. Balaras, U. Piomelli and J.M. Wallace, “Self-similar states in turbulent mixing layers”, *J. Fluid Mech.* **446**, 1 (2001).

A.J. Basu, A.Prabhu and R.Narasimha, “Vortex sheet simulation of a plane “canonical” mixing layer”, *Comp.Fluids*, **21**(1),1 (1992).

A.J. Basu, R. Narasimha, and A. Prabhu. "Modelling plane mixing layers using vortex points and sheets." *Applied mathematical modelling* **19** (2), 66-75 (1995).

G. K. Batchelor, “Computation of the Energy Spectrum in Homogeneous Two-Dimensional Turbulence”, *Phys. Fluids* **12**, II-233 (1969).

J. T. Beale and A. Majda, “Vortex methods II: Higher order accuracy in two and three dimensions.” *Math. Comput.* **39**, 29 (1982).

J.H. Bell and R.D. Mehta, “Development of a two-stream mixing layer from tripped and untripped boundary layers”, *AIAA J.* **28**, 2034 (1990).

L.P. Bernal, “The coherent structure of turbulent mixing layers. I. Similarity of the primary vortex structure. II. Secondary streamwise vortex structure”, *Ph.D. Diss.*, Calif. Inst. Tech. (1981)..

J. Bridges and F. Hussain, "Roles of initial condition and vortex pairing in jet noise.", *J. Sound Vib.* **117**, 289, (1987).

G.L. Brown and A. Roshko, “On density effects and large structure in turbulent mixing layers”, *J. Fluid Mech.*, **64**, 775 (1974).

G. L. Brown and A. Roshko, “Turbulent shear layers and wakes”, *J. Turbul.* **13**, 1 (2012).

O. Bühler, “Statistical mechanics of strong and weak point vortices in a cylinder”, *Phys.Fluids.*, **14**, 2139 (2002)

G. Carazzo, E.Kaminski and S.Tait, “The route to self-similarity in turbulent jets and plumes”, *J. Fluid Mech.*, **547**, 137 (2006).

C. Carton de Wiart, G. Winckelmans, C. Bailly, P. Chatelain, F. Thirifay and A. Roshko, “Similarity in 2-D spatially developing and long shear layers”, *Bulletin of the American Physical Society*, **55** (2010)

S. Chandrasekhar, “Stochastic problems in physics and astronomy”, *Rev. Mod. Phys.* **15**, 1 (1943).

P. Chavanis, J. Sommeria, and R. Robert, "Statistical mechanics of two-dimensional vortices and collisionless stellar systems", *Astrophys. J*. 471, 385 (1996).

P.H. Chavanis, "Kinetic theory of point vortices: diffusion coefficient and systematic drift", *Phys. Rev. E* **64**, 026309 (2001).

P.H. Chavanis, "Statistical mechanics of geophysical turbulence: application to jovian flows and Jupiter's great red spot", *Physica D*, **200**, 257 (2005).

P.H. Chavanis, "Kinetic equations for systems with long-range interactions: a unified description", *J. Stat. Mech.* P05019 (2010).

P.-H. Chavanis, "Kinetic theory of Onsager's vortices in two-dimensional hydrodynamics", *Physica A* **391**, 3657 (2012).

A.J. Chorin, "Numerical study of slightly viscous flow", *J. Fluid. Mech*. **57**, 785 (1973).

A.J. Chorin and P.S.Benard, "Discretization of a vortex sheet, with an example of roll-up", *J. Comput. Phys.* **13** (1973).

G.M. Corcos and S.J. Lin, "The mixing layer: deterministic models of a turbulent flow. Part 2. The origin of the three-dimensional motion", *J. Fluid Mech.*, **139**, 67 (1984).

G.M. Corcos and F.S. Sherman, "The mixing layer: deterministic models of a turbulent flow. Part 1. Introduction and the two-dimensional flow", *J. Fluid Mech.*, **139**, 29 (1984).

G-H. Cottet and P. D. Koumoutsakos, *Vortex methods: theory and practice*. Cambridge university press, (2000).

G-H. Cottet and S. Mac-Gallic. "Une méthode de décomposition pour une équation de type convection-diffusion combinant résolution explicite et méthode particulaire." *Comptes rendus des séances de l'Académie des sciences. Série 1, Mathématique* **297** (2), 133-136 (1983).

P.A. Davidson, *Turbulence: An Introduction for Scientists and Engineers: An Introduction for Scientists and Engineers*. Oxford University Press, 2004.

B.A.G. Delcourt and G.L. Brown, "The evolution and emerging structure of a vortex sheet in an inviscid and viscous fluid modelled by a point vortex method", *2nd Symp. Turb. Shear Flows*, London (1979).

S. Delport, M. Baelmans and J. Meyers, "Optimization of long-term mixing in a turbulent mixing layer.", AIAA 2010-4422, (2010).

P.E. Dimotakis, "The mixing transition in turbulent flows," *J. Fluid Mech.* **409**, 69 (2000).

A. D'Ovidio and C. M. Coats. "Organized large structure in the post-transition mixing layer. Part 1. Experimental evidence." *J. Fluid Mech.* **737,** 466-498 (2013).

P.G. Drazin and W. H. Reid. *Hydrodynamic stability*. Cambridge university press, (2004).

P.K. Dutta, "Discrete vortex method for separated and free shear flows", Ph.D. Thesis Indian Institute of Science (1988).

L. Euler, "Principes g´en´eraux du mouvement des fluides" MASB, 11 [printed in 1757], 274–315. Also in *Opera omnia*, ser. 2, 12, 54 – 91 (1755)

G.L.Eyink and H.Spohn, "Negative-temperature states and large-scale, long-lived vortices in two-dimensional turbulence", *J.Stat. Phys.*, **70**, 883 (1993).

G.L. Eyink and K.R. Sreenivasan, "Onsager and the theory of hydrodynamic turbulence", *Rev. Mod. Phys.* **78**, 87 (2006).

R. Feynman, R.B. Leighton and M. Sands, *The Feynman lectures on physics* (Addison-Wesley, Boston, MA) (1964).

R. Fjortoft, “Application of integral theorems in deriving criteria of stability for laminar flows and for the baroclinic circular vortex.” *Geofys. Publ* **17** (6), 1 (1950).

H. Fiedler and I. Wygnanski. "Method and apparatus for controlling the mixing of two fluids." U.S. Patent 4,257,224, issued March 24, 1981.

H. Foysi and S.Sarkar, “The compressible mixing layer: an LES study”, *Theoret. Comput. Fluid Dyn.,* DOI 10.1007/s00162-009-0176-8 (2010).

A. Friedmann and P. Poloubarinova. "Über fortschreitende Singularitäten der ebenen Bewegung einer inkompressiblen Flüssigkeit." *Recueil de Géophysique* **5,** 9-23 (1928).

J. Frohlich and D. Ruelle, “Statistical mechanics of vortices in an inviscid two-dimensional fluid”, *Commun. Math. Phys.* 87:1-36 (1982).

M.Gaster, E. Kit and I. Wygnanski, “Large-scale structures in a forced turbulent mixing layer”, *J. Fluid Mech.*, **150**, 23 (1985).

W.K. George and L. Davidson, “Role of initial conditions in establishing asymptotic flow behavior”, *AIAA J.*,**42**, 438 (2004).

A.F. Ghoniem and K.K. Ng. “Numerical study of the dynamics of a forced shear layer.” *Phys. Fluids* **30** (3), 706-721 (1987).

J.P. Gollub, and Harry L. Swinney. "Onset of turbulence in a rotating fluid." *Physical Review Letters* 35.14: 927 (1975).

F. R. Hama and E.R. Burke, “On the rolling-up of a vortex sheet”, *Inst. Fluid Dynam. Appl. Math., Univ. Maryland, Tech.Note* Bn-220 (1960).

H. von Helmholtz, “über discontinuirliche Flüssigkeits-Bewegungen.” *Monats. Konigl Preuss. Akad. Wiss. Berlin* (1868)

C.M. Ho and L.S. Huang, “Subharmonics and vortex merging in mixing layers”, *J. Fluid Mech.*, **119**, 442 (1982).

C.M. Ho and P. Huerre, “Perturbed free shear layers”, *Ann. Rev. Fluid. Mech.*, **16**, 365 (1984).

H.S. Husain and F. Hussain, “Experiments on subharmonic resonance in a shear layer.”, *J. Fluid Mech.*, **304**, 342 (1995).

O. Inoue, “Vortex simulation of a turbulent mixing layer.” *AIAA J.* **23** (3), 367-373 (1985).

O. Inoue and A. Leonard, “Vortex simulation of forced/unforced mixing layers”, *AIAA J.* **25** (11), 1417-1418 (1987).

T. Ishihara, Y. Kaneda, M. Yokokawa, K. Itakura, and A. Uno. "Small-scale statistics in high-resolution direct numerical simulation of turbulence: Reynolds number dependence of one-point velocity gradient statistics." *J. Fluid Mech*., **592**, 335-366 (2007).

G. Joyce and D. Montgomery, “Negative temperature states for the two-dimensional guiding-centre plasma”, *J. Plasma Phys.* **10**, 107 (1973).

T. Von Karman and H. Rubach. "Über den mechanismus des flüssigkeits-und luftwiderstandes." *Phys. Z* **13** (2) (1912).

Lord Kelvin (William Thomson). “Hydrokinetic solutions and observations.” *Phil. Mag.* **42** 362–377 (1871).

G. Kirchhoff, *Vorlesungen ¨uber Mathematische Physik. Mechanik* (Druck und Verlag von BG Teubner, Leipzig, 1876).

S.J. Kleis and F. Hussain, “Asymptotic state of the plane mixing layer”, *Bulletin of the American Physical Society*, **24**, 1132 (1979)

A. Kolmogorov, “The local Structure of turbulence in incompressible viscous fluid for very large Reynolds numbers [In Russian]”, *Dokl. Akad. Nauk SSSR* **30**, 299 (1941).

J.H. Konrad,“An experimental investigation of mixing in two-dimensional turbulent shear flows with applications to diffusion-limited chemical reactions”, Ph.D. thesis, Calif. Inst. Tech. (1977).

R. H. Kraichnan, “Inertial Ranges in Two-Dimensional Turbulence”, *Phys. Fluids* **10**, 1417 (1967).

R. H. Kraichnan and Shiyi Chen. “Is there a statistical mechanics of turbulence?” *Physica D: Nonlinear Phenomena* **37**(1) 160-172 (1989).

R. Krasny, “Desingularization of periodic vortex sheet roll-up”, *J. Comput. Phys.* **65**, 292 (1986).

R. Krasny, “A study of singularity formation in a vortex sheet by the point-vortex approximation”, *J. Fluid Mech.* 167, 65 (1986b).

H. Lamb. *Hydrodynamics*. (1932).

L. Landau and E. Lifshitz. *Course of theoretical physics*. Elsevier, 1980.

A.Leonard, “Vortex methods for flow simulation”, *J.Comput. Phys.* **37**, 289 (1980).

J. Liu, “Coherent structures in transitional and turbulent free shear flows”, *Annu. Rev. Fluid Mech.* **21**, 285 (1989).

H. Liepmann and J. Laufer, “Investigations of free turbulent mixing”, National Advisory Committee for Aeronautics Technical Note No. 1257 (1947).

T.S. Lundgren and Y.B. Pointin, “Statistical mechanics of two-dimensional vortices”, *J. Stat. Phys.* **17**, 323 (1977).

D. Lynden-Bell, “Statistical mechanics of violent relaxation in stellar systems”, *Mon. Not. R. Astron. Soc*. **136**, 101 (1967).

C. Marchioro and M. Pulvirenti, *Mathematical Theory of Incompressible Nonviscous Fluids* (Springer, Berlin, 1993), Vol. 96.

H. Marmanis, “The kinetic theory of point vortices”, *Proc. R. Soc. Lond. A*, **454**, 587 (1998)

T. W. Mattner, “Large-eddy simulations of turbulent mixing layers using the stretched-vortex model”, *J. Fluid Mech.*, **671**, 507 (2011)

J. Maurer and A. Libchaber. "Rayleigh-Bénard experiment in liquid helium; frequency locking and the onset of turbulence." Journal de Physique Lettres 40 (16) 419-423 (1979).

W.A. McMullan, S. Gao, and C. M. Coats. "Investigation of Coherent Structures in Turbulent Mixing Layers using Large Eddy Simulation.", AIAA 2010-1291, *Proc. 48th AIAA Aerospace sciences meeting including the new horizons forum and aerospace exposition*, 4-7 January 2010, Orlando, Florida, USA (2010).

R.D. Mehta, “Effect of velocity ratio on plane mixing layer development: Influence of the splitter plate wake”, *Experiments in Fluids* **10** (4), 194-204 (1991).

A. Michalke, “On the inviscid instability of the hyperbolictangent velocity profile.” *J. Fluid Mech.* **19** (4), 543-556 (1964).

J.B. Miles and J-S. Shih. "Similarity parameter for two-stream turbulent jet-mixing region." *AIAA J.* **6** (7), 1429-1430 (1968).

J. Miller, “Statistical mechanics of Euler equations in two dimensions”, *Phys. Rev. Lett.* 65, 2137 (1990).

J. Miller, P. B. Weichman, and M. C. Cross, “Statistical mechanics, Euler's equation, and Jupiter's Red Spot”, *Phys. Rev. A* **45**, 2328 (1992)

C.B. Millikan, “A critical discussion of turbulent flows in channels and circular tube”, in *Proceedings of the 5th International Congress on Applied Mechanics*, edited by J. P. D. Hartog and H. Peters (J. Wiley & Sons, New York, 1939), Vol. 386.

C.B. Millikan, "Some problems in the steady motion of viscous, incompressible fluids; with particular reference to a variation principle." PhD diss., California Institute of Technology, (1928).

P. Monkewitz, “Subharmonic resonance, pairing and shredding in the mixing layer.” *J. Fluid Mech.* **188** 223-252 (1988):

D. Montgomery and G.Joyce, “Statistical mechanics of ‘negative temperature’ states”, *Phys. Fluids*, **17,** 1139 (1974).

D.W.Moore, “The Discrete Vortex Approximation of a Finite Vortex Sheet.”, Calif. Inst. of Tech. Report AFOSR -1804-69 (1971).

P.J. Morris, Philip, M.G. Giridharan and G. M. Lilley, “On the turbulent mixing of compressible free shear layers.”, *Proc. Roy. Soc. London. Series A* **431** (1882), 219-243 (1990).

Y.Naka, K.Tsuboi,Y.Kametani, K.Fukagata and S.Obi, “Near-field Development of a Turbulent Mixing Layer Periodically Forced by a Bimorph PVDF Film Actuator”, *J.Fluid.Sci.Technol*., **5**, 156 (2010).

R. Narasimha, “The utility and drawbacks of traditional approaches”, *Lecture Notes in Physics*, **357**, 13, (1990)

R. Narasimha and A. Prabhu. “Equilibrium and relaxation in turbulent wakes.” *J. Fluid Mech.* **54** (01), 1-17 (1972).

R. Narasimha, A. Roshko, and M.Gharib, “Hans W. Liepmann, 1914-2009”, *Annu. Rev. Fluid Mech*. **45** (2013).

C.L.M.H Navier, “Memoire sur les lois du mouvement des fluids” *Mem acad. R. sci. paris*, 6, 389-416 (1823)

V.W. Nee and L.S.G. Kovasznay, “Simple phenomenological theory of turbulent shear flows” *Phys. Fluids* **12** (3), 473 (1969).

P.K. Newton, *The N-Vortex Problem: Analytical Techniques*, Springer-Verlag, Applied Mathematical Sciences Vol. 145, May 2001.

E.A. Novikov and Yu.B. Sedov, “Stochastic properties of a four-vortex system” *Sov. Phys. JETP* **48**,440 (1978).

L. Onsager, “Statistical hydrodynamics”, *Nuovo Cimento Suppl.* **6**, 279 (1949).

D. Oster and I.Wygnanski, “The forced mixing layer between parallel streams”, *J. Fluid Mech.* **123**, 91 (1982).

C. Pantano and S. Sarkar, “A study of compressibility effects in the high-speed turbulent shear layer using direct simulation”, *J. Fluid Mech.* **451**, 329 (2002).

R.P. Patel, “An experimental study of a plane mixing layer”, *A.I.A.A. J* . **11**, 67 (1973).

U.Paul and R.Narasimha, “The vortex sheet model for a turbulent mixing layer.”, *Phys. Scr*. T155. 014003, 1-7 (2013).

J. Pedlosky, *Geophysical Fluid Dynamics 2nd ed*. (Springer, Verlag, New York, 1987).

P.A. Raviart, *An analysis of particle methods*, in *Numerical methods in fluid dynamics*, Vol. 1127 des Lectures Notes in Mathematics Series." Springer-Verlag, Berlin (1983).

Lord Rayleigh, “On the stability, or instability, of certain fluid motions.” *Proceedings of the London Mathematical Society* **1**(1), 57-72 (1879).

O. Reynolds, "On the dynamical theory of incompressible viscous fluids and the determination of the criterion.", *Phil. Trans. Roy. Soc. London. A*: 123-164 (1895).

R. Robert and J. Sommeria, “Statistical equilibrium states for two-dimensional flows”, *J. Fluid Mech.* **229**, 291 (1991).

M.M. Rogers and R.D. Moser, “Direct simulation of a self-similar turbulent mixing layer”, *Phys. Fluids.* **6** (2), 903 (1994).

L. Rosenhead, “The formation of vortices from a surface of discontinuity”, *Proc. R. Soc. Lond. A* **134**, 170 (1931).

A. Roshko, “On the problem of turbulence.”, *Current Science* **79** (6), 834-839 (2000).

C.M. Sabin, "An Analytical and Experimental Study of the Plane, Incompressible, Turbulent Free Shear Layer with Arbitrary Velocity Ratio and Pressure Gradient," AFOSR TN 5443, Air Force Office of Scientific Research (Oct. 1963).

P. Sagaut. *Large eddy simulation for incompressible flows.* Heidelberg: Springer-Verlag, 2002.

M.M. Sano, “Kinetic theory of point vortex systems from the Bogoliubov-Born-Green-Kirkwood-Yvon hierarchy”, *Phys. Rev. E* **76,** 046312 (2007).

H. Schlichting, *Boundary Layer Theory*, 4th ed. McGraw-Hill (1960).

P.J. Schmid and D. S. Henningson. *Stability and transition in shear flows.* Vol. 142. Springer, (2001).

L. Shirkov and V. Berdichevsky, “Comparison of three-dimensional and two-dimensional statistical mechanics of shear layers for flow between two parallel plates” arXiv:0903.1760v2 (2009).

J.H. Silvestrini, “Dynamics of coherent vortices in mixing layers using direct numerical and large-eddy simulations”, *J. Braz. Soc. Mech. Sci.* **22**(1) (2000).

S. Sohn and W. Hwang, “Numerical simulations of vortex sheet evolution in stratified shear flow “, *J. Phys. Soc. Jpn*, **74**(5), 1472 (2005).

S. Sohn, D. Yoon and W. Hwang, “Long-time simulations of the Kelvin-Helmholtz instability using an adaptive vortex method”, *Phys. Rev. E* **82**, 046711 (2010).

J. Sommeria, C. Staquet and R. Robert, *J. Fluid Mech.* “Final equilibrium state of a two-dimensional shear layer”, **233**, 661 (1991).

W.B. Spencer and B. G. Jones, “Statistical investigation of pressure and velocity fields in the turbulent two-stream mixing layer”. A.I.A.A. Paper, 71-613(1971).

G.G. Stokes, “On the theories of the internal friction of fluids in motion, and of the equilibrium and motion of elastic solids”, *trans. Camb. Phil. Soc.*, 8, 287-305 (1845)

M. Sunyach, “Contribution a 1’étude des frontiéres d’écoulements turbulents libres”, D.Sc. thesis, L’Université Claude Bernard de Lyon (1971).

M.Tanahashi, S.Iwase and T.Miyauchi, “Appearance and alignment with strain rate of coherent fine scale eddies in turbulent mixing layer”, *J.Turbulence*, **2** (2001)

A. Townsend, *The Structure of Turbulent Shear Flow* (Cambridge Univ. Press 1956).

M. Van Dyke, *Perturbation Methods in Fluid Mechanics* (Academic Press, New York 1964).

C.D. Winant and F.K. Browand, “Vortex pairing: the mechanism of turbulent mixing-layer growth at moderate Reynolds number”, *J. Fluid Mech.* **63**, 237 (1974).

I. Wygnanski, I and H. E. Fiedler. "The two-dimensional mixing region." *J. Fluid Mech.* **41** (02), 327-361 (1970).

I. Wygnanski, D. Oster, H. Fiedler and B.Dziomba, “On the perseverance of a quasi-two-dimensional eddy-structure in a turbulent mixing layer”, *J. Fluid Mech.* **93**, 325 (1979).

A.J. Yule, “Two-dimensional self-preserving turbulent mixing layers at different free stream velocity ratios”, *Aero. Res. Counc. R. & M.* 3683 (1972).

APPENDIX A: Accuracy, conserved quantities and Recurrence

A1. Accuracy

One way of assessing the accuracy of the present simulations is to observe the behavior of the statistics of interests for different time-steps (Δt) and precisions. We compute case R4-1600 listed in Table 3.1, for time-steps of 0.025, 0.1, 1, 4 $l/\Delta U$. Results for momentum thickness are presented in Fig.A1 and A2 and results for single and two-vortex distributions are presented in Figs. A3 and A4 respectively. Note that there is hardly any variation in the statistics of interest between Δt = 0.025 and 1.0, the present simulations employ a time-step of $\Delta t = 0.1\ l/\Delta U$.

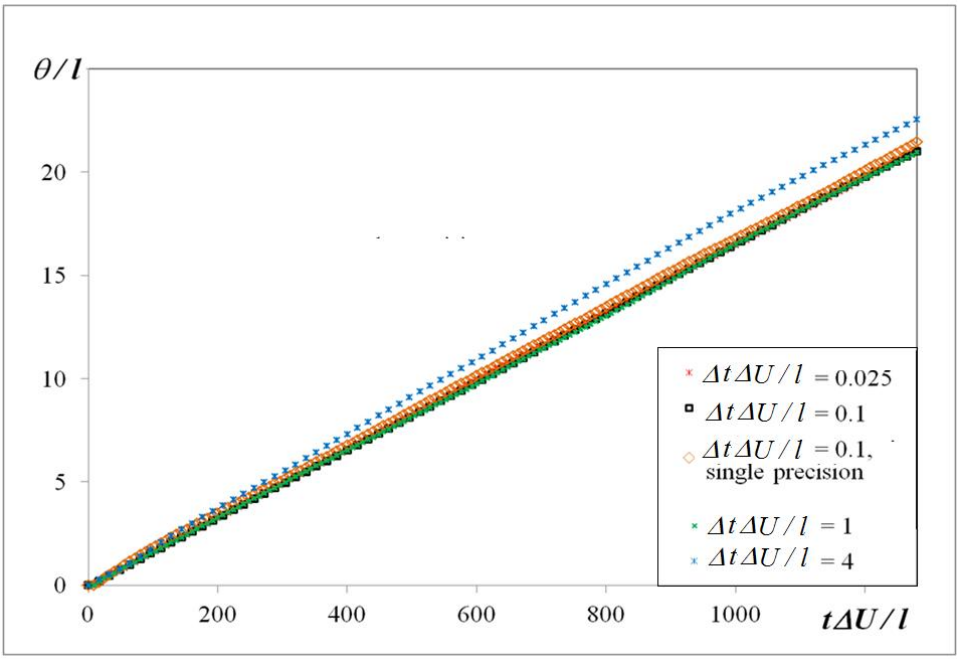

Figure A1. Evolution of Momentum thickness for different time-steps and precisions (R4-1600)

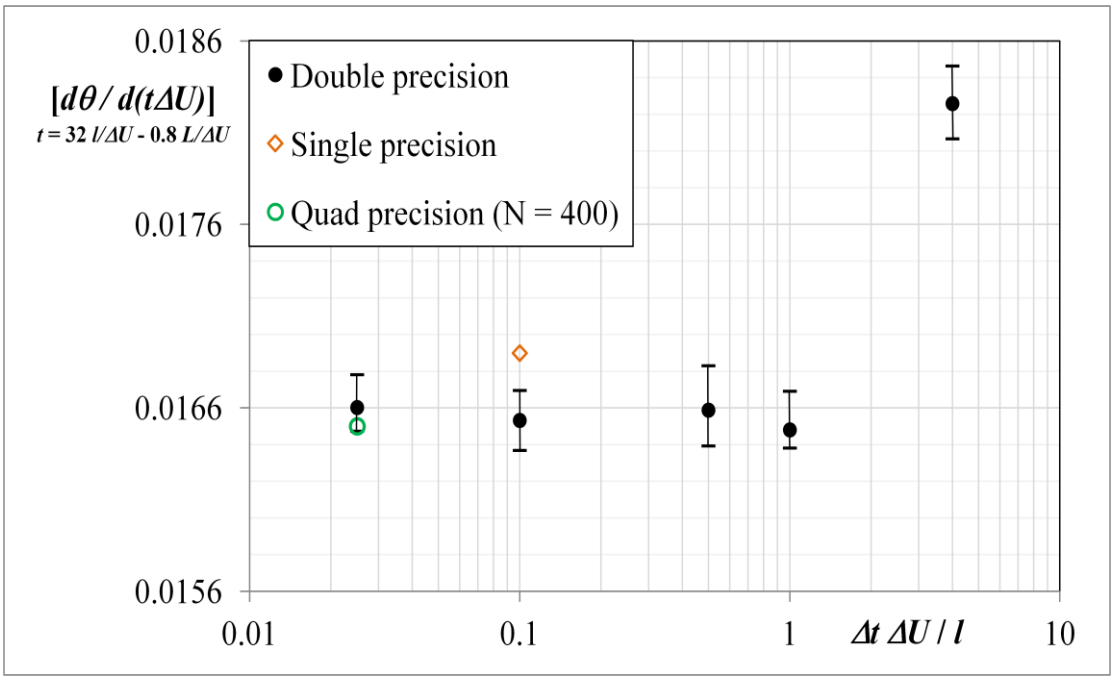

Figure A2. Spread rate computed from best fit over $t\Delta U/l$ = 32 to 1280 for different time-steps and precisions

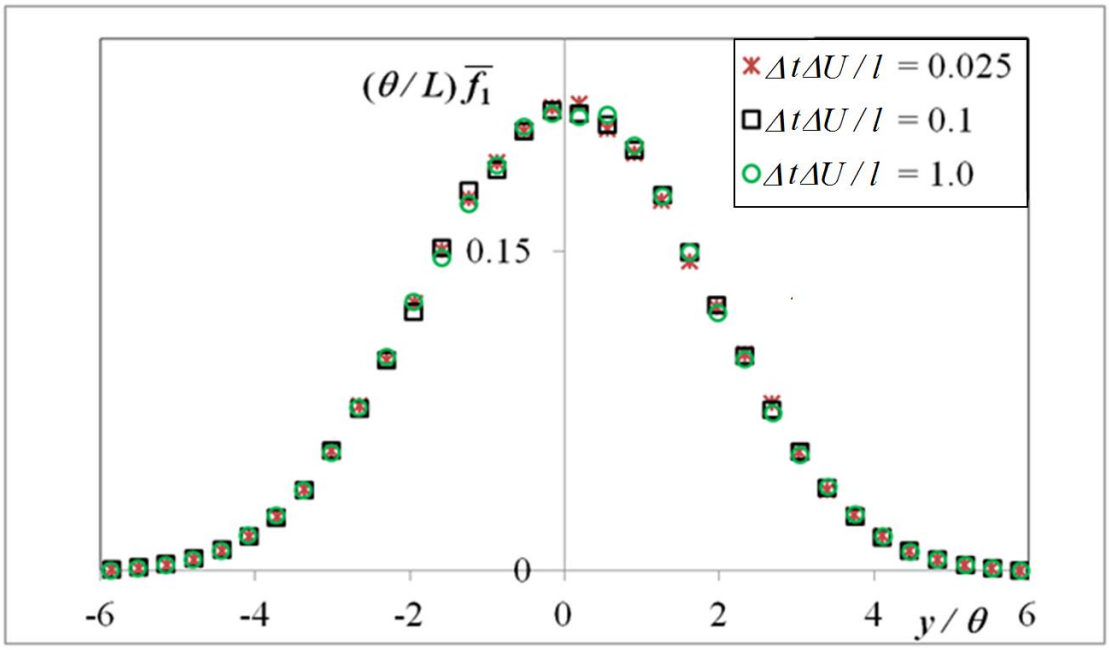

Figure A3. Single particle distribution function computed for simulations with different time-steps (R4-1600 ; $t\Delta U/L$ = 0.8)

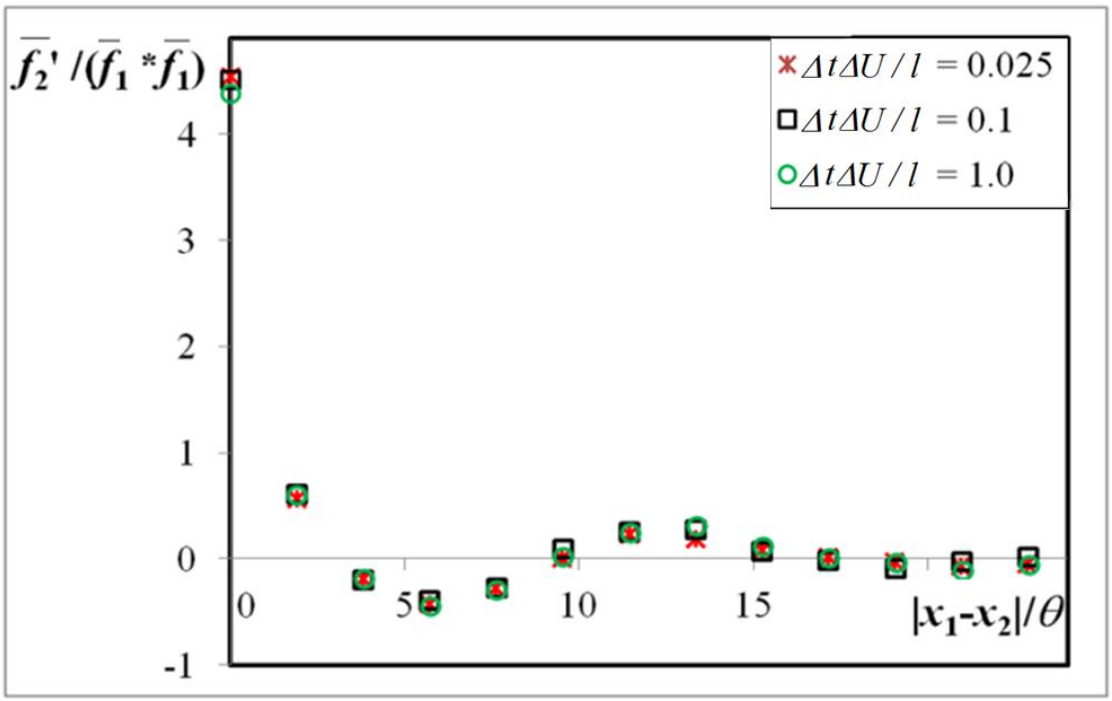

Figure A4. Two particle correlation function computed for simulations with different time-steps (R4-1600 ; $t\Delta U/L$ = 0.8 ; $y_1 = y_2 = 0.18\ \theta$)

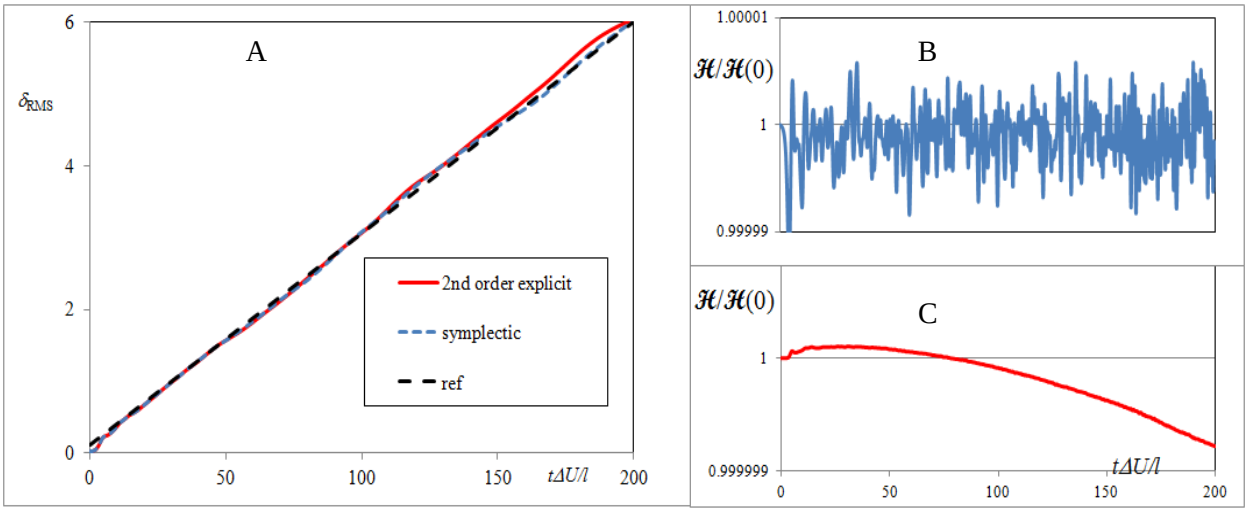

Figure A5. **A**. Robustness of evolution of thickness (δ_{RMS}) to numerical scheme. **B**. Variation of Hamiltonian with time for second order Symplectic scheme C. Variation of Hamiltonian with time for second order explicit (non-symplectic) scheme.

Explicit schemes like the RK-4 employed in this work most often lead to a monotonic decrease of the Hamiltonian with time. Hence a case can be made for the use of phase space preserving symplectic schemes for long-time simulations, as such schemes do not lead to a monotonic change in the Hamiltonian but a fluctuation about its initial value. However, symplectic schemes are often more expensive for any given order of accuracy. Figure A5 shows that for N = 200, a / l = 0.001 the evolution of thickness is nearly identical for both symplectic and nonsymplectic schemes (both second order). Furthermore, the Regime II spread rate observed in both schemes is in excellent agreement with the universal Regime II obtained in the present simulations (RK-4). Hence the additional cost of employing symplectic schemes does not seem to be essential for the statistical evolution of interest.

A2. Conserved quantities

For the present x-periodic system, the Hamiltonian is given by

$$\mathcal{H} = -\frac{\Gamma^2}{8\pi}\sum_{i=1}^{N}\sum_{j=1;j\neq i}^{N}\ln\left(\frac{1}{2}\left[\cosh\left(2\pi\left(y_i-y_j\right)/L\right)-\cos\left(2\pi\left(x_i-x_j\right)/L\right)\right]\right) \quad (A1).$$

$$\frac{d\mathcal{H}}{dt}=\sum_i\left(\frac{\partial\mathcal{H}}{\partial x_i}\frac{dx_i}{dt}+\frac{\partial\mathcal{H}}{\partial y_i}\frac{dy}{dt}\right)=\Gamma\sum_{\mathrm{i}}\left(-\frac{dy_i}{dt}\frac{dx_i}{dt}+\frac{dx_i}{dt}\frac{dy_i}{dt}\right)=0 \qquad (A2)$$

Consider an infinitesimal translation by $\{A_x, A_y\}$ and rotation by an infinitesimal angle Θ of the system

The x and y displacements of the i^{th} vortex are then given by

$$\Delta x_i = A_x - \Theta y_i\,, \qquad \Delta y_i = A_y + \Theta x_i \qquad (A3)$$

The resulting change in the Hamiltonian is given by

$$\Delta\mathcal{H}=\sum_i\left(\frac{\partial\mathcal{H}}{\partial x_i}\Delta x_i+\frac{\partial\mathcal{H}}{\partial y_i}\Delta y_i\right) \qquad (A4)$$

Using Hamilton's equations (5), and substituting (A3) in (A4) we get

$$\Delta\mathcal{H} = \Gamma\left(-A_x\frac{d}{dt}\sum_i y_i + A_y\frac{d}{dt}\sum_i x_i + \Theta\frac{d}{dt}\sum_i\left(\frac{x_i^2+y_i^2}{2}\right)\right) \tag{A5}$$

Explicit evaluation of ΔH by substitution of (A3) in (A1) gives

$$\Delta\mathcal{H} = -\frac{\Gamma^2\Theta}{8\mathrm{L}}\sum_{i=1}^{N}\sum_{j=1;j\neq i}^{N}\left\{\frac{(x_i-x_j)\sinh\left(2\pi(y_i-y_j)/L\right)-(y_i-y_j)\sin\left(2\pi(x_i-x_j)/L\right)}{\cosh\left(2\pi(y_i-y_j)/L\right)-\cos\left(2\pi(x_i-x_j)/L\right)}\right\} \tag{A6}$$

Comparing coefficients of A_x, A_y and Θ in equations (A5) and (A6), we get the conservations laws for the centroids as

$$\frac{d}{dt}\Sigma_i x_i = 0 \tag{A7}$$

$$\frac{d}{dt}\Sigma_i y_i = 0\,, \tag{A8}$$

and the rate of change of the second moment as

$$\frac{d}{dt}\Sigma_i\left(x_i^2+y_i^2\right) = -\frac{\Gamma}{4L}\sum_{i=1}^{N}\sum_{j=1;j\neq i}^{N}\left\{\frac{(x_i-x_j)\sinh\left(2\pi(y_i-y_j)/L\right)-(y_i-y_j)\sin\left(2\pi(x_i-x_j)/L\right)}{\cosh\left(2\pi(y_i-y_j)/L\right)-\cos\left(2\pi(x_i-x_j)/L\right)}\right\} \tag{A9}$$

Hence second moment is not conserved in the present model.

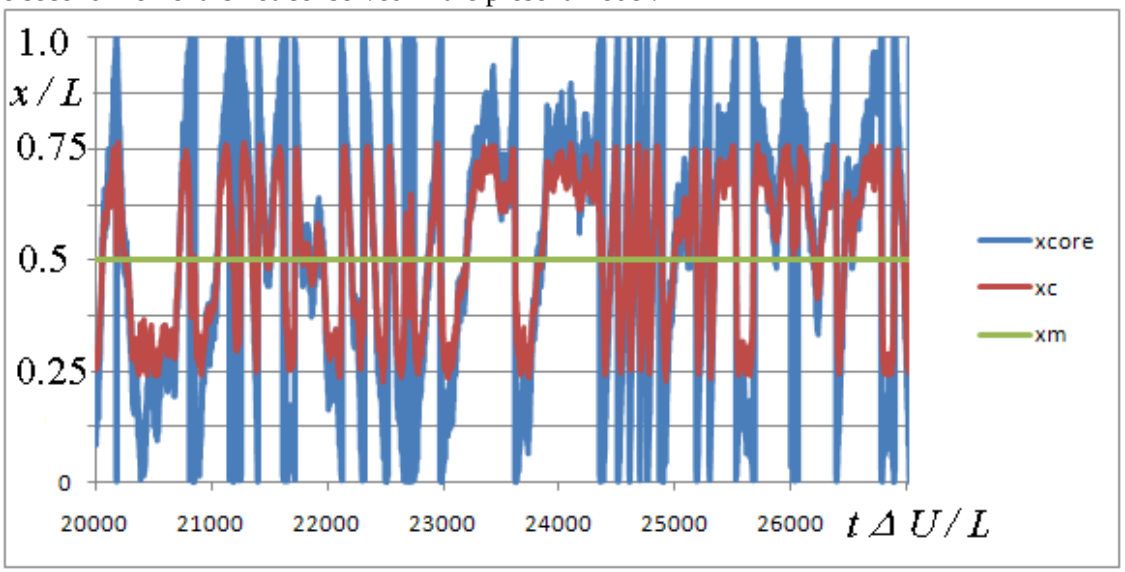

Figure A6. Conservation of x_m and non-conservation of x_c, the projected centroid of the vortices in the domain.

Further, while (A8) implies conservation of the *y*-centroid, there is a subtlety in the conservation of the *x*-centroid. As the present system is periodic in x, $\{x_i\}$ are like angular variables, and hence $x_m = \Sigma_i x_i \bmod L$ is conserved, but the 'projected' centroid of the vortices in the domain, $x_c = \Sigma_i x_i/N$, is not conserved. This is consistent with the results of the present simulations, shown in Figure A6, where x_c fluctuates between 0 and L and is close to the center of the core, x_{core} (except when x_{core} is near $x = 0$ or $x = L$) , while x_{m} is a constant.

A3. Recurrence

We make a few brief remarks on the issue of recurrence. While the Poincare' theorem suggests reversibility, it is well known in statistical mechanics that the recurrence times often increase

exponentially with N and hence can be astronomical for large-N systems (Chandrasekhar, 1943). Hence such a recurrence is not expected to be observed in any realistic-time calculation involving a reasonable value of N. However since Birkhoff and Fisher (1959) suggested that a vortex sheet (discretized using point vortices) will eventually unroll following the Poincare' theorem, we briefly explore this issue even though it is not entirely clear whether the theorem applies to this problem. Further, it is unlikely that any numerical scheme could return a system of point vortices to a close vicinity of the initial state even if the Poincare theorem holds, due to non-zero numerical noise (as discussed in Sec. 2.4). So, we explore this issue using a weak criterion of recurrence, defined by the RMS value of y-positions of the vortices being within a 20 % neighborhood of the initial value. Simulations performed with 4 to 7 vortices show (Fig. A7) that such a weak recurrence does occur (for single realizations) over very long timescales. For $N = 6$, average recurrence time $t_{\mathrm{rec}} \sim 25000\, L/\Delta U$, and is found to increase exponentially with N (Fig. A8). On extrapolation, $t_{\mathrm{rec}} \geq 10^{64}\, L/\Delta U$ for $N \geq 10^2$, which is 60 orders of magnitude longer than the maximum time of integration in the simulations. Further, instability ensures that such an unrolling is immediately followed by rolling. While we cannot be certain that the final state reached in the present simulations is representative of pure Hamiltonian dynamics, the above findings are not inconsistent with the remarks of Birkhoff and Fisher. Thus the present observation of the average equilibrium thickness being much larger than the initial thickness does not necessarily contradict the argument that rolling has to be followed by unrolling at some point of time. Instead, it only suggests that the time spent in the 'unrolled states' is only a very small fraction of the total time and hence is not reflected in the statistics involving long-time averages.

The present finding that recurrence is likely to be observed in only the very remote future is also noted by Birkhoff & Fisher, who say : "*the numerical evidence indicates that effective randomization takes place in a few wave lengths of relative motion. (~ Unrolling ~, however, presumably takes place only in the very remote future or past)*".

We may summarize our view of the Birkhoff-Fisher argument as follows. A vortex sheet approximated by an array of (more than three) point vortices will become chaotic. Our results show that the long-time statistical solutions agree with the Joyce-Montgomery and (an appropriate variant of) the Lundgren-Pointin equilibrium statistical mechanical theories, which are both averages over all microstates on the constant-Hamiltonian surface. This implies that the vortex-gas shear layer visits every microstate including the initial state on the constant-Hamiltonian surface with equal probability, i.e. the system follows micro-canonical ensemble.

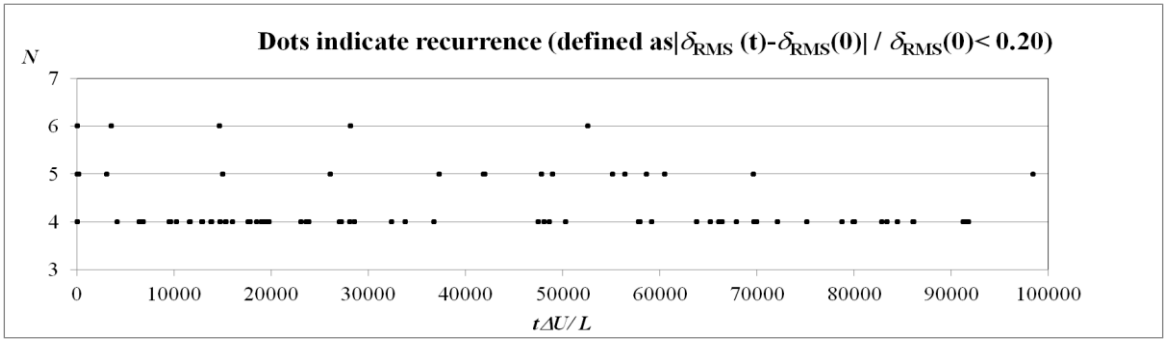

Figure.A7. Recurrence for different N. No recurrence observed for $N > 7$ for $t \leq 10^5\, L/\Delta U$.

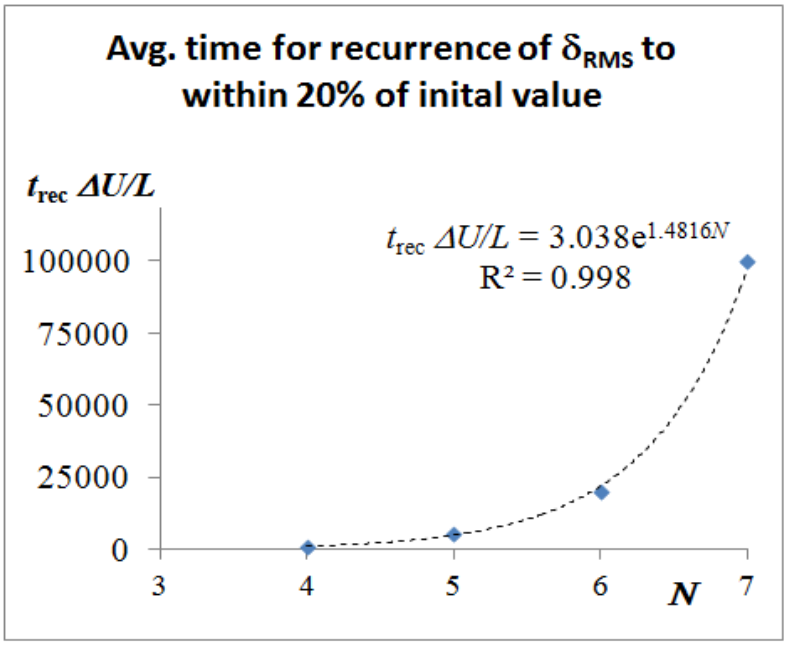

Figure.A8. Exponential increase in recurrence time with *N*.

APPENDIX B :

Some comments on the appropriate thermodynamic limit

Onsager did not deal explicitly with questions of the thermodynamic limit in his paper, but they are important for the statistical mechanics of the vortex-gas. Frohlich and Ruelle (1982) analyzed a neutral vortex-gas for the case in which the energy grows linearly with N when individual vortex strengths are held fixed. (While energy formally scales as N^2, the N^2 terms may cancel out for the neutral case and thus energy may scale as N. But this need not be the case when the positive and negative vortices separate, see Fig B1) Frohlich and Ruelle studied the limit $N \to \infty$ with the average energy per particle E/N and the number density N/A (A is the area of the domain) held fixed without any scaling of γ. They showed that in such a formulation there are no negative temperatures in the thermodynamic limit. Eyink and Spohn (1992) showed that for obtaining negative temperatures energies that scale as N^2 must be considered. Eyink & Sreenivasan (2006) present a review and discussion on the above issues, and state that a nontrivial limit with energy of $O(1)$ can be obtained only if $\gamma \sim O(1/N)$. This limit has often been adopted, including in some recent studies Chavanis(2001). Note that in all of the above mentioned studies, ρ is kept fixed.

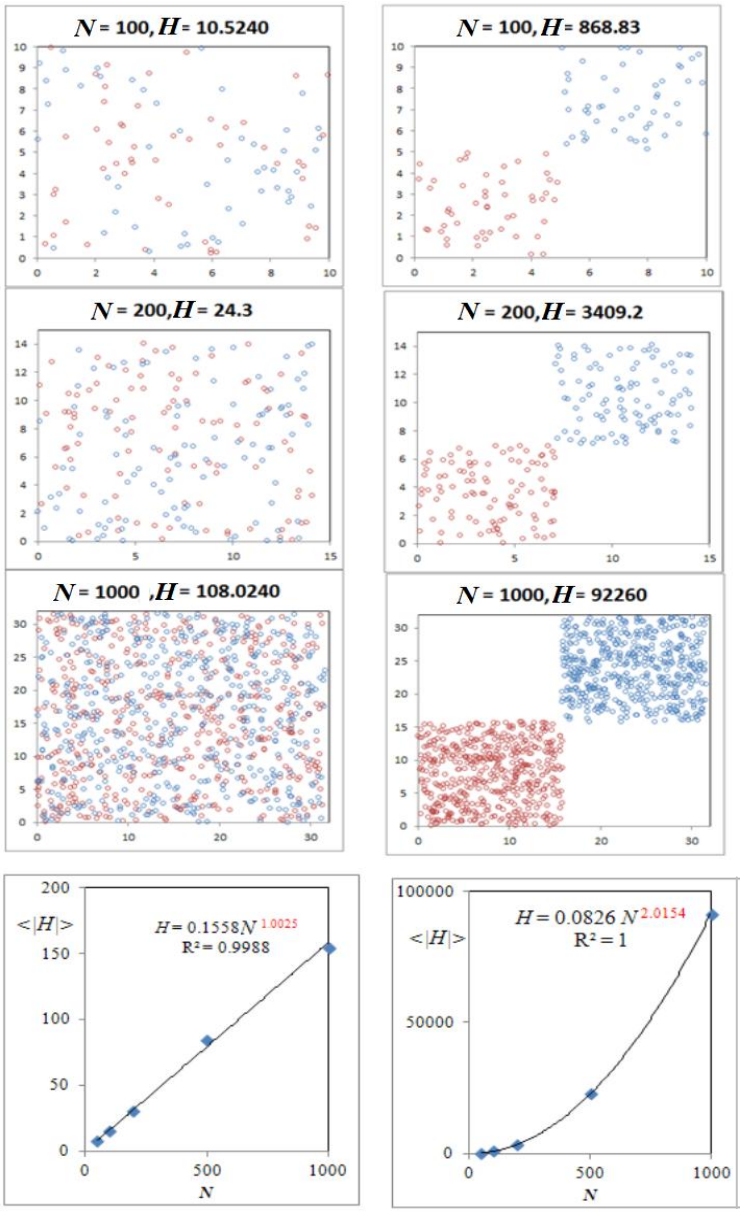

Figure B1. Scaling of Hamiltonian with *N*.

In the free-shear-layer problem all the vortices are of the same sign, and hence there is a well defined total circulation prescribed by the fluid dynamics. Hence, the natural limit is $N \to \infty, \gamma \to 0$ with $N\gamma = L\Delta U$ fixed, as it recovers the continuous vorticity distribution of a temporal shear layer in a given domain L and with a prescribed velocity difference ΔU. Thus both L and ΔU, fixed by the underlying fluid-dynamical problem, are independent of *N*.

If we also adopt the conventional fluid-dynamic definition of energy given by $E = \rho_l \mathcal{H}$, where ρ_l is the density of the fluid (which is independent of the properties of the vortex-gas), the energy scales as $(L\Delta U)^2$ and hence is *N*-independent and non-extensive (in *N*). This leads to the temperature scaling as $\rho_l N\gamma^2 = \rho_l (L\Delta U)^2/N$, which is *N*-dependent and goes to zero in the thermodynamic limit. This is an expected consequence of a non-extensive energy but an extensive entropy. Adopting the fluid dynamically relevant limits therefore leads to `strange thermodynamics'.

However, we must note that just as the temperature of the vortex-gas system (which could be negative) is not related to the temperature of the fluid (which is strictly positive), the energy of the vortex-gas system is not directly related to the energy of the fluid. This also implies that the density in the expressions for energy and temperature need not be related to the density of the fluid. Therefore, one is free to determine an appropriate `density' for the vortex-gas. To do this, we revisit Hamilton's equations (Eqs 2.4, 2.5) and recast them in a form in which the respective quantities have the usual dimensions of position, momentum and energy,

$$\frac{dX_i}{dt} = \frac{\partial E}{\partial Y_i}, \quad \frac{dY_i}{dt} = -\frac{\partial E}{\partial X_i},$$

with positions $X_i = x_i$, momenta $Y_i = \mathcal{A} y_i$ and energy $E = \rho\mathcal{H}$, where $\mathcal{A}$ is a constant factor that provides Y_i the units of momentum and ρ has units of density, so that E has the units of energy. Any rescaling of x_i and y_i by γ-dependent factors implies that such a scaling would be sensitive to the particular limits chosen, and a clear discussion is not straightforward. For the Biot-Savart equations to be recovered, $\mathcal{A}$ should be set to $\gamma\rho$. Since $\mathcal{A}$ is a constant factor, $\rho \sim 1/\gamma$. This `density' does not have a direct physical interpretation (as it is related to neither the number density of the vortices nor the density of the fluid) and only ensures that the transformed quantities in Hamilton's equations for the vortex-gas system have conventional dimensions.

But if we adopt the above definition of density in the expressions for energy and temperature, we find that in the fluid-dynamically relevant limit $\gamma \sim 1/N$, we have $E = \rho\mathcal{H} \sim (1/\gamma)(N^2\gamma^2) \sim NL\Delta U$. This is an extensive energy function, consistent with standard thermodynamics. Temperature scales as $\rho N\gamma^2 \sim N\gamma$, which is a finite non-vanishing *N*-independent fixed quantity $L\Delta U$ even in the limit $N \to \infty$. With this definition of `density', the fluid-dynamically relevant limits are also consistent with standard thermodynamics; and under these limits our simulation results when combined with the Joyce-Montgomery relation also point to the temperature having a linear dependence on $L\Delta U$.

APPENDIX C : Effect of desingularization

Hama & Burke (1960) and Moore (1971) show that an increase in the number of vortices makes the system more chaotic and creates smaller scales (in the perturbation of the discretized vortex sheet). This is understandable as the Kelvin-Helmholtz instability of a vortex sheet leads to fastest growth for the smallest wavelength, which in this case is the inter-vortex spacing. Hence the system of point vortices when used as a discretization of a vortex sheet does not lead to a smooth roll-up. Acton addressed this introducing a cut-off radius following Chorin and Benard (1972).

Krasny (1986) introduced a desingularized version of the governing equations by adding a small positive quantity $(\epsilon/L)^2$ (δ^2 in Krasny's notation) to the kernel (ϵ is proportional to the radius of spread of resulting vorticity field around each vortex in the units of *l*). This prevents arbitrarily large velocities close to each vortex. Hence the governing equations of such an *x*-periodic array of desingularized vortices of are given by

$$\frac{dx_i}{dt} = -\frac{\gamma}{2L}\sum_{j=1,j\neq i}^{N}\frac{\sinh\left(2\pi\left(y_i-y_j\right)/L\right)}{\cosh\left(2\pi\left(y_i-y_j\right)/L\right)-\cos\left(2\pi\left(x_i-x_j\right)/L\right)+(\epsilon/L)^2} \qquad (C1)$$

$$\frac{dy_i}{dt} = \frac{\gamma}{2L}\sum_{j=1,j\neq i}^{N}\frac{\sin\left(2\pi\left(x_i-x_j\right)/L\right)}{\cosh\left(2\pi\left(y_i-y_j\right)/L\right)-\cos\left(2\pi\left(x_i-x_j\right)/L\right)+(\epsilon/L)^{\,2}} \qquad (C2)$$

It is important to note that the Hamiltonian of the point-vortex system is no longer conserved, but it is possible to define an alternate Hamiltonian (C3) that will be conserved by (C1,C2).

$$\mathcal{H}_d = -\frac{\Gamma^2}{8\pi}\sum_{i=1}^{N}\sum_{j=1;j\neq i}^{N}\ln\left(\frac{1}{2}\left[\cosh\left(\frac{2\pi\left(y_i-y_j\right)}{L}\right)-\cos\left(\frac{2\pi\left(x_i-x_j\right)}{L}\right)+\left(\frac{\epsilon}{L}\right)^2\right]\right) \qquad (C3)$$

The solutions of the desingularized equations have the serious disadvantage that they cease to be a weak solution of the Euler equations when inter-vortex distances become comparable with ϵ.

In the designularized system, the vorticity field is no longer a set of delta functions, but is spread over a region around the center of each desingularized vortex. Hence the effective vortex sheet reprented by a row of such desingularized vortices (when the desingularization core is larger than the inter-vortex spacing) has finite thickness and hence is not unstable to small wavelength perturbations of the order of the inter-vortex spacing.

Desingularization therefore 'filters' out the high wave number instabilities and delays the onset of chaos in the system (but as we shall show, only to a finite time depending on the value of ϵ). A physical interpretation of this observation is the following. A desingularized array of vortices with $\epsilon > l$ approximates a thick shear layer (as opposed to a vortex sheet), as the vorticity is no longer confined to points, but over blobs of finite radius. The shear layer of finite thickness is unstable only to wavelengths larger than certain multiple of the thickness (for a piece wise linear shear layer with width δ_ω the smallest unstable wavelength is around 4.9 δ_ω and the most unstable being 7.87 δ_ω, see Chapter 6). Thus when $\epsilon \gg l$, the perturbations with wavelength of $O(l)$ that arise due to discretization are no longer unstable.

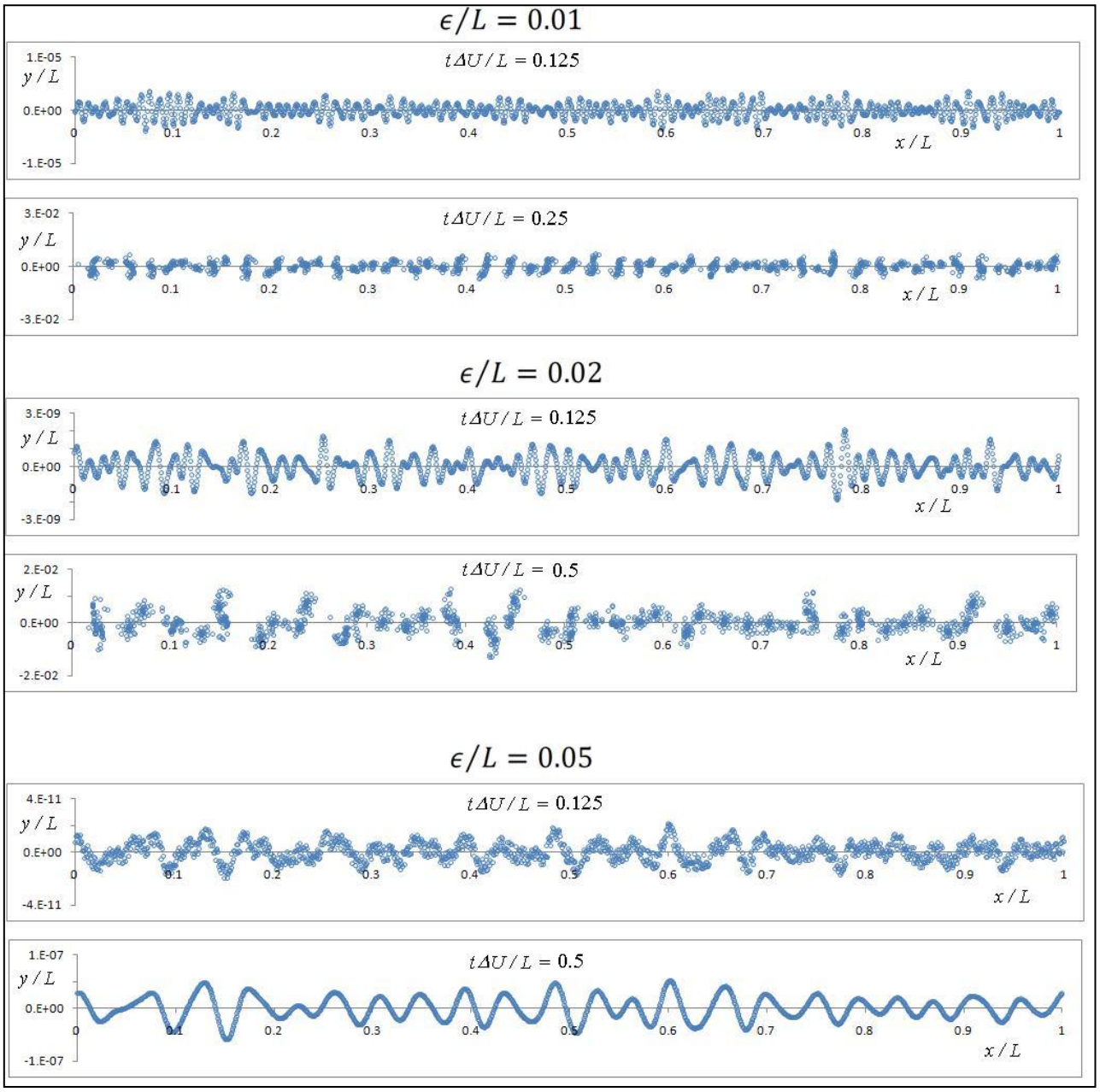

Figure C1. The initial development of the layer with different values on ϵ. (Note that *x* and *y* are not to scale). Note that with larger values of ϵ, the effective thickness (based on the velocity profile) is larger and hence the most unstable wavelength is longer and grows slower.

In order to study the effect of desingularization, simulations of case R3 (see Table 3.1) are carried out for different values of the desingularization parameter ϵ and the results are shown in Figs. C1 and C2. It can be observed that the simulations with desingularization initially grow very slowly. This is because, the fast growing - short (with respect to ϵ) wavelength disturbances in the random initial condition are suppressed as shown in Fig. C2. However, this only increases the duration of Regime I, as once coherent structures are formed (initial size of which depends on the ϵ, see Fig. C1), desingularization does not prevent chaotic interaction of coherent structures.

For ϵ = 0.01 L and $\epsilon = 0.02$ L, it is seen that the layer eventually transitions to the universal chaotic Regime II with a growth rate identical to that observed for the non-desingularized case. However, for $\epsilon = 0.05\,L$, the layer takes longer than $t\Delta U/L$ of 0.8 before onset of chaos and hence Regime II may not be very short or absent (as the onset of Regime III will begin) and is not observed within the extent of the simulation. It can be seen from Fig. C2.B that the evolution of momentum thickness of the

different cases collapse on scaling with ϵ. This is because, ϵ determines the effective thickness (based on the mean velocity profile) of the initial layer and hence the most unstable wavelength and the size and the number of the coherent structures that are initially formed at the end of the first roll up. If ϵ is of the order of L, only very few structures are will be formed in the periodic box and hence the layer will enter Regime III right away. But in the limit we are interested in, namely $L/l \to \infty$ for a given ϵ/l, there will always be sufficient number of coherent structures left in the domain after the first roll-up and subsequent development will be dominated by chaos at the level of the coherent structures which will not be suppressed by desingularization. Hence the conclusions on universality of Regime II are unchanged by desingularization.

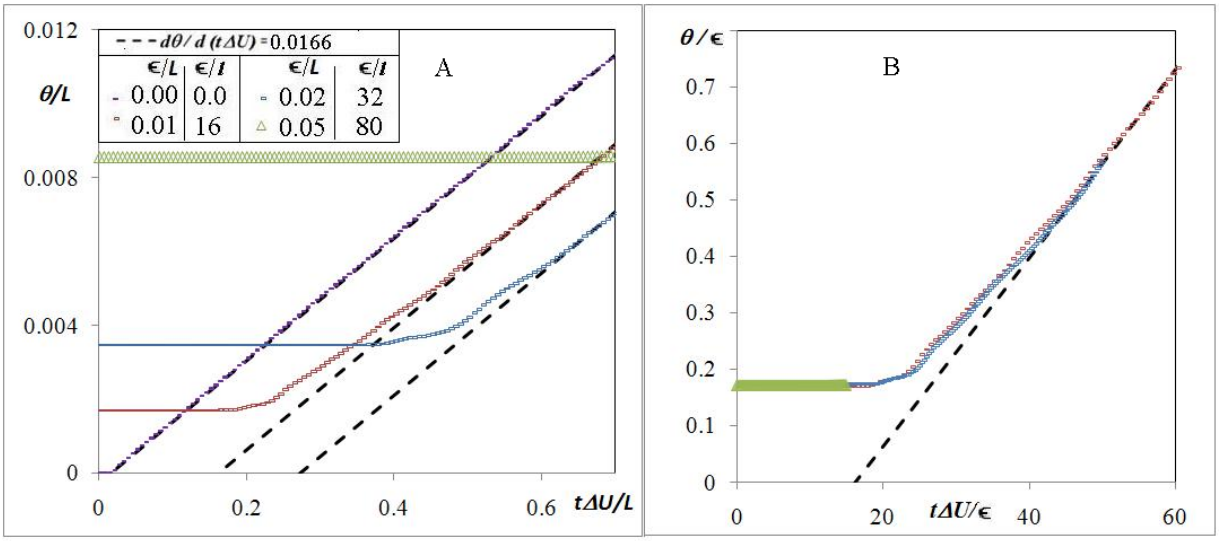

Figure C2. Effect of desingularization. case R3 (Table.3.1) is repeated with different values of desingularization parameter (ϵ). A. Increase in ϵ, while delays (in terms of $t\Delta U/L$ and $t\Delta U/l$) the onset of Regime II, has no influence on the spread rate in Regime II, and hence the observation on universality in the non-equilibrium evolution is unaffected on desingularizing the vortices (with any given ϵ/l at sufficiently large N). B. Scaling based on ϵ. Note that $\theta/\epsilon = F[t\Delta U/\epsilon]$ for $\epsilon \gg a$and $t\Delta U \ll L$.

Figure C3 shows the evolution of a single mode perturbation in a vortex-gas shear layer of finite thickness (analogous to case discussed in Sec. 6.1) for different values of desingularization. It is observed while desingularization suppresses local regions of disorder within the structure, the linear and non-linear evolution of the mode remain unaffected as long as the desingularization radius is less than 20% of the wavelength.

Therefore it may be concluded that the initial condition of an array of point-vortices is chosen to approximate a vorticity field with a well defined finite initial thickness (either by choosing $a >> l$ or employing several rows of vortices as done in Ch.6), desingularization makes no difference even in the initial large scale evolution.

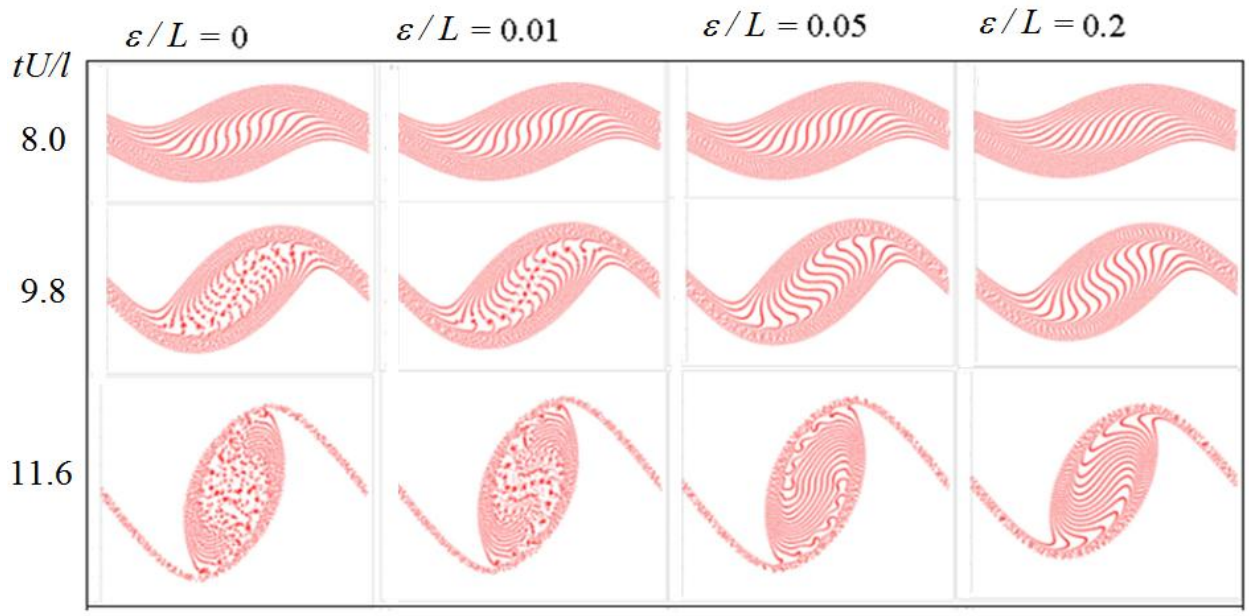

Figure C3. Effect of desingularization on the evolution of a single-mode in a thick vortex-gas free shear layer

In summary, desingularization acts as a proxy for finite thickness and hence suppresses the development of small scales. But as long as the domain is sufficiently large, the desingularized vortex-gas shear layer will be unstable to sufficiently long wavelength disturbances whose evolution is unaffected by desingularization. The subsequent roll-up, formation of coherent structures and the relaxation to the universal Regime II spread rate are observed to be robust to desingularization.

APPENDIX D : Supplementary data for spatial shear layers

Additional data from spatial vortex-gas simulations, not presented in Ch.9 is included here. Some of the following figures support statements, arguments and conclusions discussed in Ch.9 and are referred to i appropriate places.

Effect of upstream and downstream conditions on evolution of layer

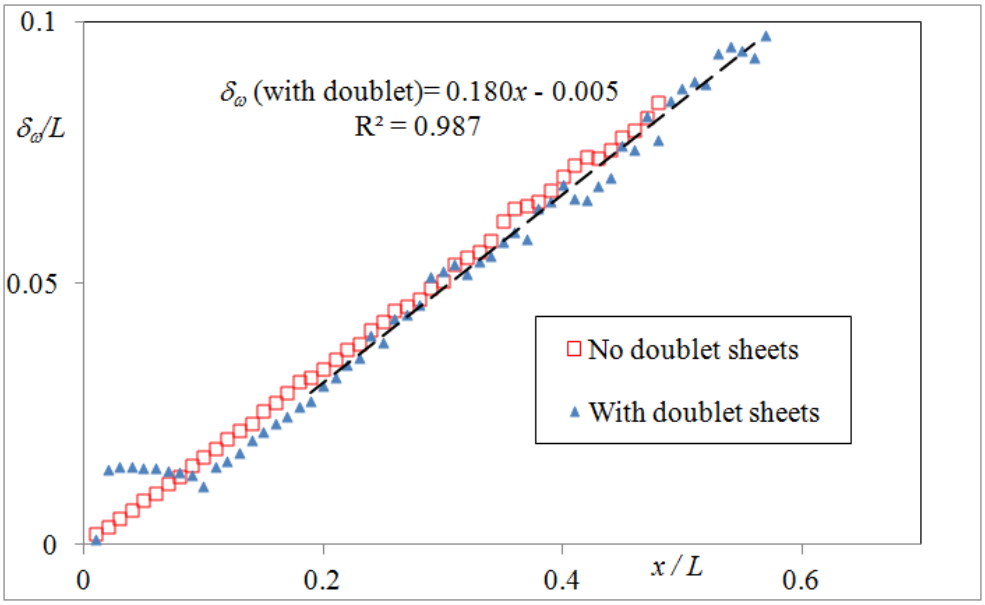

Figure D1. The robustness of self-preservation spread rate to presence of doublet sheets on splitter plate (at λ =1).

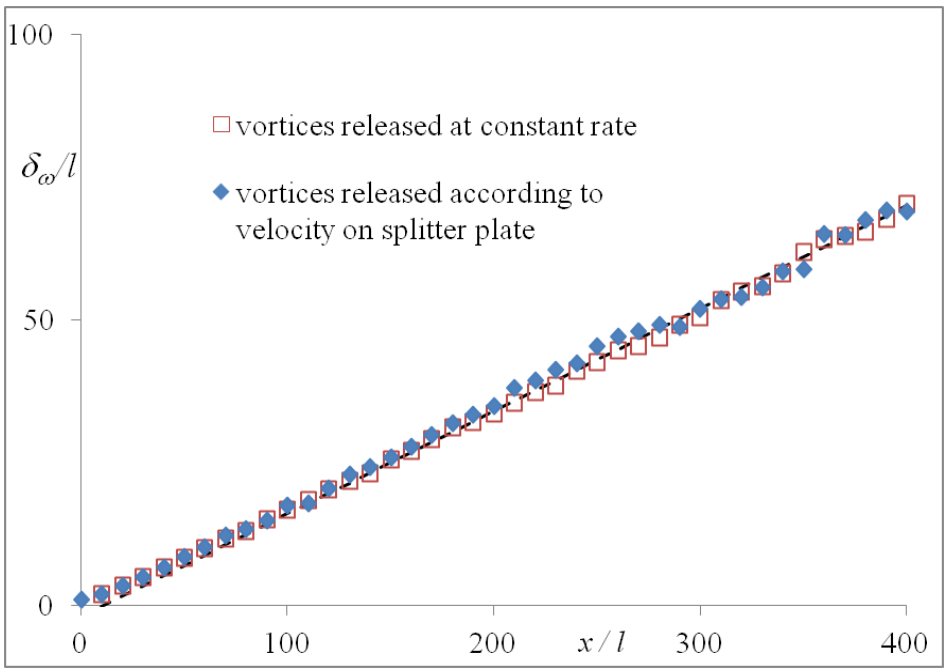

Figure D2. The robustness of self-preservation spread rate on constant or variable rate of vortex-release at the end of the splitter plate (at λ =1).

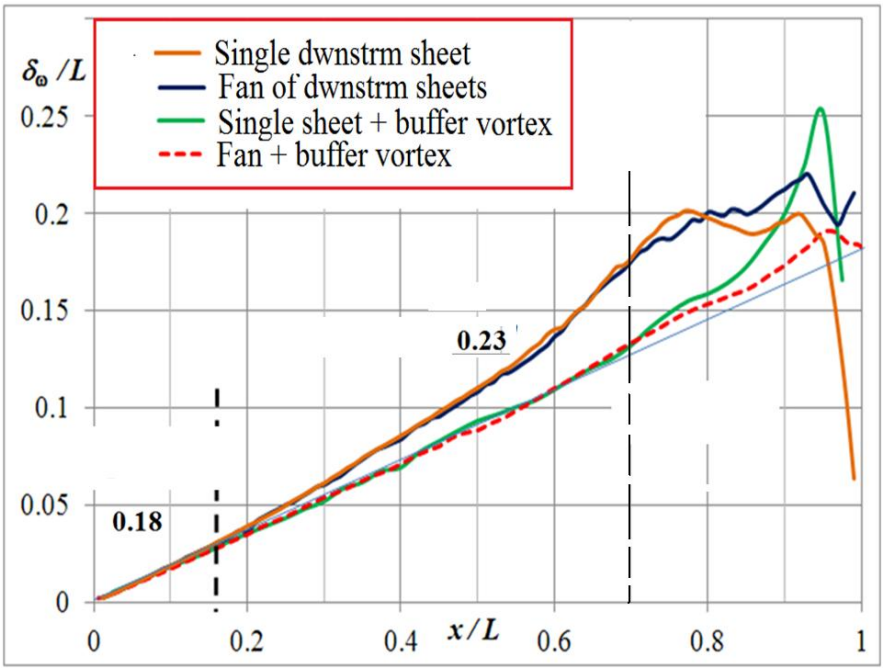

Figure D3. Effect of different downstream boundary conditions on evolution of the layer. Note that the use of a single vortex-sheet or a fan of vortex-sheets is used downstream, affects the spreading of the layer for only $x/L < 0.7$. However, the presence of a buffer vortex alters the spread rate for $x/L > 0.2$.

Supplementary results on structure analysis

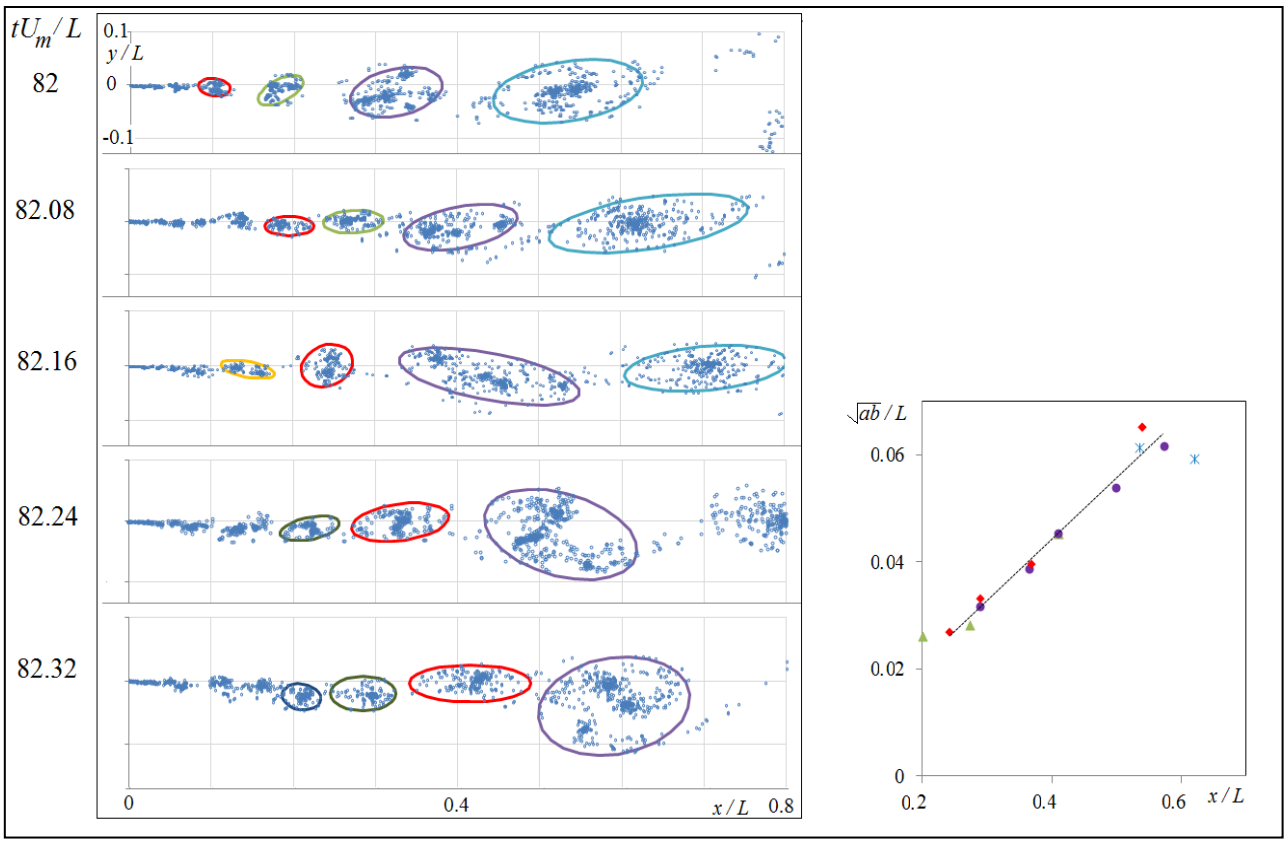

Figure D4. Analysis for λ = 1, shown in Figs. 9.7 & 9.8 for tU_m/L = 98 to 98.4 repeated for tU_m/L = 82 to 82.4. Note the qualitatively similar results are observed, suggesting the robustness of the conclusion on continuous growth of structures at λ = 1.

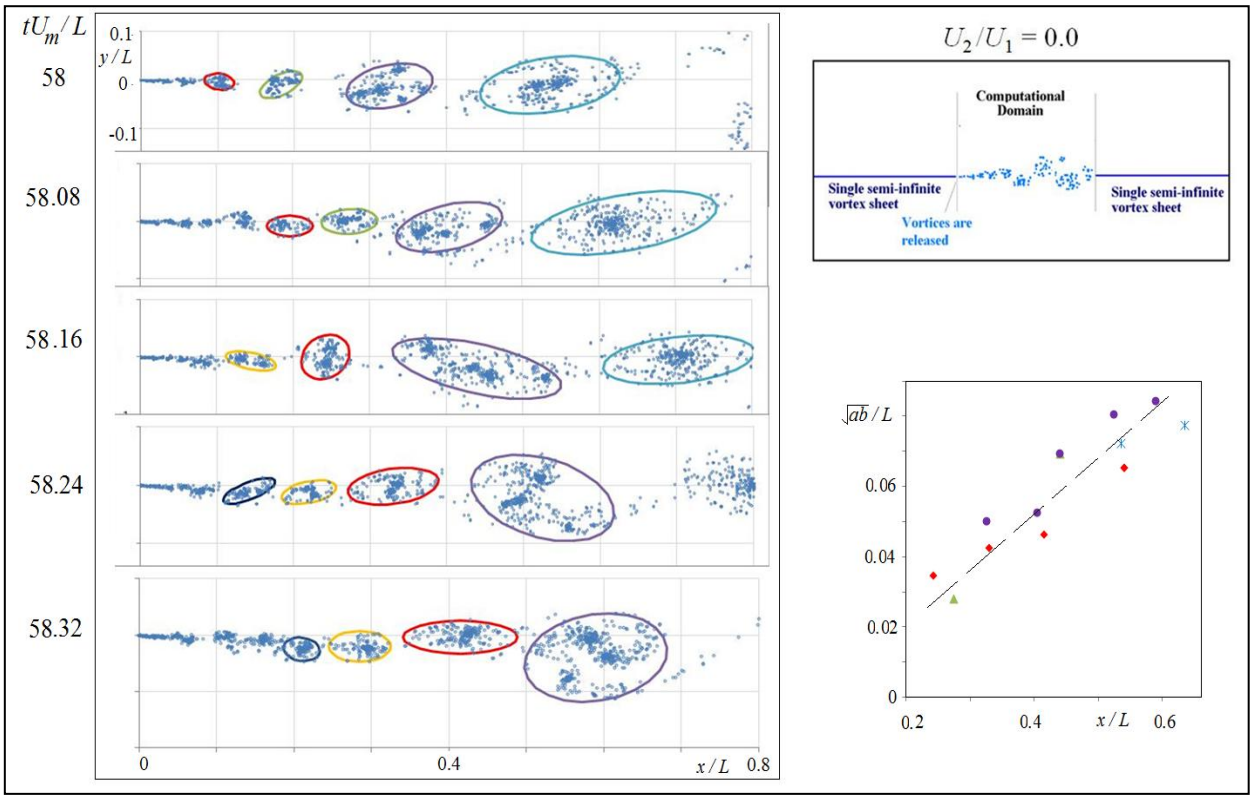

Figure D5. Analysis for λ = 1, shown in Figs. 9.7 & 9.8 for buffer-fan model repeated for a setup with a single downstream vortex-sheet and without doublet. The results suggest the robustness of the conclusion on continuous growth of structures at λ = 1 to different downstream boundary conditions.

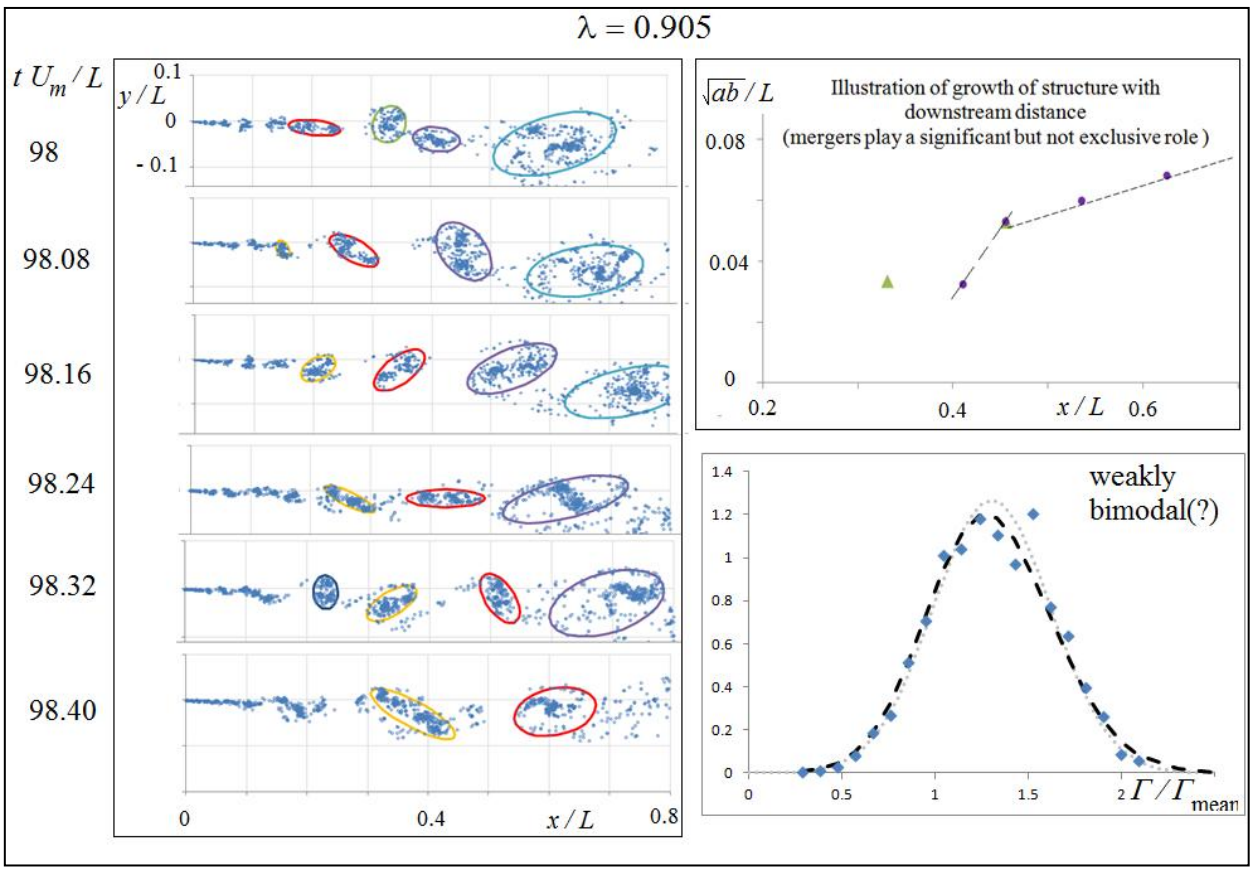

Figure D6. Analysis shown in Figs.9.7 -9. 9 for λ = 0.627, 1 repeated for an intermediate λ = 0.905. The results appear to suggest a mix of the two mechanisms.

Preliminary results on effect of top boundary

Most single-stream experimental setups involve a wall on the side on non-zero velocity at a vertical distance of less than 25% of the length of measurement zone

L+L 1947= 23% ; $x_{max}/y_{wall} \sim 4$
M+F 2003 = 100% ; $x_{max}/y_{wall} \sim 1$
H+Z = 12.5 % ; $x_{max}/y_{wall} \sim 8$
D+Coats 2013 = 14% ; $x_{max}/y_{wall} \sim 7$

Can account for report of higher or lower spreading rate (+/- 25%) !

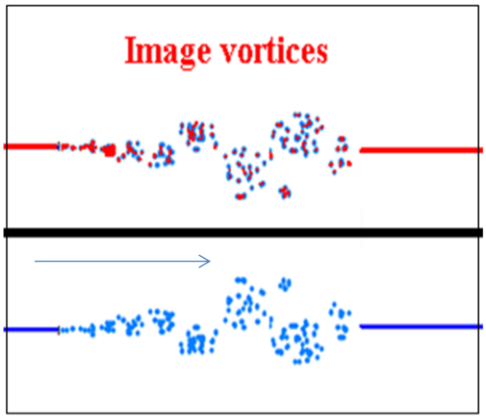

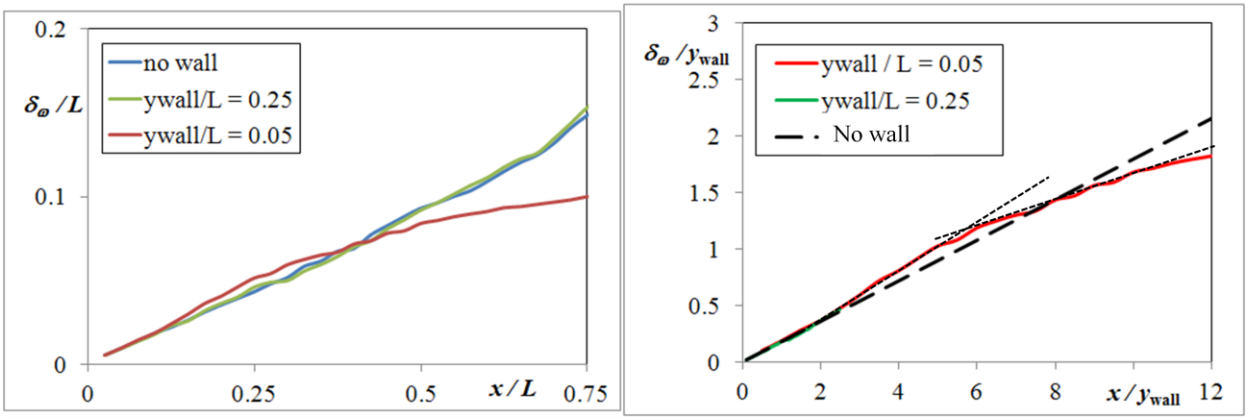

Figure D7. Effect of top wall on evolution of single-stream vortex-gas shear layer.

APPENDIX E : Comparison of Regime III(c) with the Stuart solution

A variant of equation (4.3) was solved by Stuart (1967) for the present boundary conditions (periodic in x, infinite domain in y) in the context of nonlinear stability, and the solution has been reproduced in Sommeria et al (1991).

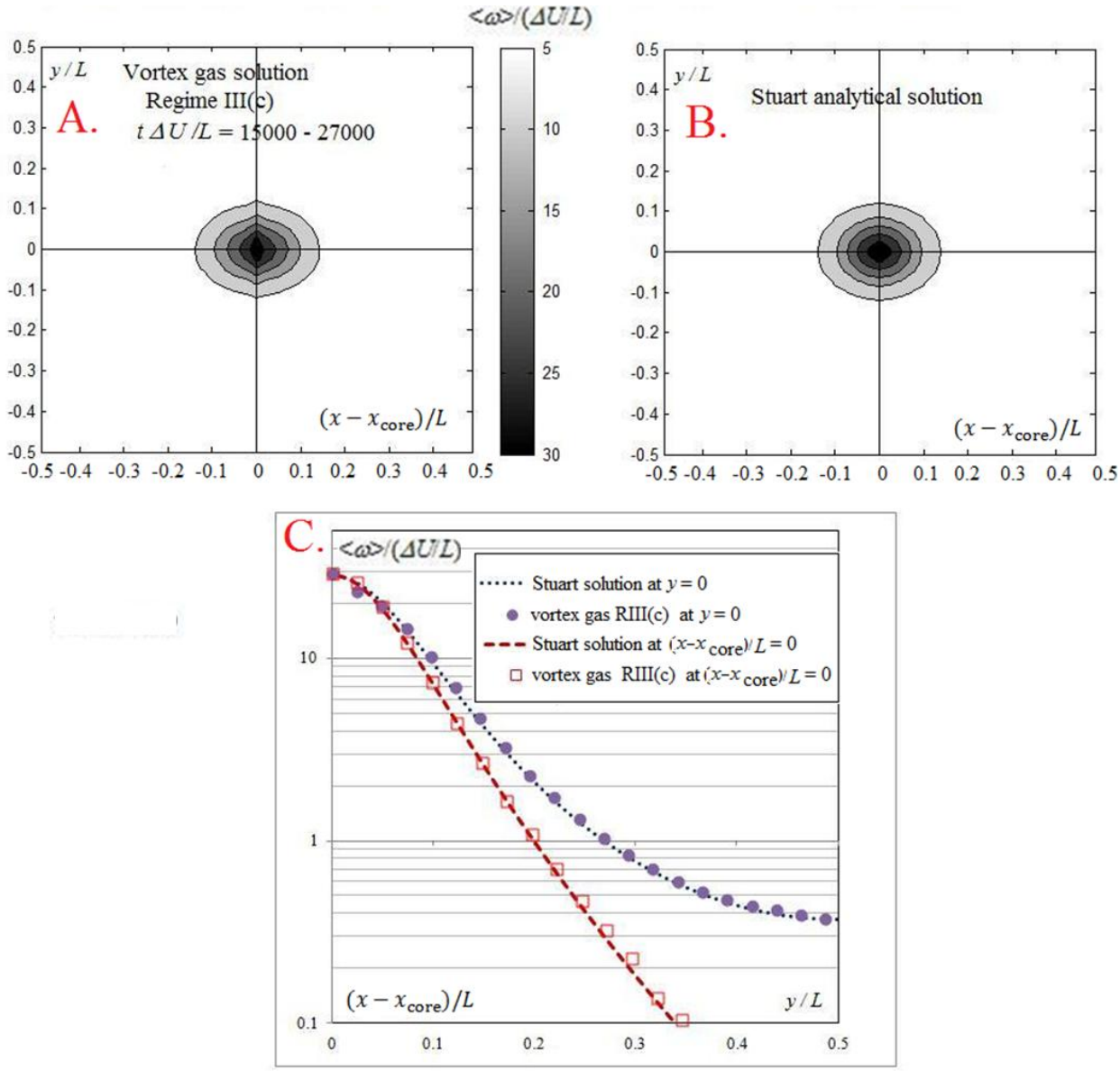

Figure E1. Comparison with the Stuart solution**. A.** Contour plot of f_1 for Regime III(c) (averaged over $t\Delta U/L$ = 15000 to 27000). **B.** Contour plot of the Stuart solution (Eqn. E1). **C.** Comparison of vortex-gas RIII(c) and the Stuart solutions along the x and y axes.

J.T. Stuart, "On finite amplitude oscillations in laminar mixing layers." *J. Fluid Mech.* **29** (3), 417-440 (1967).

In the present notation, the Stuart solution would be

$$f_1 = \frac{2k_1^2(2\pi)^2}{-BL\Delta U\left(C_1 cosh(2\pi k_1 y/L) + \sqrt{C_1^2 - 1}\, cos(2\pi k_1(x - x_{\text{core}} + 1/2)/L)\right)^2} \qquad (E1)$$

where C_1 is an adjustable constant and k_1 is any integer (that represents the period of the solution in *x*). The value of C_1 depends on the initial energy, and it was shown (Sommeria et al, 1991) that for thin strips of vorticity, like the one considered in case 400a, $C_1 \to \exp(1/2)$. We take $k_1 = 1$ (as there is a single structure in the domain) and $-BL\Delta U = 24.3$ (as estimated by the best fit in Fig. 4.13). The solution (E1) is shown in Fig.E1 and is compared with the Regime III(c) solution for the vortex gas (case 400a, same data as shown in Figs. 4.12 - 4.14).

It can be observed from Fig. E1 that the present numerical solution agrees very closely with the analytical solution of Stuart, and this taken along with the agreement observed in Figs. 4.13 and 4.14, suggest that Regime III(c) represents the final maximal entropy state of the system. It is remarkable that a solution derived in the context of nonlinear stability of a laminar mixing layer can be tied so closely to the equilibrium state of a turbulent vortex-gas free shear layer and Onsager's statistical mechanics of point-vortices.

Prof. Sommeria is gratefully acknowledged for suggesting this comparison.

An ode to
Life, Complexity and the Pursuit of Understanding
via the Vortex Gas

Life is full of complexities,
A mix of tragedies and comedies,
The joy and sorrow; pleasure and pain,
Love and hate, all for gain.

There are friends and family,
Queen and country,
There are factions and nations,
All with different denominations.

Some things are sweet but some things are sour,
There are the rich and there are the poor,
Those who believe and others who don't,
Lots of events which we want to note!

There are the tigers and the deer,
Exotic places, far and near,
The Sun and the wind that's dry
The stars in the clear night sky!

There are also clouds – white, black and gray,
Some bring rain which makes me say 'Hurray!'
From the Galaxies to the microbes, each of us has a story,
In this universe that's full of mystery !

All of this and all of this
Is but an interaction of particles,
To appreciate we may fail,
It's all just mechanics at a microscale

In order to appreciate this lore,
Check out the vortex gas,
It's a bunch of vortices and nothing more,
But you will begin to understand as you gaze.

There are structures and there are braids,
There are mergers and there are splits
There is peace and there is violence
The system is full of exuberance

There is chaos and nothing seems trivial,
But some things are mysteriously universal,
All this and many more sensations,
Are all created by simple interactions.

- Saikishan Suryanarayanan